

**National University of Ireland, Maynooth
Doctorate of Philosophy**

**Electrochemical Deposition of
Copper and Zinc Nanomaterials at
Polypyrrole Thin Films**

Enrico Andreoli, M.Sc.

Supervisors

Professor Carmel B. Breslin

Doctor Denise A. Rooney

Ph.D. Thesis

2010

Electrochemical Deposition of Copper and Zinc Nanomaterials at Polypyrrole Thin Films



NUI MAYNOOTH

Ollscoil na hÉireann Má Nuad

Enrico Andreoli, M.Sc.

**Department of Chemistry
National University of Ireland Maynooth**

September 2010

**Thesis Submitted to the National University of Ireland in Fulfillment
of the requirements for the Degree of Doctor of Philosophy**

Supervisors: Prof. Carmel B. Breslin and Dr. Denise A. Rooney

Head of Department: Prof. John Lowry

Table of Contents

Declaration.....	v
Acknowledgments.....	vi
Dedication.....	vii
Abstract.....	viii
1. Introduction and Literature Review.....	1
1.1 Research Topic and Relevance.....	2
1.2 Objectives and Achievements.....	2
1.3 Electrochemical Deposition.....	3
1.3.1 Overview of Electrochemical Deposition.....	3
1.3.2 Electrochemical Deposition on Conducting Polymers.....	4
1.3.3 Electrochemical Fabrication.....	4
1.4 Conducting Polymers.....	5
1.4.1 Conducting Polymers.....	5
1.4.1.1 Structures and Electronic Properties.....	6
1.4.1.2 Charge Transport Entities and Mechanisms.....	11
1.4.1.3 Synthesis, Properties and Applications.....	17
1.4.2 Polypyrrole.....	19
1.4.2.1 Synthesis, Properties and Morphology.....	20
1.4.2.2 Electrical Conductivity and Band Structure.....	26
1.4.2.3 Doping, redox switching and ion-exchange properties.....	27
1.4.2.4 Oxygen Reduction Reaction at PPy Film-Modified Electrodes.....	29
1.5 Electrochemistry of Copper and Zinc.....	32
1.5.1 Electrochemistry of Copper.....	32
1.5.1.1 Electronic Structure and Oxidation States of Copper.....	32
1.5.1.2 Electrochemistry of Copper.....	32
1.5.2 Electrochemistry of Zinc.....	36
1.5.2.1 Electronic Structure and Oxidation States of Zinc.....	36
1.5.2.2 Electrochemistry of Zinc.....	36
1.6 Copper and Zinc Micro/Nanostructures.....	39
1.7 References.....	40
2. Experimental.....	52
2.1 Introduction.....	53
2.2 Electrochemical Setup.....	54
2.3 Chemicals and Synthesis.....	57

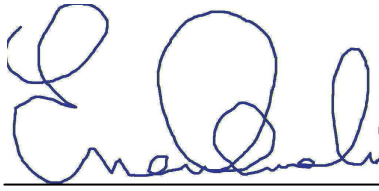
2.3.1	Chemicals.....	57
2.3.2	Synthesis of MWNT-PEI.....	57
2.3.3	Preparation of MWNT-PEI Aqueous Solution.....	58
2.4	Preparation and Characterization of Modified PPy-PSS Films	58
2.4.1	Electropolymerizations	58
2.4.1.1	Preparation of PPy-PSS Thin Films	58
2.4.1.2	Preparation of PPy-PSS-MWNT-PEI Composite Films	59
2.4.2	Electrochemical Depositions	60
2.4.2.1	Deposition of Copper-Based Micro/Nanostructures	60
2.4.2.2	Deposition of Zinc-Based Nanothin Sheets and Conversion to Metallic Zinc Micro-Dendrites	60
2.4.2.3	Fabrication of Copper-Based Microstructures	60
2.4.2.4	Formation of Metallic Copper Nanoparticles.....	61
2.4.3	Nitrate Sensing with Metallic Copper Nanoparticles Modified Electrodes.....	61
2.4.4	Catalytic Reduction of Oxygen at PPy-PSS Thin Films.....	62
2.5	Experimental Techniques.....	62
2.5.1	Experimental Equipment	62
2.5.1.1	Electrochemistry	62
2.5.1.2	Microscopy and EDX Analysis	63
2.5.1.3	Spectroscopy and X-Ray Diffraction	63
2.5.2	Electrochemical Methods.....	64
2.5.2.1	Constant Potential Amperometry	64
2.5.2.2	Cyclic Voltammetry	67
2.5.2.3	Rotating Disk Voltammetry.....	69
2.5.2.4	Electrochemical Quartz Crystal Microbalance.....	70
2.5.2.5	Electrochemical Impedance Spectroscopy	72
2.5.3	Microscopic Methods.....	77
2.5.3.1	Scanning Electron Microscopy and Energy Dispersive X-Ray Analysis.....	77
2.5.4	Spectroscopic and Diffractive Methods.....	82
2.5.4.1	Attenuated Total Reflectance Infrared Spectroscopy.....	82
2.5.4.2	Raman Spectroscopy	84
2.5.4.3	X-Ray Photoelectron Spectroscopy.....	88
2.5.4.4	X-Ray Diffraction.....	91
2.6	References	93

3. Electrochemical Deposition of Hierarchical Micro/Nanostructures of Copper Hydroxysulfates at Polypyrrole-Polystyrene Sulfonate Films.....	95
3.1 Introduction	96
3.2 Results and Discussion.....	98
3.2.1 Electrodeposition of Hierarchical Copper-Based Micro/Nanostructures	98
3.2.1.1 PPy-PSS Electrochemical Polymerization and Properties	98
3.2.1.2 Electrochemical Deposition of Hierarchical Copper-Based Micro/Nanostructures	101
3.2.2 Characterization of Hierarchical Copper-Based Micro/Nanostructures	106
3.2.2.1 Cyclic Voltammetry	106
3.2.2.2 X-Ray Diffraction.....	109
3.2.2.3 Electrochemical Quartz Crystal Microbalance.....	115
3.2.2.4 Energy Dispersive X-Ray Analysis.....	119
3.2.2.5 X-Ray Photoelectron Spectroscopy.....	123
3.2.2.6 Attenuated Total Reflectance Infrared Spectroscopy.....	128
3.2.2.7 Raman Spectroscopy	135
3.2.3 Mechanism of Deposition of Hierarchical Copper-Based Micro/Nanostructures	137
3.2.3.1 Mechanism of Formation and Hierarchical Arrangement.....	137
3.2.3.2 Mechanism of Nucleation and Growth.....	140
3.2.4 Oxygen Reduction at Polypyrrole-Polystyrene Sulfonate Films.....	144
3.3 Summary	148
3.4 References	151
4. Electrochemical Conversion of Hierarchical Copper Micro/Nanostructures to Metallic Copper Nanoparticles and their Application to Nitrate Sensing	154
4.1 Introduction	155
4.2 Results and Discussion.....	157
4.2.1 Effect of the Potential on the Electrodeposition of Copper Materials .	157
4.2.2 Fabrication of Hybrid Copper-Based Microstructures	161
4.2.3 Conversion of Hierarchical Copper-Based Micro/Nanostructures to Metallic Copper Nanoparticles	163
4.2.4 Preparation of Metallic Copper Nanoparticles at Polypyrrole-Polystyrene Sulfonate PEI-Multiwall Carbon Nanotube Nanocomposite Films.....	168
4.2.5 Nitrate Sensing with Metallic Copper Nanoparticle Modified Electrodes.....	172

4.2.5.1	PPy-PSS-CuNP Modified Electrode	172
4.2.5.2	PPy-PSS-MWNT-PEI-CuNP Modified Electrode	175
4.2.6	Electrochemical Impedance Analysis and Comparison of PPy-PSS and PPy-PSS-MWNT-PEI Thin Films	182
4.2.6.1	PPy-PSS Modified Electrodes	183
4.2.6.2	PPy-PSS-MWNT-PEI Modified Electrodes	191
4.2.6.3	Influence of MWNT-PEI on the Nitrate Sensing Performance....	197
4.3	Summary	197
4.4	References	198
5.	Electrochemical Deposition of Nanothin Sheets of Zinc Hydroxysulfates and their Conversion to Dendritic Metallic Zinc at Polypyrrole-Polystyrene Sulfonate Films	201
5.1	Introduction	202
5.2	Results and Discussion.....	203
5.2.1	Electrodeposition of Zinc-Based Nanothin Sheets	203
5.2.2	Characterization of Zinc-Based Nanothin Sheets	207
5.2.2.1	X-Ray Diffraction.....	207
5.2.2.2	Electrochemical Quartz Crystal Microbalance.....	211
5.2.2.3	Energy Dispersive X-Ray Analysis	215
5.2.2.4	X-Ray Photoelectron Spectroscopy.....	219
5.2.2.5	Attenuated Total Reflectance Infrared Spectroscopy.....	222
5.2.3	Mechanism of Deposition of Zinc-Based Nanothin Sheets.....	223
5.2.3.1	Morphology and Growth	223
5.2.3.2	Mechanism of Nucleation and Growth.....	226
5.2.4	Effect of the Experimental Conditions on the Electrochemical Deposition of Zinc-Based Nanothin Sheets.....	231
5.2.4.1	Effect of Film Thickness and Deposition Potential.....	231
5.2.4.2	Effect of Dopant and Counterion.....	234
5.2.4.3	Effect of Oxygen and pH.....	239
5.2.5	Conversion of Zinc-Based Nanothin Sheets to Metallic Zinc Dendrites	244
5.3	Summary	249
5.4	References	251
6.	Conclusions.....	253

Declaration

I hereby certify that this thesis, which I now submit for assessment on the programme of study leading to the award of PhD has not been submitted, in whole or part, to this or any other University for any degree and is, except where otherwise stated the original work of the author.

Signed: 
Enrico Andreoli

Acknowledgments

I would like to express my sincere gratitude to my supervisors Prof. Carmel B. Breslin and Dr. Denise A. Rooney for giving me the opportunity to undertake this study and for their positive, honest and continuous support.

I wish to acknowledge the Environmental Protection Agency Ireland for funding this study. I am also obliged to the Science Foundation Ireland for financing the National Access Programme at the Tyndall National Institute and to the FÁS Irish National Training and Employment Authority for funding the Science Challenge Programme.

I would like to thank all the people who contributed with their expertise and work to the realization of this research. At the Tyndall National Institute, University College Cork, Dr. Mircea Mondreanu for the Infrared and Raman analyses, Vincent Lodge for the Scanning Electron Microscopy characterizations, and Paul Roseingrave coordinator of the National Access Programme. At the Materials and Surface Science Institute, University of Limerick, Dr. Wynette Redington and Dr. Robert Gunning for the X-Ray Diffraction characterizations, and Dr. Fathima Laffir and Dr. Serguei Belochapkin for the X-Ray Photoelectron Spectroscopy analyses. At the Institute for NanoEnergy, University of Houston, Prof. Seamus Curran and Dr. Kang-Shyang Liao for their expertise on carbon nanotubes.

I am also grateful to Prof. Daria Vladikova at the Institute of Electrochemistry and Energy Systems of the Bulgarian Academy of Sciences, and to Prof. Armando Gennaro at the Chemistry Department of the University of Padua, for their availability and support.

I am particularly grateful to Dr. Valeria Annibaldi, Adelaide Dura and Dr. Sinead McDermott for their suggestions, meticulous proofreading and especially for their friendship. I am thankful to Dr. John Colleran and Catherine Fox for their availability and help.

I am grateful to all the technical staff of the Chemistry Department of the National University of Ireland Maynooth, especially to Dr. Ken Maddock, Orla Fenelon and Noel Williams.

Finally, I am deeply grateful and obliged to my wife Ewa for being the keystone of these years with her intelligence, determination and love.

*To the joy of my life,
Ewa and Jan.*

Abstract

The electrodeposition of copper- or zinc-based nanomaterials was performed on the top of polypyrrole-polystyrene sulfonate (PPy-PSS) thin films from their respective sulfate solutions in presence of dissolved oxygen.

Three main processes were responsible for the formation of the nanomaterials, namely, the capture of Cu^{2+} or Zn^{2+} ions by the film from the electrolyte solution, the formation of OH^- ions generated from the oxygen reduction reaction, and the reaction of the hydroxide ions with the metal ions to form insoluble double salts.

Copper-based hierarchical micro/nanostructure composed of copper hydroxide sulfate hydrate, $[\text{CuSO}_4]_2[\text{Cu}(\text{OH})_2]_3 \cdot 5\text{H}_2\text{O}$, and posnjakite, $\text{CuSO}_4[\text{Cu}(\text{OH})_2]_3 \cdot \text{H}_2\text{O}$, were identified using X-ray diffraction and several other surface analytical techniques. These structures were formed of nanosheets made of nanoparticles which combined into flower-like micro-clusters. The nucleation of the structures was progressive. The morphology and composition of the copper-based materials changed with the deposition potential. Microcrystals and nanosheets were combined using a two-step fabrication procedure to form new hybrid microstructures.

Metallic copper nanoparticles (CuNP) were formed from the reduction of the hierarchical micro/nanostructure. The application of a high reduction potential caused the erosion of the nanosheets and the formation of CuNP. These nanoparticles were used to detect nitrate ions. The sensing performance was improved with the introduction of polyethyleneimine-functionalized multiwall carbon nanotubes (MWNT-PEI) to the PPy-PSS films. Electrochemical impedance spectroscopy studies showed that the nanotubes increased the electronic conductivity of the reduced films. The limit of detection of the PPy-PSS-MWNT-PEI-CuNP nanocomposite was 30 μM nitrate.

Nanothin sheets made of zinc sulphate hydroxide hydrate, $\text{ZnSO}_4[\text{Zn}(\text{OH})_2]_3 \cdot 5\text{H}_2\text{O}$, were also deposited on the PPy-PSS films and characterized using a range of experimental techniques. The zinc-based sheets formed on the film surface with instantaneous nucleation and grew into a network of entangled nanosheets. The effect of the experimental conditions on the electrodeposition was studied. Interestingly, the formation of the nanosheets was only observed on PPy-PSS films, but not on films doped with other sulfated/sulfonate dopants. The zinc nanosheets were reduced to metallic zinc micro-dendrites and possibly zinc oxide nanocrystals.

Chapter 1

Introduction and Literature Review

1. Introduction and Literature Review

1.1 Research Topic and Relevance

The general topic of the present research is the development of a simple and inexpensive electrochemical tool with a controllable and diversified interfacial chemistry for the electrodeposition/fabrication of nanomaterials. The tool is a modified electrode surface at which different electrochemical processes enable the deposition of nanomaterials of various compositions and morphologies. The development of a single surface able to perform a series of simultaneous and controllable electrochemical reactions would possibly contribute to the current procedures of electrochemical deposition and fabrication. This research topic is important because the controlled deposition of nanomaterials has a scientific and technological impact in the production of, for example, integrated circuits, solar cells, flat-panel displays, memory devices, sensors and microelectromechanical systems [1, 2].

1.2 Objectives and Achievements

The main objective of the present work is to electrochemically deposit copper- and zinc-based nanomaterials on the surface of conducting polypyrrole-polystyrene sulfonate (PPy-PSS) thin films. Other objectives are to fully investigate the formation, composition and morphology of such materials using electrochemical, spectroscopic and surface analytical techniques; moreover, to attempt the fabrication of hybrid copper structures and employ the copper materials in sensing applications.

The main achievements of this work are as follows: (i) identification and characterization of the three dominant electrochemical processes at the PPy-PSS interface, namely: ion-exchange, reductive deposition/precipitation and oxygen reduction; (ii) formation and characterization of copper-based hierarchical micro/nanostructures at the PPy-PSS surface; (iii) description of the different aspects of the mechanism of nucleation and growth of the hierarchical structures; (iv) conversion of the hierarchical structures to metallic copper nanoparticles and their use for sensing nitrate ions; (v) improvement of the nitrate sensing performance by

introducing modified carbon nanotubes in the PPy-PSS films; (vi) exploitation of the three dominant electrochemical processes to fabricate combined copper-based hybrid structures; (vii) formation and characterization of zinc-based nanosheets at the PPy-PSS surface; (viii) elucidation of some aspects of the mechanism of nucleation and growth of the nanosheets; (ix) conversion of the nanosheets to metallic zinc micro-dendrites and possibly to zinc oxide nanocrystals; (x) analysis of the effect of the experimental parameters on the deposition of the zinc-based nanosheets.

1.3 Electrochemical Deposition

1.3.1 Overview of Electrochemical Deposition

When someone thinks about electrochemical deposition the first process that comes to mind is the coating of a conductor surface with a thin layer of metal (*e.g.*, silver plating). This process, known as electroplating, forms the backbone of the major industrial applications of electrochemical deposition. Electrochemical deposition is regarded as the process whereby metals and alloys are deposited upon reduction of metal ions from aqueous, organic, and fused-salt electrolytes [3]. The first electrochemical deposition of metals was reported by Luigi V. Brugnatelli in 1803 [4]. Brugnatelli reported that he had ‘gilt in a perfect manner two large silver medals’ using the voltaic pile invented by his colleague and friend, Alessandro Volta. Since then tremendous improvements have occurred in this field with copper electroplating at the forefront. Indeed, single and dual damascene processes are the fabrication methods currently used to produce high density and multi-level metallic copper interconnections of modern integrated circuits (microchips). Copper is electroplated in the trenches and vias of the dielectric wafers from a solution containing copper ions [5]. The shift from aluminum to copper in the microchip industry has been boosted not only by the prospect of a higher performance for the copper interconnections [6], but also by the precise understanding and control of the chemistry involved in the damascene copper plating process [7].

The modern field of electrochemical deposition has expanded beyond electroplating such that the most appropriate and general definition of electrochemical deposition should be stated as follows:

Electrochemical deposition is considered as any procedure involving at least one redox process that leads to the formation of a solid material deposited on the surface of a substrate.

For example synthetic hydroxyapatite (HA), which is the inorganic component of bone and teeth, has applications for hip replacements and dental implants coatings [8]. The electrochemical deposition of HA coatings on titanium is a well-known process based on the electrochemical precipitation of HA from aqueous solutions of calcium and phosphate ions. The electrochemical decomposition of water or the reduction of dissolved oxygen generates high concentration of hydroxide ions at the electrode surface and this causes the precipitation of HA [9-11]. Other similar examples are the electrogeneration of hydroxide ions for the precipitation of mesoporous nickel hydroxide for high energy alkaline rechargeable batteries or zinc oxide nanowire arrays for field-emission displays [12, 13].

1.3.2 Electrochemical Deposition on Conducting Polymers

The materials commonly electrodeposited on conducting polymers are metal particles. The interest in these materials stems from their catalytic activity for a wide range of chemical reactions [14]. The depositions are usually ‘electrodriven’ by applying a reduction potential to the polymer to cause the direct deposition of the metals on its surface. In some cases this can also be achieved by using ‘electroless’ deposition. In this case the conducting polymer transfers its electrons to the metal cations in solution to form metal particles. Polyaniline, polypyrrole, polythiophene and poly(3,4-ethylenedioxythiophene) are the main conducting polymers studied to date, and several metals such as Pt, Pd, Au, Ag, Cu and Ni have been deposited on their surfaces [14]. Depositing metals on patterned conducting polymers can be of use in the electronic industry [15]. Despite the wide variety of metal-polymer materials, little has been done to produce metal hydroxy salt deposits. The work presented here is intended to bridge some of this scientific gap.

1.3.3 Electrochemical Fabrication

In the literature the term electrochemical fabrication is used for those electrochemical procedures that generate well-ordered or combined micro/nanostructures. In most

cases the structures are obtained from the electrochemical deposition of materials inside the voids of ordered porous templates. Among the most cited works of template electrochemical fabrication are those concerning the preparation of nanowire arrays made of different materials electrodeposited inside the porous structures of alumina membranes, nanochannel alumina, or anodic aluminium oxide [16-19]. Semiconductor and conducting polymer micro-periodic structures are also fabricated inside the self-organized templates of drop-casted microbead colloidal suspensions of silica or polystyrene [20, 21].

Electrochemical fabrication can also be regarded as a building procedure whereby a deposit is constructed by combining materials electrochemically deposited in sequence. For example, in one early study conducting polymers were electrodeposited in series to fabricate an organic p-n junction diode [22]. More recently, photoactive oxide nanotubes and conducting polymers were electrodeposited in sequence to give a combined photoconductive material [23]. It is also interesting to report a 'corrosion-type' fabrication procedure called dealloying, which consists of etching an alloy made of two metals. One metal is electrochemically etched while the other one is passivated to form a nanoporous matrix [24].

1.4 Conducting Polymers

1.4.1 Conducting Polymers

Conducting polymers are materials made of conjugated macromolecules able to carry electric current. Also called organic polymeric conductors or synthetic metals, these materials come with a wide variety of structures and properties. Polyaniline (PANI), polypyrrole (PPy) and polythiophene (PT) and their derivatives are among the most common conducting polymers [25-28]. The conductivity stems from the π conjugated system (delocalized $2p_z$ orbitals) that allows the generation and movement of charge carrier entities called solitons, polarons and bipolarons. The polymers can be synthesized either chemically or electrochemically into different morphologies that find applications in many advanced technological fields, such as

sensors, actuators, electronics, optoelectronics and devices for renewable energy generation and storage [29-39].

1.4.1.1 Structures and Electronic Properties

A fundamental property of conducting polymers is the electrical conductivity, σ in S/m, which relates the current density, I in A/m², to the electric field, E in V/m, applied to the conductor, as shown in Equation 1.1.

$$I = \sigma E \quad 1.1$$

The value of σ is a quantitative measurement of the ability of a material to conduct electrical current. From Equation 1.1 it is evident that for a given electric field of intensity, E , the corresponding current density, I , increases with increasing value of σ . In general, materials are classified as insulators, semiconductors and metals depending on their σ values (Figure 1.1).

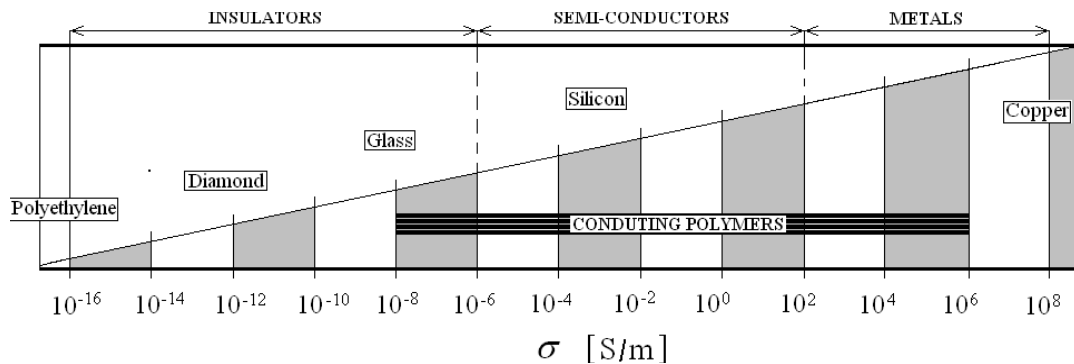


Figure 1.1 Classification of materials in order of electrical conductivity, σ . Insulators do not conduct electric charge and the typical values of σ are below 10^{-6} S/m, note that for insulating polymers, like polyethylene, the conductivity is as low as 10^{-16} S/m. Metals allow the free flow of electrons and σ values reach above 10^2 S/m with metallic copper having conductivity in the order of 10^8 S/m. Semiconductors allow the flow of those charges that have enough energy to overcome the band gap, and the conductivity values fall between those of insulators and metals. Conducting polymers have a wide range of conductivity ($10^{-8} - 10^6$ S/m).

Conducting polymers have a very broad range of conductivities, varying from that of insulators to that of metals and covering the entire range of semiconductors. Such a variety is related to the great number of different polymers, dopants and available doping levels. Typical values of conductivity for doped PANI, PPy, PT and their derivatives are in the range 10^2 - 10^5 S/m [40].

Polyacetylene (PA) was the first example of a conducting polymer to be fully characterized [41]. In 2000, A. J. Heeger, A. G. MacDiarmid and H. Shirakawa were awarded the Nobel Prize in Chemistry for their work on this polymer [42-44]. The first polymerization of acetylene was performed by Natta and co-workers in 1958 [45]. The material so prepared remained of little interest because of its poor processability. Then in 1967 [46] work was carried out which showed that it was possible to thermally control the *cis/trans* ratio during the synthesis of thin films of PA [47]. The conductivity of *trans*-rich polyacetylene was 10^{-6} S/m [48], a value that was increased by 11 orders of magnitude after exposure to iodine vapour [49-51]. Despite such a metal-like electrical conductivity, the use of PA has been precluded because of its poor thermal oxidative stability [52]. For this reason much effort has been put to prepare other conducting polymers with better stability and processability.

There are several other conducting polymers that have been developed and applied to-date [26-28]. The three main classes are based on PANI [53-62], PPy [63-72] and PT [73-82]. The structures of these polymers are all characterized by an extended π conjugated system, like the one found in polyacetylene (Figure 1.2).

All conducting macromolecules are made of hybridized sp^2 carbon atoms. The unpaired electrons contained in the $2p_z$ orbitals overlap laterally to form a set of π molecular orbitals, delocalized along the carbon σ -bond chain. The heteroatoms of PANI ($-\overset{\ominus}{\text{N}}\text{H}-$, $-\overset{\oplus}{\text{N}}=$), PPy ($>\overset{\oplus}{\text{N}}-\text{H}$) and PT ($>\overset{\oplus}{\text{S}}\text{S}$) contribute also to the π orbitals with their lone electron pairs.

An approximate way, yet simple and informative, to depict the energy distribution of the π orbitals in a conducting polymer is based on considering all $2p_z$ electrons confined in a potential well of finite length. In such a case the quantum-mechanical

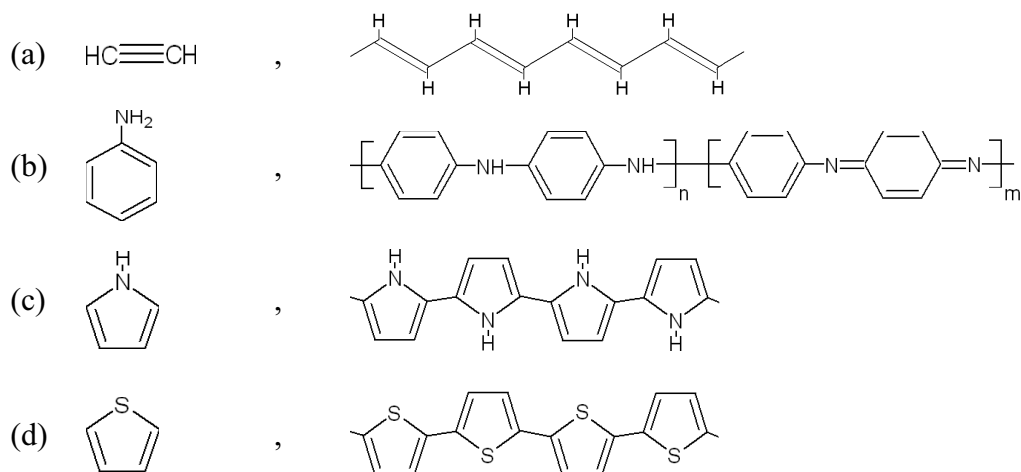


Figure 1.2 Structures of the most representative monomers and their conducting polymers. Acetylene and *trans*-PA (a). Aniline and PANI with its different oxidation states: leucoemeraldine ($m = 0$), emeraldine ($n / m = 0.5$) and pernigraniline ($n = 0$) (b). Pyrrole and PPy (c). Thiophene and PT (d). All macromolecules are characterized by a delocalized π conjugated system that in PANI, PPy and PT comprises also the lone electron pairs of the heteroatoms.

model of ‘a particle in a box’ can be used to evaluate the distribution of energy states of the π orbitals, Equation 1.2 [83].

$$E_n = \frac{h^2 n^2}{8ma^2} \quad 1.2$$

Here, n is the quantum number of the energy level, m the electron mass, a the length of the one-dimensional box and h is the Planck’s constant. The length of a macromolecule made of a large number, N , of carbon atoms placed at distance, d , from each other is given by $a \cong Nd$. The N atoms contribute a total of $N 2p_z$ electrons that fill the states up to the $n = N/2$ energy level. This level is called Highest Occupied Molecular Orbital (HOMO). The level immediately higher, $N/2+1$, is called the Lowest Unoccupied Molecular Orbital (LUMO). The energy difference, ΔE , between the HOMO and LUMO orbitals is then given by Equations 1.3 and 1.4.

$$\Delta E = E_{LUMO} - E_{HOMO} = \frac{h^2(N/2 + 1)^2}{8m(Nd)^2} - \frac{h^2(N/2)^2}{8m(Nd)^2} \quad 1.3$$

$$\Delta E \cong \frac{(h/d)^2}{8m} \cdot \frac{1}{N} \quad 1.4$$

Equations 1.2 and 1.4 are very informative about the electronic structure of conducting macromolecules. It is evident that with increasing number of carbon atoms, the number of energy levels increases (higher density of states), whereas the HOMO-LUMO energy difference decreases (lower energy gap). For very large N , the densities of states for the π -bonding and π^* -antibonding orbitals are sufficiently high to give the *conduction and valence bands*, CB and VB, respectively, with the ΔE corresponding to the *band gap* of the organic semiconductor (Figure 1.3).

The band gap is a forbidden energy region where there are no energy states available for the electrons. For this reason an electron can be excited to a higher energy state only if an amount of energy at least equal to ΔE is supplied. Once it reaches this higher energy state an electron is free to move along the polymer chain.

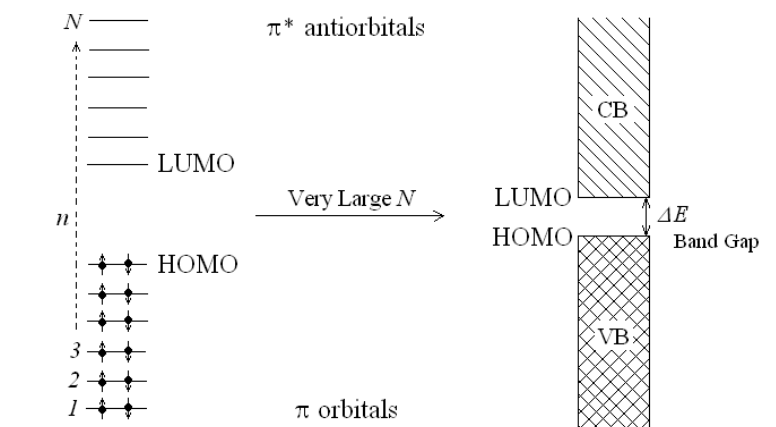


Figure 1.3 Representative energy level diagrams for a conducting polymer. The number of energy levels, N , corresponds to the number of carbon atoms. For very large N the π -bonding orbitals merge to form the valence band (VB), whereas the π^* -antibonding orbitals merge into a conduction band (CB). All the π electrons are delocalized inside VB. The top level of VB is the HOMO, whereas the bottom level of CB is the LUMO. The band gap, ΔE , of the polymer is given by the energy difference between CB and VB.

Insulating polymers have high values of band gap energy ($\Delta E > 4$ eV) and do not carry electric current [84]. Undoped conducting polymers instead have a $\Delta E \approx 2$ eV and behave like semiconductor materials [85]. The band gap of an inorganic semiconductor like silicon is 1.12 eV [86]. A band gap of 2 eV corresponds to the energy carried by a photon in the ‘red’ region, at 620 nm, of the visible spectrum. In the case of metals VB and CB overlap ($\Delta E = 0$) and form a single diffuse band

described as an electron cloud that is free to move in the crystal lattice of the metal. Conducting polymers can achieve values of electrical conductivity of the order of metals after a process of ‘charge enrichment’ called doping.

In the field of conducting polymers the term *doping* refers to any process that can generate free charge carriers in the polymer; details about the nature and function of such carriers are given in Section 1.4.1.2. The conductivity, σ , of undoped conjugated polymers is usually in the range of 10^{-8} to 10^{-3} S/m. However, this can be increased by several orders of magnitude to the ‘metallic’ regime (10^2 to 10^6 S/m) through the process of doping [43]. There are redox and non-redox methods to dope conjugated polymers.

Redox doping involves the addition, or removal, of π electrons from the polymer chains which can be done either chemically or electrochemically [87]. Oxidative doping, also called *p*-doping, occurs by treating the polymers with either oxidizing agents or by applying an oxidation potential. Both methods create ‘holes’ (more precisely polarons and/or bipolarons) where the positive charge is balanced by either the reduced agent or a counter anion from the electrolyte solution in which the electrochemical oxidation is performed. On the other hand, *n*-doping is realized with reducing agents or reduction potentials. In this case, the electroneutrality is preserved with the addition of cationic dopants.

Non-redox doping consists of generating charge carriers without adding or removing electrons [43]. PANI is the conducting polymer that is best suited for non-redox doping. In fact the quinoid-like nitrogen ($-\overset{\ominus}{\text{N}}=$) of emeraldine can be protonated to give a stable radical cation ($-\text{H}\overset{\oplus}{\text{N}}-$) with high conductivity, 10^3 - 10^4 S/m [88-90].

Photo-doping happens by exposing the polymer to electromagnetic radiation of energy greater than the band gap, in this way electron-hole pairs called excitons are formed [91-93]. Another method to dope conjugated polymers is *charge-injection doping*. This consists in the application of a suitable potential across a layered metal/insulator/polymer structure with the generation of charged species in the polymer without any associated dopant ions [94-96]. Whichever method is applied to dope the conjugated system of the polymer, the final result is the generation of some mid-gap energy levels that allow the transport of charges along the carbon backbone of the chains, as described in detail in Section 1.4.1.2.

1.4.1.2 Charge Transport Entities and Mechanisms

Solitons, *polarons* and *bipolarons* are the entities involved in the charge transport inside conducting polymers [97-99]. Such entities can be considered as the combination of two components: (1) a particle and (2) the perturbation induced by the presence/absence of the particle on its surrounding environment. In technical jargon, such a particle-perturbation combination is called a *quasi-particle*. A well known example of a *quasi-particle* is the *hole* that is generated in the valence band on excitation of an electron to the conduction band. The hole can be described as the combination of a missing electron with the electronic distortion caused by its absence on the local surroundings of the material. In energetic terms, a *quasi-particle* is considered as an elementary excitation. Yu [98] has given an intuitive and clear picture of the role of *quasi-particles* on the charge transport inside of solids. He wrote “Just as atoms, ions or molecules are the ‘building blocks’ of a crystal in the sense of structure, these elementary excitations or ‘*quasi-particles*’ are the ‘building blocks’ of a solid in the sense of motion” [98]. From this point of view, solitons, polarons and bipolarons are the elementary excitations responsible for the movement of the charges inside a conducting polymer. In order for the charges to propagate throughout the bulk of the polymer the *quasi-particles* have to move along (intrachain transport) and among (interchain transport) the polymer chains.

A *soliton* is formed at the transition point between two co-existing conjugated structures on a conducting polymer molecule (Figure 1.4). The two conjugated structures are called domains and they must possess the same ground state energy in order to form a soliton (*i.e.*, to be degenerate). In such a case, the soliton can move freely as the overall energy of the domains on both sides of the soliton is always the same [97]. For this reason a soliton is defined as a ‘moving domain wall’ [100].

Solitons can be neutral, positively or negatively charged [99]. A neutral soliton is formed in pristine *trans*-PA with an odd number of conjugated carbons, a situation in which an unpaired π electron (a radical) is left free to move along the carbon backbone (Figure 1.5). The radical electron occupies a localized electronic state exactly at the middle of the band gap, and as like any other electronic state this can be emptied to form a positive soliton or accommodate another electron to become a negative soliton (Figure 1.6).

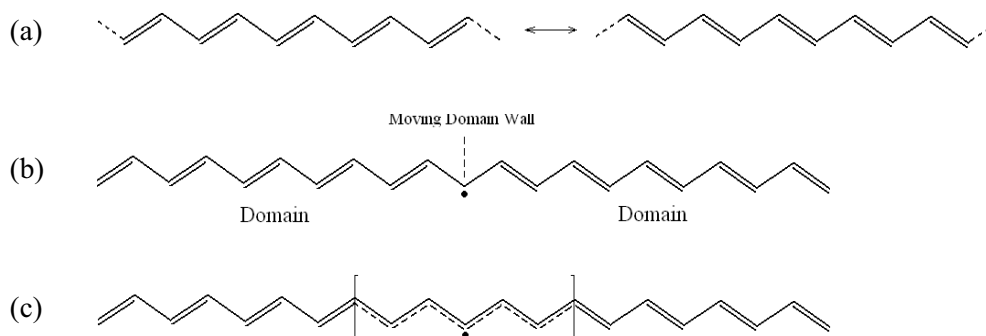


Figure 1.4 Molecular structure of a soliton. The two conjugated resonance forms of *trans*-PA have the same ground state energy and differ from one another by the exchange of the single and double carbon-carbon bonds (a). The soliton (moving domain wall) is formed at the junction point of the two conjugated forms (domains) coexisting on a single polymer molecule (b). The soliton is the result of a competition between two domains and it is characterized by a transition in bond length from one domain to the next, which gives the soliton a width (c).

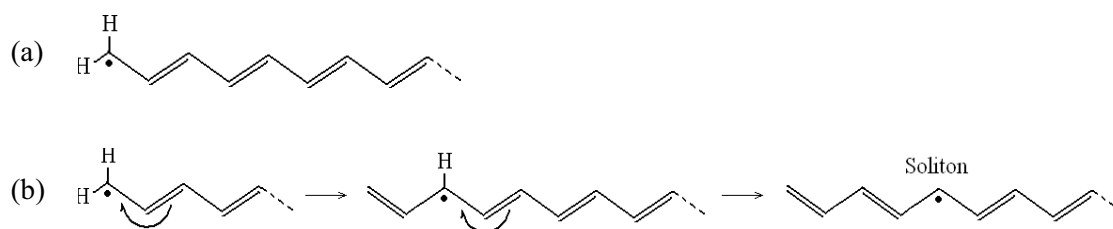


Figure 1.5 Generation and movement of a soliton. Radical π electron left unpaired at the end of a *trans*-polyacetylene molecule having an odd number of carbon atoms (a). Movement of the radical along the carbon backbone of the molecule with the generation of the corresponding soliton (b).

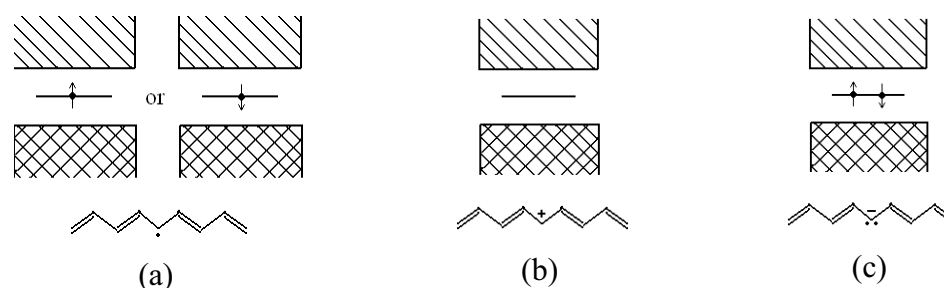


Figure 1.6 Band structure of a soliton. The localized electronic state lying exactly at mid-gap for a neutral (a), positively (b) and negatively (c) charged soliton. The neutral form has zero charge and spin $\frac{1}{2}$, the positive and negative forms have, respectively, positive and negative charges with no spin.

The condition of degeneracy of the two domains is met in the case of *trans*-PA, the only conducting polymer in which the two resonant conjugated forms have exactly the same ground state energy. For this reason solitons are primary charge carriers in *trans*-PA. Most conducting polymers have only a near degeneracy and for this reason polaron and bipolarons are the major charge carriers [99].

A *polaron* is formed upon removal, or addition, of an electron from, or to, a conducting polymer chain. The portion of polymer subjected to this process is distorted by the local excess of charge and a corresponding vibration of the polymer lattice, called phonon, is coupled to it. For this reason a polaron is considered as a *quasi*-particle formed by coupling an electron or a hole with a phonon [99]. Polarons are formed through oxidation or reduction reactions leaving a positive or negative charge, respectively, in the polymer. These charges are further stabilized and localized on the chain by interacting with an added dopant, a charged species of opposite sign that interacts electrostatically with the polaron. In this way, the polymer reduction is referred as *n*-doping and generates a radical anion coupled to a positively charged dopant, whereas oxidation, known as *p*-doping, is made of a radical cation and a negatively charged dopant (Figure 1.7). Thus, the conducting polymer can be considered as an ionic complex of oppositely charged polymer chains and dopants [97].

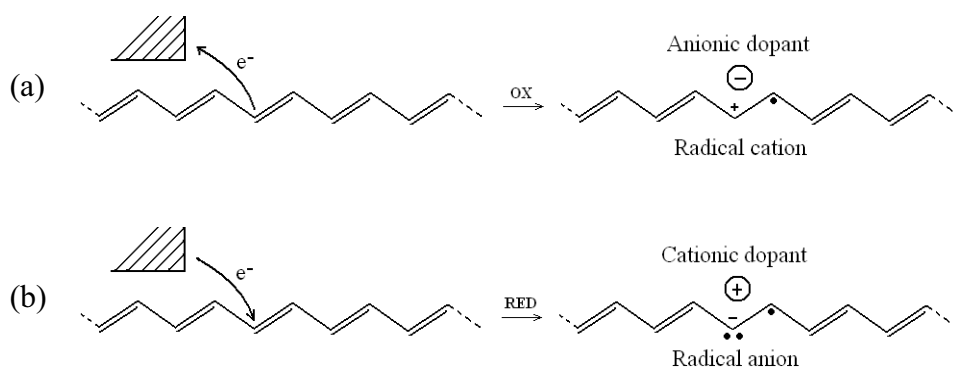


Figure 1.7 Formation and structure of a polaron. Oxidation of a conducting polymer chain by electron transfer to an electrode and formation of a polaron made of a radical cation coupled to an anionic dopant (a). Reduction of a conducting polymer chain by electron transfer from an electrode and formation of polaron made of a radical anion coupled to a cationic dopant (b).

From the structures shown in Figure 1.7, it can be inferred that a positive (hole) polaron is composed of a positive soliton and a neutral soliton localized near the negative dopant. Similarly, a negative (electron) polaron is composed of a negative soliton and a neutral soliton localized close to the positive dopant [99].

The distortion due to the presence of the polaron causes an increase, $+\Delta\epsilon^{\text{pol}}$, in energy of the HOMO (VB) and a decrease in energy, $-\Delta\epsilon^{\text{pol}}$, of the LUMO (CB) orbitals of the polymer [97]. In this way two new localized mid-gap states, corresponding to the energy levels of the polaron, are formed in the band gap. An electron is removed from the lower state to give a hole polaron, *i.e.*, radical cation, whereas an electron is added into the upper state to give an electron polaron, *i.e.*, radical anion (Figure 1.8) [99].

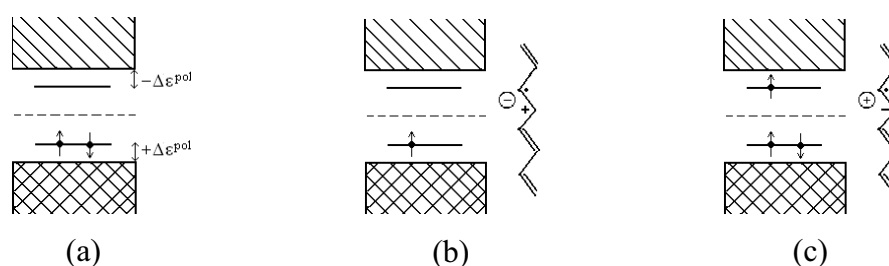


Figure 1.8 Band and molecular structures of a polaron. The local distortion in the polymer lattice causes an increase in the VB and a decrease of the CB energies by an amount equal to $\Delta\epsilon^{\text{pol}}$ (a). A positively charged polaron, with spin $\frac{1}{2}$, is formed by removing an electron from the lower bounded state (b). A negatively charged polaron, with spin $\frac{1}{2}$, is formed by adding an electron to the upper bounded state (c).

A *bipolaron* is formed by either removing another electron from a hole polaron or by adding an additional electron to an electron polaron. In this case, the distortion energy due to the local excess of charge is larger than that for a polaron due to the effect of doubling the charge, *i.e.*, $\Delta\epsilon^{\text{bip}} > \Delta\epsilon^{\text{pol}}$ (Figure 1.9).

The formation of a bipolaron is possible when the stabilization energy gained by the interaction with the distorted lattice is larger than the Coulomb repulsion between the two charges of the same sign confined in the same location [97]. A bipolaron can be considered as a localized pair of two charged solitons [99].

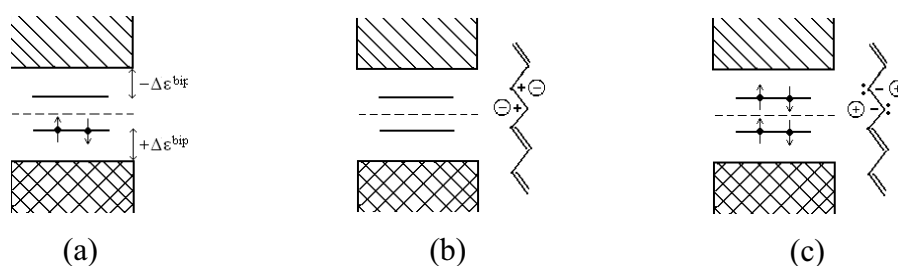


Figure 1.9 Band and molecular structures of a bipolaron. The local distortion in the polymer lattice causes an increase in the VB and a decrease of the CB energies by an amount $\Delta\epsilon^{\text{bip}}$ (a). A positively charged bipolaron, with no spin, is formed by removing two electrons from the lower bound state (b). A negatively charged bipolaron, with no spin, is formed by adding two electrons to the upper bound state (c).

The amount of dopant introduced in the polymer plays a crucial role in the formation of polarons and bipolarons. At low doping levels the conduction is governed by polarons, whereas at moderate levels bipolarons start appearing, and finally at high doping levels bipolaron bands are formed inside the band gap. A more detailed description is given in Section 1.4.2.2 for the effect of doping levels in PPy.

Polarons and bipolarons can move along the doped polymer chains (intrachain transfer) if they are surrounded by an electrostatic field of closely distributed ionic dopants (Figure 1.10). However, the movement along the chains is just one part of the overall charge transport process inside of the bulk of the polymer; in fact, the charge carriers have also to jump from chain to chain (interchain transfer) in order to cover distances longer than an average molecular backbone length.

Depending on the type of conducting polymer and on the doping level, there are different possible mechanisms of interchain transfer of charges between polymer molecules. In slightly doped *trans*-PA at low temperature, electron ‘hopping’ between charged and neutral soliton states can occur in the presence of the dopant and under the assistance of vibrational motion, *i.e.*, a phonon (Figure 1.11) [101, 102]. Instead, for a generic doped conjugated polymer the proposed charge transfer pattern between molecules is based on a bipolaron hopping mechanism [103, 104].

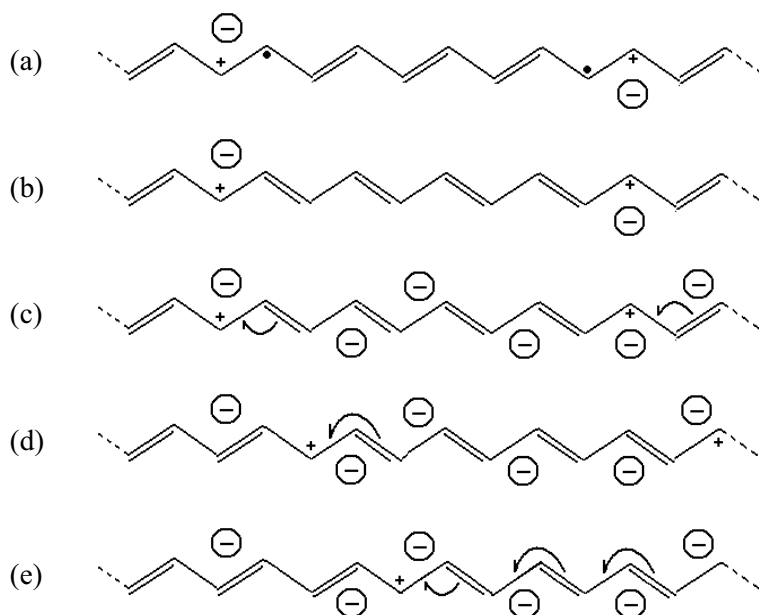


Figure 1.10 Movement of charge carriers along a conducting polymer. Two hole polarons are localized on the polymer chain (a), the two neutral solitons have recombined to form a double bond (b). In the presence of a close distribution of anionic dopants the two positive solitons start moving along the chain (c-d), the solitons can travel along the entire chain by repeated double bond rearrangements (e) [105].



Figure 1.11 Inter-soliton hopping mechanism. An electron can hop (*i.e.*, make a phonon assisted transition) between a charged soliton and a neutral soliton. The electron goes from the left to the right chain in both (a) and (b) assisted by the presence of the ionic dopant.

In conclusion, the generation of charge transport entities capable of moving along and ‘hopping’ among the polymer chains accounts for the overall mechanism of intra- and inter-molecular charge transfer inside conducting polymers. In the common cases of moderately/highly doped conducting polymers the entities responsible for the charge transfer are polarons and bipolarons.

1.4.1.3 Synthesis, Properties and Applications

The synthesis of conducting polymers is treated in detail in several review papers [31, 106-114]. Conducting polymers can be synthesized in different ways, as detailed below [110]:

- Chemical polymerization
- Electrochemical polymerization
- Photochemical polymerization
- Metathesis polymerization
- Concentrated emulsion polymerization
- Inclusion polymerization
- Solid-state polymerization
- Plasma polymerization
- Pyrolysis
- Soluble precursor polymer preparation.

Chemical polymerization is among the most widespread technique and can be used to prepare all classes of conjugated polymers. It is based on the oxidative coupling of monomers. The monomers are oxidized to radical cations that then couple with another monomer to form cation dimers. The repeated addition of monomer units to the radical cation and elimination of protons causes the growth of the polymer. The most common oxidizing agent used in aqueous and polar organic solvents is iron(III) chloride, FeCl_3 [112]. Chemical polymerization is the best choice for the synthesis of large amounts of polymer material.

Electrochemical polymerization is the most suitable synthetic route for depositing conducting polymer films onto a substrate. The monomers are oxidized at the electrode surface to form radical cations. As the concentration of radical cations is much higher than the neutral monomer at the electrode surface, coupling of the radical cations occurs. This is followed by proton elimination, leading to the formation of conducting films which strongly adhere to the electrode surface. The electrochemical route is also the easiest way to dope films with almost any ionic dopant [110]. Details about the chemical and electrochemical polymerization of pyrrole are given in Section 1.4.2.

Compared to chemical and electrochemical polymerization, the application of other polymerization techniques is much less common. Photochemical polymerization reactions are performed in the presence of photosensitizers (*e.g.*, ruthenium(II) complexes) that can be oxidized once exposed to solar light. These can then act as oxidizing agents and initiate polymerization. Plasma polymerization is useful to prepare ultrathin films on substrates, and it has the advantage that it is faster than most conventional coating protocols. Metathesis polymerization is performed with metathesis catalysts (*i.e.*, transition metal compounds with organometallic alkylating agents) and has the unique feature of preserving all the monomer double bonds in the polymer. Pyrolysis is based on heating a carbonaceous source to form extended aromatic macromolecules. The remaining techniques are in general time-consuming and often involve expensive chemicals [110].

In order to complete this short overview on the synthesis of conducting polymers, it is worth highlighting the recent development of the template and template-less synthesis of nanostructured conducting polymers [36, 38, 115]. The enormous interest in these structures is driven by the improved performance of materials once confined at the nanoscale level [116, 117]. It is also of interest to mention the synthesis of conjugated polymer networks, *i.e.*, conducting polymers with conjugated cross-links that can provide electronic communication between chains [107].

Conducting polymers have been extensively characterized using a range of electrochemical, spectroscopic and surface probing techniques [31]. The thermal and mechanical properties of the polymers are also of interest [118-121]. Cyclic voltammetry and electrochemical impedance spectroscopy are commonly employed techniques used to characterize the electrochemical and electrical properties of conducting polymers [122-125]. Optical techniques are used to evaluate electronic, electrochromic and non-linear optical behaviours [126-128]. Nuclear magnetic resonance is used for conformational studies of chain orientation and motion [129-131]. Other spectroscopic techniques include Raman spectroscopy, for molecular electronic and interaction studies [132-134], X-ray diffraction for crystalline domain and structural change analyses [135-137] and X-ray photoelectron spectroscopy for chemical and oxidation state analyses [138-140]. Scanning electron microscopy is routinely employed for morphological characterization [141-143].

The improved processability of conjugated polymers [144, 145] combined with their broad range of physical and chemical properties have greatly increased the number of technological applications of these materials. A schematic illustration of the main property-to-application correlations of conducting polymers is given in Figure 1.12.

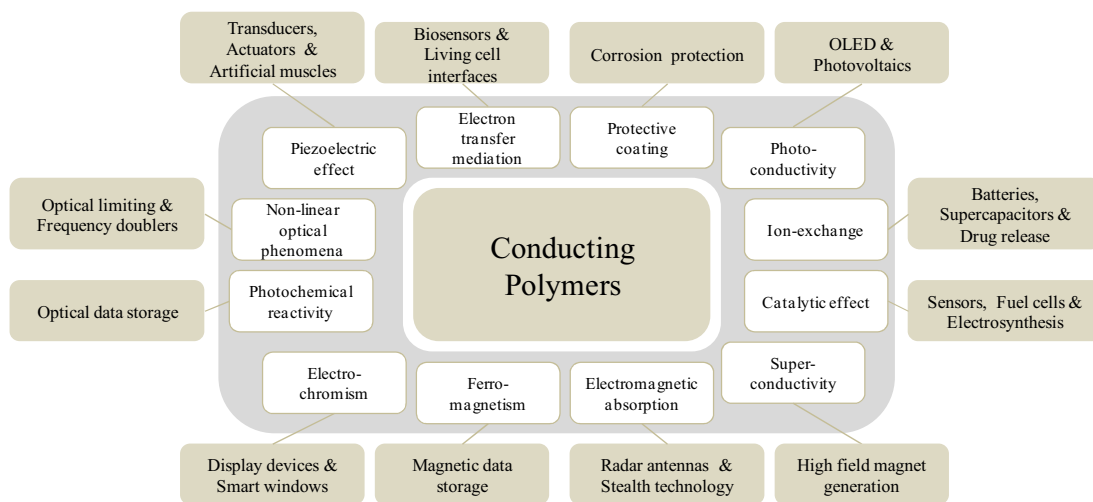


Figure 1.12 Schematic correlation between properties and applications of conducting polymers. In the ring there are the main physical and chemical properties of conducting polymers, each property is then related to its corresponding actual and possible application.

With electronic properties ranging from semiconducting to metallic and the typical flexibility of plastics, conducting polymers are likely to overtake metals and semiconductors in the electrical and electronic industries. Moreover, the development of high-performance conducting polymer nanostructures will lead to even more advanced performing sensors, catalytic surfaces, energy storage devices, memory devices and nanoelectronics [31, 38, 108, 110, 115].

1.4.2 Polypyrrole

Polypyrrole (PPy) and its derivatives are among the most studied and applied conducting polymers. PPy is easy to synthesize and has very good electronic properties and environmental stability. The only drawbacks are its insolubility and infusibility but these do not stop scientists and engineers from applying it in ever new and more advanced technological applications [146].

The first synthesis and characterization of a three-dimensional network of cross-linked pyrrole rings dates back to 1963 when black PPy was obtained from the pyrolysis of tetraiodopyrrole. The electrical conductivities of the polymer were up to 10^2 S/m [147-149]. Nowadays for surface based application, PPy is electro-synthesized with the aid of inexpensive electrochemical equipment in aqueous and organic solutions. The electrochemical synthesis allows precise control and reproducibility of the polymer properties [150]. The following sections outline details on the synthesis, molecular and electronic structures, properties and pertinent applications of PPy.

1.4.2.1 Synthesis, Properties and Morphology

Pyrrole monomer (Py) is a colourless liquid partially soluble in water with a formula of C_4H_5N . It is a heterocyclic aromatic compound with a 5-membered ring structure. The carbon and nitrogen atoms have all sp^2 hybridization, which generates an aromatic $6-\pi$ -electron system made from four carbon and two nitrogen $2p_z$ electrons. The resonance forms of Py indicate that the nitrogen electron lone pair is delocalized over the ring giving rise to a partial positive charge on the nitrogen (Figure 1.13).

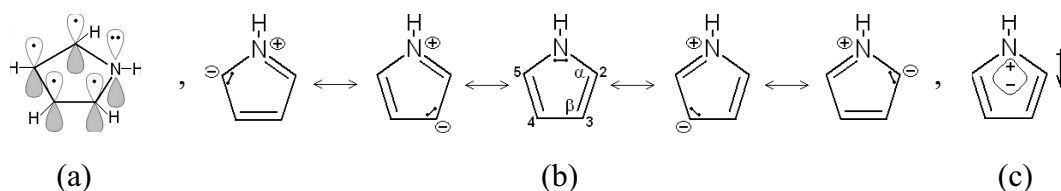


Figure 1.13 The π conjugated system of pyrrole. The carbon $2p_z$ orbitals contribute one electron each, whereas the nitrogen $2p_z$ orbital contributes two electrons of the lone pair (a). The resonance forms of Py show the nitrogen lone pair delocalized on the carbon aromatic ring (b). The resonance leads to the formation of a dipole moment pointing from the nitrogen to the electron-rich ring (c). The value of the dipole moment is 1.80 D [151].

Py is a weaker base ($pK_b = 13.6$) than aliphatic secondary amines ($pK_b \sim 9$) because of the delocalization of the nitrogen lone pair. It is also a weak acid having a $>N-H$ proton ($pK_a = 16$) weaker than that of phenol ($pK_a = 10$) [152, 153]. Py can undergo both nucleophilic and electrophilic aromatic substitution reactions. This is possible because of its ability to stabilize the negative charge of the nucleophile on the

heteroatom, and the resonant electron density present on the α carbons available to the electrophile, respectively. It is actually the latter property which guides the polymerization of Py predominantly on positions 2 and 5.

PPy is a black insoluble and infusible polymeric material stable up to 300 °C [154, 155]. It can be prepared in solution to form fine powders or on top of substrates to give films. The second method is more suitable for surface/interfacial applications. The processability can be improved by using 3- or N-substituted pyrroles [144, 145], but these polymers are beyond the scope of the thesis. The molecular structure of PPy consists of a chain of Py monomer rings connected by carbon-carbon σ bonds (Figure 1.14). In order to extend the conjugation all along the polymer chain, the Py rings must be coplanar to each other to assure the lateral overlap of the π -systems.

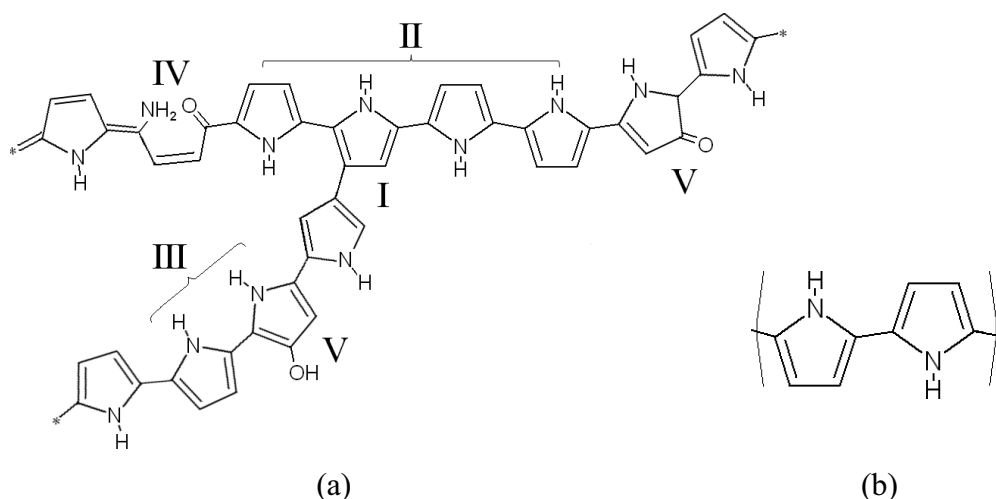


Figure 1.14 Molecular structures of polypyrrole (PPy). Possible structure of PPy chains (a). β -Coupling at the beginning of a polymer branch (I). Sequence of linear α -coupling as shown in (b), *i.e.*, rotated by 180° (II), and not rotated α -coupling (III). Defects generated by the reaction of the polymer oxidized sites with water (IV), and functional groups created by secondary oxidation reactions (V). The nature of the defects is dependent on the chemical conditions of the electrochemical synthesis. Idealized undoped chemical structure of PPy made from a pure α -coupling sequence of Py rings (b).

Any distortion from the coplanarity corresponds to a loss of conjugation which has detrimental effects on the conductivity of the polymer. The preferred bond formation between the rings is at the carbons in positions 2 and 5 (α -coupling); however bonding at positions 3 and 4 (β -coupling) is also possible, sometimes one Py ring in every three can be connected through β -coupling [156, 157]. The presence of

β -coupling is consistent with the theoretical calculations showing diminished difference in reactivity between α and β positions with increasing degree of polymerization (conjugation) [158]. The effect of β -coupling is to widen the band gap and decrease the conductivity of the polymer through the formation of branches that break the planarity and linearity of the PPy chains [159]. There are also other known defects caused by oxidation reactions with the solvent, for example with water [160] (Figure 1.14, IV).

PPy can be prepared either chemically or electrochemically and in both cases the polymer is formed through oxidative coupling. The electrochemical route is the preferred one for surface applications because it allows a better control of the film properties such as thickness and morphology, and in addition, it gives purer polymers [111, 112]. The oxidation potential of Py is lower than that of other monomers (*e.g.*, benzene and thiophene) [111, 112] making the polymerization of Py feasible in many solvents and with many oxidizing agents. In Table 1.1 there is a list of the experimental conditions commonly used for the chemical polymerization of Py, which is extracted from the work of Toshima and Hara [112].

Table 1.1 Oxidizing agents and solvents for the chemical polymerization of Py with the electrical conductivities, σ , of the corresponding PPy films.

Oxidizing Agent	Solvent	σ (S/m)
I ₂	H ₂ O	8.0×10^2
CuBr ₂	H ₂ O	4.5×10^3
FeCl ₃	H ₂ O, MeOH CH ₃ CN, C ₆ H ₆	1.1×10^4 , 1.9×10^4 3.0×10^2 , 2.0×10^3
Fe(ClO ₄) ₃ ·9H ₂ O	H ₂ O	3.3×10^3
Fe(BF ₄) ₃	H ₂ O/C ₆ H ₁₄	9.0×10^3

FeCl₃ is the most common oxidizing agent where Fe(III) is reduced to Fe(II) to oxidize the monomer, Py⁰, to the radical cation, Py⁺, and initiate the polymerization; other transition metals, like Cu(II), can also be used. The anion is incorporated into the polymer to balance the excess of positive charge carried by the polymer during

the polymerization. The nature of the anion (Cl^- , ClO_4^- or BF_4^-) and the polymerization conditions determine the electronic performance of the polymer. In this list the best performances were obtained in protic solvents with FeCl_3 as oxidizing agent, however this list is very limited compared to the much wider variety of experimental conditions routinely employed [111, 112].

The electrochemical polymerization of Py is performed on the surface of conductors (electrodes) by applying an appropriate oxidation potential by means of an external power source. The electrode is immersed in a solution of Py and supporting electrolyte. The function of the electrolyte is to allow the flow of current and provide the anionic dopant. The electropolymerization can be carried out potentiostatically (constant potential), galvanostatically (constant current) or potentiodynamically (potential scanning). Constant potential polymerization allows the precise and reproducible deposition of thin films (as thin as a few tens of nanometers), whereas the use of constant current is better suited for growing thick films or large amounts of polymer. Potential scanning, *i.e.*, cyclic voltammetry, is used when it is desirable to monitor the evolution of the electroactivity of the polymer during its growth.

In the literature there are numerous papers about the electropolymerization of Py [161-171]. An excellent review by Sadki *et al.* [172] outlines the proposed mechanisms of electropolymerization along with the most salient experimental and theoretical aspects on the topic. To-date a single mechanism able to explain all the experimental findings is not available. In fact, the number of factors that affect the polymerization is so large that each experimental set-up follows its own characteristic polymerization path. However, in the vast majority of the cases the fundamental features of the polymerization pathway are best described by the very first mechanism proposed by Diaz and co-workers (Figure 1.15) [173, 174].

In the mechanism of electropolymerization of Py proposed by Diaz, the oxidation of the monomer at the electrode surface is considered to be faster than the diffusion of the monomer from the bulk of the solution to the interface. In this way the monomer at the interface is predominantly present as a radical cation formed at potential E_1 (Figure 1.15, Reaction 1a). The high concentration of radical cations at the interface drives the coupling of two radical cations to form a diradical dication (Figure 1.15, Reaction 1b).

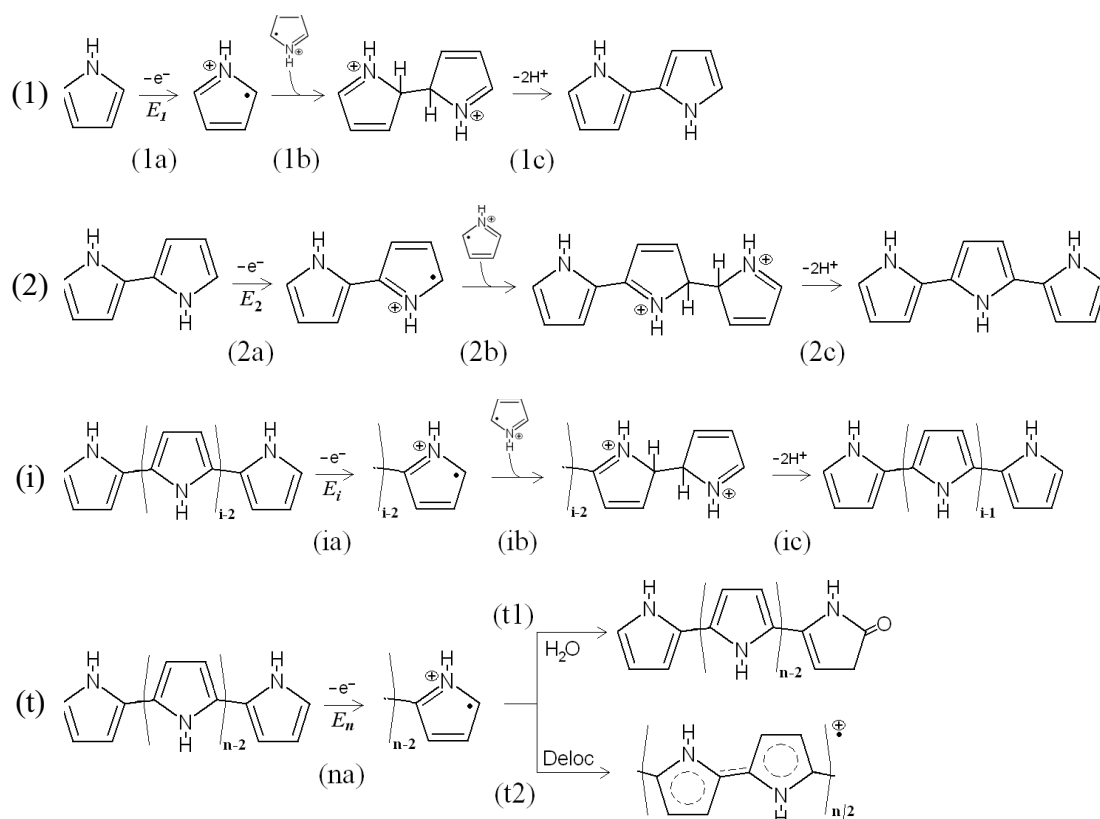


Figure 1.15 Diaz's mechanism for the electropolymerization of Py. Oxidation at potential E_1 of the monomer to the radical cation, oxidative coupling of two radical cations and elimination of protons to form a dimer (1). Oxidation at potential E_2 of the dimer to radical cation, oxidative coupling of dimer and monomer radical cations, and proton elimination to form a trimer (2). Chain propagation (i -th step) with radical coupling and proton elimination (i). Chain termination (n -th step) either by water addition or radical delocalization (t).

The diradical dication eliminates two protons to form a neutral dimer, reaction (1c). The dimer can be oxidized at the surface (2a), coupled with a monomer radical cation (2b) and deprotonated (2c). The repetition of these reactions, here shown as the i -th step, drives the growth of the polymer chain. The chain growth stops (termination) either by reaction (t1) of the macromolecular radical cation with water (in the case of aqueous solvents), or by lack of reactivity (stabilization) of the delocalized radical cation (t2) [172].

It is important to note that the stability of the radical cation increases with the number of monomers in the chain because of the improved delocalization, therefore the oxidation potentials are in the order $E_1 > E_2 > \dots > E_i > \dots > E_n$. The key consequence of this fact is that the polymer chain bears an additional oxidation

charge during and after the overall polymerization. This charge is counterbalanced by anions that sit inside the bulk polymer; such a process is called *p*-doping. The stoichiometry of the polymerization can be summarized as in Figure 1.16.

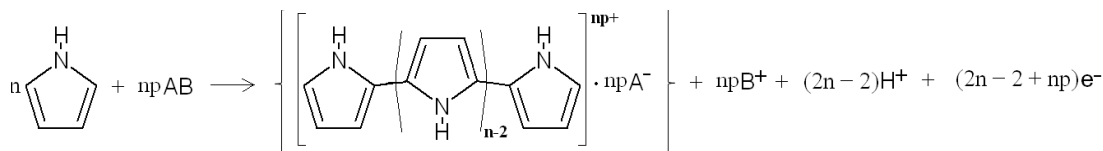


Figure 1.16 Stoichiometry of the electropolymerization of Py. In the reaction, a monomer contributes to form a polymer chain by losing $2+p$ electrons and 2 protons. The oxidative charge $+np$ borne by the polymer chain is balanced by np A^- dopant anions coming from the electrolyte, AB.

The number of electrons taken from each monomer is equal to $2+p$, two electrons for the polymerization plus p electrons for the oxidation of the polymer chain. For PPy the value of p is usually 0.25 to 0.33 corresponding to one positive charge delocalized across every 3 to 4 monomeric units [172]. These values are obtained from the elemental chemical analysis of the doped polymers, because they cannot be determined unambiguously with electrochemical techniques [175].

The coupling of the two monomers has been modelled theoretically in order to verify whether the formation of a bond between two radical cations would be feasible despite the electrostatic repulsion [176, 177]. Two possible pathways were assumed in which the radical cations were either coupled as formed (positive π radicals) or coupled after losing a proton (neutral σ radicals). The study showed that both pathways have an intrinsic energy barrier to overcome in order to proceed. In the case of the π radicals (Diaz's mechanism), the barrier is obviously the electrostatic repulsion, whereas in the case of the σ radicals the barrier is due to the removal of the protons. EPR experiments showed that no σ radicals were formed during the polymerization, thus confirming that the coupling occurred between two radical cations [178]. The mechanism proposed by Diaz is supported also by the drop of pH of the electrolyte solution during the polymerization, and it is in agreement with the doping levels measured experimentally [172].

The morphology of PPy films is very dependent on the dopant, solvent, electrolyte pH, polymerization potential and electrode substrate. All these factors are known to

have a direct influence on the film growth and then on the morphology [179-188]. The most common morphology of PPy films is the ‘cauliflower’ structure; the mean height, root-mean-square roughness, and nodule diameter have been studied in detail with AFM (Atomic Force Microscopy) and SEM (Scanning Electron Microscopy). For very long polymerization times the film loses its cauliflower structure and a worm-like fibrillar morphology is formed [182].

1.4.2.2 Electrical Conductivity and Band Structure

The electrical conductivity of PPy can have values typical of insulator/semi-conductors or metals. Immediately after the first electropolymerization of Py in 1979 [71, 72], Diaz *et al.* [70] performed a simple experiment to test this dual behavior. Two analytes were chosen in order to give two separate redox responses, one in the range of potentials where PPy was oxidized and one where it was reduced. It was soon realized that the polymer could detect only the redox activity of the first analyte, *i.e.*, PPy was electroactive only in its oxidized state. In fact, the polymer had to be oxidized in order to generate charge carriers and be conductive.

The evolution of the charge carriers – from polarons to bipolarons – in the PPy structure has been studied in great detail [189-199]. The first insight into the electrical conductivity of PPy is that the charge transport inside the polymer is only realized by positive carriers. The second insight is that the conductivity, and then the band structure, of PPy is strongly dependent on the doping level (*i.e.*, oxidation state) of the polymer (Figure 1.17) [97, 189].

In the undoped state the band gap of PPy is 3.16 eV. When the polymer is partially oxidized two states appear inside the gap, about 0.5 eV away from the band edges. These states correspond to the polarons formed at low doping levels in PPy. When PPy is further oxidized, the states move further away from the edges at about 0.75 eV; in this case bipolarons are formed at medium doping levels. Eventually, at high doping levels, two bands are formed inside the band gap (that is now 3.56 eV) from the superposition of several bipolaronic states. The two bands, about 0.4 eV broad, are responsible for the charge transport in the PPy chains when the oxidation level p is in the range of 0.25 - 0.33. These doping levels are commonly found in PPy.

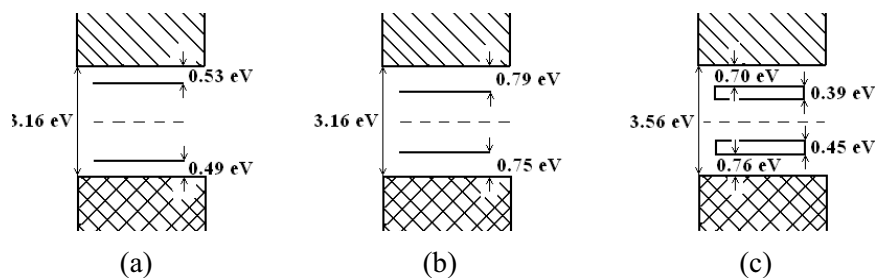


Figure 1.17 Effect of the doping level on the band structure of PPy. Two bound states are formed by removing one electron from a PPy chain, one above and one below the band gap edges (a). These are polaronic states generated at low doping levels (*i.e.*, oxidation levels). The two states are moved further away from the band edges by removing another electron from the PPy chain; in this case they become bipolaronic states formed at medium doping levels (b). At high doping levels, several bipolaronic states are overlapping to form two bands inside the band gap (c). These two bands are responsible for the high electronic conductivity in the polymer. All the numerical values are taken from the work of Bredas *et al.* [189].

The hopping mechanism of the charge carriers in conducting polymers like PPy, *i.e.*, disordered conducting polymers, has been studied in detail by Zuppiroli *et al.* [200]. In the proposed model the interchain charge transport is governed by a hopping between polaron clusters. The dopant has a primary role in this process as an attractive potential and as a tunneling bridge between neighboring chains.

1.4.2.3 Doping, redox switching and ion-exchange properties

The term ‘doping’ was originally introduced in the field of inorganic semiconductors in which traces of impurities were added to intrinsic semiconductors in order to change their electrical properties. Doped inorganic semiconductors are either *n*-type or *p*-type depending on the added impurities. Impurities that donate electrons to the crystal lattice produce *n*-type semiconductors, whereas those that accept electrons from the lattice generate *p*-type semiconductors [201]. In a similar fashion this terminology has been applied to organic semiconductors (*i.e.*, conducting polymers), but with substantial conceptual differences.

A conducting polymer is *p*-doped when the polymer chains are *oxidized* and *anionic* counterions (dopants) are taken into the bulk polymer to preserve the charge neutrality. The positive charge on the polymer chain can be generated by

electrochemical oxidation and does not necessarily require the addition of an electron acceptor as for the inorganic semiconductors. Likewise, a conducting polymer is *n*-doped when it is *reduced* and *cationic* dopants are taken into the polymer to balance its negative charge. Most conductive polymers are *p*-doped, but some *n*-doped polymers are also known [202-206].

For his Nobel lecture, laureate A. G. MacDiarmid wrote that “The concept of doping is the unique, central, underlying, and unifying theme which distinguishes conducting polymers from all other types of polymers” [43]. Indeed, conducting polymers are unique in the way they can be doped and undoped by changing their oxidation state. In doing so, the ionic dopant moves in and out of the polymer in order to maintain the electroneutrality. In the case of PPy this switching process can be sketched as in Figure 1.18.

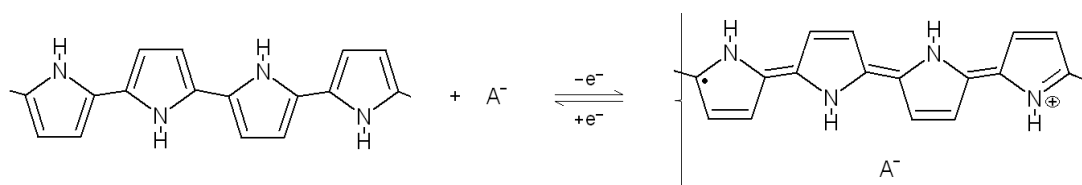


Figure 1.18 Doping and redox switching of PPy. One electron is removed from the polymer chain that then rearranges its double bonds from a benzoid-like to a quinoid-like configuration. An ionic dopant, A^- , moves into the polymer to balance the positive charge held by the polaron. The *p*-doping of PPy is a reversible process, the dopant can be expelled from the polymer by adding back the electron. The polymer can be switched between the insulating (on the left) and conducting (on the right) states by a simple electrochemical reduction/oxidation process.

The ion-exchange properties of PPy have been examined in detail [207-213]. Since the pioneering work by Shimidzu *et al.* in 1988 [207], it was immediately evident that the ion-exchange properties of PPy were dependent on the size of the anionic dopant. In this work, the ion exchange behaviour of PPy doped with a series of 1-alkyl sulfonate dopants, $C_nH_{2n+1}SO_3^-$ ($n = 3$ to 10), was evaluated in terms of dual-mode ion migration. The results showed that for small n the sulfonate dopant could move in and out of the polymer during the doping-undoping redox switching, whereas for large n , the dopant was trapped inside the polymer and cations had to migrate through the polymer interface during the switching to counterbalance the

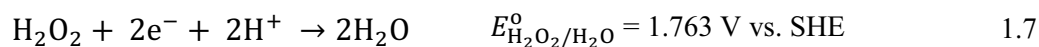
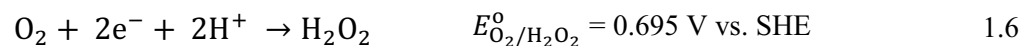
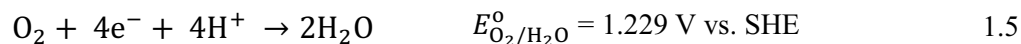
negative sulfonate groups. A mixed dual-transport (*i.e.*, both anionic and cationic) was observed for intermediate n values. However, the size of the anionic dopant is only one of the parameters that affect the ion-exchange properties of PPy.

In a more recent work by Weidlich *et al.* [213] the ion-exchange behaviour of PPy was examined and was shown to depend on both the ions incorporated into the polymer and the counterions present in the electrolyte solution. It was found that PPy/A⁻ doped with small monovalent dopants exchanged exclusively cations when electrochemically switched in a solution containing only A²⁻ bivalent counterions (*e.g.*, PPy/Cl⁻ exchanged Na⁺ in a Na₂SO₄ electrolyte). Also, PPy/A²⁻ doped with small bivalent dopants exchanged both anions and cations when switched in a solution of A⁻ with C²⁺ bivalent counterions (*e.g.*, PPy/SO₄²⁻ exchanged both Ca²⁺ and Cl⁻ in a CaCl₂ electrolyte). From these few examples, it is important to note that the ion-exchange properties of PPy, and of all other conducting polymers in general, are dependent on both the dopant present in the polymer and the ionic nature of the electrolyte in solution. PPy can also exchange OH⁻ ions when electrochemically switched in basic solutions; however the hydroxyl anions have a deactivating effect on the conductivity of the polymer. This is due to the N-H...OH hydrogen bonding which confines the polaronic positive charges on the nitrogen sites. This is the origin of the observed dramatic decrease in the conductivity of PPy after base treatment [214].

In general, the rate determining step of the doping-undoping process in PPy is governed by ion migration; in fact the electron transfer is usually much faster during the redox switching.

1.4.2.4 Oxygen Reduction Reaction at PPy Film-Modified Electrodes

The Oxygen Reduction Reaction (ORR) is of interest for the present work because it can cause interfacial pH changes and influence the electrochemistry of deposition. Also referred to as dioxygen reduction, the ORR has been recently summarized by Savéant [215] in a general review about the mechanistic aspects of molecular catalysis of electrochemical reactions. The three fundamental reactions involved in the ORR in the presence of proton donors (*e.g.*, H₂O), and their corresponding standard potentials (expressed versus the Standard Hydrogen Electrode, SHE), are listed in Equations 1.5, 1.6 and 1.7.



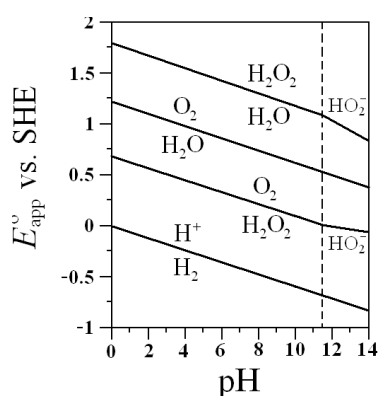
The corresponding equilibrium redox potentials at 25 °C are given in Equations 1.8, 1.9 and 1.10, respectively.

$$E_{\text{O}_2/\text{H}_2\text{O}} = E_{\text{O}_2/\text{H}_2\text{O}}^{\circ'} + \frac{0.059}{4} \log[\text{O}_2][\text{H}^+]^4 \quad 1.8$$

$$E_{\text{O}_2/\text{H}_2\text{O}_2} = E_{\text{O}_2/\text{H}_2\text{O}_2}^{\circ'} + \frac{0.059}{2} \log \frac{[\text{O}_2][\text{H}^+]^2}{[\text{H}_2\text{O}_2]} \quad 1.9$$

$$E_{\text{H}_2\text{O}_2/\text{H}_2\text{O}} = E_{\text{H}_2\text{O}_2/\text{H}_2\text{O}}^{\circ'} + \frac{0.059}{2} \log[\text{H}_2\text{O}_2][\text{H}^+]^2 \quad 1.10$$

The activity of each species is approximated with its corresponding concentration, and all activity coefficients are collected in the formal potential, $E^{\circ'}$ [216]. By replacing $-\log[\text{H}^+]$ with pH and using the apparent standard potential, E_{app}° , the following expressions, shown in Equations 1.11, 1.12 and 1.13, are obtained.



$$E_{\text{O}_2/\text{H}_2\text{O},\text{app}}^{\circ} = E_{\text{O}_2/\text{H}_2\text{O}}^{\circ'} - 0.059 \text{ pH} \quad 1.11$$

$$E_{\text{O}_2/\text{H}_2\text{O}_2,\text{app}}^{\circ} = E_{\text{O}_2/\text{H}_2\text{O}_2}^{\circ'} - 0.059 \text{ pH} \quad 1.12$$

$$E_{\text{H}_2\text{O}_2/\text{H}_2\text{O},\text{app}}^{\circ} = E_{\text{H}_2\text{O}_2/\text{H}_2\text{O}}^{\circ'} - 0.059 \text{ pH} \quad 1.13$$

Figure 1.19 Plot of Equations 1.11, 1.12 and 1.13, and of the reduction of protons.

Using these relationships and the approximation of $E^{\circ'} = E^{\circ}$ (*i.e.*, $\gamma=1$), a plot of E_{app}° as a function of pH can be generated (Figure 1.19). At $\text{pH} > 11.6$ the H_2O_2 is deprotonated to HO_2^- and the slopes of the E_{app}° become $59 \times 1/2 = 29.5 \text{ mV}$ for the

O_2/HO_2^- and $59 \times 3/2 = 88.5$ mV for the $\text{HO}_2^-/\text{H}_2\text{O}$ couples, respectively. From the plot in Figure 1.19, it is easy to see that *thermodynamically* the reduction of H_2O_2 is easier than the reduction of O_2 at all pH values, however *kinetically* the order is reversed and H_2O_2 appears as a product of the ORR [215].

The mechanism of the ORR in aqueous electrolytes is given in Figure 1.20 [215]. The conversion of an oxygen molecule to hydrogen peroxide generates two hydroxyl ions; two other hydroxyl ions are produced by the further reduction of the peroxide.

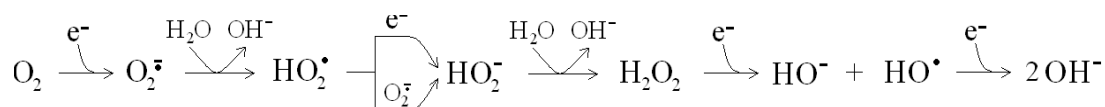


Figure 1.20 Mechanism of the Oxygen Reduction Reaction (ORR) in water-based electrolytes. An oxygen molecule is reduced to a radical anion that is then protonated. Further reduction and proton exchange generates hydrogen peroxide. The peroxide can be finally reduced to hydroxide.

The overall reduction of oxygen gives rise to the formation of four hydroxyl ions with a corresponding local increase of pH at the electrode interface. In the presence of species that are insoluble at basic pH, the ORR can cause their electroprecipitation on the electrode surface. This phenomenon can be used to perform controlled electrochemical depositions of compounds different than metals (*e.g.*, hydroxides, oxides or hydroxy-based compounds).

The ORR has been studied at PPy modified materials and electrodes. PPy-ClO₄ (perchlorate) doped films have improved efficiencies toward the conversion of molecular oxygen to water by increasing the residence time of H_2O_2 at the electrode surface [217, 218]. PPy doped with anthraquinonedisulfonate (AQDS) is catalytically active towards ORR with a preferential two electron process (H_2O_2 generation); the AQDS acts as an electron mediator for the ORR ($\text{AQDS} + 2\text{H}^+ + e^- \rightarrow \text{H}_2\text{AQDS} + \text{O}_2 \rightarrow \text{H}_2\text{O}_2 + \text{AQDS}$), whereas PPy acts as a charge transport medium [219-223]. PPy is also used as a source of nitrogen in nitrogen-enriched carbon supports prepared by pyrolysis. Co-PPy/C is a cheap catalyst compared to Pt/C and has similar catalytic activity for the ORR in proton exchange membrane fuel cells (PEMFCs). The activity is due to the N content and the surface morphologies have a

significant effect on the ORR [224-230]. Other PPy-based materials used for the ORR are Pt-PPy/C [231-233], and metal porphyrins or metal phthalocyanine incorporated PPy electrodes [234-238].

1.5 Electrochemistry of Copper and Zinc

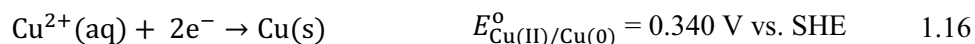
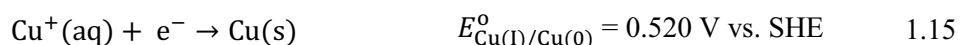
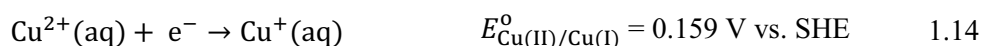
1.5.1 Electrochemistry of Copper

1.5.1.1 Electronic Structure and Oxidation States of Copper

The electronic configuration of copper is $[\text{Ar}]3d^{10}4s^1$ and the two stable isotopes are ^{63}Cu and ^{65}Cu ($Z = 29$). In the valence shell of copper there is one s electron, like for potassium $[\text{Ar}]4s^1$, and ten d electrons. The s electron can be removed to generate the oxidation state +1, Cu(I). The first ionization energy of copper (7.72 eV) is higher than that of potassium (4.34 eV) because the $3d^{10}$ shell has a lower shielding effect on the nuclear charge of copper than the noble-gas shell on the nuclear charge of the alkali metal. On the other hand, it is feasible to remove a second electron from the d shell of copper (20.29 eV) and generate the oxidation state +2, Cu(II); but it is not possible to remove it from the potassium atom where the noble-gas shell would have to be disrupted (31.81 eV). The oxidation states Cu(III) and Cu(IV) can also occur in some oxide structures but are unstable in solution [239]. The electrochemistry of copper in aqueous solutions and in the absence of hard donor atoms is then governed by the Cu(0), Cu(I) and Cu(II) oxidation states [240].

1.5.1.2 Electrochemistry of Copper

The three main reduction reactions of copper ions solvated in water are given below in Equations 1.14, 1.15 and 1.16 [240].



Having $E_{\text{Cu(I)/Cu(0)}}^{\circ} > E_{\text{Cu(II)/Cu(I)}}^{\circ}$ implies that the redox couple Cu(I)/Cu(0) can act as an oxidising agent toward the couple Cu(II)/Cu(I); in these terms Cu(I) is reduced to Cu(0) in order to oxidize Cu(I) to Cu(II). This gives the following disproportionation reaction, Equation 1.17.



In this analysis $K_{\text{disp}} = [\text{Cu}^{2+}]/[\text{Cu}^+]^2$. A simple rearrangement and substitution of the equilibrium constant gives $[\text{Cu}^+] = ([\text{Cu}^{2+}]/[\text{Cu}^+]) \times K_{\text{disp}}^{-1} \approx ([\text{Cu}^{2+}]/[\text{Cu}^+]) \times 10^{-6}$, from which it is evident that Cu(I) is only stable and present in solution in comparable amounts to Cu(II), *i.e.*, $[\text{Cu}^{2+}]/[\text{Cu}^+] = 1$, for concentrations within the μM range. In all other cases, if the starting concentration of Cu(I) is higher, the disproportionation takes place and the dominant species in solution is the Cu(II). A way to improve the Cu(II)/Cu(I) electrochemistry is to introduce ligands which are able to stabilize the oxidation state Cu(I) [240].

The fully hydrated form of Cu(II) in aqueous solutions is $\text{Cu}(\text{H}_2\text{O})_6^{2+}$. Less hydrated species are liable to hydrolysis, as shown in Equations 1.18 and 1.19 [241-243].



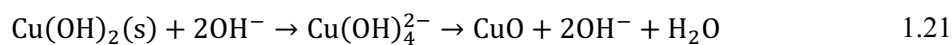
The metal-oxygen interaction inside the aqua complexes can cause the hydrolysis of the HO–H bond with the associated release of protons. In general, the hydrolysis is favoured in alkaline solutions; however at moderately alkaline pH values the Cu(II) hydroxide can precipitate, Equation 1.20.



In concentrated solutions the precipitation begins at a pH value just above 4.0. For example, in the case of $[\text{Cu}^{2+}] = 0.10 \text{ M}$, the $\text{Cu}(\text{OH})_2$ can form at $\text{pH} \geq \text{pK}_w + \frac{1}{2}\text{p}[\text{Cu}^{2+}] - \frac{1}{2}\text{pK}_{\text{sp}} = 14 + 0.5 - 9.6 = 4.9$; for this reason, the soluble hydrolytic species can be found mainly in diluted copper solutions [240].

The $\text{Cu}(\text{OH})_2(\text{s})$ is a *meta*-stable compound that is easily transformed to CuO. In fact, in the presence of an excess of OH^- the copper hydroxide is dehydrated to give the

more stable oxide, a reaction assisted by a soluble intermediate tetrahydroxycuprate(II) ion, Equation 1.21 [240].



A detailed description of the hydroxide-to-oxide transition in alkaline solution is also available in the literature [244]. The high affinity of Cu(II) for hydroxide results in the formation of soluble tri- and tetra-hydroxycuprate ions at high pH conditions, Equation 1.22 [240].



Both these species can dehydrate to give HCuO_2^- and CuO_2^{2-} , respectively. The predominance and stability regions of the various copper species in solution at different potential-pH conditions are summarized in the Pourbaix diagram of copper which is provided in Figure 1.21. In this diagram, the species placed in each region are those thermodynamically favoured at the given copper(II) concentration, potential and pH. In the case of 0.10 M Cu^{2+} the species that are stable within the diagram ranges are Cu, Cu^{2+} , Cu_2O and CuO.

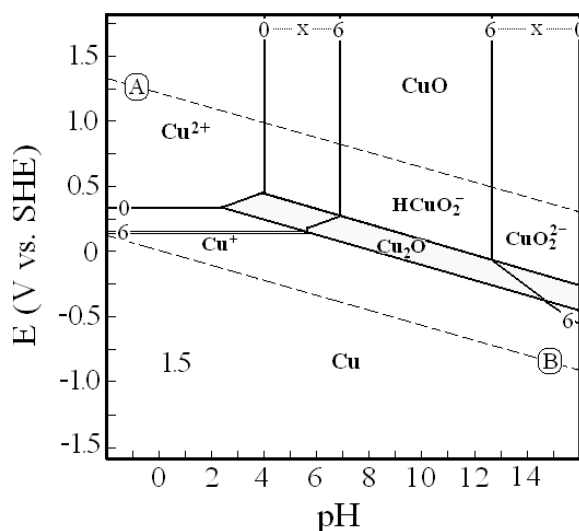


Figure 1.21 Pourbaix diagram of copper at 25 °C. The positions of the borders are dependent on the concentration of copper(II) in solution, $[\text{Cu}^{2+}] = 10^{-x}$ M with x from 0 to 6. Note that for concentrations of copper(II) higher than 0.10 M, the hydroxycuprate ions do not form at pH below 14, and that the CuO and Cu_2O regions extend beyond that pH. The dashed lines A and B refer to the reduction of oxygen ($\text{O}_2 + 2\text{H}_2\text{O} + 4\text{e}^- \rightarrow 4\text{OH}^-$) and the hydrogen evolution reaction ($2\text{H}^+ + 2\text{e}^- \rightarrow \text{H}_2$), respectively [245, 246].

In the presence of sulfate anions (*e.g.*, when using CuSO_4 as an electrolyte), the Pourbaix diagram is modified by the formation of insoluble species, for example copper hydroxysulfates (Figure 1.22). In this case, the diagram was calculated with the MEDUSA software developed by Puigdomenech at the KTH Royal Institute of Technology, Sweden [247] based on the SOLGASWATER algorithm [248]. The calculations were performed on the original software database, as a function of potential and pH taking into account the electrochemical stability of sulfate anions under the considered conditions [249]. As it can be seen from the diagram, between pH values of 1.0 and 7.0, the deposition of three species, namely, chalcocyanite ($\text{CuSO}_4(\text{s})$), antlerite ($\text{CuSO}_4[\text{Cu}(\text{OH})_2]_2$), and brochantite ($\text{CuSO}_4[\text{Cu}(\text{OH})_2]_3$) is predicted. In generating these results other insoluble species were considered, posnjakite ($\text{CuSO}_4[\text{Cu}(\text{OH})_2]_3 \cdot \text{H}_2\text{O}$) and dolerophanite (CuOCuSO_4) that do not appear in the diagram. Most of the scientific literature describing the insoluble products of copper and sulfate ions is related to the chemistry of copper patinas in corrosion science [250-252].

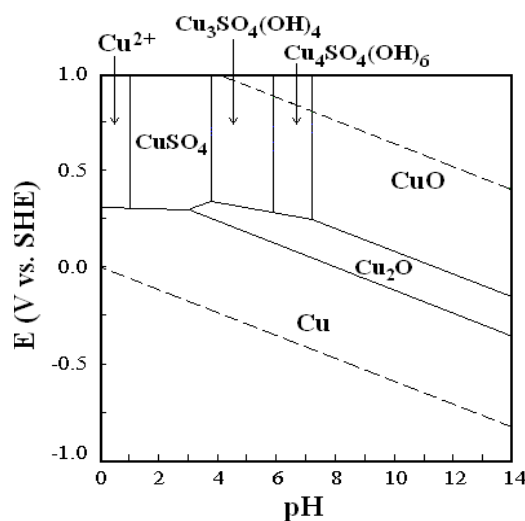


Figure 1.22 Pourbaix diagram of copper in the presence of sulfate anions at 25 °C. The concentrations of copper and sulfate are the same, $[\text{Cu}^{2+}] = [\text{SO}_4^{2-}] = 0.10 \text{ M}$. The present diagram was calculated with the MEDUSA software [247] run in PREDOM2 modality and with all the listed products of sulfate reduction deactivated.

The electrochemistry of copper at PPy films can be affected by different factors. For example, Cu^{2+} can be exchanged by PPy doped with trapped polyanions. The resulting effect is to increase the surface concentration and shift the reduction of copper towards less negative potentials ($E \propto \log[\text{Cu}^{2+}]$). Moreover, there are known examples of direct Cu-PPy interaction between the copper ions and either the

conducting polymer or its dopants. Spectroscopic evidence of Cu-PPy complexation has been found in polymers doped with small ions where copper interacts directly with the pyrrolic nitrogen [253-256]. The interaction between copper and pyrrolic nitrogen has been recently observed for copper ions onto nanothin PPy films [257]. In addition, Cu-dopant interactions have been found in the presence of sulfonated dopants where copper is bounded to the $-\text{SO}_3^-$ groups [258, 259].

The electrochemistry of copper can also be affected by other reduction processes at the PPy interface. The oxygen reduction at PPy films (Section 1.4.2.4) can generate hydroxides and cause the electroprecipitation of hydroxyl-based Cu species. This process can happen in the presence of other ions, *e.g.*, sulfate, and generate some of the basic sulfate species discussed later in Chapters 3 and 5.

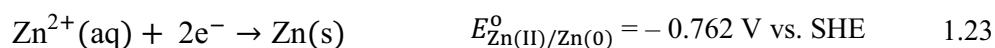
1.5.2 Electrochemistry of Zinc

1.5.2.1 Electronic Structure and Oxidation States of Zinc

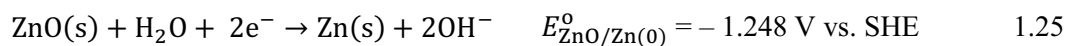
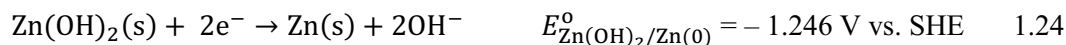
The electronic configuration of zinc is $[\text{Ar}]3d^{10}4s^2$ and the two main stable isotopes are ^{64}Zn and ^{66}Zn ($Z = 30$). In the valence shell of zinc there are two s electrons and ten d electrons. The two s electrons can be readily removed to generate the oxidation state +2, Zn(II); in fact, the first and second ionization energies of zinc (9.39 eV and 17.89 eV, respectively) are low enough to be effectively counterbalanced by the solvation or lattice formation energies. For this reason the ubiquitous oxidation state of zinc is the +2. The oxidation state +1, Zn(I), is formed only in particular circumstances (*e.g.*, in fused ZnCl_2 salts) as a Zn_2^{2+} dimer characterized by the presence of a metal-metal bond, whereas Zn^+ , a very strong reducing agent, is never formed [239]. The oxidation state +3, Zn(III), is not accessible because of the very high third ionization energy (40.0 eV) that is required to remove an electron from the full 3d outer shell. The electrochemistry of zinc in aqueous solutions accounts only for the Zn(0) and Zn(II) oxidation states [245, 260].

1.5.2.2 Electrochemistry of Zinc

The main reduction reaction of zinc ion solvated in acidified water is shown in Equation 1.23 [245, 260].



In basic solutions there are three other reactions that are connected to the formation of zinc hydroxide/oxide and to the amphoteric nature of the zinc(II) ion, Equations 1.24, 1.25 and 1.26.



The solubility product of Zn(OH)_2 is given in Equation 1.27 as follows.



In concentrated solutions the precipitation of Zn(OH)_2 begins at a pH value just above 5.0. For example, in the case of $[\text{Zn}^{2+}] = 0.10 \text{ M}$ the hydroxide can form at $\text{pH} \geq \text{p}K_{\text{w}} + \frac{1}{2}\text{p}[\text{Zn}^{2+}] - \frac{1}{2}\text{p}K_{\text{sp}} = 14 + 0.5 - 8.2 = 5.2$.

The stability regions of the various zinc species in solution at different potential-pH conditions are summarized in the Pourbaix diagram of zinc, shown in Figure 1.23. In this diagram, the species placed in each region are those thermodynamically favoured at the given zinc(II) concentration, potential and pH.

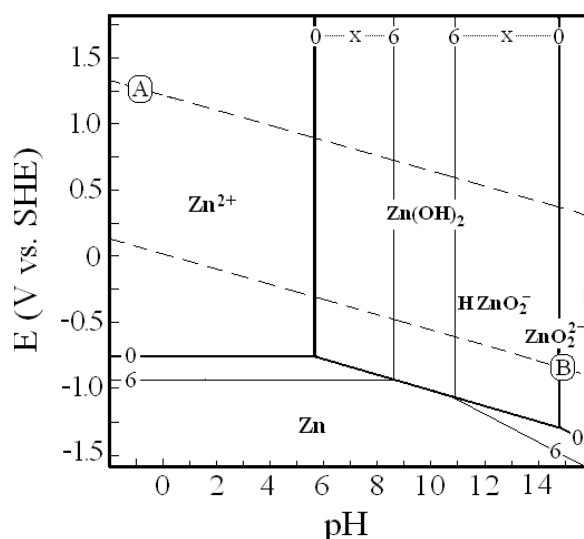


Figure 1.23 Pourbaix diagram of zinc at 25 °C. The positions of the borders are dependent on the concentration of Zn(II) in solution, $[\text{Zn}^{2+}] = 10^{-x} \text{ M}$ with x from 0 to 6. Note that for concentrations of Zn(II) higher than 0.10 M, the hydroxyzincate ions do not form at pH below 14, and that the Zn(OH)_2 region extends beyond that pH. The dashed lines A and B refer to the reduction of oxygen ($\text{O}_2 + 2\text{H}_2\text{O} + 4\text{e}^- \rightarrow 4\text{OH}^-$) and proton ($2\text{H}^+ + 2\text{e}^- \rightarrow \text{H}_2$), respectively [245, 261].

The HZnO_2^- and ZnO_2^{2-} species are generated from the dehydration of the hydroxizincates, $\text{Zn}(\text{OH})_3^-$ and $\text{Zn}(\text{OH})_4^{2-}$, respectively.

In the presence of sulfate anions (*e.g.*, when using ZnSO_4 as electrolyte), the Pourbaix diagram is modified by the formation of insoluble species, such as zinc hydroxysulfates (Figure 1.24), and obtained by using the same software as mentioned previously for copper (Section 1.5.1.2). As it can be seen from the diagram, between pH values 6.0 and 8.0 the software predicts the deposition of zinc hydroxysulfate, $\text{ZnSO}_4 \cdot [\text{Zn}(\text{OH})_2]_3$. At lower pH water soluble ZnSO_4 is formed. Other insoluble species, that do not appear in the diagram, like the $\text{ZnO} \cdot \text{ZnSO}_4$, were also considered in the calculations.

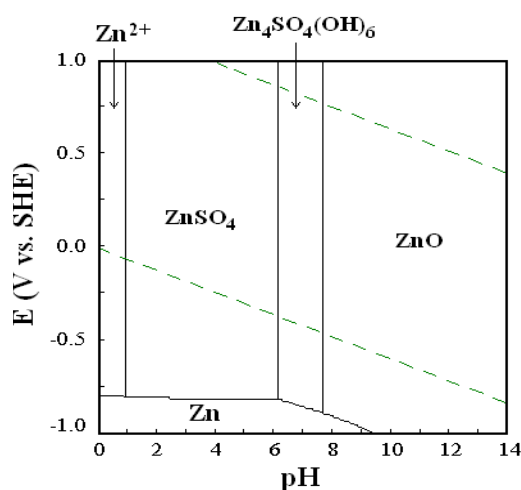


Figure 1.24 Pourbaix diagram of zinc in the presence of sulfate anions at 25 °C. The concentrations of zinc and sulfate are the same, $[\text{Zn}^{2+}] = [\text{SO}_4^{2-}] = 0.10 \text{ M}$. The present diagram has been calculated with the MEDUSA software [247] run in PREDOM2 modality and with all the listed products of sulfate reduction deactivated.

Most of the scientific literature about the insoluble products of zinc and sulfate ions are related to the corrosion chemistry of zinc [262-265] and to the class of materials named layered hydroxide salts [266].

To date there have been very few studies on the interaction of zinc with PPy. Most studies have focused on the deposition of protective PPy layers onto zinc electrodes for corrosion control [267-271]. Other fields of interest are zinc ion sensing on PPy modified electrodes [272, 273], or the development of zinc-based batteries in which PPy is employed in the cathodic compartment [274, 275]. The oxygen reduction at PPy films (Section 1.4.2.4) in the presence of zinc and other anions, *e.g.* sulfate, can generate some of the zinc hydroxysulfate species previously discussed.

1.6 Copper and Zinc Micro/Nanostructures

The term ‘nanostructure’ is used to classify those materials that are confined in a volume with at least one dimension spanning from the subnanometer to several hundred of nanometers range ($1 \text{ nm} = 10^{-9} \text{ m}$). Nanomaterials can occur in different forms such as nanoparticles, nanowires, nanosheets, thin films and bulk materials made of nanoscale building blocks [276-278]. Nanoparticles, nanowires, nanosheets and nanocubes are usually referred as 0-, 1-, 2- and 3-dimensional (D) nanostructures, respectively; whereas their arrangement in combined structures of higher dimensionality are referred to as hierarchical micro/nanostructures. For example, ‘2-3 flowers’ are 3D flower-like hierarchical micro/nanostructures made from the assembly of many 2D nanosheets [279]. The design and synthesis of hierarchical structures, sometimes resembling those of biological materials, is a very important field of research where micro/nanomaterials are prepared with improved performances [280-283].

Hierarchical flower-like copper micro/nanostructures are prepared hydrothermally in alkaline solutions. Typically, the preparation takes from hours to days, depending on the temperature and concentration of the base. Recently, CuO rose-like architectures have been prepared from copper powder in the presence of $(\text{NH}_4)_2\text{S}_2\text{O}_8$ in warm KOH solution [284]. CuO sheet-like architectures were also generated by oxidation of copper foils in NaOH solution or in a copper(II) acetate solution by adding ammonia [285-288]. The formation of nanosheets was attributed to the layered structure of $\text{Cu}(\text{OH})_2$ that could act as a ‘template’ and maintain its shape during the CuO growth. A detailed description of the assembling process from $\text{Cu}(\text{OH})_2$ to CuO nanoleaves has been given by Xu *et al.* [244]. In all these cases nanothin copper sheets were formed in the presence of a hydroxide source, which is necessary to produce the precursor, $\text{Cu}(\text{OH})_2$.

Copper nanoparticles are prevalently prepared and applied as catalysts for electroanalytical sensing applications [289, 290]. The interest in nanoparticles, otherwise referred to as quantum dots, stems in the quantum-confinement of electrons in very small volumes which gives rise to a novel and improved reactivity [291-293]. Copper nanoparticles are synthesized in colloidal suspension or electrodeposited on the electrode surface [294, 295], the latter being the most

common route for electrochemical sensing applications. Copper metal or oxide nanoparticles [296] are catalytically active toward several target analytes, like, for example, nitrates, nitrites, oxygen, hydrogen peroxide, carbohydrates and aminoacids [289, 290].

Zinc layered hydroxide salts are of interest for the synthesis of hybrid organic/inorganic microporous materials with considerable chemical and structural diversity [297, 298], and for the preparation of oversized zinc hydroxysulfate nanosheets that are useful precursors of the technologically important ZnO [299, 300]. In relation to this, a paper on the evolution of ZnO rods to zinc hydroxysulfate plates has recently been published [301]. At present, layered hydroxide salts are attracting the attention of researchers because of their potential applications in several technological areas like anion scavengers, selective cation exchangers, metal oxide precursors, anti-corrosion agents, metal nanoparticle templates, polymer nanocomposite fillers, and as polymer additives for energy storage devices and polymer electrolytes [266].

1.7 References

- [1] Franssila S; *Introduction to Microfabrication*; 2004, 1st ed., Wiley
- [2] Köhler M, Fritzsche W; *Nanotechnology: An Introduction to Nanostructuring Techniques*; 2004, 1st ed., Wiley
- [3] Paunovic M, Schlesinger M; *Fundamentals of Electrochemical Deposition*; 2006, 2nd ed., Wiley-Interscience
- [4] Hunt LB; *Gold Bulletin*, **1973**, 6(1), 16
- [5] Chiang C, Kawa J; *Design for Manufacturability and Yield for Nano-Scale CMOS*; 2007, 1st ed., Springer
- [6] Hu CK, Harper JME; *Materials Chemistry and Physics*, **1998**, 52(1), 5
- [7] Vereecken PM, Binstead RA, Deligianni H, Andricacos PC; *IBM Journal of Research and Development*, **2005**, 49(1), 3
- [8] Brown PW, Constantz B; *Hydroxyapatite and Related Materials*; 1994, 1st ed., CRC Press
- [9] Huang LY, Xu KW, Lu J; *Journal of Materials Science-Materials in Medicine*, **2000**, 11(11), 667
- [10] Kuo MC, Yen SK; *Materials Science & Engineering C-Biomimetic and Supramolecular Systems*, **2002**, 20(1-2), 153
- [11] Zhang YY, Tao J, Pang YC, Wang W, Wang T; *Transactions of Nonferrous Metals Society of China*, **2006**, 16(3), 633

-
- [12] Zheng MJ, Zhang LD, Li GH, Shen WZ; *Chemical Physics Letters*, **2002**, 363(1-2), 123
- [13] Tan YW, Srinivasan S, Choi KS; *Journal of the American Chemical Society*, **2005**, 127(10), 3596
- [14] Tsakova V; *Journal of Solid State Electrochemistry*, **2008**, 12(11), 1421
- [15] Holdcroft S; *Advanced Materials*, **2001**, 13(23), 1753
- [16] Klein JD, Herrick RD, Palmer D, Sailor MJ, Brumlik CJ, Martin CR; *Chemistry of Materials*, **1993**, 5(7), 902
- [17] Routkevitch D, Bigioni T, Moskovits M, Xu JM; *Journal of Physical Chemistry*, **1996**, 100(33), 14037
- [18] Zhang XY, Zhang LD, Chen W, Meng GW, Zheng MJ, Zhao LX; *Chemistry of Materials*, **2001**, 13(8), 2511
- [19] Jin CG, Xiang XQ, Jia C, Liu WF, Cai WL, Yao LZ, Li XG; *Journal of Physical Chemistry B*, **2004**, 108(6), 1844
- [20] Braun P, Wiltzius P; *Advanced Materials*, **2001**, 13(7), 482
- [21] Kazimierska E, Muchindu M, Morrin A, Iwuoha E, Smyth MR, Killard AJ; *Electroanalysis*, **2009**, 21(3-5), 595
- [22] Aizawa M, Shinohara H, Yamada T, Akagi K, Shirakawa H; *Synthetic Metals*, **1987**, 18(1-3), 711
- [23] Ouyang M, Bai R, Xu Y, Zhang C, Ma CA, Wang M, Chen HZ; *Transactions of Nonferrous Metals Society of China*, **2009**, 19(6), 1572
- [24] Sun L, Chien CL, Searson PC; *Chemistry of Materials*, **2004**, 16, 3125
- [25] Nalwa HS; *Handbook of Organic Conductive Molecules and Polymers*; 1997, Wiley
- [26] Chandrasekhar P; *Conducting Polymers, Fundamentals and Applications: a Practical Approach*; 1999, 1st ed., Springer
- [27] Skotheim TA, Reynolds JR; *Handbook of conducting polymers*; 2007, 3rd ed., CRC Press
- [28] Inzelt G; *Conducting Polymers: A New Era in Electrochemistry*; 2008, 1st ed., Springer
- [29] Waltman RJ, Bargon J; *Canadian Journal of Chemistry-Revue Canadienne De Chimie*, **1986**, 64(1), 76
- [30] Diaz AF, Rubinson JF, Mark HB; *Advances in Polymer Science*, **1988**, 84, 113
- [31] Stenger-Smith JD; *Progress in Polymer Science*, **1998**, 23(1), 57
- [32] Gurunathan K, Murugan AV, Marimuthu R, Mulik UP, Amalnerkar DP; *Materials Chemistry and Physics*, **1999**, 61(3), 173
- [33] Gerard M, Chaubey A, Malhotra BD; *Biosensors & Bioelectronics*, **2002**, 17(5), 345
- [34] Trojanowicz M; *Microchimica Acta*, **2003**, 143(2-3), 75
- [35] Forrest SR; *Nature*, **2004**, 428(6986), 911
- [36] Jang J; *Conducting Polymer Nanomaterials and their Applications*, Emissive Materials: Nanomaterials, 2006, 199, Springer
- [37] Fang FF, Choi HJ, Joo J; *Journal of Nanoscience and Nanotechnology*, **2008**, 8(4), 1559
- [38] Li C, Bai H, Shi GQ; *Chemical Society Reviews*, **2009**, 38(8), 2397
-

-
- [39] Xia L, Wei ZX, Wan MX; *Journal of Colloid and Interface Science*, **2010**, 341(1), 1
- [40] Kaiser AB; *Advanced Materials*, **2001**, 13(12-13), 927
- [41] Curran S, Stark-Hauser A, Roth S; *Polyacetylene*, Organic Conductive Molecules and Polymers, 1997, 2, Wiley
- [42] Heeger AJ; *Reviews of Modern Physics*, **2001**, 73(3), 681
- [43] MacDiarmid AG; *Reviews of Modern Physics*, **2001**, 73(3), 701
- [44] Shirakawa H; *Reviews of Modern Physics*, **2001**, 73(3), 713
- [45] Natta G, Mazzanti G, Corradini P; *Atti dell'Accademia Nazionale dei Lincei, Cl. Sci. Fis., Mat. Nat., Rend.*, **1958**, 25, 2
- [46] Ito T, Shirakawa H, Ikeda S; *Journal of Polymer Science Part A-Polymer Chemistry*, **1974**, 12(1), 11
- [47] Ito T, Shirakawa H, Ikeda S; *Journal of Polymer Science Part A-Polymer Chemistry*, **1975**, 13(8), 1943
- [48] Shirakawa H, Ito T, Ikeda S; *Makromolekulare Chemie-Macromolecular Chemistry and Physics*, **1978**, 179(6), 1565
- [49] Chiang CK, Druy MA, Gau SC, Heeger AJ, Louis EJ, MacDiarmid AG, Park YW, Shirakawa H; *Journal of the American Chemical Society*, **1978**, 100(3), 1013
- [50] Chiang CK, Park YW, Heeger AJ, Shirakawa H, Louis EJ, MacDiarmid AG; *Journal of Chemical Physics*, **1978**, 69(11), 5098
- [51] Harada I, Tasumi M, Shirakawa H, Ikeda S; *Chemistry Letters*, **1978**, (12), 1411
- [52] Yen SPS, Somoano R, Khanna SK, Rembaum A; *Solid State Communications*, **1980**, 36(4), 339
- [53] Bhadra S, Khastgir D, Singha NK, Lee JH; *Progress in Polymer Science*, **2009**, 34(8), 783
- [54] Jing XB, Wang LX, Wang XH, Geng YH, Wang FS; *Acta Polymerica Sinica*, **2005**, (5), 655
- [55] Negi YS, Adhyapak PV; *Journal of Macromolecular Science-Polymer Reviews*, **2002**, C42(1), 35
- [56] Gospodinova N, Terlemezyan L; *Progress in Polymer Science*, **1998**, 23(8), 1443
- [57] Anand J, Palaniappan S, Sathyanarayana DN; *Progress in Polymer Science*, **1998**, 23(6), 993
- [58] Kang ET, Neoh KG, Tan KL; *Progress in Polymer Science*, **1998**, 23(2), 277
- [59] Mattoso LHC; *Quimica Nova*, **1996**, 19(4), 388
- [60] Bhattacharya A, De A; *Progress in Solid State Chemistry*, **1996**, 24(3), 141
- [61] Genies EM, Boyle A, Lapkowski M, Tsintavis C; *Synthetic Metals*, **1990**, 36(2), 139
- [62] Genies EM, Lapkowski M, Tsintavis C; *New Journal of Chemistry*, **1988**, 12(4), 181
- [63] Wei M, Lu Y; *Synthetic Metals*, **2009**, 159(11), 1061
- [64] Duchet J, Legras R, Demoustier-Champagne S; *Synthetic Metals*, **1998**, 98(2), 113
- [65] Machida S, Miyata S, Techagumpuch A; *Synthetic Metals*, **1989**, 31(3), 311
-

-
- [66] Cheung KM, Bloor D, Stevens GC; *Polymer*, **1988**, 29(9), 1709
- [67] Rapi S, Bocchi V, Gardini GP; *Synthetic Metals*, **1988**, 24(3), 217
- [68] Diaz AF, Hall B; *IBM Journal of Research and Development*, **1983**, 27(4), 342
- [69] Diaz AF, Castillo JI, Logan JA, Lee WY; *Journal of Electroanalytical Chemistry*, **1981**, 129(1-2), 115
- [70] Diaz AF, Castillo JI; *Journal of the Chemical Society - Chemical Communications*, **1980**, (9), 397
- [71] Kanazawa KK, Diaz AF, Gill WD, Grant PM, Street GB, Gardini GP; *Synthetic Metals*, **1980**, 1(3), 329
- [72] Kanazawa KK, Diaz AF, Geiss RH, Gill WD, Kwak JF, Logan JA, Rabolt JF, Street GB; *Journal of the Chemical Society-Chemical Communications*, **1979**, (19), 854
- [73] Zhang BZ, Zhao XY; *Journal of Materials Science*, **2009**, 44(11), 2765
- [74] Sato M, Tanaka S, Kaeriyama K; *Synthetic Metals*, **1986**, 14(4), 279
- [75] Mo Z, Lee KB, Moon YB, Kobayashi M, Heeger AJ, Wudl F; *Macromolecules*, **1985**, 18(10), 1972
- [76] Sato M, Tanaka S, Kaeriyama K; *Journal of the Chemical Society - Chemical Communications*, **1985**, (11), 713
- [77] Tourillon G, Garnier F; *Journal of Electroanalytical Chemistry*, **1984**, 161(1), 51
- [78] Tourillon G, Garnier F; *Journal of Polymer Science Part B-Polymer Physics*, **1984**, 22(1), 33
- [79] Tourillon G, Garnier F; *Journal of the Electrochemical Society*, **1983**, 130(10), 2042
- [80] Kaneto K, Yoshino K, Inuishi Y; *Solid State Communications*, **1983**, 46(5), 389
- [81] Waltman RJ, Bargon J, Diaz AF; *Journal of Physical Chemistry*, **1983**, 87(8), 1459
- [82] Kaneto K, Kohno Y, Yoshino K, Inuishi Y; *Journal of the Chemical Society-Chemical Communications*, **1983**, (7), 382
- [83] McQuarrie DA; *Quantum chemistry*; 2007, 2nd ed., University Science Books
- [84] Kao KC; *Recent Research Developments in Polymer Science*, **1999**, 3, 247
- [85] Yang SJ, Olishevski P, Kertesz M; *Synthetic Metals*, **2004**, 141(1-2), 171
- [86] Haynes JR, Briggs HB; *Physical Review*, **1952**, 86(4), 647
- [87] Kanatzidis MG; *Chemical & Engineering News*, **1990**, 68(49), 36
- [88] MacDiarmid AG, Epstein AJ; *Faraday Discussions*, **1989**, 88, 317
- [89] MacDiarmid AG, Chiang JC, Richter AF, Epstein AJ; *Synthetic Metals*, **1987**, 18(1-3), 285
- [90] Chiang JC, MacDiarmid AG; *Synthetic Metals*, **1986**, 13(1-3), 193
- [91] Yan M, Rothberg LJ, Kwock EW, Miller TM; *Physical Review Letters*, **1995**, 75(10), 1992
- [92] Kersting R, Lemmer U, Deussen M, Bakker HJ, Mahrt RF, Kurz H, Arkhipov VI, Bassler H, Gobel EO; *Physical Review Letters*, **1994**, 73(10), 1440
- [93] Abe S, Schreiber M, Su WP, Yu J; *Physical Review B*, **1992**, 45(16), 9432
-

- [94] Ziemelis KE, Hussain AT, Bradley DDC, Friend RH, Ruhe J, Wegner G; *Physical Review Letters*, **1991**, 66(17), 2231
- [95] Burroughes JH, Bradley DDC, Brown AR, Marks RN, Mackay K, Friend RH, Burns PL, Holmes AB; *Nature*, **1990**, 347(6293), 539
- [96] Burroughes JH, Jones CA, Friend RH; *Nature*, **1988**, 335(6186), 137
- [97] Bredas JL, Street GB; *Accounts of Chemical Research*, **1985**, 18(10), 309
- [98] Yu L; *Solitons and Polarons in Conducting Polymers*; 1987, World Scientific Pub. Co. Inc.
- [99] Heeger AJ, Kivelson S, Schrieffer JR, Su WP; *Reviews of Modern Physics*, **1988**, 60(3), 781
- [100] Su WP, Schrieffer JR, Heeger AJ; *Physical Review Letters*, **1979**, 42(25), 1698
- [101] Kivelson S; *Physical Review Letters*, **1981**, 46(20), 1344
- [102] Yamabe T, Tanaka K, Yamanaka S, Koike T, Fukui K; *Journal of Chemical Physics*, **1985**, 82(12), 5737
- [103] Chance RR, Bredas JL, Silbey R; *Physical Review B*, **1984**, 29(8), 4491
- [104] Tolbert LM; *Accounts of Chemical Research*, **1992**, 25(12), 561
- [105] Nordén B; (*Advanced Information*) *The Nobel Prize in Chemistry, 2000: Conductive polymers*, 2000
- [106] Garcia-Alvarez JL; *Current Organic Chemistry*, **2008**, 12(14), 1199
- [107] Weder C; *Chemical Communications*, **2005**, (43), 5378
- [108] Jagur-Grodzinski J; *Polymers for Advanced Technologies*, **2002**, 13(9), 615
- [109] Reddinger JL, Reynolds JR; *Radical Polymerisation Polyelectrolytes, Molecular Engineering of Pi-Conjugated Polymers*, *Advances in Polymer Science*, Volume 145, 1999, Springer
- [110] Kumar D, Sharma RC; *European Polymer Journal*, **1998**, 34(8), 1053
- [111] Feast WJ, Tsibouklis J, Pouter KL, Groenendaal L, Meijer EW; *Polymer*, **1996**, 37(22), 5017
- [112] Toshima N, Hara S; *Progress in Polymer Science*, **1995**, 20(1), 155
- [113] Martin CR; *Accounts of Chemical Research*, **1995**, 28(2), 61
- [114] Diaz AF, Lacroix JC; *New Journal of Chemistry*, **1988**, 12(4), 171
- [115] Tran HD, Li D, Kaner RB; *Advanced Materials*, **2009**, 21(14-15), 1487
- [116] Ozin GA; *Advanced Materials*, **1992**, 4(10), 612
- [117] Gleiter H; *Advanced Materials*, **1992**, 4(7-8), 474
- [118] Satoh M, Kaneto K, Yoshino K; *Synthetic Metals*, **1986**, 14(4), 289
- [119] Chan HSO, Teo MYB, Khor E, Lim CN; *Journal of Thermal Analysis*, **1989**, 35(3), 765
- [120] Yue J, Epstein AJ, Zhong Z, Gallagher PK, MacDiarmid AG; *Synthetic Metals*, **1991**, 41(1-2), 765
- [121] Truong VT, Ennis BC, Turner TG, Jenden CM; *Polymer International*, **1992**, 27(2), 187
- [122] Bhadani SN, Gupta MK, Sengupta SK; *Journal of Applied Polymer Science*, **1993**, 49(3), 397
- [123] Yan BZ, Yang J, Li YF, Qian RY; *Synthetic Metals*, **1993**, 58(1), 17
- [124] Walton DJ, Hall CE, Chyla A; *Analyst*, **1992**, 117(8), 1305

-
- [125] Tanguy J, Hoclet M; *Synthetic Metals*, **1991**, 43(1-2), 2995
- [126] Della-Casa C, Fraleoni-Morgera A, Lanzi M, Costa-Bizzarri P, Paganin L, Bertinelli F, Schenetti L, Mucci A, Casalboni M, Sarcinelli F, Quatela A; *European Polymer Journal*, **2005**, 41(10), 2360
- [127] Somani P, Mandale AB, Radhakrishnan S; *Acta Materialia*, **2000**, 48(11), 2859
- [128] Mortimer RJ; *Electrochimica Acta*, **1999**, 44(18), 2971
- [129] Goddard YA, Vold RL, Hoatson GL; *Macromolecules*, **2003**, 36(4), 1162
- [130] Mucci A, Schenetti L; *Macromolecular Chemistry and Physics*, **1995**, 196(8), 2687
- [131] Kurosu H, Kikuchi M, Ando I; *Journal of Polymer Science Part B-Polymer Physics*, **1995**, 33(5), 769
- [132] da Silva JEP, de Torresi SIC, de Faria DLA, Temperini MLA; *Synthetic Metals*, **1999**, 101(1-3), 834
- [133] Gruger A, Novak A, Regis A, Colomban P; *Journal of Molecular Structure*, **1994**, 328, 153
- [134] Furukawa Y, Sakamoto A, Ohta H, Tasumi M; *Synthetic Metals*, **1992**, 49(1-3), 335
- [135] Hota PR, Parida RK, Das SC; *Journal of Reinforced Plastics and Composites*, **2009**, 28(3), 265
- [136] Cheah K, Forsyth M, Truong VT; *Synthetic Metals*, **1999**, 101(1-3), 19
- [137] Cai LT, Yao SB, Zhou SM; *Journal of Electroanalytical Chemistry*, **1997**, 421(1-2), 45
- [138] Golczak S, Kanciurzevska A, Fahlman M, Langer K, Langer JJ; *Solid State Ionics*, **2008**, 179(39), 2234
- [139] Suzer S, Birer O, Sevil UA, Guven O; *Turkish Journal of Chemistry*, **1998**, 22(1), 59
- [140] Idla K, Talo A, Niemi HEM, Forsen O, Ylasaari S; *Surface and Interface Analysis*, **1997**, 25(11), 837
- [141] Xue P, Tao XM, Tsang HY; *Applied Surface Science*, **2007**, 253(7), 3387
- [142] Dominguez-Ballart M, Bachas LG, Salvado V; *Quimica Analitica*, **2000**, 19(1), 49
- [143] Cacialli F, Bruschi P; *Journal of Applied Physics*, **1996**, 80(1), 70
- [144] Pron A, Rannou P; *Progress in Polymer Science*, **2002**, 27(1), 135
- [145] Bhattacharya A, De A; *Journal of Macromolecular Science-Reviews in Macromolecular Chemistry and Physics*, **1999**, C39(1), 17
- [146] Wang LX, Li XG, Yang YL; *Reactive & Functional Polymers*, **2001**, 47(2), 125
- [147] Bolto BA, Weiss DE; *Australian Journal of Chemistry*, **1963**, 16(6), 1076
- [148] Bolto BA, McNeill R, Weiss DE; *Australian Journal of Chemistry*, **1963**, 16(6), 1090
- [149] McNeill R, Weiss DE, Wardlaw JH, Siudak R; *Australian Journal of Chemistry*, **1963**, 16(6), 1056
- [150] Simonet J, Raultberthelot J; *Progress in Solid State Chemistry*, **1991**, 21(1), 1
-

-
- [151] Buckingham AD, Harris B, Lefevre RJW; *Journal of the Chemical Society*, **1953**, (MAY), 1626
- [152] Joule JA, Mills K; *Heterocyclic Chemistry*; 2010, 5th ed., Wiley-Blackwell
- [153] Allinger NL, Cava MP, De Jongh DC, Johnson, Lebel, Steven; *Organic Chemistry*; 1971, 1st ed., Worth Publishers
- [154] Mohammadi A, Yamini Y, Alizadeh N; *Journal of Chromatography A*, **2005**, 1063(1-2), 1
- [155] Elyashevich GK, Rosova EY, Sidorovich A, Kuryndin IS, Trchova M, Stejskal J; *European Polymer Journal*, **2003**, 39(4), 647
- [156] Pfluger P, Street GB; *Journal of Chemical Physics*, **1984**, 80(1), 544
- [157] Pfluger P, Krounbi M, Street GB, Weiser G; *Journal of Chemical Physics*, **1983**, 78(6), 3212
- [158] Waltman RJ, Diaz AF, Bargon J; *Journal of Physical Chemistry*, **1984**, 88(19), 4343
- [159] Jang J, Oh JH, Li XL; *Journal of Materials Chemistry*, **2004**, 14(19), 2872
- [160] Otero TF, Tejada R, Elola AS; *Polymer*, **1987**, 28(4), 651
- [161] Sayyah SM, Abd El-Rehim SS, El-Deeb MM; *Journal of Applied Polymer Science*, **2003**, 90(7), 1783
- [162] Zhou M, Pagels M, Geschke B, Heinze J; *Journal of Physical Chemistry B*, **2002**, 106(39), 10065
- [163] Zhou M, Heinze J; *Electrochimica Acta*, **1999**, 44(11), 1733
- [164] Zhou M, Heinze J; *Journal of Physical Chemistry B*, **1999**, 103(40), 8451
- [165] Zhou M, Heinze J; *Journal of Physical Chemistry B*, **1999**, 103(40), 8443
- [166] Zhou M, Rang V, Heinze J; *Acta Chemica Scandinavica*, **1999**, 53(11), 1059
- [167] Li YF, Fan YF; *Synthetic Metals*, **1996**, 79(3), 225
- [168] Kupila EL, Kankare J; *Synthetic Metals*, **1995**, 74(3), 241
- [169] Kupila EL, Kankare J; *Synthetic Metals*, **1993**, 55(2-3), 1402
- [170] Kim YT, Collins RW, Vedam K, Allara DL; *Journal of the Electrochemical Society*, **1991**, 138(11), 3266
- [171] Zhong CJ, Tian ZQ, Tian ZW; *Science in China Series B-Chemistry*, **1990**, 33(6), 656
- [172] Sadki S, Schottland P, Brodie N, Sabouraud G; *Chemical Society Reviews*, **2000**, 29(5), 283
- [173] Genies EM, Bidan G, Diaz AF; *Journal of Electroanalytical Chemistry*, **1983**, 149(1-2), 101
- [174] Funt BL, Diaz AF; *Organic Electrochemistry: an Introduction and a Guide*; 1991, Marcel Dekker
- [175] Feldberg SW; *Journal of the American Chemical Society*, **1984**, 106(17), 4671
- [176] Shichiri T, Toriumi M, Tanaka K, Yamabe T, Yamauchi J, Deguchi Y; *Synthetic Metals*, **1989**, 33(3), 389
- [177] Tanaka K, Shichiri T, Toriumi M, Yamabe T; *Synthetic Metals*, **1989**, 30(3), 271
- [178] Waltman RJ, Bargon J; *Tetrahedron*, **1984**, 40(20), 3963
-

-
- [179] Chainet E, Billon M; *Journal of Electroanalytical Chemistry*, **1998**, 451(1-2), 273
- [180] Silk T, Hong Q, Tamm J, Compton RG; *Synthetic Metals*, **1998**, 93(1), 59
- [181] Silk T, Hong Q, Tamm J, Compton RG; *Synthetic Metals*, **1998**, 93(1), 65
- [182] Kaynak A; *Materials Research Bulletin*, **1997**, 32(3), 271
- [183] Li J, Wang E, Green M, West PE; *Synthetic Metals*, **1995**, 74(2), 127
- [184] Unsworth J, Innis PC, Lunn BA, Jin ZS, Norton GP; *Synthetic Metals*, **1992**, 53(1), 59
- [185] Witkowski A, Freund MS, Brajtertoth A; *Analytical Chemistry*, **1991**, 63(6), 622
- [186] Ko JM, Rhee HW, Park SM, Kim CY; *Journal of the Electrochemical Society*, **1990**, 137(3), 905
- [187] Otero TF, Delarreta E; *Synthetic Metals*, **1988**, 26(1), 79
- [188] Hahn SJ, Stanchina WE, Gajda WJ, Vogelhut P; *Journal of Electronic Materials*, **1986**, 15(3), 145
- [189] Bredas JL, Scott JC, Yakushi K, Street GB; *Physical Review B*, **1984**, 30(2), 1023
- [190] Kaufman JH, Colaneri N, Scott JC, Street GB; *Physical Review Letters*, **1984**, 53(10), 1005
- [191] Kaufman JH, Colaneri N, Scott JC, Kanazawa KK, Street GB; *Molecular Crystals and Liquid Crystals*, **1985**, 118(1-4), 171
- [192] Nechtschein M, Devreux F, Genoud F, Vieil E, Pernaut JM, Genies E; *Synthetic Metals*, **1986**, 15(1), 59
- [193] Devreux F, Genoud F, Nechtschein M, Villeret B; *Synthetic Metals*, **1987**, 18(1-3), 89
- [194] Batz P, Schmeisser D, Gopel W; *Solid State Communications*, **1990**, 74(6), 461
- [195] Batz P, Schmeisser D, Gopel W; *Physical Review B*, **1991**, 43(11), 9178
- [196] Shimoi Y, Abe S; *Physical Review B*, **1994**, 50(20), 14781
- [197] Xie SJ, Mei LM, Lin DL; *Physical Review B*, **1994**, 50(18), 13364
- [198] Singh R, Narula AK, Tandon RP, Mansingh A, Chandra S; *Journal of Applied Physics*, **1996**, 79(3), 1476
- [199] Vorotyntsev MA, Vieil E, Heinze J; *Journal of Electroanalytical Chemistry*, **1998**, 450(1), 121
- [200] Zuppiroli L, Bussac MN, Paschen S, Chauvet O, Forro L; *Physical Review B*, **1994**, 50(8), 5196
- [201] Orton JW; *The Story of Semiconductors*; 2004, Oxford University Press
- [202] Akoudad S, Roncali J; *Chemical Communications*, **1998**, (19), 2081
- [203] Kvarnstrom C, Neugebauer H, Ivaska A, Sariciftci NS; *Journal of Molecular Structure*, **2000**, 521, 271
- [204] King G, Higgins SJ; *Journal of Materials Chemistry*, **1995**, 5(3), 447
- [205] Dale SM, Glidle A, Hillman AR; *Journal of Materials Chemistry*, **1992**, 2(1), 99
-

- [206] Ding H, Pan Z, Pigani L, Seeber R, Zanardi C; *Electrochimica Acta*, **2001**, 46(17), 2721
- [207] Shimidzu T, Ohtani A, Honda K; *Bulletin of the Chemical Society of Japan*, **1988**, 61(8), 2885
- [208] Lim JY, Paik WK, Yeo IH; *Synthetic Metals*, **1995**, 69(1-3), 451
- [209] Inzelt G, Kertesz V, Nyback AS; *Journal of Solid State Electrochemistry*, **1999**, 3(5), 251
- [210] Lisowska-Oleksiak A, Zalewska T; *Solid State Ionics*, **1999**, 119(1-4), 97
- [211] Skaarup S, Bay L, Vidanapathirana K, Thybo S, Tofte P, West K; *Solid State Ionics*, **2003**, 159(1-2), 143
- [212] Syritski V, Opik A, Forsen O; *Electrochimica Acta*, **2003**, 48(10), 1409
- [213] Weidlich C, Mangold KM, Juttner K; *Electrochimica Acta*, **2005**, 50(7-8), 1547
- [214] Zotti G, Schiavon G, Zecchin S, Daprano G; *Synthetic Metals*, **1996**, 80(1), 35
- [215] Saveant JM; *Chemical Reviews*, **2008**, 108(7), 2348
- [216] Bard AJ, Faulkner LR; *Electrochemical Methods: Fundamentals and Applications*; 2000, 2nd ed., Wiley
- [217] Jakobs RCM, Janssen LJJ, Barendrecht E; *Electrochimica Acta*, **1985**, 30(11), 1433
- [218] Jakobs RCM, Janssen LJJ, Barendrecht E; *Electrochimica Acta*, **1985**, 30(8), 1085
- [219] Zhang GQ, Zhao S, Yang FL, Liu LF; *Electroanalysis*, **2009**, 21(22), 2420
- [220] Zhang GQ, Yang FL, Gao MM, Liu LF; *Journal of Physical Chemistry C*, **2008**, 112(24), 8957
- [221] Zhang GQ, Yang FL, Yang WS; *Reactive & Functional Polymers*, **2007**, 67(10), 1008
- [222] Zhang GQ, Yang FL; *Chinese Journal of Catalysis*, **2007**, 28(6), 504
- [223] Zhang GQ, Yang WS, Yang FL; *Journal of Electroanalytical Chemistry*, **2007**, 602(2), 163
- [224] Yuan XX, Zeng X, Zhang HJ, Ma ZF, Wang CY; *Journal of the American Chemical Society*, **2010**, 132(6), 1754
- [225] Lee K, Zhang L, Lui H, Hui R, Shi Z, Zhang JJ; *Electrochimica Acta*, **2009**, 54(20), 4704
- [226] Millan WM, Thompson TT, Arriaga LG, Smit MA; *International Journal of Hydrogen Energy*, **2009**, 34(2), 694
- [227] Reddy ALM, Rajalakshmi N, Ramaprabhu S; *Carbon*, **2008**, 46(1), 2
- [228] Chen J, Zhang WM, Officer D, Swiegers GF, Wallace GG; *Chemical Communications*, **2007**, (32), 3353
- [229] Bashyam R, Zelenay P; *Nature*, **2006**, 443(7107), 63
- [230] Yuasa M, Yamaguchi A, Itsuki H, Tanaka K, Yamamoto M, Oyaizu K; *Chemistry of Materials*, **2005**, 17(17), 4278
- [231] Su FB, Tian ZQ, Poh CK, Wang Z, Lim SH, Liu ZL, Lin JY; *Chemistry of Materials*, **2010**, 22(3), 832
- [232] Jiwei L, Jingxia Q, Miao YQ, Chen JR; *Journal of Materials Science*, **2008**, 43(18), 6285

-
- [233] Li J, Lin XQ; *Journal of the Electrochemical Society*, **2007**, 154(10), B1074
- [234] Zhou Q, Li CM, Li J, Cui XQ, Gervasio D; *Journal of Physical Chemistry C*, **2007**, 111(30), 11216
- [235] Song EH, Paik WK; *Bulletin of the Korean Chemical Society*, **1998**, 19(2), 183
- [236] Elzing A, Vanderputten A, Visscher W, Barendrecht E; *Journal of Electroanalytical Chemistry*, **1987**, 233(1-2), 113
- [237] Ikeda O, Okabayashi K, Yoshida N, Tamura H; *Journal of Electroanalytical Chemistry*, **1985**, 191(1), 157
- [238] Osaka T, Nishikawa M, Nakamura S; *Denki Kagaku*, **1984**, 52(6), 370
- [239] Cotton FA, Geoffrey W; *Advanced Inorganic Chemistry*; 1988, 5th ed., John Wiley & Sons Inc.
- [240] Rorabacher DB, Schroeder RR; *Electrochemistry of Copper*, Encyclopedia of Electrochemistry: Inorganic Electrochemistry, Volume 7b, 2006, Wiley-VCH
- [241] Paulson AJ, Kester DR; *Journal of Solution Chemistry*, **1980**, 9(4), 269
- [242] Sylva RN, Davidson MR; *Journal of the Chemical Society-Dalton Transactions*, **1979**, (2), 232
- [243] Perrin DD; *Journal of the Chemical Society*, **1960**, (AUG), 3189
- [244] Xu HL, Wang WZ, Zhu W, Zhou L, Ruan ML; *Crystal Growth & Design*, **2007**, 7(12), 2720
- [245] Feser R; *Uniform Corrosion of Metals in Acid, Neutral and Alkaline Electrolytes*, Encyclopedia of Electrochemistry: Inorganic Electrochemistry, Volume 4, 2006, Wiley-VCH
- [246] Beverskog B, Puigdomenech I; *Journal of the Electrochemical Society*, **1997**, 144(10), 3476
- [247] Puigdomenech I; *Abstracts of Papers of the American Chemical Society*, **2000**, 219, 248
- [248] Eriksson G; *Analytica Chimica Acta-Computer Techniques and Optimization*, **1979**, 3(4), 375
- [249] Bilal BA, Tributsch H; *Journal of Applied Electrochemistry*, **1998**, 28(10), 1073
- [250] De la Fuente D, Simancas J, Morcillo M; *Corrosion Science*, **2008**, 50(1), 268
- [251] Kratschmer A, Wallinder IO, Leygraf C; *Corrosion Science*, **2002**, 44(3), 425
- [252] Fitzgerald KP, Nairn J, Atrens A; *Corrosion Science*, **1998**, 40(12), 2029
- [253] Liu YC, Hwang BJ; *Journal of Electroanalytical Chemistry*, **2001**, 501(1-2), 100
- [254] Liu YC, Hwang BJ; *Thin Solid Films*, **1999**, 339(1-2), 233
- [255] Li S, Qiu YB, Guo XP; *Reactive & Functional Polymers*, **2009**, 69(10), 743
- [256] Inoue MB, Nebesny KW, Fernando Q, Castilloortega MM, Inoue M; *Synthetic Metals*, **1990**, 38(2), 205
- [257] Ohkubo Y, Onishi S, Ohtake T, Ogawa K; *Journal of Chemical Engineering of Japan*, **2010**, 43(4), 406
- [258] Watanabe N, Morais J, Alves MCM; *Journal of Physical Chemistry B*, **2002**, 106(43), 11102
- [259] Alves MCM, Watanabe N, Ramos AY, Tolentino HCN; *Journal of Synchrotron Radiation*, **2001**, 8, 517
-

- [260] Stroka J, Maksymiuk K, Galus Z; *Electrochemistry of Zinc, Cadmium, and Lead*, Encyclopedia of Electrochemistry: Inorganic Electrochemistry, Volume 7b, 2006, Wiley-VCH
- [261] Beverskog B, Puigdomenech I; *Corrosion Science*, **1997**, 39(1), 107
- [262] Muster TH, Cole IS; *Corrosion Science*, **2004**, 46(9), 2319
- [263] Odnevall I, Leygraf C; *Corrosion Science*, **1994**, 36(6), 1077
- [264] Ruizamil A, Ramirezgarcia A, Garciamartinez O; *Anales De Quimica*, **1976**, 72(3), 213
- [265] Ramirezg.A, Gutierre.P, Canoruiz J, Garciam.a.O; *Anales De Quimica*, **1974**, 70(9-10), 687
- [266] Carbajal Arizaga GG, Satyanarayana KG, Wypych F; *Solid State Ionics*, **2007**, 178(15-18), 1143
- [267] Hermelin E, Petitjean J, Lacroix JC, Chane-Ching KI, Tanguy J, Lacaze PC; *Chemistry of Materials*, **2008**, 20(13), 4447
- [268] Vatsalarani J, Geetha S, Trivedi DC, Warriier PC; *Journal of Power Sources*, **2006**, 158(2), 1484
- [269] Bazzaoui M, Martins L, Bazzaoui EA, Martins JI; *Journal of Electroanalytical Chemistry*, **2002**, 537(1-2), 47
- [270] Bazzaoui M, Bazzaoui EA, Martins L, Martins JI; *Synthetic Metals*, **2002**, 128(1), 103
- [271] Aeiyyach S, Zaid B, Lacaze PC; *Electrochimica Acta*, **1999**, 44(17), 2889
- [272] Pandey PC, Singh G; *Sensors and Actuators B-Chemical*, **2002**, 85(3), 256
- [273] Pandey PC, Singh G, Srivastava PK; *Electroanalysis*, **2002**, 14(6), 427
- [274] Grgur BN, Gvozdenovic MM, Stevanovic J, Jugovic BZ, Marinovic VM; *Electrochimica Acta*, **2008**, 53(14), 4627
- [275] Beck F, Ruetschi P; *Electrochimica Acta*, **2000**, 45(15-16), 2467
- [276] Bicelli LP, Bozzini B, Mele C, D'Urzo L; *International Journal of Electrochemical Science*, **2008**, 3(4), 356
- [277] Burda C, Chen XB, Narayanan R, El-Sayed MA; *Chemical Reviews*, **2005**, 105(4), 1025
- [278] Cao G; *Nanostructures & Nanomaterials: Synthesis, Properties & Applications*; 2004, 1st ed., Imperial College Press
- [279] Lee JH; *Sensors and Actuators B-Chemical*, **2009**, 140(1), 319
- [280] Carpinteri A, Cornetti P, Pugno N, Sabora A; *Microsystem Technologies-Micro-and Nanosystems-Information Storage and Processing Systems*, **2009**, 15(1), 27
- [281] Carpinteri A, Pugno NM; *International Journal of Fracture*, **2008**, 150(1-2), 221
- [282] Fratzl P, Weinkamer R; *Progress in Materials Science*, **2007**, 52(8), 1263
- [283] Lakes R; *Nature*, **1993**, 361(6412), 511
- [284] Yu YL, Zhang JY; *Materials Letters*, **2009**, 63(21), 1840
- [285] Zheng LK, Liu XJ; *Materials Letters*, **2007**, 61(11-12), 2222
- [286] Zhang WX, Ding SX, Yang ZH, Liu AP, Qian YT, Tang SP, Yang SH; *Journal of Crystal Growth*, **2006**, 291(2), 479

-
- [287] Liu JP, Huang XT, Li YY, Duan JX, Ai HH; *Materials Chemistry and Physics*, **2006**, 98(2-3), 523
- [288] Zhang WX, Wen XG, Yang SH; *Inorganic Chemistry*, **2003**, 42(16), 5005
- [289] Campbell FW, Compton RG; *Analytical and Bioanalytical Chemistry*, **2010**, 396(1), 241
- [290] Welch CW, Compton RG; *Analytical and Bioanalytical Chemistry*, **2006**, 384(3), 601
- [291] Schmid G; *Nanoparticles: From Theory to Application* 2004, 1st ed., Wiley-VCH
- [292] El-Sayed MA; *Accounts of Chemical Research*, **2001**, 34(4), 257
- [293] Olsen AW, Klabunde KJ; *Inherent Chemical Reactivities of Small Metal Particles*, Encyclopedia of Physical Science and Technology, Inorganic Chemistry, 2001, Academic Press
- [294] Valle-Orta M, Diaz D, Santiago-Jacinto P, Vazquez-Olmos A, Reguera E; *Journal of Physical Chemistry B*, **2008**, 112(46), 14427
- [295] Welch CM, Hyde ME, Banks CE, Compton RG; *Analytical Sciences*, **2005**, 21(12), 1421
- [296] Jammi S, Sakthivel S, Rout L, Mukherjee T, Mandal S, Mitra R, Saha P, Punniyamurthy T; *Journal of Organic Chemistry*, **2009**, 74(5), 1971
- [297] Zhang H, Wang XM, Zhang KC, Teo BK; *Journal of Solid State Chemistry*, **2000**, 152(1), 191
- [298] Rujiwatra A, Mander GJ, Kepert CJ, Rosseinsky MJ; *Crystal Growth & Design*, **2005**, 5(1), 183
- [299] Gao XD, Li XM, Yu WD, Peng F, Zhang CY; *Materials Research Bulletin*, **2006**, 41(3), 608
- [300] Pearton SJ, Norton DP, Ip K, Heo YW, Steiner T; *Progress in Materials Science*, **2005**, 50(3), 293
- [301] Wang L, Liu G, Zou L, Xue D; *Journal of Alloys and Compounds*, **2010**, 493, 471

Chapter 2

Experimental

2. Experimental

2.1 Introduction

The present research work was performed by using different materials, procedures and experimental equipment. The materials were divided into two main groups as electrode substrates and deposited materials. The electrode substrates were high purity glassy carbon, gold and platinum. The deposited materials were either conducting polymers electrochemically formed on the electrode substrates, or copper and zinc based materials deposited onto these polymers. The polymer of choice was polypyrrole (PPy), while the dopant was polystyrene sulfonate (PSS). Pyrrole (Py) was electropolymerized in the presence of PSS to give the PSS-doped polypyrrole films (PPy-PSS).

Copper and zinc hydroxysulfate materials were deposited at the interface of the PPy-PSS thin films. Copper-based micro/nanostructures were prepared and electrochemically assembled into combined copper-based structures, or reduced to form metallic copper nanoparticles. A nitrate sensor was developed by using these nanoparticles. The performance of the sensor was improved with the incorporation of modified multiwall carbon nanotubes in the PPy-PSS thin films. The multiwall carbon nanotubes (MWNT) were chemically modified with polyethyleneimine (PEI) to give water soluble MWNT-PEI. Zinc-based nanothin sheets were also electrodeposited onto PPy-PSS films and transformed to metallic zinc micro-dendrites upon reduction.

The PPy-PSS thin films and copper/zinc based electrodeposits were characterized electrochemically, spectroscopically and with surface analytical techniques, using cyclic voltammetry, electrochemical quartz crystal microbalance, rotating disk electrode, electrochemical impedance spectroscopy, attenuated total reflectance infrared spectroscopy, Raman spectroscopy, scanning electron microscopy with energy dispersive X-ray analysis, X-ray photoelectron spectroscopy and X-ray diffraction. All details about the electrodeposition, characterisation and application of the PPy-PSS thin films and copper/zinc based materials are given in the following sections together with a short description of each experimental technique.

2.2 Electrochemical Setup

The vast majority of the materials developed and characterized in the present work were prepared electrochemically. A scheme of the electrochemical setup that was used is shown in Figure 2.1. The electrochemical cell (EC) was a glass cylinder of 10 or 20 ml volume that had a Teflon lid with openings for electrodes, gas inlet and aliquot additions. The cell was a standard three electrode system with a working electrode (WE), a reference electrode (RE), and a counter electrode (CE). The three electrodes were immersed in the electrolyte solution and connected to a potentiostat, which was controlled by a computer unit, *e.g.*, a laptop (lpt). The gas cylinder was either nitrogen or oxygen depending on the experimental conditions. In some experiments, it was necessary to add known aliquots of chemicals to the electrolyte solution with a micropipette (mp). A magnetic stirrer (ms) was used to stir and homogenize the solution whenever required.

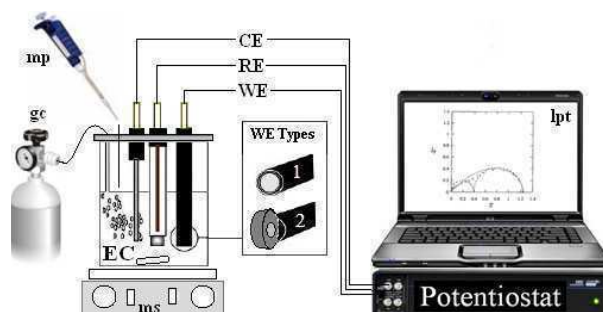


Figure 2.1 Scheme of the electrochemical setup used in the present work. The main components were the electrochemical cell (EC) and a potentiostat controlled by a laptop (lpt). The working, reference and counter electrodes (WE, RE and CE) were connected to the potentiostat. The cell was connected to a gas cylinder (gc) and had a further opening for additions with micropipette (mp), and could be stirred with a magnetic stirrer (ms).

A different cell was used only with the rotating disk electrode where the size of the electrode required the use of 50 ml of electrolyte solution. Also, a dedicated system was used for the electrochemical quartz crystal microbalance measurements.

The working electrodes were prepared from rods of high purity glassy carbon, gold and platinum (99.99+ %, 3.0 or 4.0 mm in diameter), supplied by Goodfellow Cambridge Ltd. A piece of rod of about half centimeter was cut and set in a Teflon or PVC holder with epoxy resin. The electrical contact was made with a copper wire attached at one end of the piece with highly conducting silver-loaded resin. The working electrodes were all disk electrodes with either a regular (1) or flat (2) shape as shown in Figure 2.1. The regular and flat electrodes were used for electrochemical and surface characterization, respectively. The quality of the electrical contact was checked with a multimeter to ensure that the resistance between the surface of the electrodes and the connection to the potentiostat was lower than 1.0 Ω . Prior to each experiment, the working electrodes were polished to a mirror finish using in order 30, 15, 6 and 1 μm diamond suspensions on microcloth supplied by Buehler, sonicated in distilled water and then in ethanol, and finally rinsed with Milli-Q water.

The reference electrodes were either saturated calomel electrode (SCE) or silver / silver chloride saturated electrode (Ag/AgCl sat.). The standard electrode potential of the SCE in aqueous solution at 25 $^{\circ}\text{C}$ is 0.241 V vs. SHE (SHE is the standard hydrogen electrode), whereas for the Ag/AgCl reference it is 0.197 V vs. SHE. The reference electrodes were serviced regularly by changing the internal filling solution with a saturated solution of super-purum KCl (99.999+ %), and by checking the open circuit potential against a virgin SCE. In this work, all potentials are relative to the SCE reference electrode, unless otherwise stated.

The counter electrodes were either a wire or plate of high purity platinum (99.99+ %). The plate counter electrode was used for larger working electrode areas and current densities as it provided an unrestrained flow of charge. The counter electrodes were brushed regularly with silicon carbide based abrasive paper (Buehler P2500), smooth cleaned with a cloth, sonicated in distilled water and finally rinsed with Milli-Q water.

All experiments were performed at room temperature. In the majority of the cases the atmosphere was air, although nitrogen and oxygen were also used in order to study the effect of the latter on the electrochemical systems. The supporting electrolytes were aqueous solutions of inorganic and organic salts. The potential windows were

set within the limits of proton reduction and water oxidation and the experiments were performed inside these potential ranges eliminating in this way the interference of any possible discharge processes.

The electrochemical cell was controlled by a potentiostat, as summarized in Figure 2.2. In this scheme, the working (WE), reference (RE) and counter (CE) electrodes are connected to the potentiostat which is interfaced to a function generator. The potentiostat controls both the potential and the current of WE, V_{WE} and I_{WE} , respectively. The potential of WE is varied by controlling the potential difference between WE and RE ($V_{WR} = V_{WE} - V_{RE}$), where V_{RE} is constant. The flow of charge in the cell is $I_{CE} = I_{RE} + I_{WE}$. Since the potentiostat applies a high input impedance to RE, the value of I_{RE} is zero. It follows that the flow of charge is between WE and CE, *i.e.*, $I_{WE} = I_{CE}$. In order to sustain this current the potential difference between WE and CE ($V_{WC} = V_{WE} - V_{CE}$) must be correspondingly adjusted. This is possible only by changing V_{CE} since V_{WE} is fixed. The potentiostat is then able to control the potential of WE, V_{WE} , by comparing it to the constant potential of RE, and to allow the corresponding flow of charge through WE, I_{WE} , by adjusting the potential of CE.

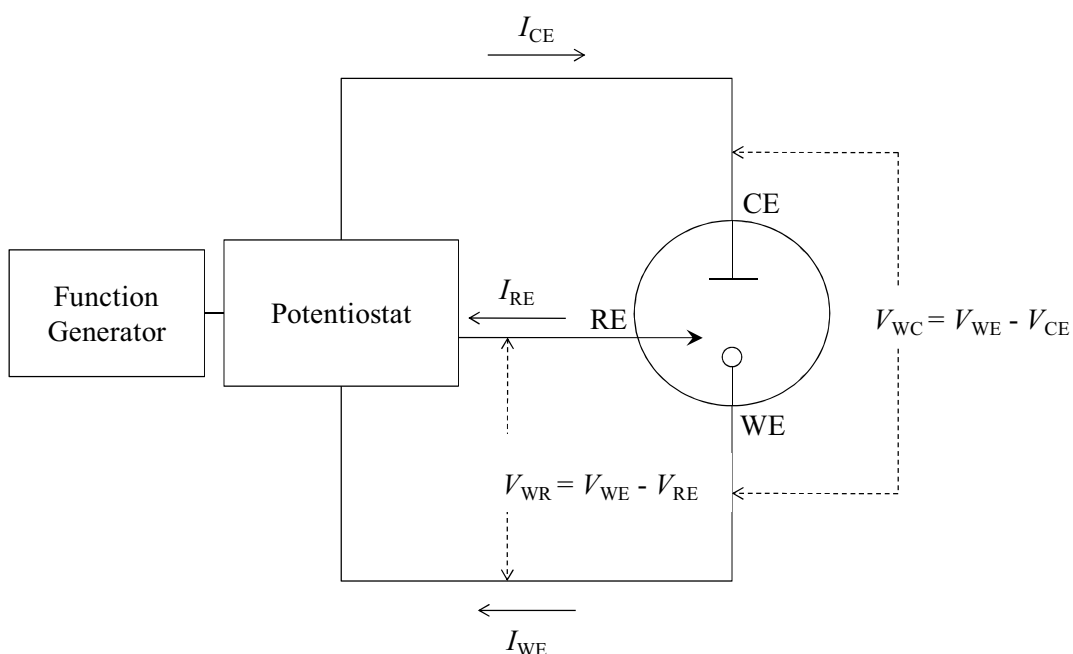


Figure 2.2 Schematic representation of the connection between the potentiostat and electrochemical cell. The potentiostat is connected to the working (WE), reference (RE), counter (CE) electrodes, and the function generator.

2.3 Chemicals and Synthesis

2.3.1 Chemicals

The chemicals and solvents used in the present work were pyrrole (98 %), poly(sodium 4-styrenesulfonate) $M_w \sim 70,000$ g/mol, poly(vinylsulfonic acid, sodium salt) solution 25 % in water (technical grade, total impurities ≤ 30 % insoluble matter), heparin sodium salt (≥ 140 USP units/mg), β -cyclodextrin sulfated sodium salt (7-11 mol per mol β CD), sodium dodecyl sulfate (≥ 99.0 %), potassium chloride (≥ 99.0 %), sodium sulfate (≥ 99.0 %), copper sulfate pentahydrate (99.999 %), zinc sulphate heptahydrate (≥ 99.0 %), multiwall carbon nanotubes 10-30 nm diameter and 0.5-40 μ m length (95 %), polyethylenimine branched $M_w \sim 25,000$ g/mol (total impurities ≤ 1 % water), dimethylformamide (≥ 99.0 %), methanol (≥ 99.0 %), acetone (≥ 99.5 %), and hydrogen peroxide (35 % in water). The water was distilled and Milli-Q purified in the laboratory (14 $M\Omega$ ·cm, pH = 5.0). All chemicals and solvents were supplied by Sigma-Aldrich with the exception for the multiwall carbon nanotubes which were supplied by Helix Material Solutions. High purity nitrogen and oxygen gases (99.95 %) were supplied by BOC.

2.3.2 Synthesis of MWNT-PEI

The multiwall carbon nanotubes (MWNT) modified with polyethylenimine (PEI) were synthesized as follows: 1.0 g of MWNT and 5.6 g of PEI were placed in a stoppered round-bottomed flask (250 ml) with 60 ml of dimethylformamide (DMF). This mixture was first sonicated for 10 min in order to obtain a homogeneous dispersion. The flask was then placed in a silicone oil bath and vigorously stirred at 50 °C for 5 d. After this time, 150 ml of methanol was added to the reaction mixture that was left stirring and cooling for 1 h. The mixture was vacuum-filtered on a Whatman Teflon filter with 0.45 μ m mean-diameter pores. The black paste collected on the filter was washed and mixed repeatedly with several small aliquots of methanol (total 100 ml). This was then transferred to a clean round-bottomed flask (250 ml) to which 100 ml of methanol was added. After a short period of sonication, the dispersion was stirred at room temperature for 2 h and then filtered again. At this

stage, the liquid filtrate appeared transparent and colourless indicating that most of the unreacted PEI was removed from the product. The paste was further washed with 250 ml of Milli-Q water in order to remove any remaining PEI and methanol. Finally, the resulting paste was washed with 10 ml of acetone and left drying for 30 min under vacuum. The resulting product consisted of black friable chunks. These were transferred into a glass dish, finely grounded with a spatula and dried overnight at 60 °C on a bed of silica gel beads. The resulting black powder was collected and stored in a desiccator.

2.3.3 Preparation of MWNT-PEI Aqueous Solution

The powder obtained in the previous section was used to prepare a stock solution of MWNT-PEI dissolved in water. 60 mg of MWNT-PEI powder were added to 10 ml of Milli-Q water in a glass vial. The suspension was sonicated for 1 h and left stirring at room temperature for 24 h. The solution was then centrifuged at 14000 rpm for 10 min in order to separate any undissolved carbon nanotubes. The deep black supernatant was collected with a Pasteur pipette with great care, in order to avoid the resuspension of the precipitate. The amount of MWNT-PEI dissolved in the solution was estimated by removing the water from 5 ml of stock solution and obtaining approximately 4 mg of residue, corresponding to a concentration of MWNT-PEI in water of about 0.08 % w/w. The stock solution was stable and no carbon nanotube precipitation was observed over a period of one year.

2.4 Preparation and Characterization of Modified PPy-PSS Films

2.4.1 Electropolymerizations

2.4.1.1 Preparation of PPy-PSS Thin Films

A stock amount of pyrrole (Py) was vacuum-distilled and stored in the dark at -20 °C under nitrogen. The electropolymerization experiments were run in aqueous solutions made from fresh aliquots of distilled Py and dopants. The main salt used as a dopant was poly(sodium 4-styrenesulfonate) (PSS). The other salts were poly(vinylsulfonic acid, sodium salt) (PVS), sodium dodecyl sulfate (DS),

β -cyclodextrin sulfated sodium salt (β CD), heparin sodium salt (Hep), and potassium chloride. The molar concentrations of the polyanions in solutions were calculated from the molecular weight of the corresponding monomer units.

The polypyrrole-polystyrene sulfonate (PPy-PSS) thin films were prepared with a standard three-electrode cell on glassy carbon (GC), gold (Au) or platinum (Pt) electrodes. The electrolyte solution was made of 0.15 M Py and 50 mM PSS dissolved in Milli-Q water. The polymer was grown at a constant potential of 0.60 V vs. SCE to give uniform thin films. Electropolymerization was stopped after a certain charge was reached, usually 40 mC/cm². The thickness of the PPy-PSS films was calculated as 120 nm using a volume-to-charge ratio of 3.00×10^{-4} cm³/C [1]. Other PPy films were prepared using a similar procedure with the dopants stated above.

2.4.1.2 Preparation of PPy-PSS-MWNT-PEI Composite Films

PPy-PSS films were modified with the MWNT-PEI carbon nanotubes prepared as in Section 2.3.2. In order to incorporate the nanotubes in the polymer matrix, the nanotubes were drop-cast on the surface of a GC electrode and the Py electropolymerized at the modified surface. The electrode was first pretreated to make the surface hydrophilic and allow a smooth distribution of the nanotubes. The pretreatment was performed in two steps [2-4]. A clean GC electrode (4 mm diameter) was placed in a stirred phosphate buffer solution (0.20 M NaH₂PO₄/Na₂HPO₄, pH = 6.8) and held at 1.80 V vs. SCE for 5 min. Immediately after, a CV scan was performed from 0.30 to 1.25 V vs. SCE at 25 mV/s until a reproducible cyclic voltammogram was obtained (usually about 30 cycles). The electrode was then washed with Milli-Q water and acetone. After drying, the surface acquired a blue iridescent colour. A 5 μ l drop of MWNT-PEI solution was evenly cast onto the electrode surface. The drop was dried with the aid of an infrared lamp. At this stage, the electrode surface became dull and grey. The electrode was then immersed in a 0.15 M Py and 50 mM PSS solution, the PPy film was formed onto the carbon nanotube deposit at 0.60 V vs. SCE until a charge of 40 mC/cm² was reached. The resulting PPy-PSS-MWNT-PEI composites were washed and characterized.

2.4.2 Electrochemical Depositions

2.4.2.1 Deposition of Copper-Based Micro/Nanostructures

The copper-based micro/nanostructures were formed electrochemically on top of PPy-PSS or PPy-PSS-MWNT-PEI films (Section 2.4.1). After the electropolymerization, the electrodes were thoroughly rinsed with Milli-Q water and immersed in a 0.10 M CuSO₄ solution. The potential of the electrode was set at a constant value of 0.10 V vs. SCE until a certain charge was passed and the copper-based structures were formed. The potentiostatic deposition was performed with solutions that were either used as prepared in air or saturated with oxygen. In the latter case, the copper sulfate solutions were bubbled and stirred with high purity oxygen for at least 60 min prior to the electrodeposition. The same was done with nitrogen in order to evaluate the effect of oxygen on the deposition of the micro/nanostructures. Once the deposition was completed the working electrodes were extensively rinsed with Milli-Q water and left to dry. The electrodes modified with the copper-based micro/nanostructures were then ready for characterization.

2.4.2.2 Deposition of Zinc-Based Nanosheets and Conversion to Metallic Zinc Micro-Dendrites

The zinc-based nanosheets were deposited on the PPy-PSS films in a similar manner to that described in Section 2.4.2.1. The electrodes were placed in a 0.10 M ZnSO₄ solution and a constant potential was applied in order to form the zinc deposits. The potential ranged from 0.00 V vs. SCE to more negative values, but never lower than -1.00 V vs. SCE. The nanosheets were formed both in air and oxygen saturated solutions. These were then reduced in 0.10 M Na₂SO₄ at different potentials, the lowest being -2.50 V vs. SCE, and metallic zinc micro-dendrites were formed. The electrodepositions were stopped after different deposition charges in order to examine the growth of the nanosheets.

2.4.2.3 Fabrication of Copper-Based Microstructures

The same procedure as described in Section 2.4.2.1 was applied for the fabrication of copper-based microstructures, but at different potentials and for different time

periods. A PPy-PSS film was freshly polymerized on the working electrode that was then rinsed and immersed in the copper sulfate solution. Three different potentials 0.10 V, 0.00 V and -0.10 V vs. SCE were applied to three different films. After the electrodeposition the electrodes were rinsed with Milli-Q water and characterized. Different copper-based structures were formed at each potential. In order to fabricate hybrid copper-based microstructures a step potential at -0.10 V vs. SCE was applied to a new PPy-PSS film for a few seconds, followed by a deposition at 0.10 V vs. SCE on the same film and in the same electrolyte solution. Following modification, the electrodes were rinsed and characterized.

2.4.2.4 Formation of Metallic Copper Nanoparticles

The copper-based micro/nanostructures prepared as described in Section 2.4.2.1 were converted to metallic copper nanoparticles through a reduction potential step. In this case the micro/nanostructures were formed over a longer period of time in order to obtain a larger number of larger structures. This took more than 60 min in air and about 10 min in oxygen saturated solutions. The modified electrodes were then rinsed and transferred to a 0.10 M Na_2SO_4 solution. A high reduction potential of -2.00 V vs. SCE was then applied for 5 min. A large amount of hydrogen gas was generated at the newly formed metallic copper nanoparticles (the hydrogen evolution reaction was almost absent on pristine PPy-PSS films), however the composite film was undamaged by the gas evolution. After reduction, the electrode surface was characterized by a bright and shiny pinkish colour.

2.4.3 Nitrate Sensing with Metallic Copper Nanoparticles Modified Electrodes

The nitrate sensing tests were performed using a Rotating Disk Electrode (RDE). The copper nanoparticles were formed on PPy-PSS and PPy-PSS-MWNT-PEI composite films as described in Section 2.4.2.4. The modified electrodes were immersed in a 0.10 M Na_2SO_4 supporting solution. The RDE was set at a constant potential of -1.20 V vs. SCE and at 2000 rpm. The corresponding amperometric signal was recorded as a function of time. Once the signal reached a plateau, a series of nitrate aliquots were added into the solution. At each addition a current step was registered as a response to the introduced nitrate. The aliquots were added with increasing concentration from 1 to 100 μM . Nitrate ions were also detected using

cyclic voltammetry. In this case, the copper nanoparticles were prepared on a regular disk electrode. The nitrate ions were added to a 0.10 M Na₂SO₄ solution where the modified electrodes were immersed and scanned from -0.60 to -1.50 V vs. SCE at a rate of 10 mV/s. The current signal for nitrate sensing was recorded at -1.20 V vs. SCE. The nitrate aliquots ranged from 0.1 to 10 mM. In order to confirm the catalytic activity of the copper nanoparticles, the responses of the polymer and polymer-nanotube electrodes without copper nanoparticles were compared to that of copper modified electrodes.

2.4.4 Catalytic Reduction of Oxygen at PPy-PSS Thin Films

The oxygen reduction reaction was evaluated with the RDE electrode. The catalytic activities at the bare and PPy-PSS modified electrodes were compared in a 0.10 M Na₂SO₄ solution saturated with nitrogen or oxygen. The potential was scanned at 1 mV/s from 0.30 V to -0.60 V vs. SCE and the current-potential waves of oxygen reduction were recorded at a rotation speed of 2000 rpm. Furthermore, the reduction of oxygen at the thin films was examined with cyclic voltammetry and chrono-coulometry. The cycles were run in the same range of potential as for the RDE experiments but at a scan rate of 10 mV/s. The coulometric quantification was performed at three different potentials 0.10, 0.00 and -0.10 V vs. SCE.

2.5 Experimental Techniques

2.5.1 Experimental Equipment

2.5.1.1 Electrochemistry

The electrochemical experiments were performed with a Solartron 1285 potentiostat and a CH Instrument 400A potentiostat. The electrochemical impedance analyses were carried out using a Solartron 1287A potentiostat coupled to a Solartron 1260A frequency response analyzer. The rotating disk electrode was a Pine MRS Rotor System equipped with glassy carbon, gold and platinum E3 Series RDE tips. The electrochemical quartz crystal microbalance was a CH Instrument 400A equipped with a CH127 cell and CH125A gold crystal electrodes (polished, bounded and mounted, 100 Å Ti + 1000 Å Au).

2.5.1.2 Microscopy and EDX Analysis

The microscopy characterization was performed with three different scanning electron microscopes. A Hitachi S-3200-N with a tungsten filament electron source, maximum magnification of 300,000x and resolution of 3.5 nm was used for most of the analyses. This microscope was equipped with an Oxford Instrument INCAx-act EDX system with silicon drift detector. The other two SEMs were available at the Tyndall National Institute (Cork, Ireland). Lower magnification work was carried out with Hitachi S-4000 with a cold cathode field emission electron source (FE-SEM), maximum magnification 300,000x and resolution of 1.5 nm. This microscope was equipped with Princeton Gamma Technology Avalon 8000 EDX system with a liquid nitrogen cooled Li(Si) detector. FEI Nova NanoSEM 630 ultra-high resolution with a field emission gun (FEG), a maximum magnification of 1,000,000x and a resolution of 1 nm was also employed for higher resolution imaging work. This microscope was equipped with Oxford Instrument X-MAX 80 large area Si diffused detector for high resolution elemental mapping. In order to obtain high resolution images the samples were sputter coated with gold or gold/palladium ultrathin films with an AGAR Automatic Sputter Coater equipped with an AGAR Terminating Film Thickness Monitor unit.

2.5.1.3 Spectroscopy and X-Ray Diffraction

The spectroscopic equipment was available at the Tyndall National Institute (Cork, Ireland). The infrared spectroscopy characterization was performed with a Varian FTS-7000 FT-IR equipped with a Pike Miracle ATR built in diamond crystal. The depth of penetration of the crystal at 45° was 2.0 µm. The Raman characterization was performed with Reinshaw inVia reflex Raman Microscope. The source was an Argon ion laser (514 nm) with a beam spot of 1.1 µm. The X-ray photoelectron spectroscopy equipment was a KRATOS AXIS 165 available from the Materials and Surface Science Institute (MSSI) at the University of Limerick. This was equipped with a monochromatic Al source with a spot size of 1 mm. The X-ray diffraction analyses were performed in collaboration with the MSSI, the diffractometer was a Philips X'Pert PRO MPD with a Cu X-ray source.

2.5.2 Electrochemical Methods

The two fundamental observables of any electrochemical system are the current (I) and potential (E). The potential is the driving force of the current. A typical electrochemical experiment consists of controlling one of the two observables while recording the time evolution of the other. Notably, the response of the electrochemical system to the external perturbation is influenced by many variables such as the nature and morphology of the materials, the concentration of the species in solution and the temperature. A range of electrochemical techniques was used in this study and brief details on each approach are provided in the following sections.

2.5.2.1 Constant Potential Amperometry

Constant potential amperometry, also known as chronoamperometry, consists of applying a fixed potential, E , to an electrode in contact with a redox system ($O + ne^- \rightarrow R$) and recording the time variation of the resulting current, $I = f(t)$. In the specific case of a step potential experiment under diffusion control, the current response of the system is given by the *Cottrell* equation [5], Equation 2.1.

$$I(t) = \frac{nFAD_O^{1/2} C_O^\infty}{\pi^{1/2} t^{1/2}} \quad 2.1$$

Here, D_O and C_O^∞ are the diffusion coefficient and bulk concentration of the oxidized species, respectively, n is the number of electrons involved in the redox process, and A is the electrode area. This equation is valid for the semi-infinite diffusion condition and when the applied potential is strong enough to ensure the entire depletion of the oxidized species at the electrode surface immediately after the application of the potential step (the same considerations are also valid for the oxidation of R).

The current response is expected to decay asymptotically to zero with the square root of time due to the progressive thickening of the diffusion layer. This relationship holds over relatively short time periods when the process is dominated by planar diffusion. Over long times, the spherical character of the electrode becomes important and the current decays to values different to zero, *i.e.*, $nFAD_O C_O^\infty / r$ where r is the radius of the electrode [6]. The waveform and amperometric response of a generic redox system is shown in Figure 2.3.

Sometimes it is more informative to plot the charge (Q) passed through the electrochemical cell as function of time, in such a case the technique used is chronocoulometry. The charge can be calculated at any time from the integral of the current. Relating the experimental observation to the charge is particularly useful when considering the overall extent of the redox process instead of its instantaneous rate (*i.e.*, the current).

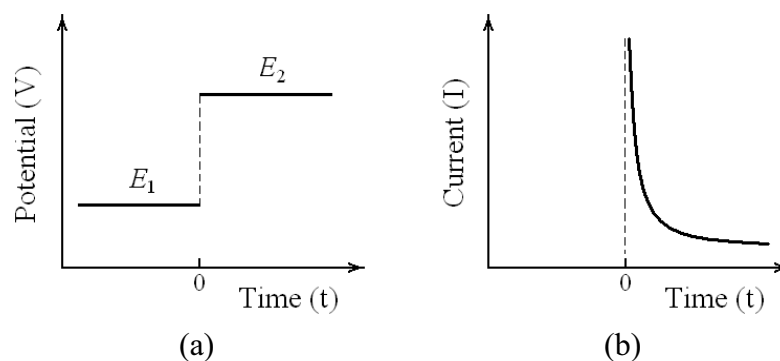


Figure 2.3 Chronoamperometric response of a hypothetical redox couple following a potential step perturbation. The potential is applied at time $t = 0$, the redox couple is active only at potential E_2 not at E_1 (a). Diffusion controlled amperometric decay displaying the increasing thickness of the diffusion layer (b).

In the case of potentiostatic electrodeposition experiments, the chronoamperometric response is very different than that described by Equation 2.1. In fact, the Cottrell equation illustrates the current response of soluble species that do not adhere at any stage to the electrode surface. The nucleation and growth of electrodeposits are a vast topic that has been studied in considerable detail both experimentally and theoretically [7-9]. The special case of the potentiostatic current-time transient for three-dimensional multiple nucleation with diffusion control growth has been modelled by Scharifker and Hills [10]. According to this model there are two theoretical diagnostic relationships, one for the instantaneous nucleation (*i.e.*, all the growing nucleation sites are formed at the same time at the start of the electrodeposition), and one for the progressive nucleation (*i.e.*, new nucleation sites are generated during the growth period). The two nondimensional relationships are provided for instantaneous (Equation 2.2) and progressive (Equation 2.3) nucleation, respectively [10].

$$\left(\frac{I}{I_m}\right)^2 = \frac{1.9542}{t/t_m} \left\{1 - \exp\left[-1.2564\left(\frac{t}{t_m}\right)\right]\right\}^2 \quad 2.2$$

$$\left(\frac{I}{I_m}\right)^2 = \frac{1.2254}{t/t_m} \left\{1 - \exp\left[-2.3367\left(\frac{t}{t_m}\right)\right]\right\}^2 \quad 2.3$$

The general current response for the potentiostatic nucleation and growth of electrodeposits, taking into account the effect of nuclei overlapping, is shown in Figure 2.4. The current free from overlapping effects (I_{free}) increases linearly with time in the case of instantaneous nucleation, and with t^2 in the case of progressive nucleation.

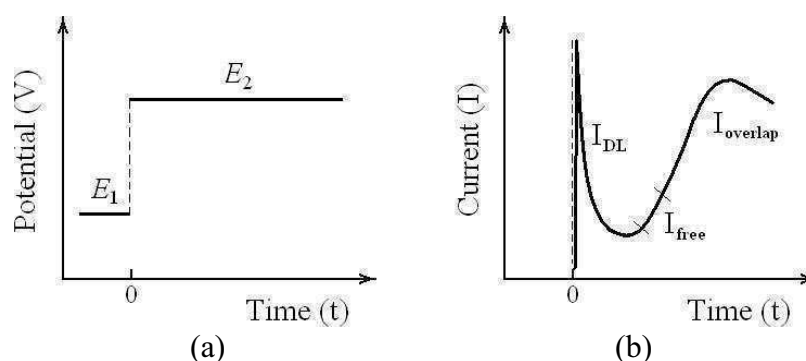


Figure 2.4 Chronoamperometric response of a hypothetical electrodeposition following a potential step perturbation. The potential is applied at time $t = 0$, the nucleation and growth are active only at potential E_2 not at E_1 (a). Diffusion controlled amperometric response displaying the current of double layer charging, I_{DL} , the current of nucleation and growth without overlapping effects, I_{free} , and finally the current going through a maximum with a following decrease due to the nuclei overlapping, I_{overlap} (b) [7].

From these examples, it is clear that the current-time transient response recorded during a constant potential experiment holds plenty of information of the various phenomena involved in the electrochemical deposition of materials at the electrode surface.

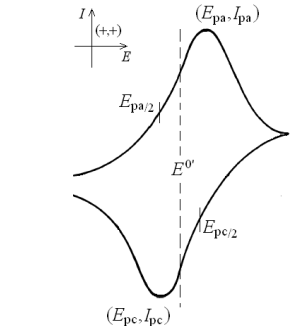
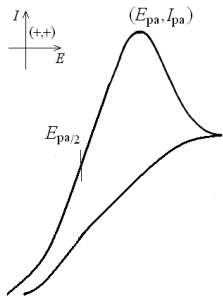
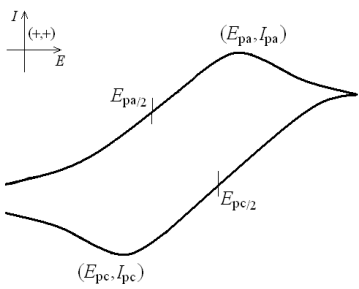
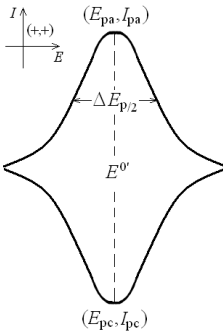
2.5.2.2 Cyclic Voltammetry

Cyclic Voltammetry (CV) is one of the potential sweep methods where the potential of the electrode is scanned linearly and repeatedly with time, *i.e.*, $E(t) = E(0) \pm vt$, between the starting potential $E(0)$ and the inverting potential $E(t_{\text{inv}})$; where t_{inv} corresponds to the instant at which the scan is reversed. The potential scan rate, v , usually varies from mV/s to V/s [6]. Linear sweep voltammetry (LSV) can be considered as a special case of CV in which the potential is scanned only once in one direction. CV and LSV are particularly useful in assessing the redox activity and behaviour of electrochemical systems.

There are four main CV responses that depend on the reversibility of the redox process and whether the redox species are adsorbed or not on the electrode surface as shown in Table 2.1. Each response is characterized by a different shape of the corresponding cyclic voltammogram, which is described by three key parameters, the peak current (I_p), the peak potential (E_p) and the potential width at half peak ($|E_p - E_{p/2}|$). The dependence of each parameter on the potential scan rate, v , allows the characterization of the electrochemical system. The E_p does not change with v for reversible (Nernstian) systems. The I_p changes linearly with $v^{1/2}$ for reversible and irreversible systems, and with v for reversible adsorbed species. The correlation between I_p and $v^{1/2}$ for *quasi*-reversible systems depends on the scan rate and the electron-transfer rate constant. Generally, there is no correlation between I_p and $v^{1/2}$ at high scan rates and for reactions which display slow electron-transfer kinetics. The exact diagnostic equations used to probe the redox characteristics are described in detail in various electrochemistry textbooks [5, 11].

The typical shape of the voltammetric peak can be described as a result of an initial increase in current, before $E^{0'}$, due to the increased number of species reduced (or oxidized) at the electrode. This is followed by a decrease of current, after $E^{0'}$, due to the formation and thickening of the diffusion layer. Obviously, the two opposite effects result in a maximum of current, I_p . Once the diffusion layer has become thick enough (usually around 180 mV after the peak maximum) the curve exhibits Cottrell behaviour (Equation 2.1) [12].

Table 2.1 Cyclic voltammograms with their respective peak current (I_p) and potential (E_p) characteristics. The electrochemical system is reversible when the concentrations of the electroactive species at the electrode surface are governed at any time by the Nernst equation. The integer, n , is the number of electrons involved in the redox process, and α is the corresponding transfer coefficient. The factor $\Delta(\Lambda, \alpha)$ is a function of α and $\Lambda = k^0/(\nu DF/RT)^{1/2}$, where D is the diffusion coefficient of the electroactive species and k^0 is the standard heterogeneous rate constant. The values of this factor are available in the literature [5]. All potentials are expressed at 25 °C.

Reversible	Irreversible
 <p style="text-align: center;">$I_p \propto \nu^{1/2}$</p> <p style="text-align: center;">E_p independent of ν</p> <p style="text-align: center;">$E_p - E_{p/2} = 59/n \text{ mV}$</p>	 <p style="text-align: center;">$I_p \propto \nu^{1/2}$</p> <p style="text-align: center;">E_p increases as ν increases</p> <p style="text-align: center;">$E_p - E_{p/2} = 48/\alpha n \text{ mV [5]}$</p>
Quasi-reversible	Adsorption
 <p style="text-align: center;">I_p not proportional to $\nu^{1/2}$</p> <p style="text-align: center;">E_p increases as ν increases</p> <p style="text-align: center;">$E_p - E_{p/2} = 26\Delta(\Lambda, \alpha) \text{ mV}$</p>	 <p style="text-align: center;">$I_p \propto \nu$</p> <p style="text-align: center;">E_p independent of ν</p> <p style="text-align: center;">$\Delta E_{p/2} = 90/n \text{ mV}$</p>

2.5.2.3 Rotating Disk Voltammetry

Rotating disk voltammetry (RDV) consists of performing a potential sweep (either linear or cyclic) at a rotating disk electrode (RDE). The RDE is a disk electrode that is placed into a solution and spun at a controlled angular speed, ω (rad/s). The rotation causes a controlled flux of solution towards and perpendicular to the electrode surface, which is then radially and evenly distributed on the disk. The solution that is in immediate contact with the electrode moves along with the disk. This forced convection allows the fast establishment of a reproducible and easily adjustable high steady-state mass transport rate, a condition especially useful for the evaluation of surface catalytic activities (*e.g.*, oxygen reduction reaction) [6, 13]. The thickness, δ in cm, of the diffusion layer at the RDE is inversely proportional to the square root of the angular speed, $\omega^{1/2}$, Equation 2.4 [5].

$$\delta(\omega) = 1.61 \frac{D^{1/3} \nu^{1/6}}{\omega^{1/2}} \quad 2.4$$

Here, D is the diffusion coefficient, in cm^2/s , of the electroactive species and ν the kinematic viscosity, in cm^2/s , of the solvent. The classical RDV experiment consists of recording a linear sweep voltammogram at low scan rate (1 to 10 mV/s) to obtain a sigmoidal wave typical of the steady-state mass transport condition (Figure 2.5). The limiting current, I_L (which is the highest current achievable when the electron transfer rate constant, k_e , is extremely large, *i.e.*, in totally mass-transfer-limited condition), is given by the *Levich*, Equation 2.5. In this equation, n is the number of electron transferred in the half reaction, F is the Faraday's constant (96485.34 C/mol), and C^∞ is the bulk concentration of the species in mol/cm^3 .

$$I_L = 0.62nFAD^{2/3}\omega^{1/2}\nu^{-1/6}C^\infty \quad 2.5$$

The condition of total mass-transfer-limited current is not always satisfied. The *Koutechý-Levich* equation takes into account the effect of a sluggish irreversible electron transfer rate constant, k_e , on the RDV current response, I , Equation 2.6 [13].

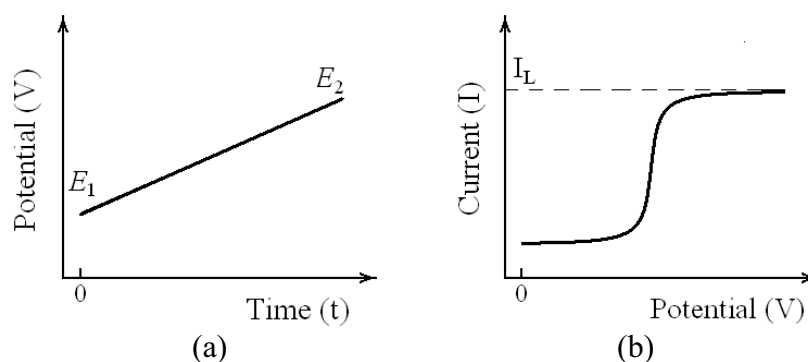


Figure 2.5 Voltammetric response of a hypothetical potential sweep at a rotating disk electrode (RDE). The potential sweep is applied at time $t = 0$, the potential rises linearly between the starting and ending potentials, E_1 and E_2 (a). Diffusion controlled voltammetric response under totally mass-transfer-limiting condition. The redox current starts in the middle of the potential scan and levels off at a limiting value, I_L (b).

$$\frac{1}{I} = \frac{1}{I_L} + \frac{1}{nFAk_e C^\infty} \quad 2.6$$

It is evident that for small values of k_e (sluggish electron transfer) the achievable maximum value of I at any given potential is always lower than I_L . Moreover, it is clear that for a given electrode geometry, potential sweep, solution and angular speed (*i.e.*, fixed n , A , ν , C^∞ , D and ω), the limiting current is only dependent on the rate constant, k_e .

2.5.2.4 Electrochemical Quartz Crystal Microbalance

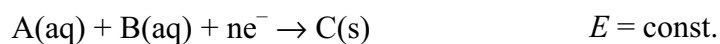
The electrochemical quartz crystal microbalance (EQCM) is an *in-situ* electrochemical technique that allows the recording of frequency (mass) changes at the electrode surface. The sensitive element of the EQCM is an AT-cut quartz crystal which exhibits a converse piezoelectric effect, meaning that the application of a voltage across the crystal causes a corresponding mechanical strain. In quartz this deformation is elastic and can be recovered upon removal of the voltage. Accordingly, the application of an alternating potential causes a vibrational motion with amplitude parallel to the surface of the crystal. The result is an acoustic wave that propagates across the thickness of the crystal (δ_q) and reflects back once at the

surface. A resonant condition between outgoing and reflected waves is established when the acoustic wavelength is exactly double of the crystal thickness ($2\delta_q$). The velocity of such a standing wave is $v_{tr} = 2\delta_q f_o$, that is the length covered by the wave per second and f_o is the frequency of the acoustic wave. The velocity, v_{tr} , is a fixed property of the crystal ($v_{tr}^2 = \mu_q/\rho_q$ where μ_q is the shear stress and ρ_q the density of quartz). Hence, any change in thickness ($\Delta\delta$) causes a corresponding inverse change in frequency (Δf). The two relative changes are mutually related by $\Delta f/f_o = -\Delta\delta/\delta_q$, and then by $\Delta f/f_o = -2f_o\Delta\delta/v_{tr}$. If the change of thickness is caused by a uniform deposition of an amount, Δm , of material on the surface area, A , of the crystal, $\Delta\delta = \Delta m/(A\rho_m)$ where ρ_m is the material density, the frequency change becomes $\Delta f = -2f_o^2\Delta m/(A\rho_m v_{tr})$ assuming that v_{tr} in the material is the same as that in quartz. By imposing the additional condition $\rho_m = \rho_q$ (which also gives $\mu_m = \mu_q$) it follows that Equation 2.7 is obtained [14].

$$\Delta f = -\frac{2f_o^2}{A\sqrt{\mu_q\rho_q}}\Delta m \quad 2.7$$

This is the Sauerbrey equation and is valid for rigid thin layers in order to respect the constraint imposed by the density and shear rate equalities ($\rho_m = \rho_q$ and $\mu_m = \mu_q$). As a rule of thumb, Equation 2.7 is valid provided that the mass change Δm is less than 1 % of the mass of the quartz crystal [15]. It is important to note that the EQCM output is a frequency change and not a mass change, the frequency to mass conversion is performed with Equation 2.7. With $A = 0.2 \text{ cm}^2$ and $f_o = 8 \text{ MHz}$ AT-cut quartz crystal electrode, $\rho_q = 2.648 \text{ g/cm}^3$ and $\mu_q = 2.947 \times 10^{11} \text{ g/(cm}^2\text{s)}$, the EQCM sensitivity is about 1.4 ng/Hz, corresponding to about 20 picomoles of Cu or Zn.

The EQCM allows the simultaneous recording of the current-potential and mass changes at the AT-cut quartz crystal electrode. The technique can be used to measure the *mass-to-charge* ratio of electrodeposited materials and compare it to theoretical values in order to identify their nature. The potentiostatic deposition of a generic compound can be outlined as follows:



The *average* mass-to-charge ratio R for the electrodeposition of C is given by Equation 2.8.

$$R = \frac{\Delta m_C}{|Q_C|} = \pm \frac{M(C)}{nF} \quad 2.8$$

Here, Δm_C and Q_C are the experimental mass and charge of deposition calculated from the frequency change and the time integral of the current, respectively. The ratio R is simply the deposited mass per unit of charge (g/C), and it corresponds to the ratio of the molar mass of the deposit, $M(C)$, and the charge consumed per mole of it, nF . The absolute value of Q_C is used in order to obtain $R > 0$ for increasing mass ($\Delta m_C > 0$) and $R < 0$ for decreasing mass ($\Delta m_C < 0$) for both oxidation ($Q_C > 0$) and reduction ($Q_C < 0$) processes.

The *instantaneous* mass-to-charge ratio, R_{inst} , is a transient representation of the mass-to-charge ratio at any time, t , of the experiment, Equation 2.9.

$$R_{inst} = \frac{dm_C}{|dQ_C|} = \frac{dm_C}{dt} / \left| \frac{dQ_C}{dt} \right| \quad 2.9$$

It can be calculated as the quotient of the first time-derivatives of the mass $m_C(t)$ and charge $Q_C(t)$ functions. Compared to R which gives an overall description of the deposited species, the ratio R_{inst} provides a transient representation of the species at each instant of the deposition. It follows that the instantaneous values of R can disclose more information on the evolution and phenomena of the electrodeposition.

2.5.2.5 Electrochemical Impedance Spectroscopy

The powerful aspect of electrochemical impedance spectroscopy (EIS) is its ability of discerning different processes depending on their time scale. Slow processes such as the diffusion of ions inside the bulk of conducting polymer can be probed at low frequencies, whereas fast processes such as the formation of a surface double-layer are probed at high frequency.

The electrical impedance is given by the ratio of voltage and current in the regime of alternating current, $Z = V/I$. It is a measure of the impediment to the flow of the

current, *i.e.*, at a fixed electric voltage, the charge flow decreases with increasing impedance ($I = \text{Const}/Z$).

A voltage or current is alternating when its variation in time is proportional to $\cos(\omega t)$ or $\sin(\omega t)$. Each element in a circuit, for example a resistor, capacitor or inductor, exhibits a characteristic response to the alternating voltage $V = V_o \cos(\omega t)$.

In the case of a resistor the voltage and current are related through the resistance $R = V/I$ which gives Equation 2.10.

$$I = \frac{V_o}{R} \cos(\omega t) = I_o \cos(\omega t) \quad 2.10$$

The impedance of the resistor, $Z_R = V_o/I_o = R$, is independent of the angular frequency, ω , and voltage and current are in phase. The resistor allows the current to follow the potential without any delay and the impedance corresponds to the resistance.

A capacitor has a capacitance of $C = Q/V$ with $I = dQ/dt = CdV/dt$ that gives Equation 2.11.

$$I = -\omega C V_o \sin(\omega t) = \omega C V_o \cos\left(\omega t + \frac{\pi}{2}\right) = I_o \cos\left(\omega t + \frac{\pi}{2}\right) \quad 2.11$$

The impedance of the capacitor, $Z_C = V_o/I_o = 1/\omega C$, is dependent on the angular frequency, ω , and the current is $\pi/2$ ahead the voltage. The charging/discharging of the capacitor keeps the current ahead while the voltage is changing, *i.e.*, the voltage across the capacitor lags behind the current. The charge required is the same at all frequencies for fixed C and V_o ($Q = CV_o$); hence, the impedance of the capacitor is lower at high frequencies in order to allow higher currents.

In the case of an inductor the inductance is $L = V/(dI/dt)$ with $I = \int (dI/dt)dt = (1/L) \int V(t)dt$ which gives Equation 2.12.

$$I = \frac{1}{\omega L} V_o \sin(\omega t) = \frac{1}{\omega L} V_o \cos\left(\omega t - \frac{\pi}{2}\right) = I_o \cos\left(\omega t - \frac{\pi}{2}\right) \quad 2.12$$

The impedance of the inductor, $Z_L = V_o/I_o = \omega L$, is dependent on the angular frequency, ω , and the current is $\pi/2$ behind the voltage. The current lags behind the voltage that forces it through the inductor which obstructs any increase/decrease of

current. It follows that the opposing effect of the inductor rises with increasing rate of current change. Hence, the impedance of the inductor is larger at higher frequencies.

A limit of the analysis presented to this point is the non linearity of the I - V relations for the capacitor ($V \propto \int I(t)dt$) and inductor ($V \propto dI(t)dt$). A linearization of these relations would allow the use of Kirchoff's laws and simplify the analysis of electrical circuits. The solution can be obtained through the differentiation and integration of the exponential function $e^x = de^x/dx = \int e^x dx$, and by using the Euler formula $e^{ix} = \cos x + i\sin x$, where $i^2 = -1$. The complex voltage, $V = V_o e^{i(\omega t + \phi)}$, is then expected to be both alternating and linear with the current, Equations 2.13, 2.14 and 2.15.

$$I = \frac{V_o e^{i(\omega t + \phi)}}{R} = \left(\frac{1}{R}\right) V \quad 2.13$$

$$I = C \frac{d[V_o e^{i(\omega t + \phi)}]}{dt} = i\omega C V_o e^{i(\omega t + \phi)} = \left(\omega C e^{i\frac{\pi}{2}}\right) V \quad 2.14$$

$$I = \frac{1}{L} \int V_o e^{i(\omega t + \phi)} dt = \frac{1}{i\omega L} V_o e^{i(\omega t + \phi)} = \left(\frac{1}{\omega L e^{i\frac{\pi}{2}}}\right) V \quad 2.15$$

In all cases the complex voltage and complex current are linearly related by $I = YV$, the complex impedance is the inverse of the complex admittance Y , $Z = 1/Y$. The corresponding complex impedances of the lumped elements are given in Equations 2.16, 2.17 and 2.18.

$$\text{Resistor :} \quad Z_R = R \quad 2.16$$

$$\text{Conductor :} \quad Z_C = \frac{1}{\omega C} e^{-i\frac{\pi}{2}} \quad 2.17$$

$$\text{Inductor :} \quad Z_L = \omega L e^{i\frac{\pi}{2}} \quad 2.18$$

The expression $Z = |Z|e^{i\phi}$ gives the same modules and phases, ($|Z|$, ϕ), obtained before for the resistor (R , 0), capacitor ($1/\omega C$, $-\pi/2$) and inductor (ωL , $\pi/2$).

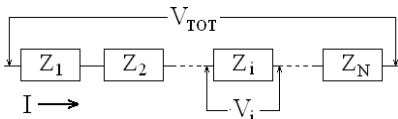
A general element of major importance in electrochemistry is the constant phase element, CPE, which complex impedance is given by Equation 2.19.

$$\begin{array}{l} \text{Constant} \\ \text{phase} \\ \text{element} \end{array} : \quad Z_{CPE} = \frac{1}{A\omega^n} e^{-i\frac{\pi}{2}n} \quad 2.19$$

The importance of the CPE stems from the fact that it describes those non ideal conditions that are most commonly found in real electrochemical systems. It is seen that Equation 2.19 corresponds to a resistor with $R = 1/A$ for $n = 0$, to a capacitor with $C = A$ for $n = 1$, and to an inductor with $L = 1/A$ for $n = -1$. The CPE is frequently used to represent a non ideal resistance, giving $0 < n \leq 0.2$, or a non ideal capacitor, giving $0.8 \leq n < 1$. The Warburg element is another important element that describes semi-infinite diffusion of charges and corresponds to a CPE with $n = 0.5$, Equation 2.20. The module and phase of the Warburg element are $(1/B, -\pi/4)$. In those cases where $0.4 \leq n \leq 0.6$ the CPE can be interpreted as non ideal semi-infinite diffusion.

$$\begin{array}{l} \text{Warburg} \\ \text{element} \end{array} : \quad Z_W = \frac{1}{B\sqrt{\omega}} e^{-i\frac{\pi}{4}} \quad 2.20$$

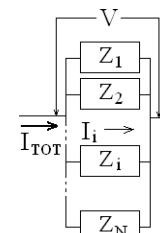
The linearity established between complex voltage and complex current allows the application of Kirchoff's laws that are still valid for complex quantities. The total impedance, Z_{TOT} , of N impedances, Z_i , in series is given by Equation 2.21.



$$Z_{TOT} = \frac{V_{TOT}}{I} = \sum_{i=1}^N Z_i \quad 2.21$$

$$V_{TOT} = \sum_{i=1}^N V_i = I \sum_{i=1}^N Z_i$$

The Z_{TOT} of N impedances, Z_i , in parallel is given by Equation 2.22.



$$\frac{1}{Z_{TOT}} = \frac{I_{TOT}}{V} = \sum_{i=1}^N \frac{1}{Z_i} \quad 2.22$$

$$I_{TOT} = \sum_{i=1}^N I_i = V \sum_{i=1}^N \frac{1}{Z_i}$$

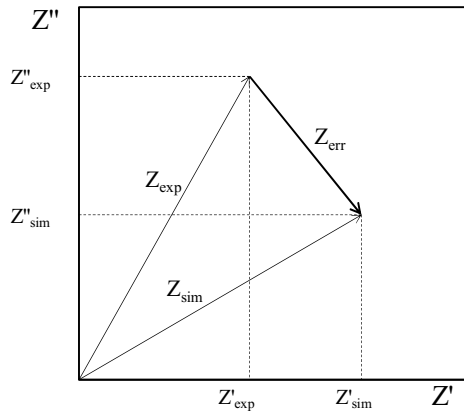
This theoretical treatment is applicable to electrochemical systems that behave linearly in steady state condition. In order to satisfy such a requirement the input signal must be small enough to keep the overall state of the system unchanged. Typical values for the input voltage, V_o , range from 3 to 5 mV while the frequency is usually scanned from 10^{-3} to 10^5 Hz.

In a classical EIS experiment the input signal is an alternating voltage and the output signal is a corresponding alternating current with the same frequency and different phase. The phase angle, ϕ , and impedance, Z , Z' and $|Z|$, are computed. There are two ways of representing the impedance graphically. In the Nyquist or complex plane plot the real and imaginary components (Z' , Z'') are plotted as x and y axis in a Cartesian system. In the Bode plot the module and phase of the impedance ($|Z|$, ϕ) are plotted against the frequency. These data are then fitted with a theoretical model derived from a hypothetical equivalent electric circuit that can emulate the electrical behaviour of the electrochemical system. Different models can fit the same set of data, thus in order to find the correct one two criteria are best followed. The correct model is the one which gives a rational and justified physicochemical description of the electrochemical system, and which deviates the least from the experimental data (*i.e.*, with the minimum residual difference between experimental and simulated data, $R\%$).

The weighted percentage residual ($R\%$) is a good indication of the fit between experimental and simulated data and can be estimated using Equation 2.23 (N = number of data points). The percentage error ($\varepsilon\%$) of each data point is calculated from Equations 2.24 and 2.25 which terms are represented in Figure 2.6.

$$R\% = \frac{\sum_N \varepsilon\%}{N} \quad 2.23$$

In the present work, a value of $R\% \leq 3\%$ is considered indicative of a good fit between experimental and simulated data. More information and details about EIS can be found in several published sources [5, 11, 16-18].



$$\varepsilon\% = \frac{|Z_{err}|}{|Z_{exp}|} \times 100 \quad 2.24$$

$$\frac{|Z_{err}|}{|Z_{exp}|} = \frac{\sqrt{(Z'_{exp} - Z'_{sim})^2 + (Z''_{exp} - Z''_{sim})^2}}{\sqrt{Z'^2_{exp} + Z''^2_{exp}}} \quad 2.25$$

Figure 2.6 Vectorial representation of the error impedance (Z_{err}) between experimental (Z_{exp}) and simulated (Z_{sim}) impedances.

2.5.3 Microscopic Methods

2.5.3.1 Scanning Electron Microscopy and Energy Dispersive X-Ray Analysis

The aim of electron microscopy is the imaging of objects at the nanoscale level [19]. The essential feature of a microscope is the interaction between objects and waves which are high-energy electrons in the case of electron microscopy. In scanning microscopes the image is composed sequentially point-by-point. The three key features of a microscope are resolution, contrast and magnification. The enlarged image (magnification) must present distinguishable details (resolution and contrast) in order to deliver a thorough representation of the object. The resolution, d , between two adjacent objects is proportional to the wavelength of the incident beam, λ . In scanning electron microscopy the wavelength of the electron beam is shorter at a higher acceleration voltage, thus, in principle, it does not represent a limiting factor for the resolution [20]. The information and content of electron-generated images is restricted by both instrumental and operational limits. The operator has much influence on the generation of artefacts during the preparation and manipulation of the samples. Therefore, the contents of the images require skilful and critical considerations before being accepted [19].

The scanning electron microscope (SEM) consists of an electron-optical column mounted on a vacuum chamber [21]. The gun placed on top of the column is typically a thermoionic cathode made of tungsten that emits electrons. The electrons are pushed down into the column by an accelerating voltage ranging from 1 to 30 kV. Magnetic lenses and scan coils are used to focus and scan the electron beam on the specimen. The pressure in the specimen chamber is 10^{-3} - 10^{-5} Pa ($\sim 10^{-7}$ mmHg). The specimen is placed on a stage that can move with nanometric precision along the x, y and z axis.

The interaction of the high-energy electrons with the sample generates different types of signals categorized into two groups depending on whether they are generated by elastic or inelastic interactions [22]. The elastic scattering results from the deflection of incident electrons by atomic nuclei or shell electrons with similar energy. This, in turns, results in backscattered electrons (BSE) with negligible energy loss and scattering angles larger than 90° . The inelastic scattering results from interactions of the incident electrons with the nuclei and core electrons of the material, and generates signals with substantial energy loss transferred to the sample. Secondary electrons (SE), Auger electrons, X-ray emission and cathodo-luminescence belong to this group. The incident beam has a characteristic penetration volume in the sample and each signal originates from a different part of it (Figure 2.7). The BSE electrons have high enough energy (> 50 eV) to emerge from underneath the sample surface. Images made from BSE electrons are characterized by Z contrast, *i.e.*, the brightness of the elements is proportional to the atomic number (Z) as the backscattering yield increases with increasing Z. The resolution of these images is of the order of $1 \mu\text{m}$ because of the high energy of the BSE electrons. The SE electrons have low energy (< 50 eV) and consequently carry topographical information of the sample surface. The low energy of SE electrons allows a resolution of about 10 nm. Auger electrons are emitted from atoms ionized by the incident electron beam and their energy is characteristic of the elements. The energy of Auger electrons is very low and the resultant escape depth is only of a few nanometers.

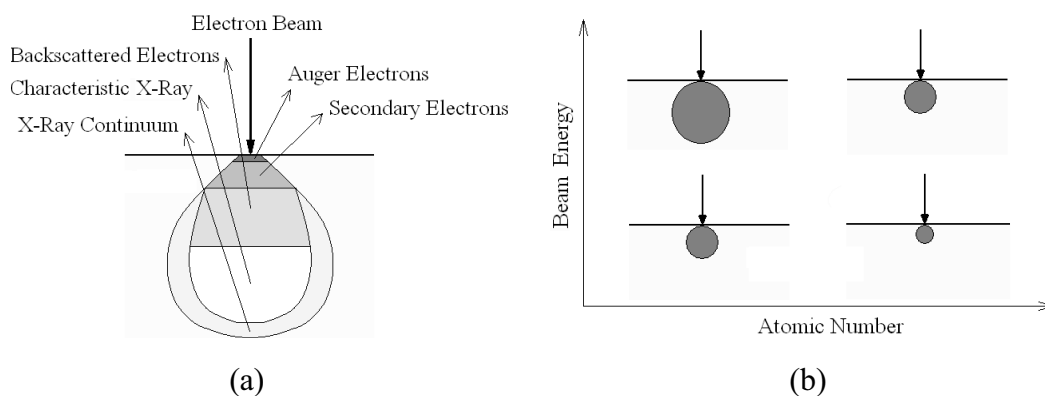


Figure 2.7 Schematic representation of the electron-material interaction in scanning electron microscopy (SEM). Section of the volume of interaction of the electron beam with the sample surface and corresponding areas from which all the different signals originate (a). Size of the interaction volume as a function of atomic number of the elements in the sample and the energy of the electron beam (b).

The characteristic X-ray signal is used to perform the chemical microanalysis of the sample surface. This technique is called energy dispersive X-ray (EDX) analysis and is discussed later in greater detail. Cathodo-luminescence is produced through electron relaxation emitting infrared, visible and ultraviolet photons. Such a signal can be collected and elaborated to give images with a resolution of 50 nm [22].

The large majority of SEM images are obtained from SE electrons. The image formation is performed by a device made of three components namely a scintillator, a light pipe and a photomultiplier tube. The scintillator converts the SE electrons into light, the light is collected by a light pipe which conveys it into a photomultiplier tube, and here the light is converted back into electrons. The electrons are eventually converted to a visual signal displayed on a cathode ray tube. The brightness and contrast of the image generated are directly dependent on the surface topography (Figure 2.8). The yield of the SE electron emission from the specimen is also dependent on the atomic number of the component in the sample; low atomic number elements naturally emit low yields of SE electrons when excited by an electron source.

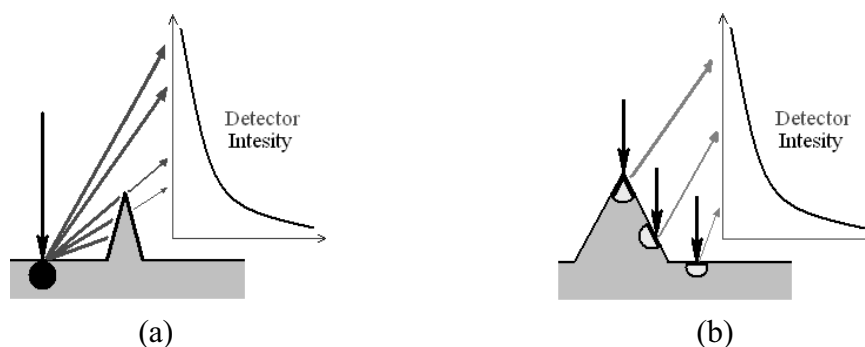


Figure 2.8 Schematic illustration of the effect of surface topography and detector position on the detection of secondary electrons (SE). Effect of surface roughness on the intensity of the collected signal (a). An obstructing tip is placed in between the beam spot and the detector, the SE electrons emitted behind the tip are gradually absorbed giving the image its 3D appearance. Effect of the emission region on the intensity of the collected signal (b). The beam focused on the top of the tip has a higher exposure and consequently a more intense associated signal.

Charging phenomena at the surface of non conductive samples can interfere with the emission of SE electrons. Therefore in order to improve the yield of SE emission and the surface conductivity, the samples are typically sputter coated with a thin layer of noble metals, *e.g.*, Au (10 nm).

Energy dispersive X-ray analysis (EDX) is routinely carried out in combination with SEM. EDX allows the localized micro-elemental analysis of the top few micrometers of the sample. X-ray signals are generated when the high-energy electron beam hits the sample surface. A characteristic X-ray signal is produced from the interaction of a beam electron with an inner shell electron of the sample. The inner electron is ejected and replaced by an outer shell electron. This process requires the emission of X-rays with energies corresponding to the energy separation of the levels involved in the electronic transition. Since each element has its characteristic orbital energies, the X-rays emitted by the sample are linked to its chemical composition. An X-ray continuum is also generated through the deceleration of the beam electrons which gives the broad background signal present in all EDX spectra, also referred as Bremsstrahlung. This background has much lower intensity than the elemental peaks and does not represent an issue in the qualitative analysis of the samples.

The transitions involved in the characteristic X-ray emission are labelled after the K, L, M, N electronic shells. The EDX lines are also named α , β or γ depending on which outer shell electrons make the transition to fill the electron vacancy. Transitions of electrons immediately after the emptied level are α , the following level are β and γ in order of increasing energy. The main EDX lines of copper are the $K\alpha$ ($L \rightarrow K$, ~ 8050 keV), $K\beta$ ($M \rightarrow K$, ~ 8900 keV), $L\alpha$ ($M \rightarrow L$, ~ 930 keV) and $L\beta$ ($N \rightarrow L$, ~ 950 keV); whereas for zinc they are the $K\alpha$ ($L \rightarrow K$, ~ 8640 keV), $K\beta$ ($M \rightarrow K$, ~ 9570 keV), $L\alpha$ ($M \rightarrow L$, ~ 1010 keV) and $L\beta$ ($N \rightarrow L$, ~ 1030 keV) [23].

An EDX spectrum consists of a series of peaks placed at specific energies depending on the chemical element and with intensity proportional to the number of counts. The number of counts is proportional to both the amount of chemical element in the sample and to the energy carried by the associated X-ray signal. X-rays of higher energy give more intense peaks. This is connected with the working principle of the EDX detectors. The energy of the incoming X-rays is measured in terms of the amount of ‘ionization’ produced in the detector material. The most common detectors are based on a semiconductor p-n junction in which the number of hole/electron pairs generated by the incoming X-ray signal is roughly the number of times the band-gap fits with the energy carried by the signal. The two main types of detector are the lithium-drift silicon detector, Si(Li), and the silicon drifted detector, SDD. The advantage of the latter is that it does not need to be cryogenically cooled using liquid nitrogen.

The resolution of the EDX probe is given by the size of the volume of interaction of the electron beam with the sample. The size is usually a few microns. Smaller probing spots are achievable at lower energy and with highly collimated beams (feasible conditions with Field-Emission Scanning Electron Microscopes).

The EDX qualitative and quantitative analysis is mainly affected by the surface roughness (Figure 2.9) [24, 25]. The interaction of the BSE electrons with the surrounding zones of the probed point (the beam spot) can cause the emission of X-rays that add up to the signal belonging to the point of analysis. The extent of such interference is a major limitation that affects the quantitative analysis. A quantitative EDX analysis is practicable only with high-quality flat-polished sample surfaces, and it must be performed against a known standard prepared and analyzed in the same

way. Quantitative analysis is possible by comparison of relative peak heights of the sample and a standard of known composition measured under the same conditions, however various correction factors due to matrix effects must be taken into account in order to obtain reliable data [24, 25]. These correction factors are related to atomic number (Z), absorption (A) and fluorescence (F) effects and are corrected by using a characteristic ZAF factor which correlates the intensity of the peak to the concentration of the element.

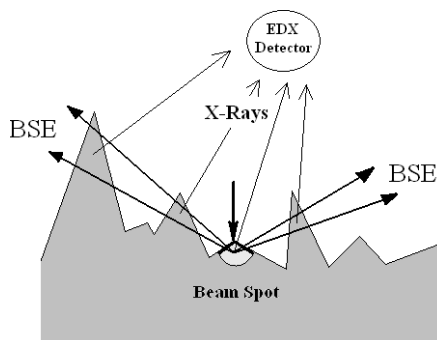


Figure 2.9 Schematic illustration of the effect of the surface roughness on the detection of the X-ray signal. The interaction of the backscattered electrons (BSE) with the surrounding roughness causes the acquisition of a mixed signal by the EDX detector.

2.5.4 Spectroscopic and Diffractive Methods

2.5.4.1 Attenuated Total Reflectance Infrared Spectroscopy

Infrared spectroscopy (IR) is based on the vibrational motion of atoms inside materials [26, 27]. The most useful range of vibrational energies is between 400 cm^{-1} and 4000 cm^{-1} , the mid-IR. A material can absorb the energy corresponding to the vibrational transitions of its functional groups and/or species. The energy is absorbed when the vibrational transitions involve a change of dipole moment.

The dipole moment of a material arises from an asymmetrical distribution of the positive and negative charges [27]. Such charges can be displaced by the IR radiation to give an oscillating dipole moment related to a specific vibrational mode. This vibrational mode can be IR active or inactive. In order to be active, the displacement of the charge distributions must break a symmetry element present in the material. This is actually the only circumstance in which the energy carried by the radiation can be transferred to the material. The IR absorption intensity is proportional to the

square of the change in dipole moment, it follows that the probability of IR transitions is greater for vibrations with larger dipole moment change.

The Fourier transform (FT) is a mathematical operation that relates two functions defined in domains with reciprocal units [28]. Given a signal $s(a)$ in the generic domain a , its Fourier transform $S(b)$ is another signal in the domain b with unit reciprocal to a , *i.e.*, $[b] = 1/[a]$. The most common case is the FT of a signal from the time (s) to the frequency (s^{-1}) domain, but in the case of IR spectroscopy the transformation of the signal is from the spatial (cm) to its reciprocal (cm^{-1}) domains. The key apparatus that allows the measurement of the IR spectrum in the spatial domain is the Michelson interferometer with a movable mirror [28]. The signal generated by the interferometer is the superimposition of the IR source beam to its reflection from a movable mirror, it follows that the signal is spatially modulated by the position of the mirror. Such a signal is sent through the sample and then to the detector. Eventually, it is Fourier transformed to the final spectrum in the wavenumber domain.

An IR beam is reflected at the interface between two materials when going from high to low refraction index media, *e.g.*, from medium 1 to medium 2 with refraction indexes $n_1 > n_2$ [27]. The portion of radiation that is reflected back into the medium of origin 1 is dependent on the angle of incidence, α_1 , which is the angle between the beam and the line perpendicular to the interface. If α_1 is small most of the radiation goes through the interface into medium 2, but if $\alpha_1 > \alpha_c$ the radiation is all internally reflected. The critical angle, α_c , corresponds to the incident angle at which the reflected beam travels parallel to the interface, *i.e.*, at which the angle of the refracted beam is $\alpha_2 = \pi/2$. The sine of α_c is equal to the ratio n_2/n_1 (in fact from Snell's law, $n_1 \sin \alpha_1 = n_2 \sin \alpha_2$, if $\alpha_2 = \pi/2$ then $\sin \alpha_c = (n_2/n_1) \sin(\pi/2) = n_2/n_1$). When $\alpha_1 > \alpha_c$ the beam enters slightly in the medium 2 with lower refraction index in the form of an exponentially decaying wave before being totally reflected. The totally reflected beam is attenuated by the absorption of part of the energy carried by the evanescent wave. Therefore, the described effect is called attenuated total reflectance (ATR).

The penetration depth d_p of the evanescent wave is given by Equation 2.26, in which θ is the incident angle and λ the wavelength of the incident radiation [29].

$$d_p = \frac{\lambda}{2\pi n_1 \sqrt{\sin^2 \theta - (n_2/n_1)^2}} \quad 2.26$$

The ATR effect is used in conjunction with FTIR to study the infrared spectroscopy of surfaces. An internal reflectance plate made of a high index refraction material is placed in intimate contact with the surface allowing the recording of the IR spectrum of a few micrometers into the sample. The ATR-FTIR measurement can be run in multiple or single reflection mode. The best sampling material is diamond for its high refractive index, hardness and chemical inertia. The spectra obtained with this technique are similar to those obtained with classical transmission techniques but with two major differences. The first is that the band intensity increases with increasing wavelength, in fact at higher λ the penetration depth is greater and the corresponding absorption is larger (Equation 2.26). The second difference is the presence of band shape distortions caused by the wavenumber dependence of the sample refraction index $n_2(\bar{\nu})$ in the region of the absorption band. If n_2^0 is the average refraction index and $\bar{\nu}_c$ in the wavenumber at the center of the absorption band, it follows that $n_2(\bar{\nu} < \bar{\nu}_c) > n_2^0$ and $n_2(\bar{\nu} > \bar{\nu}_c) < n_2^0$. From Equation 2.26, the penetration depth is higher in the low-wavenumber side, $\bar{\nu} < \bar{\nu}_c$, where the refraction index of the sample is larger than average, whereas it is lower in the high-wavenumber side, $\bar{\nu} > \bar{\nu}_c$, where the refraction index is smaller than average. The result is a distorted band with the low energy side more intense than the high energy one. The maximum of the resulting band can be shifted toward lower energies because of this distortion. This shift is the reason for the different position of the same band recorded in transmission and ATR modes. In general, one must take into account such differences when comparing transmission and ATR spectra. A way to reduce this shift is to keep $\sin \alpha_1$ and n_1 high enough to equalize the effect of n_2 on the denominator of Equation 2.26 [27]. Databanks and practical approaches for the interpretation of IR spectra can be found in the literature [30].

2.5.4.2 Raman Spectroscopy

Raman spectroscopy is based on the inelastic scattering of monochromatic radiation. After interacting and exchanging energy with a molecule (or crystal), a photon is

scattered away with an energy that is either lower or higher than its original energy. The energy difference is characteristic of the material [31-33].

Vibrational transitions occur both in IR and Raman spectroscopy. The main differences between the two are the energy of the incident radiation and the nature of the radiation-material interaction. In the case of IR spectroscopy the energy of the incident radiation is in the infrared range and it must correspond exactly to the energy difference between two vibrational states in order to be absorbed. In the case of Raman spectroscopy the incident radiation is a UV-Vis monochromatic beam (a laser) and its energy does not necessarily have to correspond to the separation of two states in order to give scattering. The energy absorbed during Raman scattering brings the molecule from its ground state to a generic 'virtual state' different than any energy level of the molecule. This energy is then either released as it was absorbed (Rayleigh scattering), or shifted by a certain discrete value (Raman scattering).

The IR and normal Raman transitions are shown in Figure 2.10. The IR transition requires a smaller and exact amount of energy compared to the Raman transitions. The Rayleigh scattering (R) is just the elastic scattering of the incident photon. Raman scattering has two possible transitions, Stokes (S) and anti-Stokes (A) lines corresponding to the transition of the molecule between different vibrational levels within the same electronic ground state, E_0 . In the case of the Stokes line, the starting vibrational level is the ground state, the ending one is a vibrational level at higher energy (absorption). In the case of the anti-Stokes line, the starting vibrational level is above the ground state, and the ending one is the ground level (emission). The population of the vibrational levels above the ground level is low at ambient temperature (Boltzmann distribution). As a consequence, the anti-Stokes lines are much less intense than the Stokes lines.

Considering the nature of the IR and Raman phenomena, the measurement of the effect of the two processes is performed in a different way. The samples are irradiated with beams of infrared energy for IR and of UV-Vis energy for Raman. The resulting absorption in the IR is detected in line with the beam source, whereas the scattered Raman energy is detected at a right angle with the beam source. Raman scattering is a very weak process (low probability process) and only one of 10^8 incident photons is Raman scattered. For this reason the measurement must be

performed with very high energy sources like lasers. Consequently, sample deterioration is one of the limitations of Raman spectroscopy.

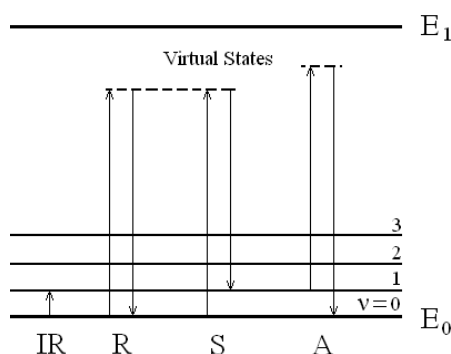


Figure 2.10 Infrared and normal Raman energy transitions within the same molecular electronic level E_0 . The infrared (IR) transition corresponds to the absorption of the incoming radiation with energy matching the separation between the vibrational levels 0 and 1 (v is the vibrational quantum number). The Rayleigh scattering (R) is the absorption and emission of radiations of the same energy. The Raman scattering Stokes (S) and anti-Stokes (A) lines are produced by the absorption and emission of vibrational energy upon the interaction with the incoming radiation. The virtual states do not correspond to any energy level of the molecule and the energy transitions for Raman scattering are much larger than those for IR absorption.

The absolute energy of Raman scattering is in the UV-Vis range, but it is customary to express the energy of the Raman signals relative to the Rayleigh one. In this way the Raman bands are characterized by a Raman shift that is given by the difference in wavelength between the Stokes (or anti-Stokes) line and the Rayleigh line. It follows that the Raman shifts belong to the infrared energy range.

In order to be Raman active a vibrational mode must include a nonzero rate change of the molecular polarizability. This aspect can be elucidated with a simple, yet classical, treatment of the radiation-molecule interaction [31]. The electric field of the laser beam can be described by Equation 2.27.

$$E = E_0 \cos(2\pi\nu_0 t) \quad 2.27$$

Here, E_0 and ν_0 are the amplitude and frequency of the laser, respectively. The oscillating electric field can induce a dipole moment, P , in the molecule given by Equation 2.28.

$$P = \alpha E = \alpha E_0 \cos(2\pi\nu_0 t) \quad 2.28$$

Here, α is the polarizability of the molecule which describes how easy it is for the electric field to deform the charge distribution of the molecule. For small vibrational amplitudes the polarizability is a linear function of the nuclear displacement coordinate, q , Equation 2.29.

$$\alpha = \alpha_0 + \left(\frac{\partial\alpha}{\partial q}\right)_0 q \quad 2.29$$

Here, α_0 is the polarizability at the equilibrium position, and $(\partial\alpha/\partial q)_0$ is the rate of change of α with respect to the change in nuclear displacement, q , evaluated at equilibrium. The nuclear displacement of a molecule vibrating at frequency ν_m is given by Equation 2.30.

$$q = q_0 \cos(2\pi\nu_m t) \quad 2.30$$

Here, q_0 is the vibrational amplitude. The substitution of Equation 2.30 in Equation 2.29 and the resulting α in Equation 2.28 gives Equation 2.31.

$$P = \alpha_0 E_0 \cos(2\pi\nu_0 t) + \left(\frac{\partial\alpha}{\partial q}\right)_0 q_0 E_0 \cos(2\pi\nu_0 t) \cos(2\pi\nu_m t) \quad 2.31$$

The application of the trigonometrical identity $\cos x \cdot \cos y = \frac{1}{2}[\cos(x - y) + \cos(x + y)]$ gives Equation 2.32.

$$P = \alpha_0 E_0 \cos(2\pi\nu_0 t) + \frac{1}{2} \left(\frac{\partial\alpha}{\partial q}\right)_0 q_0 E_0 \{ \cos[2\pi(\nu_0 - \nu_m) t] + \cos[2\pi(\nu_0 + \nu_m) t] \} \quad 2.32$$

Here, the first term is an oscillating dipole moment that emits radiation at the same frequency, ν_0 , of the incident beam corresponding to Rayleigh scattering, while the second term emits radiations at frequencies $(\nu_0 - \nu_m)$ and $(\nu_0 + \nu_m)$ corresponding to Raman scattering with the Stokes and anti-Stokes lines, respectively. This simple treatment confirms that in order to be Raman active the vibrational mode, ν_m , must have $(\partial\alpha/\partial q)_0 \neq 0$, *i.e.*, the rate change of the polarizability must be nonzero.

Two other important phenomena must be considered when interpreting a Raman spectrum, these are the resonance Raman scattering (RR) and the resonance

fluorescence (RF) (Figure 2.11). The RR occurs when the incident radiation brings the molecule to a virtual energy level of the excited electronic state. This phenomenon happens when the frequency of incident radiation is in the range of an electronic transition of the molecule. In this situation the Raman bands originating from this particular electronic transition are enhanced by a factor of 10^3 to 10^5 . The RF occurs when the molecule is excited exactly to a discrete level of the excited electronic state. It follows that the molecule decays via a radiationless transition and then emits radiation. This radiation can interfere with the Stokes bands, in such a case it is useful to examine the anti-Stokes emission.

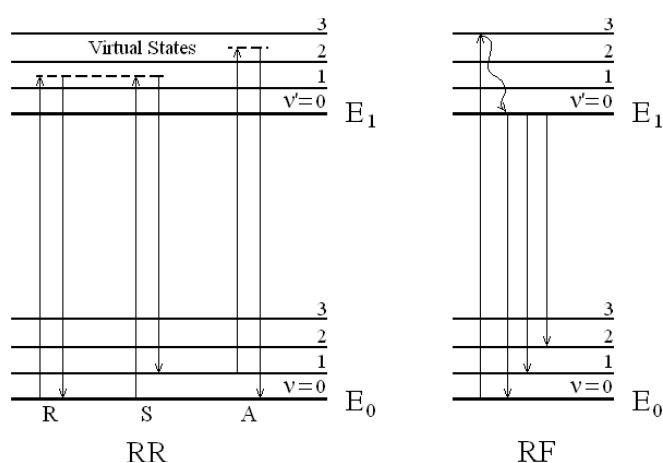


Figure 2.11 Resonance Raman (RR) scattering and Resonance Fluorescence (RF) energy transitions between two different molecular electronic levels, E_0 and E_1 . The RR transition corresponds to the absorption of the incoming radiation with energy higher than the first electronic excited state. The virtual states do not correspond to any vibrational energy level of the excited electronic state. The RF corresponds to the release of part of the absorbed energy via radiationless decay followed by emission of light. The life time of the RR excited state is very short (10^{-14} s), the one of the RF state is much longer ($10^{-8} - 10^{-5}$ s).

2.5.4.3 X-Ray Photoelectron Spectroscopy

X-ray photoelectron spectroscopy (XPS) is based on the analysis of the kinetic energy distribution of electrons photo-emitted from the surface of solids [34-36]. An X-ray beam (usually Al $K\alpha$) is radiated onto the sample. As a result, the core electrons of the atoms present on the surface are photoionized with the emission of low energy electrons. The energy balance of the overall process is shown in Figure 2.12. A photon of energy $h\nu$ causes the emission of a core electron with residual

kinetic energy of $E_K' = h\nu - E_b - \phi_s$, where E_b and ϕ_s are the two energy barriers that must be overcome in order to free the electron. E_b is the binding energy corresponding to the energy difference between the electronic core level and the Fermi level, while ϕ_s is the work function of the sample corresponding to the energy necessary to remove an electron from the Fermi level to the vacuum level of energy, E_V . After having left the sample, the electron enters the spectrometer that is purposely placed in electrical contact with the sample so that their Fermi levels coincide. An additional energy barrier has to be overcome, that is the difference in work functions between spectrometer and sample, $\phi_{spec} - \phi_s$. The kinetic energy detected by the spectrometer is then $E_K = E_K' - (\phi_{spec} - \phi_s)$ which gives $E_K = h\nu - E_b - \phi_{spec}$ by substituting the expression for E_K' . The binding energy, E_b , characteristic for each atom and its chemical surrounding can be computed as shown in Equation 2.33 [35].

$$E_b = h\nu - E_K - \phi_{spec} \quad 2.33$$

This equation states that the binding energy can be calculated from the energy of the incident beam, the work function of the spectrometer and by measuring the kinetic energy of the photoelectron.

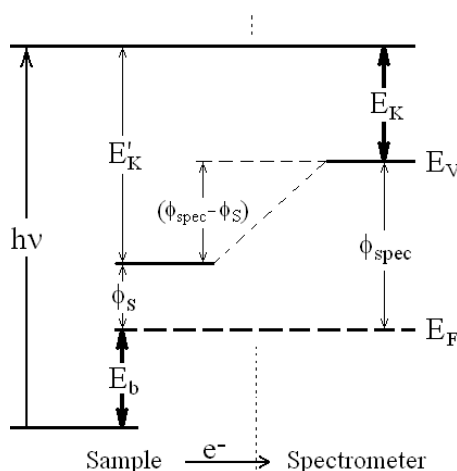


Figure 2.12 Energy level diagram for the XPS measurement of electron binding energies. A core electron is photo-excited by a photon of energy $h\nu$. The photoelectron travels towards the spectrometer where it is detected. The binding energy, E_b , of the photoelectron is calculated from its kinetic energy, E_K , at the spectrometer, as from Equation 2.33.

Auger electrons are also emitted together with the core electrons. The core orbital left empty after photoexcitation is filled with an electron from the outer orbitals, the energy released in this transition is absorbed by a third electron that is emitted as an Auger electron. The Auger electron has lower kinetic energy than the core electrons, and from Equation 2.33 it follows that its apparent ‘binding energy’ is higher than that of a core electron. This finding, however, is just an artifact due to the application of an equation that describes the photoemission of a core and not an Auger electron.

The thickness of the superficial layer probed by the X-ray beam is between 1 to 10 nm. In fact, the typical photoelectron energy range is 100 to 1500 eV corresponding to a mean free path of just 0.5 to 3.0 nm. It follows that among all photoexcited electrons, only those from the outermost 5 to 20 atomic layers can actually leave the sample. If I_z is the flux of photoelectrons generated at depth z , the flux I_d detected by the spectrometer is given by Equation 2.34 [34].

$$I_d(z) = I_z e^{-z/(\lambda \cos\theta)} \quad 2.34$$

Here, $z/\cos\theta$ is the distance covered by the electron in the solid before leaving the sample, and θ is the angle of emission. The parameter λ is the electron attenuation length and it follows that only about 35 % of the photoelectrons generated at the depth of 1λ is detectable, 15 % at 2λ , 5 % at 3λ and 0.5 % at 5λ . In XPS, the value of λ goes from 0.5 to 2.0 nm, hence the deepest detectable point is around 10 nm at normal electron emission, $\cos\theta = 1$. However, it must be stressed that the analysis is strongly biased by the signal coming from the outer layers of the sample.

The binding energy of the electrons is distinctive of the electronic structure of the atoms, therefore the energy position of the XPS peaks can be unambiguously associated to the different chemical elements (with the exception of hydrogen and helium). Besides allowing the qualitative identification of the elements, the binding energy is sensitive to the chemical environment of the photo-excited site. Although the core electrons are not directly involved in the formation of chemical bonds, any alteration of the valence electrons distribution is reflected on the core electron binding energies. In particular, the oxidation state of the elements is responsible for well known and characterized chemical shifts of the XPS peaks. Other known features of the XPS signals are the presence of satellite shake-up and

shake-off peaks. The shake-up effect occurs during the emission of the photoelectron when a portion of its kinetic energy is used to excite the valence electrons to higher energy levels. This reduces the kinetic energy of the photoelectron with the generation of satellite peaks shifted to higher binding energy compared to the parent peak. The extent of the shift is discrete and equivalent to the quantized electron transition. The shake-off effect, instead, corresponds to the transfer of more energy to the valence electrons with consequent ionization of the atom. The resulting satellites are also shifted to higher binding energy, but are less intense and distributed over a wide range of energy. As a result, they appear as a broad feature merged with the background.

The quantitative analysis of the surface is possible when the atoms are homogeneously distributed with depth. The intensity, I , of the photo-emission of a specified atom is related to its concentration C , defined as the number of such atoms in the volume of analysis, and by the atomic sensitivity factor S , where $I = C \times S$. The relative amount of a generic atom, j , in a surface made of N components is then given by $c_j = C_j / \sum C_i = (I_j / S_j) / \sum (I_i / S_i)$.

2.5.4.4 X-Ray Diffraction

X-ray diffraction (XRD) is based on the interaction between X-ray radiation and the atoms or molecules of a crystalline material [37]. The incident beam is scattered in all directions by the atoms of the crystal which act as X-ray emitters. A diffracted beam can be considered as composed of a large number of scattered rays which interact constructively with one another. In the classical description of X-ray interaction, a crystalline structure is considered as made of a series of crystallographic planes containing co-planar atoms (Figure 2.13). The incident beam hits the planes at an angle, θ , to be then scattered away along a specular direction. The superposition of two diffracted rays is dependent on their path difference which is given by the length of the segments $AB + BC = 2d\sin\theta$. The two rays reinforce one another when the path difference is a multiple integer, n , of the wavelength, λ , of the incident beam, *i.e.*, when the rays emerge from the crystal in phase. In such a case one can write the Bragg's law which is given in Equation 2.35.

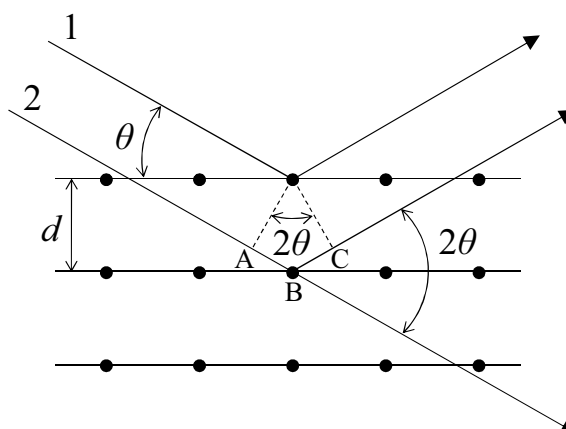


Figure 2.13 Schematic representation of the interaction of an X-ray beam with a crystal. Two rays, 1 and 2, are scattered by the atoms of two adjacent crystallographic planes at distance d . The grazing angle of the incident beam on the planes is indicated as θ , the angle between incident and diffracted beams is 2θ . The path difference between the two rays is given by the lengths of the segments AB and BC.

$$n\lambda = 2d\sin\theta$$

2.35

For a fixed radiation, $\lambda = \text{const}$, the scattered X-rays interact constructively along specific directions corresponding to characteristic diffraction angles. These angles are usually indicated as 2θ in relation to the angle between the incident and diffracted beams (Figure 2.13). The values of 2θ are directly related to the interplanar distance, d -spacing, of the planes inside the crystal. In this way, an X-ray spectrum can be recorded as a function of 2θ , where the peak positions are related to the crystalline structure, *i.e.*, d -spacing, of the sample. In the case of a mixture of crystalline materials, the resulting diffractogram is given by the addition of their individual spectra.

An X-ray diffractometer is composed of various parts which are the X-ray source, the beam optics, necessary to collimate the rays before and after the sample, the sample holder and the X-ray detector. Another fundamental part of the instrument is the goniometer which functions to hold and move the source, optics and detector in order to scan the diffraction angle. The diffractometer used in the present work is a $\theta:\theta$ instrument, *i.e.*, the source and detector are both rotated towards each other, while the sample is kept fixed, in order to scan an overall angle of 2θ .

2.6 References

- [1] Holzhauser P, Bouzek K; *Journal of Applied Electrochemistry*, **2006**, 36(6), 703
- [2] Beilby AL, Sasaki TA, Stern HM; *Analytical Chemistry*, **1995**, 67(5), 976
- [3] Nagaoka T, Yoshino T; *Analytical Chemistry*, **1986**, 58(6), 1037
- [4] Engstrom RC; *Analytical Chemistry*, **1982**, 54(13), 2310
- [5] Bard AJ, Faulkner LR; *Electrochemical Methods: Fundamentals and Applications*; 2000, 2nd ed., Wiley
- [6] Zoski CG; *Handbook of Electrochemistry*; 2007, Elsevier Science
- [7] Paunovic M, Schlesinger M; *Fundamentals of Electrochemical Deposition*; 2006, 2nd ed., Wiley-Interscience
- [8] Schmelzer JWP; *Nucleation Theory and Applications*, 2005, 1st ed., Wiley-VCH
- [9] Paunovic M; *Electrochemical Deposition*, Encyclopedia of Electrochemistry, Volume 5, 2007, Wiley-VCH
- [10] Scharifker B, Hills G; *Electrochimica Acta*, **1983**, 28(7), 879
- [11] Brett CMA, Brett AMO; *Electrochemistry: Principles, Methods, and Applications*; 1993, Oxford University Press
- [12] Bernd S; *Linear Sweep and Cyclic Voltammetry*, Encyclopedia of Electrochemistry: Inorganic Electrochemistry, Volume 3, 2003, Wiley-VCH
- [13] Mount AR; *Hydrodynamic Electrodes*, Encyclopedia of Electrochemistry: Inorganic Electrochemistry, Volume 3, 2003, Wiley-VCH
- [14] Buttry DA, Ward MD; *Chemical Reviews*, **1992**, 92(6), 1355
- [15] Hillman AR; *The Electrochemical Quartz Crystal Microbalance*, Encyclopedia of Electrochemistry: Inorganic Electrochemistry, Volume 3, 2003, Wiley-VCH
- [16] Barsoukov E, Macdonald JR; *Impedance Spectroscopy: Theory, Experiment, and Applications*; 2005, Wiley
- [17] Krause S; *Impedance Methods*, Encyclopedia of Electrochemistry: Inorganic Electrochemistry, Volume 3, 2003, Wiley-VCH
- [18] Varma R, Selman JR; *Techniques for Characterization of Electrodes and Electrochemical Processes*; 1991, Wiley
- [19] Evennett PJ, C H; *Microscopy Overview*, Encyclopedia of Analytical Science, 2005, Elsevier
- [20] Perez-Arantequi J, Mulvey T; *Electron Microscopy*, Encyclopedia of Analytical Science, 2005, Elsevier
- [21] Szykowska MI; *Scanning Electron Microscopy*, Encyclopedia of Analytical Science, 2005, Elsevier
- [22] Zhou W, Wang ZL; *Scanning Microscopy for Nanotechnology: Techniques and Applications*; 2006, 1st ed., Springer
- [23] Deslattes RD, Kessler Jr. EG, Indelicato P, de Billy L, E. L, Anton J, Coursey JS, Schwab DJ, Chang J, Sukumar R, Olsen K, Dragoset RA NIST X-Ray Transition Energies. <http://www.nist.gov/physlab/data/xraytrans/index.cfm> (April 2010)

-
- [24] Goldstein J, Newbury DE, Joy DC, Lyman CE, Echlin P, Lifshin E, Sawyer L, Michael JR; *Scanning Electron Microscopy and X-ray Microanalysis*; 2003, 3rd ed., Springer
- [25] Kanani N; *Electroplating: Basic Principles, Processes and Practice*; 2005, Elsevier Science
- [26] McKelvy ML; *Infrared Spectroscopy: Introduction*, Encyclopedia of Analytical Chemistry: Applications, Theory, and Instrumentation, 2001, Wiley
- [27] Colthup NB; *Infrared Spectroscopy*, Encyclopedia of Physical Science and Technology - Analytical Chemistry, 2001, Elsevier
- [28] Griffiths PR, De Haseth JA; *Fourier Transform Infrared Spectrometry*; 2007, 2nd ed., Wiley Interscience
- [29] Fringeli UP; *ATR and Reflectance IR Spectroscopy, Applications*, Encyclopedia of Spectroscopy and Spectrometry, 2000, Academic Press
- [30] Coates J; *Interpretation of Infrared Spectra, A Practical Approach*, Encyclopedia of Analytical Chemistry: Applications, Theory, and Instrumentation, 2001, Wiley
- [31] Van Duyne RP, Haynes CL; *Raman Spectroscopy*, Encyclopedia of Physical Science and Technology - Analytical Chemistry, 2001, Elsevier
- [32] Ferraro JR, Nakamoto K, Brown CW; *Introductory Raman Spectroscopy*; 2003, Elsevier
- [33] Smith E, Dent G; *Modern Raman Spectroscopy: A Practical Approach*; 2005, Wiley
- [34] Tougaard S; *X-Ray Photoelectron Spectroscopy*, Encyclopedia of Analytical Science, 2005, Elsevier
- [35] Chusuei CC, Goodman DW; *X-Ray Photoelectron Spectroscopy*, Encyclopedia of Physical Science and Technology - Analytical Chemistry, 2001, Elsevier
- [36] Turner NH; *X-ray Photoelectron and Auger Electron Spectroscopy*, Encyclopedia of Analytical Chemistry, 2000, Wiley
- [37] Cullity BD; *Elements of X-ray diffraction*; 1978, 2nd ed., Addison-Wesley Publishing Company

Chapter 3

Electrochemical Deposition of Hierarchical Micro/Nanostructures of Copper-Hydroxysulfates at Polypyrrole-Polystyrene Sulfonate Films

3. Electrochemical Deposition of Hierarchical Micro/Nanostructures of Copper Hydroxysulfates at Polypyrrole-Polystyrene Sulfonate Films

3.1 Introduction

Hierarchy in materials is related to the presence of structural elements organized at different scales [1]. This is the case of the copper hydroxysulfate structures presented in this chapter, where clusters made of sheets can be further broken down into wires and particles, as shown in Figure 3.1.

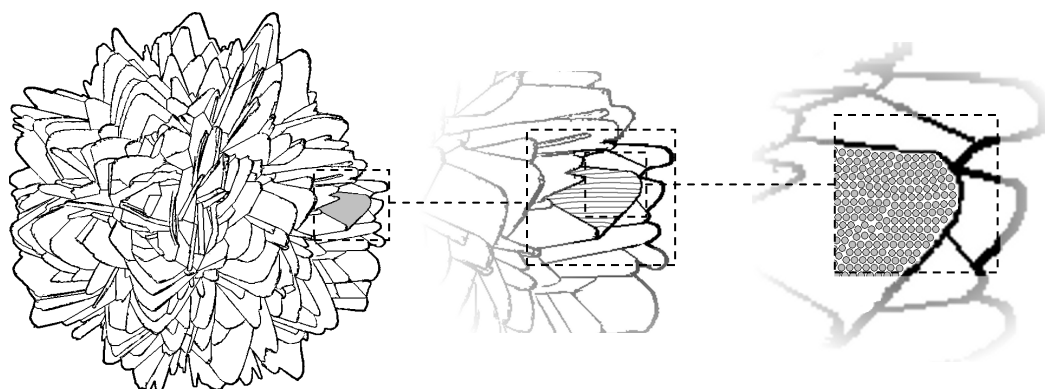


Figure 3.1 Hierarchical organization of the different elements present in the copper-based micro/nanostructures. A microcluster is broken down into its composing elements, namely, nanothin sheets, nanowires and nanoparticles. The actual micrographs of the structural elements are described in Section 3.2.3.1, Figure 3.33.

The majority of the hierarchical copper structures are made of copper oxides [2-4], copper sulfides [5-7], or their mixtures [8]. These materials can be used in several applications, such as supercapacitors [9], gas sensors [10], for the removal of pollutants [11], for the preparation of super-hydrophobic surfaces [4, 8, 12], and anodes for lithium-ion batteries [13]. Other hierarchical materials are obtained from the basic salts of copper, for example from copper hydroxyphosphates [14], copper hydroxycarbonates [15], or copper hydroxysulfates [16]. The development of

suitable applications for these materials has received limited consideration until recently, when industrial applications were considered for layered hydroxide salts [17]. Generally, all these materials are prepared through hydrothermal treatments in the presence of a base.

The hierarchical copper-based micro/nanostructures, discussed in this chapter, are prepared electrochemically on the surface of polypyrrole (PPy) thin films (Section 3.2.1). It is important to highlight that these materials have never been prepared electrochemically on conducting polymers before. The resulting structures are composed of copper hydroxysulfates, as shown by the electrochemical and spectroscopic characterizations (Section 3.2.2). The mechanism of nucleation and growth of the micro/nanostructures is also examined (Section 3.2.3) disclosing some interesting aspects on the progressive formation of the nanostructures at the film surface. Furthermore, the oxygen reduction reaction, which takes place during the electrochemical deposition of the structures, is also considered and characterized (Section 3.2.4).

The electrochemical deposition of the copper-based micro/nanostructure is performed at the surface of polypyrrole-polystyrene sulfonate (PPy-PSS) thin films. The electrochemistry of the film is a key factor in the overall deposition of the micro/nanostructures. These PPy-PSS films enable the capture of copper ions from the electrodeposition solution, and facilitate the reduction of dissolved oxygen to hydroxide ions. This is essential for the electrocrystallization of the copper hydroxysulfates. The properties of the PPy films are well documented in the literature [18-22] as such polymers have already been studied in detail. However, the exploitation of the PPy-PSS film properties for the controlled electroprecipitation of hierarchical micro/nanostructures is novel and has not been published to date. The characterization of the chemical composition and structure of the micro/nanostructures and the detailed examination of their mechanism of nucleation and growth are also two other important aspects of the present work.

This chapter is introductory to Chapter 4 where the same structures are further transformed into hybrid microstructures and eventually converted to metallic copper nanoparticles, which are then tested for nitrate sensing applications.

3.2 Results and Discussion

3.2.1 Electrodeposition of Hierarchical Copper-Based Micro/Nanostructures

3.2.1.1 PPy-PSS Electrochemical Polymerization and Properties

The electrodeposition of the hierarchical copper-based micro/nanostructures was performed on PPy-PSS thin films. These films were electropolymerized at a constant potential, as described in Section 2.4.1. The electropolymerization of pyrrole (Py) is fast and highly reproducible, as shown from the five traces presented in Figure 3.2. The 120 nm thin films are formed in less than 60 s. The film thickness is estimated as described in Section 2.4.1.1. The current profiles, depicted in Figure 3.2, are typical of pyrrole electropolymerization with both an increase and a plateau of current due to the polymer nucleation and film growth, respectively [23, 24]. The charge-time plots, shown in the inset, indicate a linear relationship between the charge and the electropolymerization period, from about 15 to 60 s. The lower rate of electropolymerization, evident during the first 15 s, corresponds to the nucleation of the film on the electrode substrate.

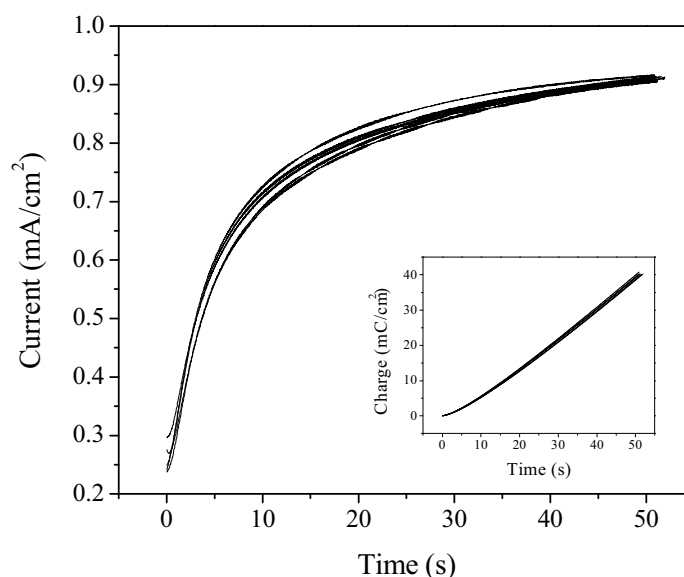


Figure 3.2 Potentiostatic current-time and charge-time plots for the electropolymerization of Py in 0.15 M Py and 50 mM PSS aqueous solution at 0.60 V vs. SCE on an AT-cut quartz crystal gold electrode to an overall charge of 40 mC/cm². The superimposition of the five different curves demonstrates the reproducibility of the electropolymerization reaction.

The corresponding mass-charge plot is given in Figure 3.3. There is a linear increase in mass with charge, once the charge exceeds 5 mC/cm². The doping level, p , of the polymer (Section 1.4.2.1, Figure 1.16) can be estimated with Equation 3.1 from the average slope of these mass-charge curves, which was computed as $R = 0.525$ mg/C.

$$R = \frac{m}{Q} = \frac{M(-Py-) + p M(-SS-)}{(n + p)F} \quad 3.1$$

This equation is derived from Equation 2.8 (Section 2.5.2.4) for the specific case of PPy-PSS films. $M(-Py-)$ and $M(-SS-)$ are the formula weights of the polypyrrole and polystyrene sulfonate repeating units, 65.07 g/mol and 181.18 g/mol, respectively, and the number of electrons, $n = 2$. The value of p was calculated as 0.28. This value is in agreement with the doping levels reported in the literature [25].

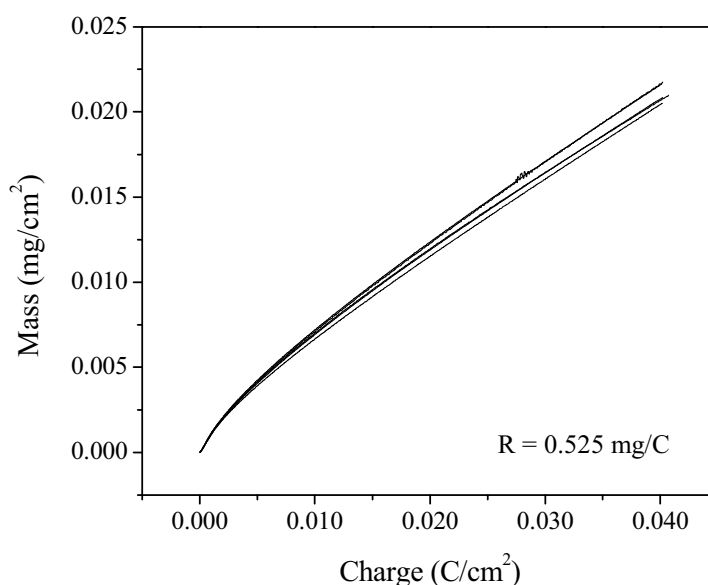


Figure 3.3 Mass-charge curves recorded under the conditions described in Figure 3.2.

The ion exchange properties of the PPy-PSS films were compared to those of polypyrrole doped with chloride anions, PPy-Cl. The cyclic voltammograms and the corresponding mass-potential plots of the two polymers, cycled in Na₂SO₄ and KCl, respectively, are shown in Figure 3.4. The voltammogram of the PPy-PSS film shows the presence of two peaks, corresponding to a *quasi*-reversible redox process

centered at around -0.40 V vs. SCE. A simultaneous change in mass is recorded and this is related to the gain and loss of cations as the PPy-PSS films are cycled between the redox states.

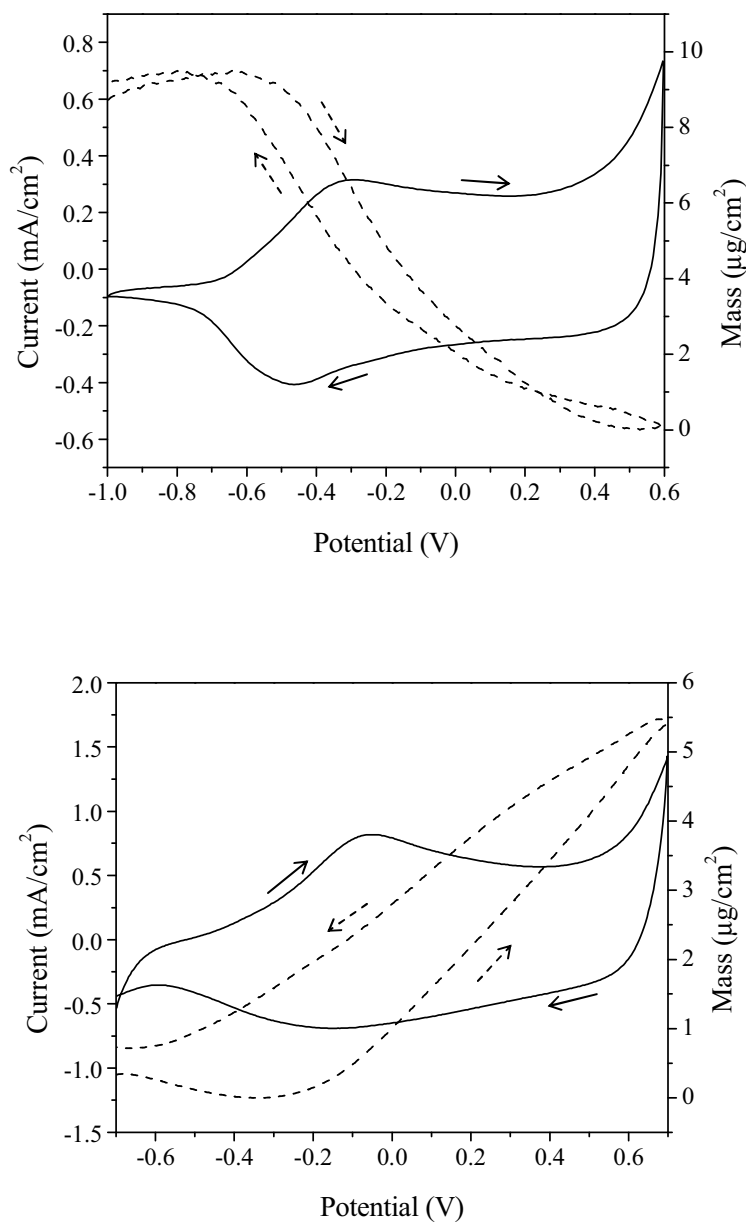


Figure 3.4 Cyclic voltammetric (current —) and gravimetric (mass ---) responses of PPy-PSS cycled in 0.10 M Na₂SO₄ at 50 mV/s (top) and PPy-Cl cycled in 0.10 M KCl at 25 mV/s (bottom). The PPy-PSS was formed in 0.15 M Py and 50 mM PSS solution at 0.60 V vs. SCE on an AT-cut quartz crystal gold electrode to a charge of 40 mC/cm². The PPy-Cl was formed in 0.15 M Py and 0.10 M KCl solution under identical conditions of potential and working electrode to a charge of 50 mC/cm².

On reduction of the PPy-PSS film in a solution of Na_2SO_4 , there is an increase in mass. This is consistent with the ingress of Na^+ from the electrolyte solution. During reduction, PPy^+ is converted to PPy^0 . In order to maintain electroneutrality, either the anionic dopant species are expelled or cationic species are incorporated from the solution. Alternatively, a combination of both phenomena can occur. In this case, the PSS^- anions are too large and bulky to be expelled and the film behaves as a cation exchanger, with the ingress of Na^+ cations. Upon oxidation, the film is oxidized to PPy^+ , consequently the Na^+ ions are expelled from the film to maintain charge balance. As a result the oxidized PPy^+PSS^- film is formed, as described in detail in Section 1.4.2.3. The mass is fully recovered during the positive and negative sweeps, indicating good stability during the steady-state switching between the oxidized and reduced states.

The response of the PPy-Cl film is very different. The voltammogram is characterized by a peak couple centered at about -0.10 V vs. SCE. The reduction wave is much broader than that of PPy-PSS, indicating a slower reduction process. The mass change in this case is reversed to that of PPy-PSS. Chloride ions, Cl^- , are incorporated into the film during oxidation in order to balance the positive charge of the polymer, PPy^+ , while they are expelled during reduction. Hence, in this case, the polymer acts as an anion exchanger.

In both polymer systems, the voltammetric current is low on the left-hand side of the redox peaks, *i.e.*, at potentials below -0.60 V vs. SCE, whereas it is much larger on the right-hand side, at potentials above 0.00 V vs. SCE. This difference in the magnitude of the current between reduced and oxidized states is due to the fact that PPy^0 is an insulator, while PPy^+ is a good conductor (Section 1.4.2.2). These features are all in good agreement with the results reported in the literature [22, 25, 26].

3.2.1.2 Electrochemical Deposition of Hierarchical Copper-Based Micro/Nano-structures

The cation exchange properties of the PPy-PSS films can be used to capture Cu^{2+} ions from aqueous copper solutions. In order to determine the potential at which the Cu^{2+} cations are captured, the mass of the polymer was monitored as a function of the applied potential. A potential sweep from 0.60 to 0.10 V vs. SCE was applied to

a PPy-PSS thin film immersed in a 0.10 M CuSO₄ solution and the change in mass of the film was measured. For comparative purposes, similar experiments were performed with PPy-Cl and PPy-PSS films in KCl and NaPSS solutions, respectively. The results are shown in Figure 3.5.

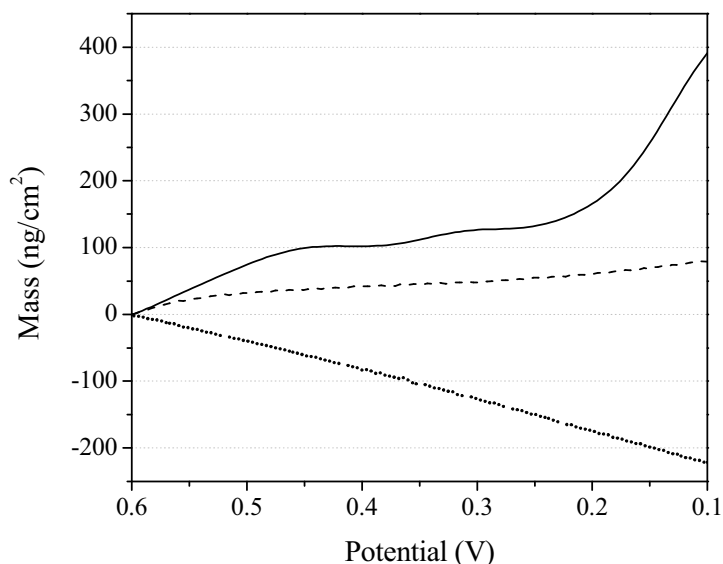


Figure 3.5 Mass changes recorded upon applying a reduction potential sweep from 0.60 to 0.10 V vs. SCE at a PPy-PSS film in 0.10 M CuSO₄ (—) and in 0.10 M NaPSS (- - -), or at a PPy-Cl film in 0.10 M KCl (· · · · ·). The films were 120 nm thick and deposited on an AT-cut quartz crystal gold electrode. The scan rates were 10 mV/s for PPy-PSS and 25 mV/s for PPy-Cl.

It is seen from Figure 3.5 that the mass of the PPy-PSS film increases steadily during the sweep demonstrating that Cu²⁺ ions are incorporated into the PPy-PSS film. An increase in mass is also observed when the same film is immersed in a 0.10 M NaPSS solution, confirming the capture of cations. In the latter case the mass increase is considerably lower because Na⁺ is lighter than Cu²⁺. When the same potential sweep is applied to a PPy-Cl film in a 0.10 M KCl solution, a mass decrease is observed, confirming the release of Cl⁻ anions. It is interesting to note that the mass changes for Na⁺ and Cl⁻ are linear as a function of potential, whereas for Cu²⁺ the mass increases more rapidly below 0.20 V vs. SCE. This potential is close to the standard reduction potential of the Cu²⁺/Cu system, $E_{\text{Cu(II)/Cu(0)}}^{\circ} = 0.099$ V vs. SCE. It follows that at potentials close to 0.10 V vs. SCE, there are two possible processes occurring at the PPy-PSS film surface which are the capture and

reduction of Cu^{2+} ions. The reduction of copper is pH dependent and copper metal is one of the possible reduction products (Section 1.5.1.2). The effect of the deposition potential is addressed in Chapter 4.

The reduction of Cu^{2+} ions at PPy-PSS thin films was further examined by performing a very slow sweep of potential in 0.10 M CuSO_4 . The potential was scanned from 0.30 to -0.40 V vs. SCE at a scan rate of 0.1 mV/s. Also, for comparison, the same reduction sweep was carried out in 0.10 M ZnSO_4 (Figure 3.6). The wave corresponding to the reduction of Cu^{2+} ions to copper metal was recorded at potentials lower than 0.10 V vs. SCE, in agreement with the value of $E_{\text{Cu(II)/Cu(0)}}^0$. This is clearly evident in Figure 3.6, where a steep increasing current is registered at potentials below 0.10 V vs. SCE.

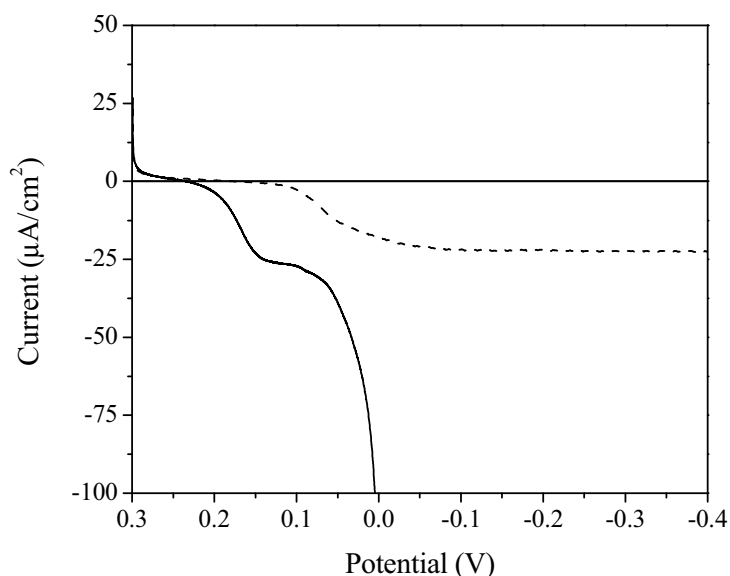


Figure 3.6 Current-potential plots recorded at PPy-PSS films in 0.10 M CuSO_4 (—) and in 0.10 M ZnSO_4 (---) upon applying a reduction potential sweep at 0.1 mV/s. The films were 120 nm thick and deposited on glassy carbon electrodes.

Furthermore, an additional reduction process is recorded between 0.20 and 0.10 V vs. SCE, just before the steep reduction wave. This process is characterized by a current plateau, about $-25 \mu\text{A}/\text{cm}^2$, which is very similar to the current obtained in ZnSO_4 . In the case of Zn^{2+} the standard reduction potential is much lower than that of copper, $E_{\text{Zn(II)/Zn(0)}}^0 = -1.003$ V vs. SCE (Section 1.5.2.2). For this reason the current plateau is related to a different process from the reduction of Zn^{2+} to zinc

metal. Accordingly, the current plateau in the case of the copper system is also related to another process that occurs in addition to the capture and reduction of the Cu^{2+} ions. It was found that this process is the reduction of dissolved oxygen, as discussed in Section 3.2.4. It follows that the PPy-PSS thin films can perform three simultaneous electrochemical processes in the considered range of potential, namely copper capture, copper reduction and oxygen reduction.

The electrochemical deposition of hierarchical copper-based micro/nanostructures was performed on PPy-PSS thin films in 0.10 M CuSO_4 aerated solutions at a constant potential of 0.10 V vs. SCE (Section 2.4.2.1). The electrochemical deposition of the copper-based structures was reproducible and took less than 30 min. Typical current-time and charge-time plots recorded under these conditions are shown in Figure 3.7. At 0.10 V vs. SCE the PPy-PSS films remain conducting, as evident from the cyclic voltammograms presented in Figure 3.4, and the reduction current is due to reduction processes at the PPy-PSS interface.

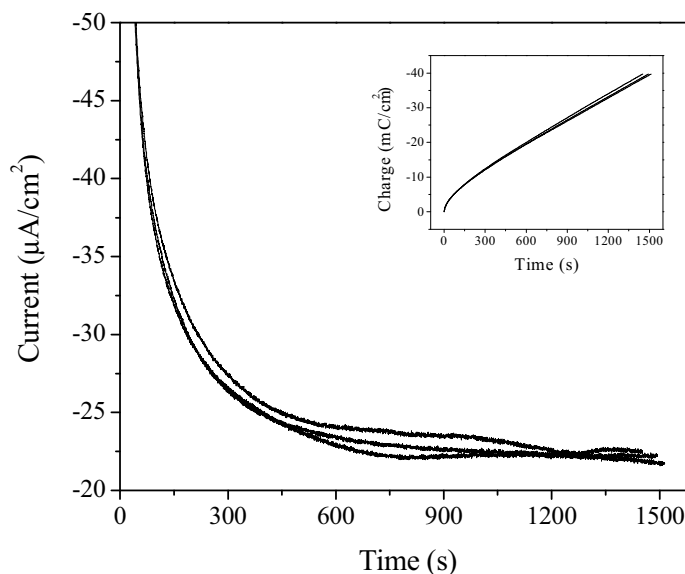


Figure 3.7 Current- and charge-time plots recorded during the deposition of hierarchical copper-based micro/nanostructures at PPy-PSS films in aerated 0.10 M CuSO_4 at 0.10 V vs. SCE. The films were 120 nm thick and deposited on glassy carbon electrodes.

After the first 10 min, the reduction current reaches and fluctuates in the range of -22 to $-24 \mu\text{A}/\text{cm}^2$. This suggests that sheet-like deposits grow and overlap with each other at different rates. In fact current fluctuations of this kind are typical of

multilayer nucleation taking overlap into account [27]. The copper-based structures formed on the PPy-PSS film surface are shown in Figure 3.8. These flower-like structures are made of a large number of nanosheets organized in hemispherical clusters. The thickness of the nanosheets ranges from 50 to 200 nm, while the overall size of the clusters is about 10 μm . The building blocks of these micro/nanostructures are nanoparticles, which aggregate to form nanowires, nanosheets and microclusters, as described in detail in Section 3.2.3.1.

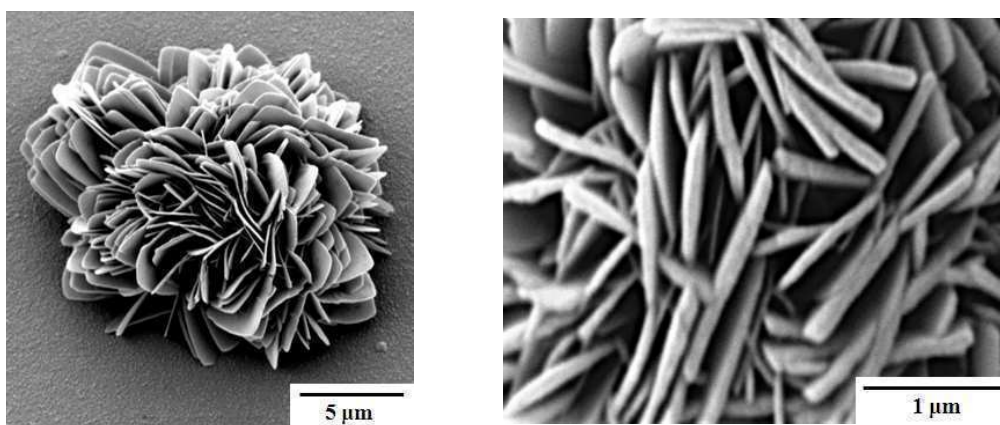


Figure 3.8 Hierarchical copper-based micro/nanostructure electrochemically deposited on PPy-PSS thin films (120 nm) from a 0.10 M CuSO_4 at the constant potential of 0.10 V vs. SCE. Overall structure (left) and close up of the nanosheets (right).

The structures presented in Figure 3.8 are truly novel. In fact, they are the first example of copper-based flower-like structures electrochemically deposited on conducting polymers. In addition, they are made of mixtures of copper hydroxide and sulfate (Section 3.2.2). The hierarchical copper structures known to date are prepared hydrothermally in alkaline solutions and are usually made of copper oxides (Section 1.6).

The presence of dissolved oxygen in the CuSO_4 solution is a necessary condition in order to form the copper-based structures. This is shown clearly from the data presented in Figure 3.9 where current-time and charge-time plots are compared in nitrogen and oxygen saturated solutions. In the absence of oxygen, the current drops immediately to very low values and no deposit is formed at the film even after 7000 s. On the other hand, in the oxygen saturated solution, the deposition current is much higher than that recorded in an aerated solution and hierarchical structures are

formed at a higher rate. The deposition in the presence of oxygen is approximately ten times faster, in comparison to the aerated solutions (Figures 3.7 and 3.9). It appears that dissolved oxygen is reduced at the PPy-PSS film to form hydroxide ions (Section 3.2.4). This causes an increase in the local pH at the PPy-PSS interface which facilitates the electrocrystallization of the hierarchical micro/nanostructures.

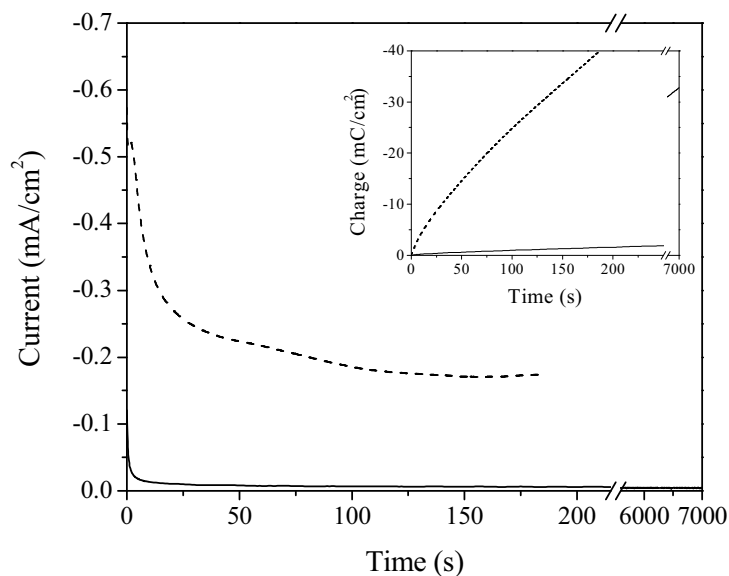


Figure 3.9 Current- and charge-time plots recorded at 0.10 V vs. SCE for the PPy-PSS films in nitrogen (—) and oxygen (---) saturated 0.10 M CuSO_4 solutions. The films were 120 nm thick on glassy carbon electrodes.

3.2.2 Characterization of Hierarchical Copper-Based Micro/Nanostructures

3.2.2.1 Cyclic Voltammetry

The copper-based micro/nanostructures were analyzed electrochemically using cyclic voltammetry, CV (Section 2.5.2.2). A PPy-PSS film modified with the copper-based structures was reduced at -1.00 V vs. SCE for 5 min in 0.10 M Na_2SO_4 prior to the analysis. A cyclic potential scan was then performed between -1.00 and 0.70 V vs. SCE in the same solution. This short pretreatment was used to reduce the background current of the PPy-PSS film. Representative data are shown in Figure 3.10. In the resulting voltammograms four peaks are evident and these are labeled as A, B, C and D (solid traces). The background electroactivity of the polymer was also

considered by running the same scan on a pristine PPy-PSS film (dashed trace). The redox couples A/D and B/C are attributed to Cu(0)/Cu(I) and Cu(I)/Cu(II) one-electron processes in accordance with the work carried out by Cioffi *et al.* [28]. In this work, copper nanoclusters mainly composed of Cu₂O were potentiostatically deposited on PPy-Cl thin films. The cyclic voltammogram of such clusters has numerous features that are also found in the voltammograms presented here.

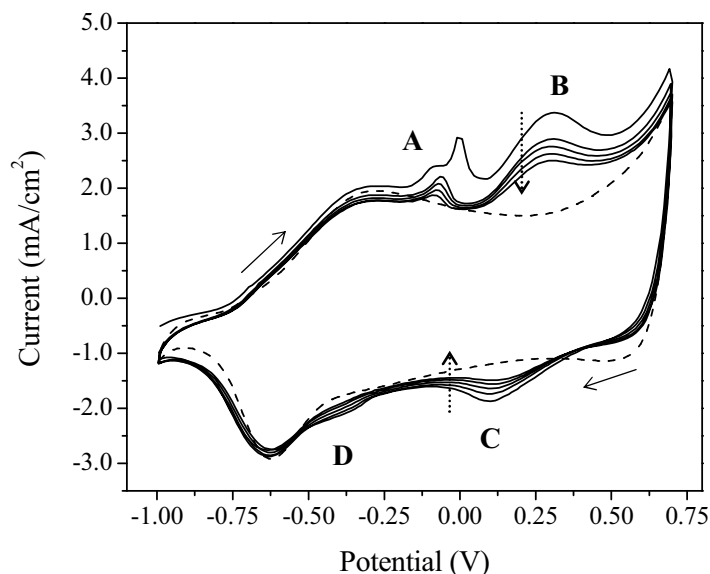


Figure 3.10 Cyclic voltammograms recorded at 100 mV/s in 0.10 M Na₂SO₄ for hierarchical copper-based micro/nanostructures prepared at PPy-PSS thin films (120 nm) deposited at a platinum electrode. The first five cycles of a copper modified film (—) are compared to those of a pristine film (---). The dotted arrows show the decrease in the peak current with increasing cycle number, while the solid arrows show the direction of the scan. The amount of charge consumed during the copper deposition was 23.9 mC/cm². The polymer film with the copper-based structures was reduced at -1.00 V vs. SCE for 5 min in 0.10 M Na₂SO₄ prior to the scan.

The peak potentials at about 0.10 V vs. SCE (peak C) and 0.30 V vs. SCE (peak B) of the couple B/C are in very good agreement with those reported by Cioffi *et al.* [28]. The potential of peak B is also in good agreement with that observed for the sweep dissolution of copper deposits formed potentiostatically at PPy-ClO₄ (perchlorate-doped polypyrrole) films [29]. In this work the formation of Cu⁺-PPy complexes was confirmed as well. The potential of peak A is slightly shifted (-100 mV vs. SCE) compared to that reported by Cioffi *et al.* [28], and peak D

appears also at more negative potentials. However, the position of this latter peak is dependent on the film thickness [28]. In general all peaks fade with increasing cycle number due to the progressive dissolution of the deposited copper.

Interestingly, the reduction currents of peak D are lower in magnitude compared to those of peak C, although it is difficult to compare them directly given the large background current from the PPy-PSS film. Peaks C and D are very different to the corresponding ones observed for pure copper, where the current arising from the conversion of Cu(I) to Cu(0) is considerably higher than the current for the conversion of Cu(II) to Cu(I) in alkaline media [30-33]. Of particular interest is the first cycle which is recorded after reduction at -1.00 V vs. SCE. In this case, peak A corresponds to the conversion of Cu(0) to Cu(I) and assuming that only the Cu(I) generated through this process is available for conversion to Cu(II), then the peak heights of A and B should be similar. The fact that this is not the case suggests that Cu(I) is already present and this now accounts for the higher peak currents recorded for peak B. During the reverse sweep, it appears that not all the Cu(I) generated at peak C is converted to Cu(0) at peak D. This gives rise to Cu(I) which is converted to Cu(II) during the subsequent forward cycle and is consistent with the higher peak currents observed for peak B during repetitive cycling. It is then reasonable to consider that part of the copper coming from the micro/nanostructures is in the Cu(I) state, which in turn is responsible for the higher redox activity at peaks B and C.

The relative amount of Cu(I) generated from the copper-based micro/nanostructures was estimated from the oxidation charge of peak B (Figure 3.11). The peak current from the second cycle was subtracted by the background current of the pristine film in order to obtain the net faradaic current for the conversion of Cu(I) to Cu(II). This current was then integrated to give the oxidation charge (inset of Figure 3.11). The charge underneath the peak is 4.3 mC/cm², corresponding to about 18 % of the charge consumed during the copper deposition (23.9 mC/cm²). By assuming a 100 % current efficiency for a two-electron deposition process, this leads to a Cu(I) fraction of 36 % of the total mass of deposited copper. It is important to note that this value was estimated after a reduction treatment (-1.00 V vs. SCE for 5 min), and this may influence the composition, favoring the lower oxidation states. Furthermore, the high background current from the PPy-PSS films makes the charge analysis more complicated.

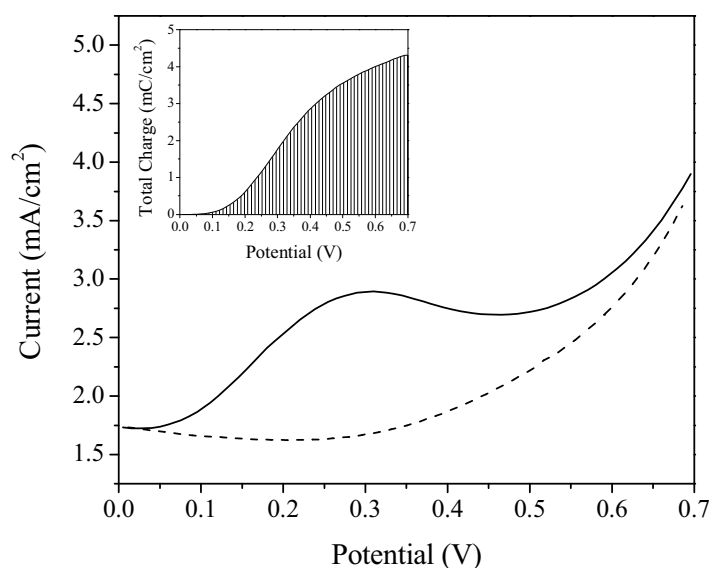


Figure 3.11 Current- and charge-potential plots for the oxidation of the Cu(I) present on the electrode with the hierarchical copper-based micro/nanostructures. The current of the copper modified film (—, peak B second cycle in Figure 3.10) was subtracted by the background current of the pristine film (---). The charge of the subtracted peak was 4.3 mC/cm^2 , in the inset. The experimental conditions are specified in Figure 3.10.

3.2.2.2 X-Ray Diffraction

The copper-based micro/nanostructures were characterized using X-ray diffraction, XRD (Section 2.5.4.4). In order to identify the crystalline components of the copper-based structures, the XRD spectra of the bare and copper-modified electrodes were analyzed and compared. The XRD spectrum of a glassy carbon (GC) bare electrode is shown in Figure 3.12. The two broad signals at about 20.0° and 44.0° are characteristic of the background trace of GC, as reported in the literature [34]. To facilitate the identification of the smaller peaks, the background trace was subtracted from the raw data to obtain the spectrum in Figure 3.13. The sharp peaks at 35.3° and 41.7° are due to the presence of Ag from the silver-loaded resin used to assemble the electrode (Section 2.2). These peaks appear down-shifted compared to those found in the literature at 38.1° and 44.3° for Ag [35], because the silver contact was placed about 5 mm below the surface of analysis (*i.e.*, the electrode surface). The origin of the other peaks is unknown, but they are likely to be related to the presence of crystalline fillers in the electrode mount made of rigid PVC.

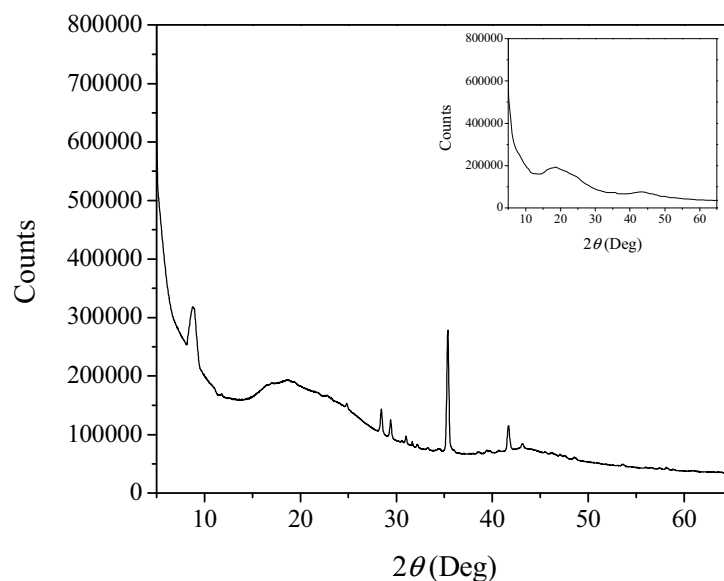


Figure 3.12 XRD spectrum of a bare glassy carbon flat electrode used for the electrodeposition of hierarchical copper-based micro/nanostructures. In the inset the background trace that was subtracted from the raw spectrum, in order to obtain the spectrum presented in Figure 3.13, is shown.

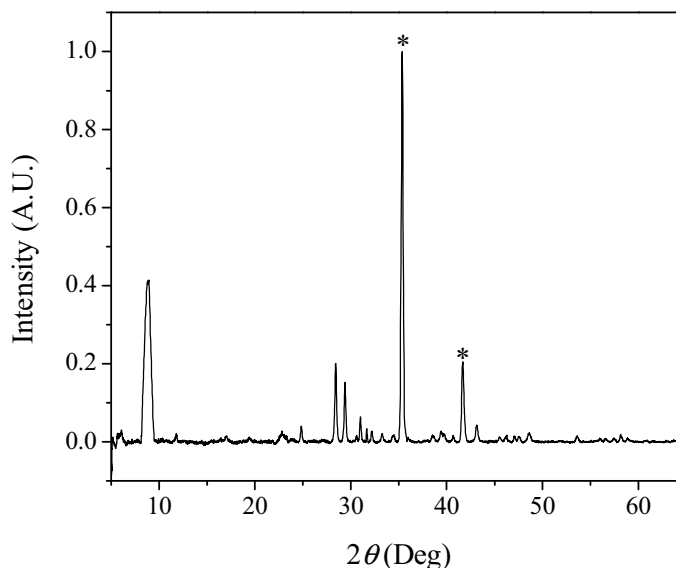


Figure 3.13 XRD spectrum of a bare glassy carbon flat electrode obtained from the subtraction of the raw spectrum and background trace given in Figure 3.12. The labeled peaks (*) were identified as silver metal due to the silver loaded-resin used for the electrical contact between glassy carbon rod and copper wire (Section 2.2).

It is known that nanothin films of PPy form ordered arrays of helical PPy-doped macromolecules organized in micro-islands [36, 37]. The XRD of PPy-Tos (Tosylate) film reported in the literature [38] shows the presence of one broad diffraction peak at about 25° . The actual position of the peak is dependent on the dopant. The XRD of the PPy-PSS film has not been reported. However, the small amount of polymer and the sub-micrometer size of the crystallites in the PPy-PSS film [36] should only give a weak broad peak. The XRD spectrum of the copper-based structures deposited on PPy-PSS is given in Figure 3.14. Clearly, the background trace is dominated by the two signals of GC [34]. The smaller and sharper peaks are enlarged in Figure 3.15, but again, the signal is dominated by the GC substrate. However, on subtracting the background trace several diffraction peaks are evident, as shown in Figure 3.16. This spectrum is compared to that obtained with the GC substrate in Figure 3.17. In the spectrum of the copper-based structures the Ag peaks of the substrate are absent. Also, the position and shape of the peak at 8.2° is different compared to the one at 8.9° of the substrate. However, the peaks at 28.4° and 29.4° correspond well in the two spectra.

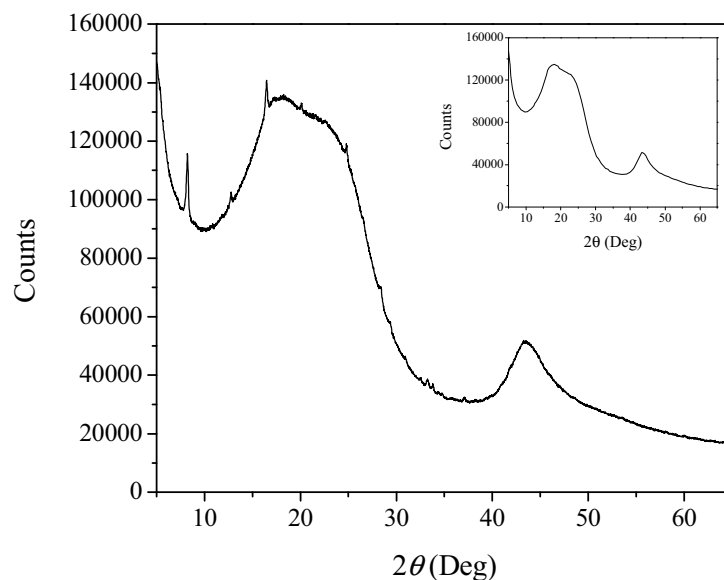


Figure 3.14 XRD spectrum of the hierarchical copper-based micro/nanostructures electrodeposited on 120 nm PPy-PSS film from oxygen saturated 0.10 M CuSO_4 solution at 0.10 V vs. SCE. The electrode material was glassy carbon and the copper was deposited to a charge of 0.2 C/cm^2 . In the inset, the background trace that was subtracted from the raw spectrum to obtain the spectrum shown in Figure 3.16.

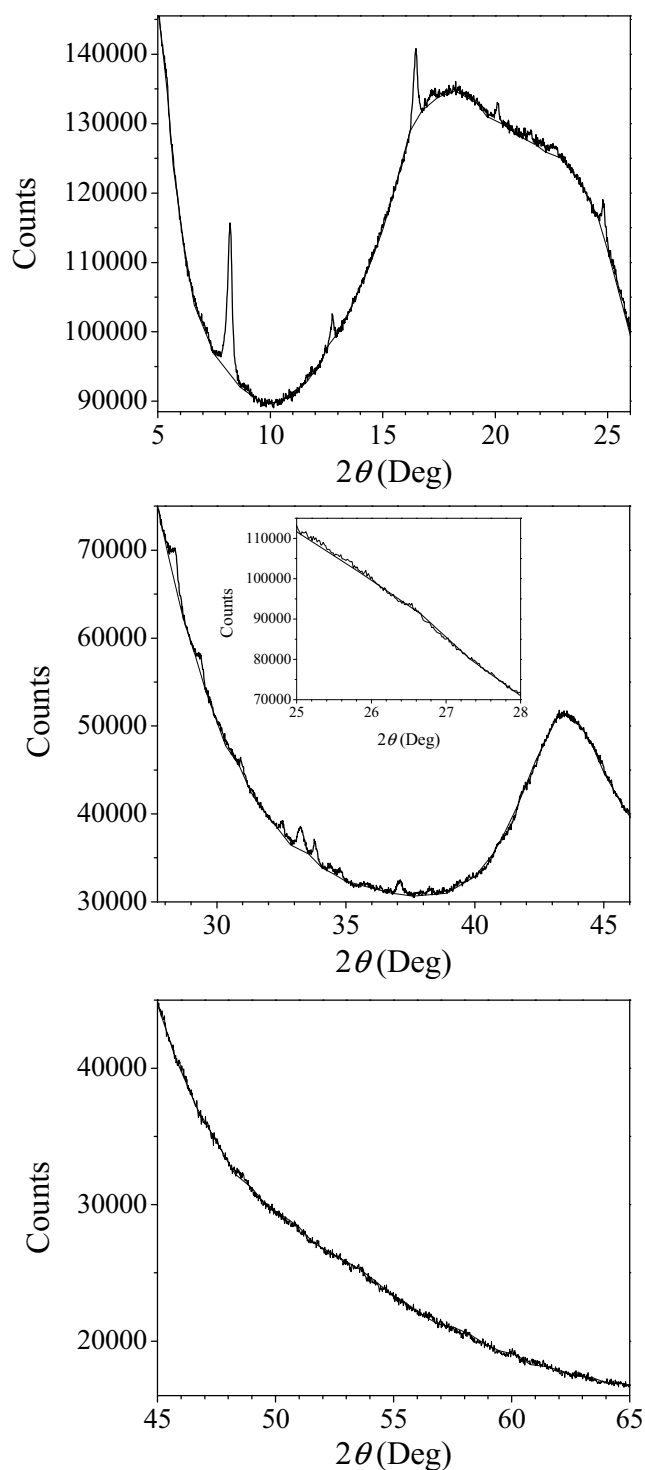


Figure 3.15 Enlargements of the XRD raw and background superimposed spectra of the hierarchical copper-based micro/nanostructures shown in Figure 3.14. Small diffraction peaks are visible in the portions of the raw spectrum emerging above the background trace. The subtraction of the background spectrum from the raw spectrum allows the clear identification of the diffraction peaks due to the copper-based micro/nanostructures, as shown in Figure 3.16.

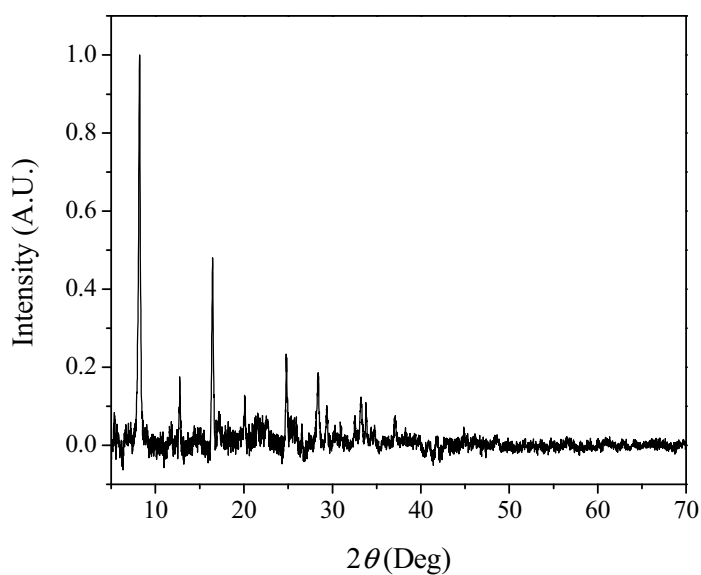


Figure 3.16 XRD spectrum of the hierarchical copper-based micro/nanostructures obtained from the subtraction of the background trace from the raw spectrum which are given in Figure 3.14.

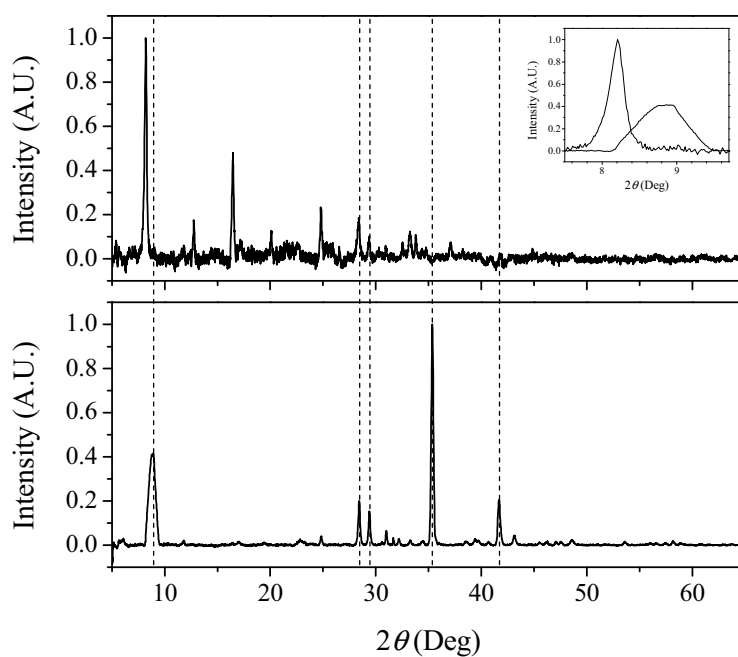


Figure 3.17 Comparison of the XRD spectra of hierarchical copper-based micro/nanostructures (top) and bare glassy carbon electrode (bottom). The inset shows the superimposition of the peaks of the two spectra in the low diffraction angle region, where the peak width and position are clearly different. The dashed lines indicate the position of the main peaks of the bare GC electrode.

The assignment of the XRD peaks of the hierarchical copper-based micro/nanostructures is reported in Figure 3.18 and Table 3.1. It is evident that the majority of the peaks is related to the presence of copper sulfate hydroxide hydrate, $[\text{CuSO}_4]_2[\text{Cu}(\text{OH})_2]_3 \cdot 5\text{H}_2\text{O}$ (ICDD PDF 00-041-0007).

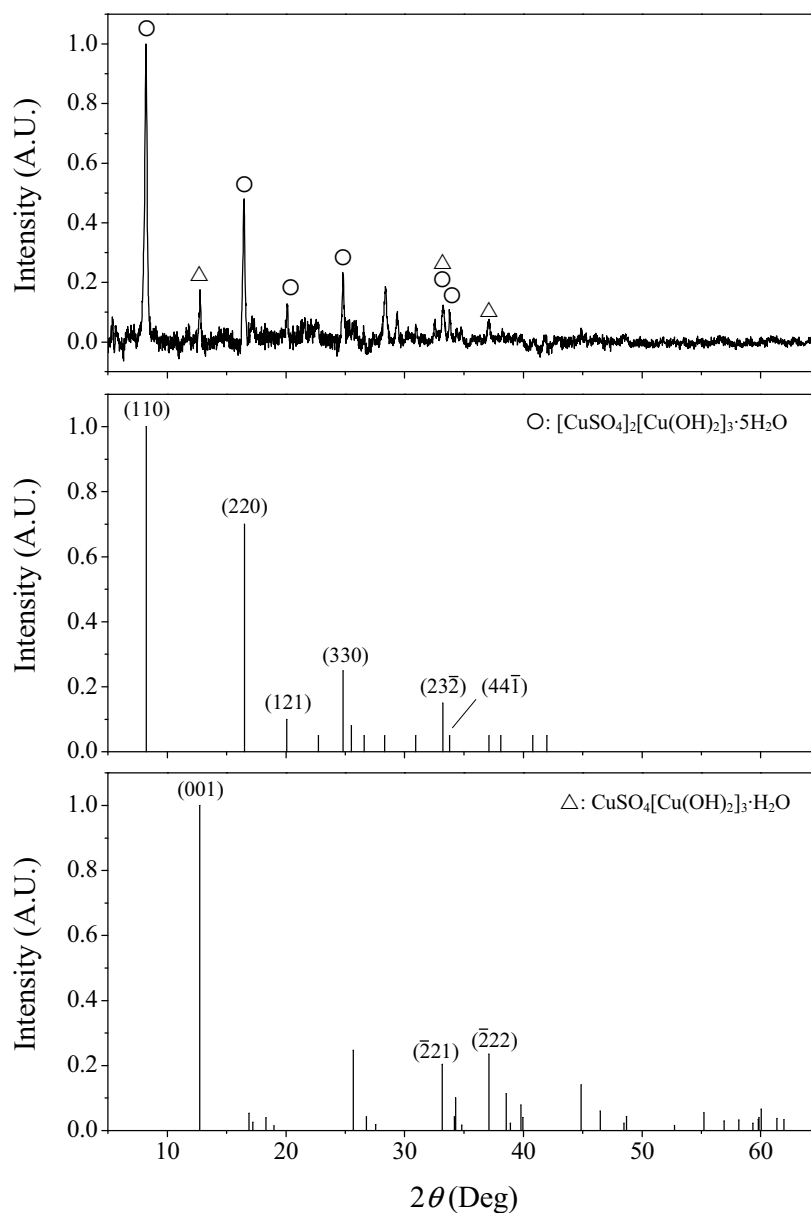


Figure 3.18 XRD peak assignment for the hierarchical copper-based micro/nanostructures prepared as described in Figure 3.14. The diffraction peaks were identified as those of copper sulfate hydroxide hydrate (O: $[\text{CuSO}_4]_2[\text{Cu}(\text{OH})_2]_3 \cdot 5\text{H}_2\text{O}$, ICDD PDF 00-041-0007) and posnjakite (Δ : $\text{CuSO}_4[\text{Cu}(\text{OH})_2]_3 \cdot \text{H}_2\text{O}$, ICDD PDF 043-670). The corresponding Miller indexes, (hkl) , are given for each of the assigned peaks. The experimental and reference peak positions and intensities are listed in Table 3.1.

Table 3.1 Comparison of the XRD peaks of experimental hierarchical copper-based micro/nanostructures and reference compounds: copper sulfate hydroxide hydrate, $[\text{CuSO}_4]_2[\text{Cu}(\text{OH})_2]_3 \cdot 5\text{H}_2\text{O}$, and posnjakite, $\text{CuSO}_4[\text{Cu}(\text{OH})_2]_3 \cdot \text{H}_2\text{O}$. The reference data are provided by the International Center of Diffraction Data (ICDD).

Experimental		References			
Position ($^{\circ}2\theta$)	Intensity (A.U.)	$[\text{CuSO}_4]_2[\text{Cu}(\text{OH})_2]_3 \cdot 5\text{H}_2\text{O}$		$\text{CuSO}_4[\text{Cu}(\text{OH})_2]_3 \cdot \text{H}_2\text{O}$	
		Position ($^{\circ}2\theta$)	Intensity (A.U.)	Position ($^{\circ}2\theta$)	Intensity (A.U.)
8.209	1.00	8.241	1.00	–	–
12.754	0.18	–	–	12.750	1.00
16.464	0.48	16.494	0.70	–	–
20.091	0.13	20.073	0.10	–	–
24.786	0.23	24.816	0.25	–	–
33.242	0.12	33.216	0.15	33.160	0.20
33.777	0.11	33.797	0.05	–	–
37.103	0.07	37.121	0.05	37.100	0.23

An additional crystalline phase is identified as posnjakite, $\text{CuSO}_4[\text{Cu}(\text{OH})_2]_3 \cdot \text{H}_2\text{O}$ (ICDD PDF 043-670). In this case the intensity of the peaks is lower meaning that this phase is present in minor quantity compared to the copper sulfate hydroxide hydrate (assuming that the two phases have similar relative intensity ratios). The identification of these two compounds is in agreement with the EQCM, XPS and ATR-IR characterizations as shown in Sections 3.2.2.3, 3.2.2.5 and 3.2.2.6, respectively.

3.2.2.3 Electrochemical Quartz Crystal Microbalance

The mass and charge of the hierarchical copper-based micro/nanostructures formed at PPy-PSS thin films were monitored using an electrochemical quartz crystal microbalance, EQCM (Section 2.5.2.4). The copper-based structures were deposited from oxygen-saturated 0.10 M CuSO_4 solutions. The resulting current-time and mass-charge responses are shown in Figure 3.19. The current-time profile is typical of the electrochemical growth of overlapping nuclei (Section 2.5.2.1, Figure 2.4); a detailed description of this profile is given in Section 3.2.3.2. The mass-charge curve is characterized by three individual segments, as shown more clearly in Figure 3.20.

A linear regression was performed on each segment in order to obtain the slopes of the mass-charge curve which absolute values correspond to the mass-to-charge ratios, R , of the deposited micro/nanostructures (Section 2.5.2.4, Equation 2.8). These experimental ratios were then compared to those calculated for the different copper species that could be deposited on the films. In this way some species could be excluded or included as possible deposited materials.

The segments A, B and C of the mass-charge curve are associated with three different stages of the copper-based micro/nanostructures deposition, namely nucleation, nuclei overlapping and multilayer growth, as described in detail in Section 3.2.3.2. As shown in Figure 3.20, the value of R changes during the deposition starting from 0.802 mg/C for the nucleation, 1.323 mg/C for the nuclei overlapping and finally 1.161 mg/C for the multilayer growth. These values of R are compared to the values calculated from a series of possible reduction reactions. The calculated R values are provided in Table 3.2.

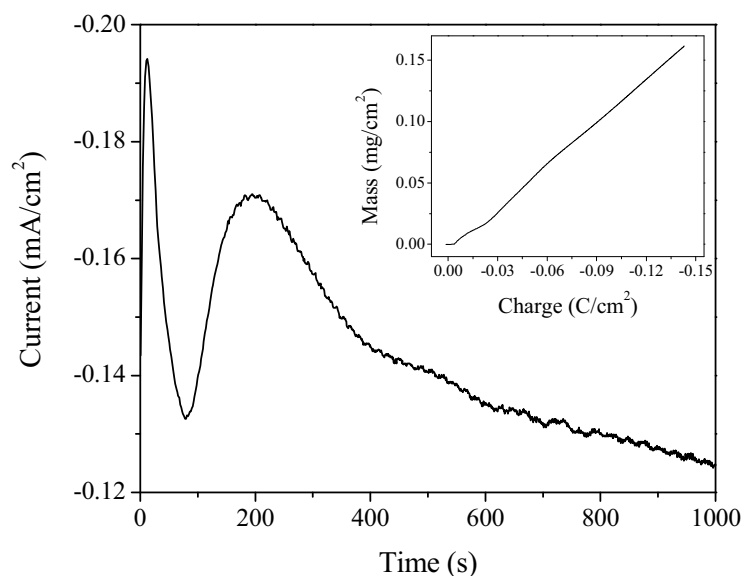


Figure 3.19 Current-time and mass-charge responses for the deposition of hierarchical copper-based micro/nanostructures at PPy-PSS films in oxygen saturated 0.10 M CuSO₄ solution at 0.10 V vs. SCE. The PPy-PSS film was 120 nm thick and deposited on an AT-cut quartz crystal gold electrode.

In Table 3.2, the values of R of several possible species that could be deposited on the PPy-PSS film are listed together with their corresponding products and formation reactions. Some sulfate species are included in the list because of the

results obtained from the spectroscopic characterization of the copper-based structures. Indeed, the presence of sulfate ions in the structures was confirmed using XPS and ATR-IR (Sections 3.2.2.5 and 3.2.2.6). The copper sulfate species considered in this discussion are those known from the literature [39, 40] such as antlerite $\text{CuSO}_4[\text{Cu}(\text{OH})_2]_2$, brochantite $\text{CuSO}_4[\text{Cu}(\text{OH})_2]_3$, posnjakite $\text{CuSO}_4[\text{Cu}(\text{OH})_2]_3 \cdot \text{H}_2\text{O}$, langite $\text{CuSO}_4[\text{Cu}(\text{OH})_2]_3 \cdot 2\text{H}_2\text{O}$, copper sulfate hydroxide hydrate $[\text{CuSO}_4]_2[\text{Cu}(\text{OH})_2]_3 \cdot 5\text{H}_2\text{O}$, and dolerophanite CuOCuSO_4 .

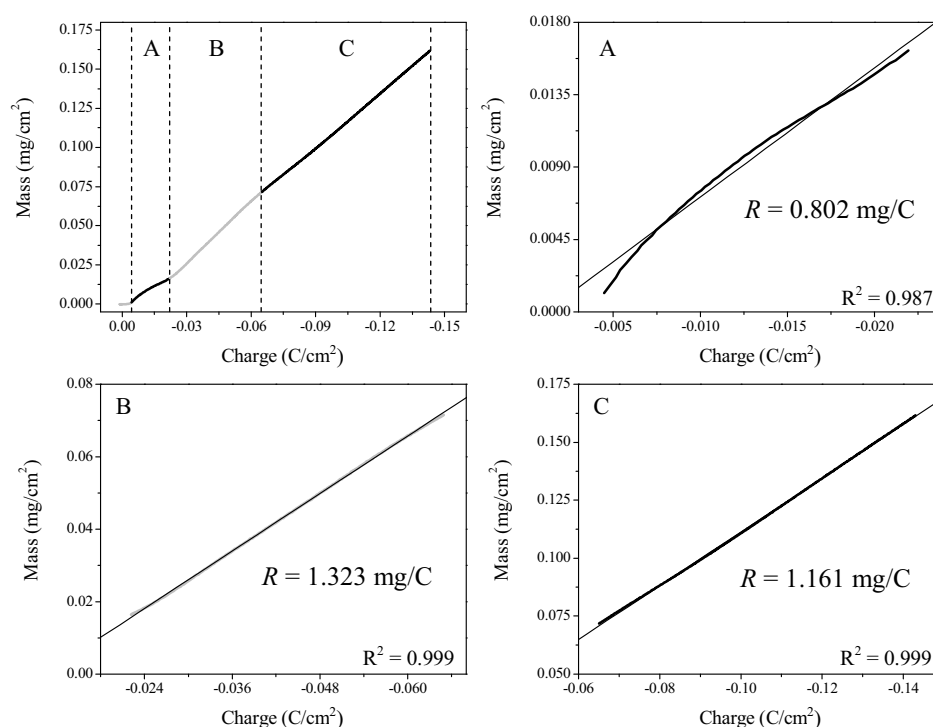


Figure 3.20 Linear regressions of the mass-charge curve for the deposition of hierarchical copper-based micro/nanostructures at PPy-PSS films in oxygen saturated 0.10 M CuSO_4 at 0.10 V vs. SCE. The three segments are labeled in the first plot (top-left), each segment is then individually interpolated in the corresponding plots A, B and C. The absolute values of the slope (*i.e.*, the mass-to-charge ratio R) and the correlation coefficient (R^2) of the regression lines are reported in each plot.

The initial information that can be drawn from the comparison of the experimental and tabulated values of R is that Cu, Cu_2O , CuO and $\text{Cu}(\text{OH})_2$ alone cannot be the composing materials of the copper-based micro/nanostructures. In fact the calculated R values for these reactions, Table 3.2, are much lower than the experimental values. In other words, these species are lighter than those actually deposited. In the case of

the nucleation stage, the slope of the mass-charge segment is 0.802 mg/C which is closely related to the deposition of hydrated forms of brochantite (e.g., posnjakite $\text{CuSO}_4[\text{Cu}(\text{OH})_2]_3 \cdot \text{H}_2\text{O}$ with 0.812 mg/C). However, this segment is not actually linear ($R^2 = 0.987$) suggesting the evolution of the deposition process towards a steady condition. Consequently, the slope of this segment is just an average of values of R that change rapidly during the nucleation (Section 3.2.3.2).

Table 3.2 Possible reactions and products for the electrochemical deposition of hierarchical copper-based micro/nanostructures with relative values of molar mass (M) and mass-to-charge ratio (R).

Electrodeposition reactions & products	M (g/mol)	R (mg/C)
$\text{Cu}^{2+} + 2 \text{e}^- \rightarrow \text{Cu}$	63.5	0.329
$2 \text{Cu}^{2+} + 0.5 \text{O}_2 + 4 \text{e}^- \rightarrow \text{Cu}_2\text{O}$	143.1	0.371
$\text{Cu}^{2+} + 0.5 \text{O}_2 + 2 \text{e}^- \rightarrow \text{CuO}$	79.5	0.412
$\text{Cu}^{2+} + 0.5 \text{O}_2 + \text{H}_2\text{O} + 2 \text{e}^- \rightarrow \text{Cu}(\text{OH})_2$	97.6	0.506
$3 \text{Cu}^{2+} + \text{O}_2 + 2 \text{H}_2\text{O} + \text{SO}_4^{2-} + 4 \text{e}^- \rightarrow \text{CuSO}_4[\text{Cu}(\text{OH})_2]_2$ Antlerite	354.7	0.919
$4 \text{Cu}^{2+} + 1.5 \text{O}_2 + 3 \text{H}_2\text{O} + \text{SO}_4^{2-} + 6 \text{e}^- \rightarrow \text{CuSO}_4[\text{Cu}(\text{OH})_2]_3$ Brochantite	452.3	0.781
$4 \text{Cu}^{2+} + 1.5 \text{O}_2 + 4 \text{H}_2\text{O} + \text{SO}_4^{2-} + 6 \text{e}^- \rightarrow \text{CuSO}_4[\text{Cu}(\text{OH})_2]_3 \cdot \text{H}_2\text{O}$ Posnjakite	470.3	0.812
$4 \text{Cu}^{2+} + 1.5 \text{O}_2 + 5 \text{H}_2\text{O} + \text{SO}_4^{2-} + 6 \text{e}^- \rightarrow \text{CuSO}_4[\text{Cu}(\text{OH})_2]_3 \cdot 2\text{H}_2\text{O}$ Langite	488.3	0.843
$5 \text{Cu}^{2+} + 1.5 \text{O}_2 + 8 \text{H}_2\text{O} + 2\text{SO}_4^{2-} + 6 \text{e}^- \rightarrow [\text{CuSO}_4]_2[\text{Cu}(\text{OH})_2]_3 \cdot 5\text{H}_2\text{O}$ Copper sulfate hydroxide hydrate	702.0	1.212
$2 \text{Cu}^{2+} + 0.5 \text{O}_2 + \text{SO}_4^{2-} + 2 \text{e}^- \rightarrow \text{CuOCuSO}_4$ Dolerophanite	239.1	1.239

The other two segments are effectively linear ($R^2 = 0.999$), and their slopes are representative of steady deposition processes. The mass-to-charge ratios for these segments are 1.323 mg/C and 1.161 mg/C. These values are closer to the R of dolerophanite, 1.239 mg/C, and copper sulfate hydroxide hydrate, 1.212 mg/C (Table 3.2). The formation of dolerophanite, CuOCuSO_4 , is excluded because it reacts rapidly with water to yield pseudomorphs of antlerite [41]. Instead, the formation of copper sulfate hydroxide hydrate, $[\text{CuSO}_4]_2[\text{Cu}(\text{OH})_2]_3 \cdot 5\text{H}_2\text{O}$, is in excellent agreement with the XRD characterization of the hierarchical structures (Section 3.2.2.2). In this characterization, it was shown that the structures are composed of a mixture of copper sulfate hydroxide hydrate and posnjakite. Also, the

partial formation of posnjakite phase, 0.812 mg/C, could explain an experimental value of R , 1.161 mg/C, slightly lower than that of a pure copper sulfate hydroxide hydrate phase, 1.212 mg/C. It follows that, in agreement with the XRD results, the EQCM characterization confirms the electrodeposition of a mixture of copper sulfate hydroxide hydrate and posnjakite.

3.2.2.4 Energy Dispersive X-Ray Analysis

The chemical composition of the hierarchical copper-based micro/nanostructures was analyzed using energy dispersive X-ray analysis, (EDX) (Section 2.5.3.1). The SEM (Scanning Electron Microscopy) micrograph and the corresponding EDX spectrum of the hierarchical structures are shown in Figure 3.21. The spectral peaks are identified as those of copper, oxygen and sulfur. The presence of sulfur and oxygen is in agreement with the results of XPS and ATR-IR (Sections 3.2.2.5 and 3.2.2.6). The fact that carbon, the main component of the electrode and polymer film materials, was not detected by the electron beam implies that the probing volume was contained in the hierarchical cluster and that the correspondent EDX spectrum is representative of the composition of the cluster. However, it should be noted that the signal from carbon is lower than the other elements, Cu, S and O, on account of its low atomic number.

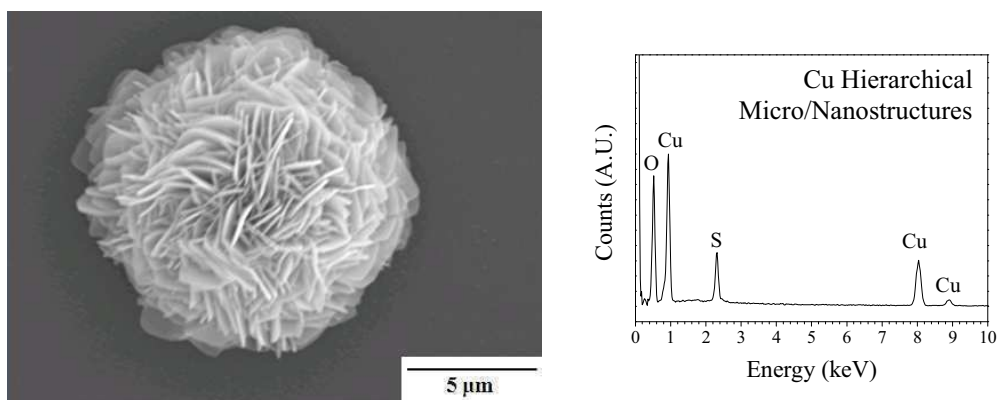


Figure 3.21 SEM micrograph and EDX spectrum of the hierarchical copper-based micro/nanostructures prepared at PPy-PSS films in oxygen saturated 0.10 M CuSO_4 at 0.10 V vs. SCE on a glassy carbon electrode. The EDX peaks were assigned as described in Figure 3.22.

The EDX spectra of several copper standards were also collected in order to compare them to the copper-based micro/nanostructures. The relevant EDX spectra and the

accompanying SEM micrographs are shown in Figure 3.22. The surface morphologies of the standards are all different, as shown by the SEM micrographs. In the case of the oxides the relative intensity of the copper and oxygen peaks are affected by the position of the point of analysis. This anomaly is possibly due to the roughness of the materials which affects the amount of X-rays that reach the detector. However, these variations were minimized by directing the electron beam on the side of the material directly facing the EDX detector. In this way the error in the ratio of the Cu/O signal was reduced to less than 15 %.

The EDX spectrum recorded for the copper metal (99.99 %) has three characteristic peaks that are also present in the spectrum of the micro/nanostructures. The copper oxides (99.99 % Cu₂O and 99.9999 % CuO) have the same three peaks in addition to the oxygen peak that increases by a factor of about 2.6 on going from copper(I) to copper(II) oxide. The copper(II) sulfate pentahydrate (99.999 %) has an additional peak corresponding to sulfur.

The EDX spectrum of the copper-based micro/nanostructures is compared to those of the standards in Figure 3.23. The spectra are all normalized to the intensity of the peak of Cu(L α) to allow for easier comparison of the peak intensities. It is evident that the oxygen content of the micro/nanostructures is well above that of the oxides, whereas it is lower than that of the copper sulfate standard. The sulfur content is also lower in the copper-based structures compared to copper sulfate. Also, the copper-based structures have both a sulfur and oxygen content lower than that of copper sulfate pentahydrate. These spectral features are consistent with the hypothesis that the micro/nanostructures are made from a mixture of copper sulfate hydroxides.

The intensity of the EDX peak is proportional to the concentration of the corresponding element in the sample [42, 43]. It follows that the ratio of the peak heights in the EDX spectrum is proportional to the stoichiometric ratio of the elements in the material. However, the stoichiometric ratio obtained in this way is only indicative since the quantitative analysis is affected by various factors (Section 2.5.3.1). Consequently, the stoichiometric ratio of two elements of an unknown substance can only be tentatively estimated by comparing it to the ratio of the same elements in a standard material of similar composition. This comparison was done for the copper-based micro/nanostructures and the resulting data are summarized in Table 3.3.

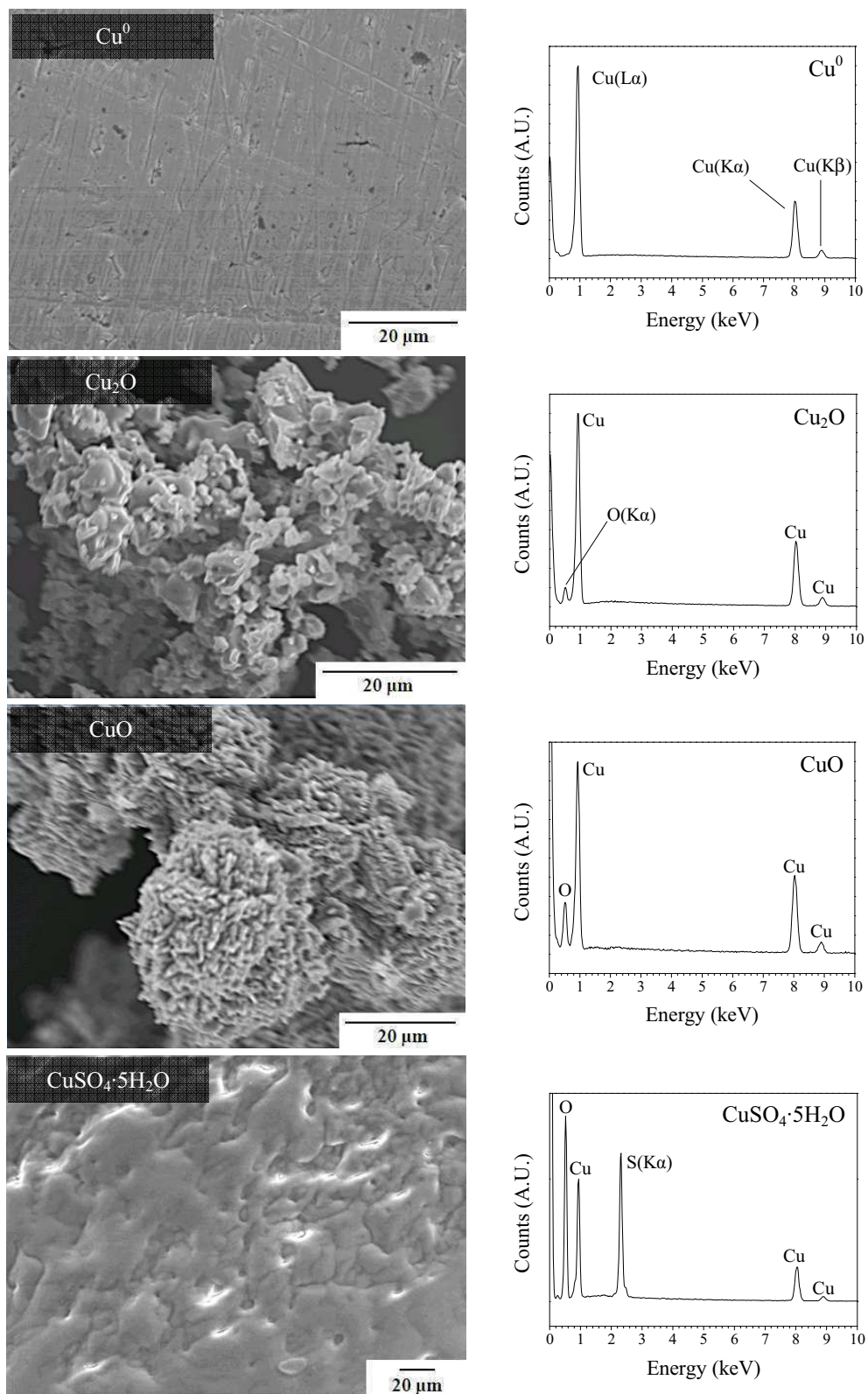


Figure 3.22 SEM micrographs and EDX spectra of standards of copper metal, copper(I) oxide, copper(II) oxide and copper(II) sulfate pentahydrate. The EDX peaks were assigned to Cu (L α 0.93 keV, K α 8.04 keV, K β 8.90 keV), O (K α 0.52 keV) and S (K α 2.31 keV).

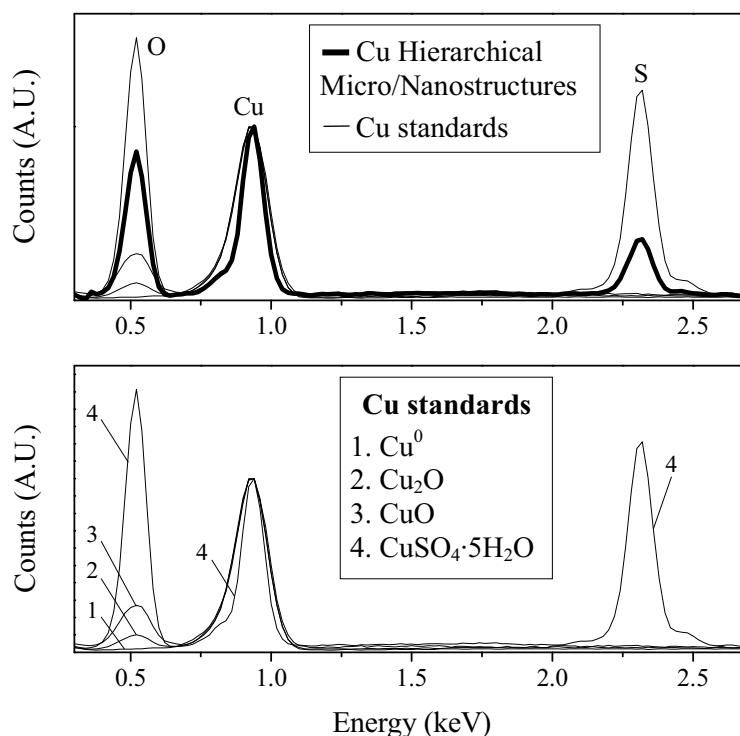


Figure 3.23 Comparison of EDX spectra of the hierarchical copper-based micro/nanostructures (Figure 3.21) and copper standards (Figure 3.22). The spectra were normalized to the Cu(L α) peak. The selected lines are Cu(L α), O(K α) and S(K α).

Table 3.3 Peak height and stoichiometric ratio of copper and sulfur (Cu/S) of the hierarchical copper-based micro/nanostructures. The ratio is compared to those of antlerite, brochantite, posnjakite and copper sulfate hydroxide hydrate.

	Cu/S Ratio	
	Peak height*	Stoichiometric
CuSO ₄ ·5H ₂ O	0.83	1
Cu Hierarchical	2.84	3.4**
CuSO ₄ [Cu(OH) ₂] ₂ , antlerite	—	3.0
CuSO ₄ [Cu(OH) ₂] ₃ , brochantite	—	4.0
CuSO ₄ [Cu(OH) ₂] ₃ ·H ₂ O, posnjakite	—	4.0
[CuSO ₄] ₂ [Cu(OH) ₂] ₃ ·5H ₂ O, copper sulfate hydroxide hydrate	—	2.5

* The peak height ratio was calculated from the ratio of the peak heights of the elements.

** The stoichiometric ratio of the hierarchical structures was extrapolated from its peak height ratio by multiplying it by the quotient of the stoichiometric and peak height ratios of copper sulfate pentahydrate.

The stoichiometric ratios of the copper sulfate pentahydrate, antlerite, brochantite, posnjakite and copper sulfate hydroxide hydrate were calculated from their corresponding chemical formulas, whereas the ratio for the copper-based structures was calculated, as reported in the footnotes of Table 3.3. The Cu/S ratio, 3.4, estimated for the hierarchical copper-based structures compares reasonably well with antlerite, brochantite and posnjakite. However, the level of agreement with the copper sulfate hydroxide hydrate, with a value of 2.5, is poor. The presence of this species was confirmed with XRD and EQCM measurements (Sections 3.2.2.2 and 3.2.2.3). This level of disagreement proves that the elemental quantification with EDX must be considered carefully on a case-by-case basis especially when used with surfaces of different morphologies (Section 2.5.3.1).

3.2.2.5 X-Ray Photoelectron Spectroscopy

The chemical composition and oxidation state of the elements present on the surface of the hierarchical copper-based micro/nanostructures were characterized using X-ray photoelectron spectroscopy, XPS (Section 2.5.4.3). A PPy-PSS film modified with copper-based structures was reduced at -1.00 V vs. SCE for 5 min in 0.10 M Na_2SO_4 prior to the analysis. The XPS survey and high-resolution spectra of the modified films are given in Figure 3.24. Five chemical elements were identified in the survey spectra, namely Cu, S, O, C and N. The first three were also identified using EDX (Section 3.2.2.4) and are the component elements of the copper-based micro/nanostructures. The other two, C and N, are due to the PPy-PSS film since the area of analysis ($1 \text{ mm} \times 1 \text{ mm}$) was large enough to probe both the structures and the surrounding polymer film.

The high-resolution spectrum of the copper signal (Cu 2p_{3/2}) shows three different peaks at 934.9 eV, 937.3 eV and 943.8 eV (Figure 3.24). A fourth peak is found at 932.7 eV from the deconvolution of the signal. The peak at 934.9 eV is related to the presence of Cu(II), whereas the small peak at 932.7 eV is indicative of Cu(I) and/or Cu(0) [31]. The other two peaks are satellites of their parent peak at 934.9 eV and are due to the shake-up effects (Section 2.5.4.3) typically observed for Cu(II) oxide, sulfates and hydroxysulfates [44]. According to the literature, the parent peak of copper oxide is found at about 933.8 eV [31], while that of copper sulfate is observed

at about 934.9 eV [45, 46]. It follows that the present peak is more likely to be related to copper sulfate rather than to copper oxide species. Moreover, a similar parent peak is observed for copper hydroxysulfates [44].

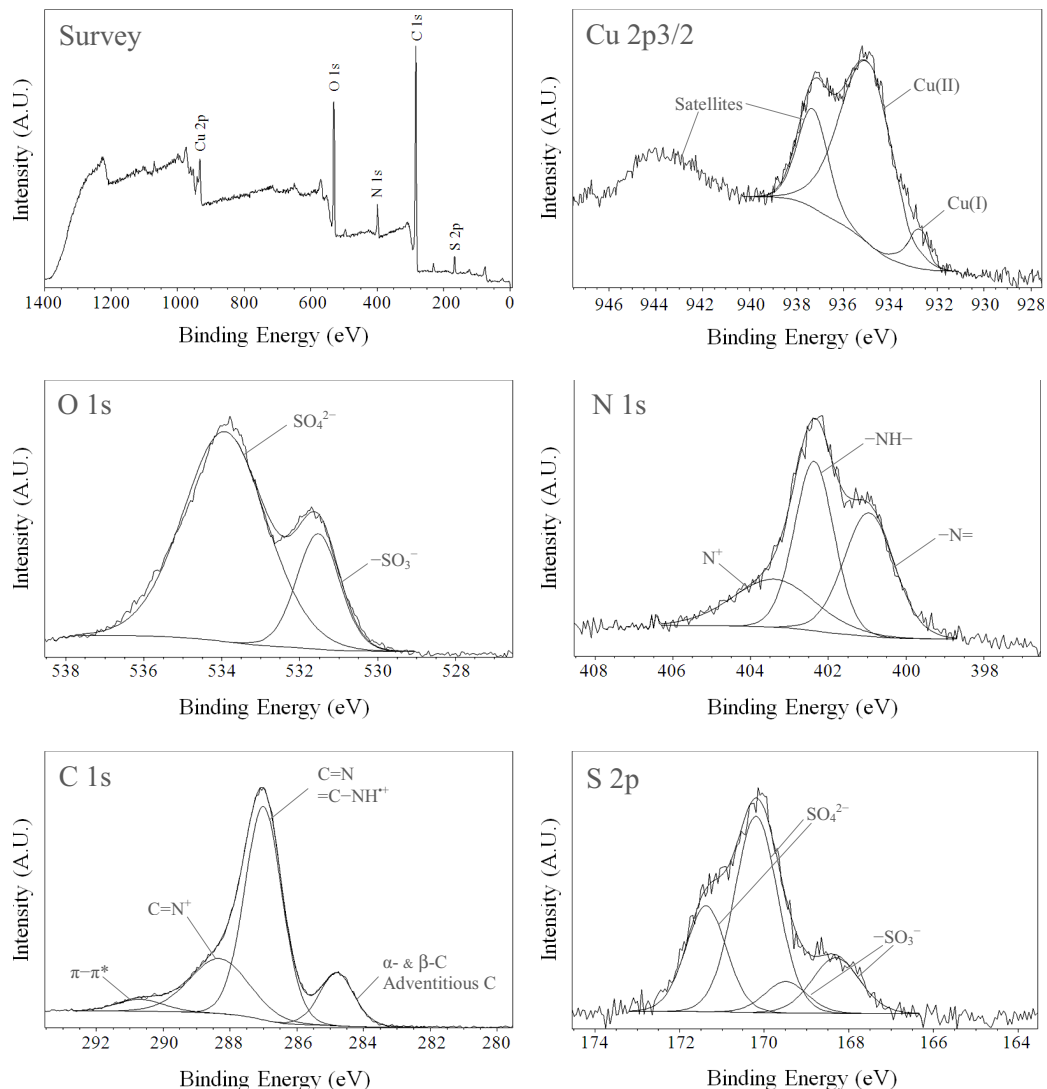


Figure 3.24 XPS spectra of the hierarchical copper-based micro/nanostructures formed at the PPy-PSS films in aerated 0.10 M CuSO_4 at 0.10 V vs. SCE. The copper-based structures were reduced at -1.00 V vs. SCE for 5 min in 0.10 M Na_2SO_4 prior to the analysis.

Hayez *et al.* [44] showed that it is possible to distinguish between copper sulfates and copper hydroxysulfates using XPS. According to their work, the peak found after deconvolution at 932.7 eV is associated with the presence in the material of Cu–O–Cu oxide-like bonds, whereas the main peak at 934.9 eV is related to Cu–O– SO_3 sulfate-like bonds. It is shown that the percentage contribution of the

oxide-like peak to the combined sulfate-like and oxide-like signal is specific for each copper compound. The percentage of oxide-like character of each compound is given in the literature [44], 0 % for CuSO_4 anhydrous, 30 % for $\text{CuSO}_4 \cdot 5\text{H}_2\text{O}$, 35 % for brochantite, $\text{CuSO}_4[\text{Cu}(\text{OH})_2]_3$, and 50 % for antlerite $\text{CuSO}_4[\text{Cu}(\text{OH})_2]_2$. The present value is roughly 12 % which is closer to CuSO_4 anhydrous than to the other compounds. It follows that the surface of the hierarchical micro/nanostructures is rich in copper sulfate. This conclusion is also supported by the presence of two satellite peaks which is a feature found in the spectrum of copper sulfate [44, 47].

The high-resolution spectrum of the sulfur signal (S 2p) shows two separate peaks at 168.3 eV and 170.2 eV, and a shoulder at 171.3 eV (Figure 3.24). The deconvolution of the signal allows the identification of a peak underneath the shoulder and of a fourth peak at 169.5 eV. The peaks are identified as two doublets, S 2p_{1/2} and S 2p_{3/2}, due to spin-orbit coupling of the sulfur atoms. The doublet at 168.3 eV and 169.5 eV is due to the sulfonate groups of the PPy-PSS film [48], whereas the doublet at 170.2 eV and 171.3 eV is due to the sulfate ions of the copper-based micro/nanostructures [49, 50].

The high-resolution spectrum of the oxygen signal (O 1s) shows two separate peaks at 531.5 eV and 533.9 eV (Figure 3.24). According to the literature the former peak can be assigned to the sulfonate oxygen of the dopant present in the polymer film, while the latter to the overall oxygen contribution of sulfate ions, water and polymer oxidized moieties [51, 52].

The high-resolution spectrum of the carbon signal (C 1s) shows two separate peaks at 284.8 eV and 287.0 eV, and a tail at higher binding energy (Figure 3.24). The deconvolution of the signal allows the identification of two other peaks underneath the tail at 288.3 eV and 290.7 eV, respectively. According to the literature [52] the peaks can be assigned as follows. The peak at 284.8 eV is related to the α - and β -carbons of the PPy rings along with the aromatic carbons of PSS and adventitious carbon. The dominant peak at 287.0 eV is given by several contributions, namely the imine-like (C=N), polaron (=C-NH⁺) and hydroxylated (C-OH) defects of PPy. Instead, the peak at 288.3 eV is attributed to the bipolarons (-C=N⁺) and carbonylic defects (C=O) of PPy. The last peak at 290.7 eV is a shake-up satellite of the peak at

284.8 eV and is caused by the $\pi-\pi^*$ electronic excitation of PPy. The dominating peak at 287.0 eV is indicative of the large number of imine-like functions present in the polymer film, as supported by the analysis of the nitrogen signal reported below. These functions are generated from the deprotonation of the pyrrolic nitrogen following the production of hydroxide ions from the reduction of dissolved oxygen (Section 3.2.4).

The high-resolution spectrum of the nitrogen signal (N 1s) shows two peaks at 400.9 eV and 402.4 eV, and a tail at higher binding energy (Figure 3.24). The deconvolution of the signal allows the identification of another peak underneath the tail at 403.4 eV. According to the literature [53], the nitrogen signal of pristine PPy has three peaks at about 397.8 eV, 399.7 eV and 400.5 eV. These peaks correspond to the deprotonated, neutral and oxidized/protonated nitrogen, respectively. The present set of peaks is evidently shifted to higher binding energy compared to that of pristine PPy. The shift is about 3 eV, hence additional considerations are required in order to ascertain that this signal is actually due to the pyrrolic nitrogen. The binding energy separations between the three peaks, 1st peak from the 2nd, 2nd peak from the 3rd, and 1st peak from the 3rd, are comparable in each set of peaks. In fact, the energy separations in the present case are 1.5, 1.0 and 2.5 eV, while for the pristine polypyrrole the values are 1.9, 0.8 and 2.7 eV. Another consistent feature is that the doping level can be estimated from the ratio of the area of the third peak (oxidized nitrogen) to the total area of the nitrogen signal. The value obtained is 0.23 which is in good agreement with the doping level of 0.28 calculated from the mass-charge curves recorded during electropolymerization (Section 3.2.1.1). It follows that the signal can indeed be attributed to the pyrrolic nitrogen. Actually, a shift of the N 1s signal towards higher binding energy has been already observed in polypyrrole films modified with copper due to the interaction of Cu(I) ions with nitrogen [54, 55]. The occurrence of Cu(I) in the present case is in good agreement with the results of cyclic voltammetry (Section 3.2.2.1), which show the existence of a Cu(I)/Cu(II) redox couple in the film modified with copper-based micro/nanostructures. The presence of Cu(I) is also in agreement with the Cu 2p_{3/2} peak at 932.7 eV, as shown earlier. In addition, the presence of copper in the PPy-PSS film was confirmed using EDX, as shown in Figure 3.25. In this case, the analysis was confined to an area free from the copper-based micro/nanostructures to give the element composition of the

PPy-PSS film. It is then reasonable to assume that during the deposition of the hierarchical micro/nanostructures a portion of copper was also deposited in the film as Cu(I).

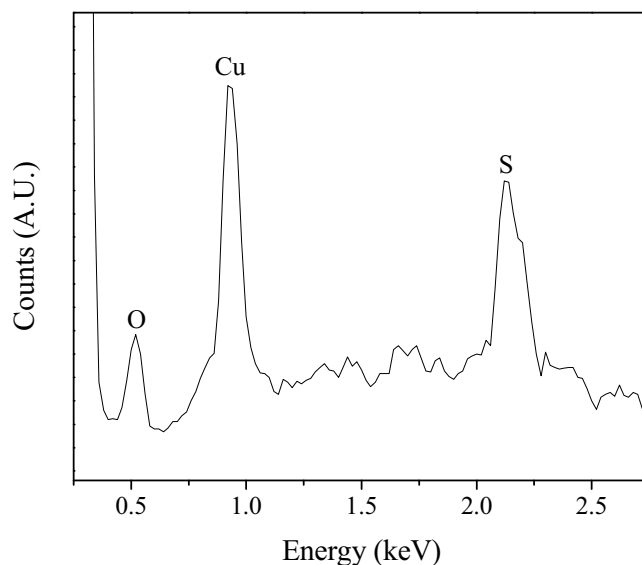


Figure 3.25 EDX spectrum of the PPy-PSS film after deposition of the hierarchical copper-based micro/nanostructures in 0.10 M CuSO_4 at 0.10 V vs. SCE. The electron beam was focused on a part of the film free and far removed from any copper-based micro/nanostructures in order to avoid interference. Three peaks are identified as copper, oxygen and sulfur. The sulfur arises from the sulfonate groups of the dopant, while the dopant contributes also to the oxygen signal.

The last important aspect of the N 1s signal is the size of the peak at 400.9 eV due to the imine-like nitrogen ($-\text{N}=\text{}$) which is surprisingly large. This peak results from the deprotonation of the amine-like nitrogen ($-\text{NH}-$) during the deposition. It is shown in the literature [56] that by treating PPy with 0.5 M NaOH, the area of the imine-like nitrogen peak can account for 50 % of the overall area of the N 1s signal after the deprotonation of the pyrrolic nitrogen. In the present case the relative contribution of the deprotonated moieties is about 37 %, a value that can only be achieved by base treatment. Clearly, the deprotonation of the pyrrolic nitrogen during the copper deposition is a consequence of the generation of hydroxide ions from the reduction of dissolved oxygen (Section 3.2.4). This is further evidence that the local pH at the polymer film is much higher than in the bulk solution during the electrochemical deposition of the hierarchical structures.

3.2.2.6 Attenuated Total Reflectance Infrared Spectroscopy

The component species of the hierarchical copper-based micro/nanostructures were further analyzed using attenuated total reflectance infrared spectroscopy, ATR-IR (Section 2.5.4.1). The ATR-IR spectra were recorded for both freshly deposited and electrochemically reduced micro/nanostructures from 450 cm^{-1} to 4000 cm^{-1} . The background spectrum of the PPy-PSS film was also taken. Representative spectra are shown in Figure 3.26. In all the spectra there are two weak bands at $2000\text{--}2400\text{ cm}^{-1}$. These are characteristic of the internal reflection element of the ATR sampling equipment. All other bands originate from either the PPy-PSS film or the copper-based micro/nanostructures.

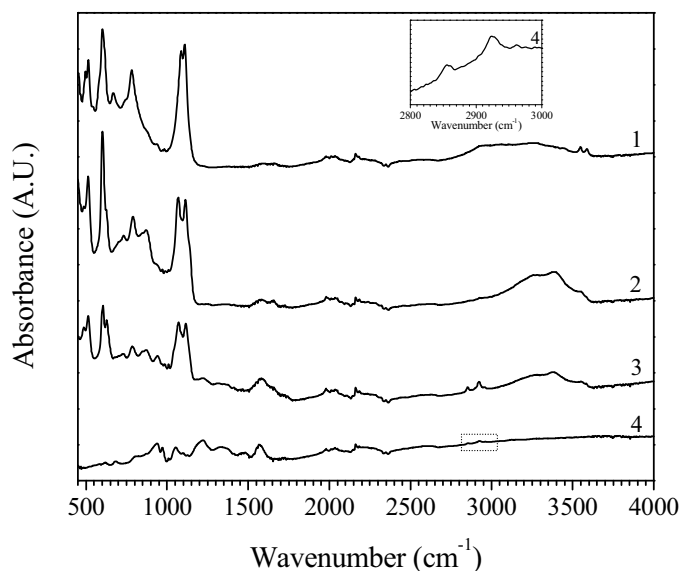


Figure 3.26 ATR-FTIR spectra of the hierarchical copper-based micro/nanostructures prepared at PPy-PSS films in oxygen saturated 0.10 M CuSO_4 at 0.10 V vs. SCE . The spectra correspond to structures that were freshly deposited (1), reduced at -0.70 V vs. SCE (2) and at -1.50 V vs. SCE (3) for 15 min in aerated $0.10\text{ M Na}_2\text{SO}_4$. The spectrum of PPy-PSS is also shown (4) with a magnification of a selected region in the inset.

The small band at $1500\text{--}1650\text{ cm}^{-1}$ is due to the $\text{C}=\text{C}$ stretching of the PPy rings, whereas the two separate peaks centered at about 2900 cm^{-1} are due to the CH_2 asymmetric and symmetric stretching of PSS [57, 58]. These bands are present in the spectrum of the PPy-PSS film, as clearly shown in the inset of Figure 3.26, and are also evident in the spectra recorded for the copper-based micro/nanostructures.

Interestingly, these bands are more intense when the copper-based micro/nanostructures are reduced at -1.50 V vs. SCE, as evident in spectrum 3. This may be related to the swelling of the film in response to the ingress of solvated cations upon reduction, resulting in the exposure of the polymer to the ATR crystal.

The main absorption bands of both the pristine and reduced micro/nanostructures are located in two characteristic regions from 450 to 1250 cm^{-1} and from 3050 to 3650 cm^{-1} . Reliable IR data from the literature could only be obtained for antlerite and brochantite [59-61]. Consequently, the following analysis is focused on using such data, characteristic of copper hydroxysulfates, in order to assign the various infrared peaks to their corresponding vibrational modes. Also, the data allow the determination of the contribution, if any, that the antlerite and brochantite would make to the composition of the copper micro/nanostructures.

In Table 3.4 the band positions and assignments of antlerite and brochantite reported by Ramamurthy and Secco [59, 60], are compared to the data of the copper-based micro/nanostructures. On the basis of this comparison the bands in the spectra of the pristine and reduced structures are assigned to certain vibrational modes.

The ATR-IR spectra of the copper-based micro/nanostructures in the range 450 - 1250 cm^{-1} are enlarged in Figure 3.27. The first feature common to all spectra is the band at 1000 - 1200 cm^{-1} characterized by a splitting which is also found in the transmission IR spectra of antlerite, $\text{CuSO}_4[\text{Cu}(\text{OH})_2]_2$, and brochantite, $\text{CuSO}_4[\text{Cu}(\text{OH})_2]_3$ [59, 60]. This band is assigned to the fundamental vibrational ν_3 mode of SO_4 (Figure 3.28), and the splitting of this band is due to the bound state of sulfate in the crystalline structure of the material. In the case of brochantite, the splitting generates two peaks at 1085 cm^{-1} and 1120 cm^{-1} , whereas for antlerite three peaks are observed at 1080 cm^{-1} , 1100 cm^{-1} and 1155 cm^{-1} [59, 60].

Another fundamental vibrational mode of SO_4 is the ν_4 (Figure 3.28) which is observed for the free sulfate ion at 613 cm^{-1} [59]. A splitting of the band related to this mode is observed in the spectra of antlerite and brochantite with three and two main peaks, respectively [59, 60]. In the case of the micro/nanostructures the band splitting is only obtained after reduction at -1.50 V vs. SCE, with the corresponding peaks at 604 cm^{-1} and 628 cm^{-1} in agreement with those of brochantite (Table 3.4).

Table 3.4 Positions of the ATR-IR peaks of the hierarchical copper-based micro/nanostructures from the spectra reported in Figure 3.26, related to the fundamental vibrational modes of SO_4 . The assignment of the peaks is given with respect to the spectra of antlerite $\text{CuSO}_4[\text{Cu}(\text{OH})_2]_2$ and brochantite $\text{CuSO}_4[\text{Cu}(\text{OH})_2]_3$ as reported by Ramamurthy and Secco [59, 60]. The intensity of the peaks is given beside their wavenumbers (the labels are defined at the bottom of the table).

Assignment	Wavenumber (cm^{-1})				
	$\text{CuSO}_4[\text{Cu}(\text{OH})_2]_2$	$\text{CuSO}_4[\text{Cu}(\text{OH})_2]_3$	Cu Hierarchical		
			Pristine	-0.70 V / 15 min	-1.50 V / 15 min
$\nu_3 (\text{SO}_4)$	1155 (s)	—	—	1141 (sh)	—
	1100 (s)	1120 (s)	1109 (s)	1113 (s)	1115 (s)
	1080 (s)	1085 (s)	1087 (s)	1070 (s)	1071 (s)
$\nu_1 (\text{SO}_4)$	990 (s)	980 (m)	983 (vw)	988 (vw)	985 (w)
$\nu_4 (\text{SO}_4)$	670 (m)	—	669 (m)	—	—
	640 (s)	625 (s)	617 (sh)	625 (w)	628 (s)
	610 (s)	600 (s)	601 (s)	601 (s)	604 (s)
$\nu_2 (\text{SO}_4)$	518 (m)	513 (m)	515 (m)	514 (m)	515 (m)
	488 (m)	484 (s)	497 (m)	486 (w)	487 (m)
	457 (m)	462 (m)	453 (m)	—	—

s = strong; m = medium; w = weak; vw = very weak; sh = shoulder

It is evident that, prior to the reduction, the pristine micro/nanostructures have only a single band at 601 cm^{-1} . On reduction at -0.70 V vs. SCE a shoulder at 625 cm^{-1} emerges. This shoulder becomes a fully defined peak after reduction at -1.50 V vs. SCE. The position of the two resulting peaks is in agreement with those of brochantite, which would indicate that during the reduction treatment the copper-based micro/nanostructures are progressively converted to brochantite and/or posnjakite, the compositions of which differ by one water molecule.

The other two fundamental vibrational modes of SO_4 are the ν_1 and ν_2 (Figure 3.28). In the case of the ν_1 mode, the associated band for each of the hierarchical structures is significantly lower in intensity than the analogous band in either the spectrum of antlerite or brochantite.

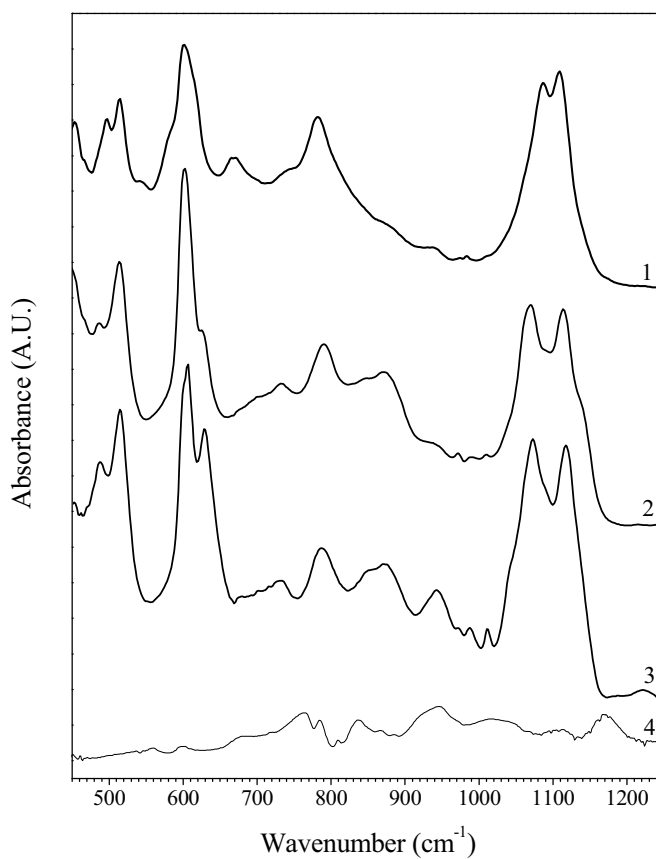


Figure 3.27 ATR-IR spectra of the hierarchical copper-based micro/nanostructures deposited onto PPy-PSS thin films in the 450 - 1250 cm^{-1} wavenumber region, corresponding to the sulfate vibrational modes. The spectra correspond to copper-based micro/nanostructures that were freshly deposited (1), reduced at -0.70 V vs. SCE (2) or -1.50 V vs. SCE (3) for 15 min. The spectrum of PPy-PSS is also shown (4).

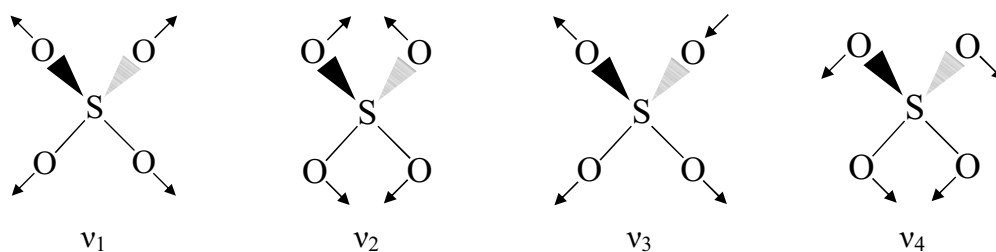


Figure 3.28 Fundamental vibrational modes of the sulfate ion. The mode ν_1 is due to the symmetric S-O stretch and it requires a loss of the tetrahedral symmetry in order to be IR active. The ν_2 mode is due to the symmetric S-O bends and is doubly degenerate. The asymmetric stretching ν_3 and bending ν_4 modes are both triply degenerate.

In the case of the ν_2 mode, there is a clear agreement between the spectrum of the pristine hierarchical structures with those of brochantite and antlerite for the three peaks at 453, 497 and 515 cm^{-1} (Table 3.4). The peak at 453 cm^{-1} is shifted upon reduction to lower wavenumbers outside the range of the recorded spectra.

The peak position of the fundamental vibrational modes of the sulfate ion is dependent on the binding state of the ion [62]. The single peak of the pristine micro/nanostructures at 601 cm^{-1} is related to the presence of loosely bound sulfate ions [59]. After reduction -0.70 V vs. SCE, the shoulder at 617 cm^{-1} might be indicative of the occurrence of a weak interaction involving the sulfate ions [59].

After reduction at -1.50 V vs. SCE, the band at 601 cm^{-1} is clearly split into two peaks due to the presence of stronger interactions [59]. In the spectra of all the pristine and reduced structures, the splitting at 1000-1250 cm^{-1} is also indicative of strong interaction [59, 60]. In the case of antlerite and brochantite, the bands at 600 and 1100 cm^{-1} are both split into multiple peaks. The fact that this is not the case for the pristine structures might indicate the deposition of a different form of copper hydroxysulfate which gives a distinctive spectrum partially related to those of antlerite and brochantite. Such a material could also explain the presence of only one of the distinctive peaks of antlerite in the pristine structures at 670 cm^{-1} [59, 60], while the other two at 640 cm^{-1} and 1155 cm^{-1} are missing. The deposition of a different form of copper hydroxysulfate is supported by the results obtained from the XRD, EQCM and XPS analyses (Sections 3.2.2.2, 3.2.2.3 and 3.2.2.5) which demonstrate the formation of a mixture of copper sulfate hydroxide hydrate and posnjakite.

The ATR-IR spectra of the copper-based micro/nanostructures in the range 3050-3650 cm^{-1} are enlarged in Figure 3.29. In this range there are two main features, a broad band with two wide maxima at about 3260 cm^{-1} and 3380 cm^{-1} , and a couple of well resolved peaks above 3500 cm^{-1} . These features are related to three different kinds of OH groups present in the copper-based deposits. The two wide maxima are assigned to OH groups with a medium and a high degree of hydrogen bonding, respectively, while the two narrow peaks are related to free non-hydrogen bonded OH groups [59, 60]. In the case of the freshly deposited copper-based structures the broad band is almost flat, whereas the two peaks related to the free OH

are easily distinguishable above the background. The relative intensity of the two features is reversed after reduction. The broad band is now better defined with two discernible maxima, while the two resolved peaks are hardly noticeable. It follows that the reduction treatment causes a transition from free to bound OH groups at both -0.70 and -1.50 V vs. SCE.

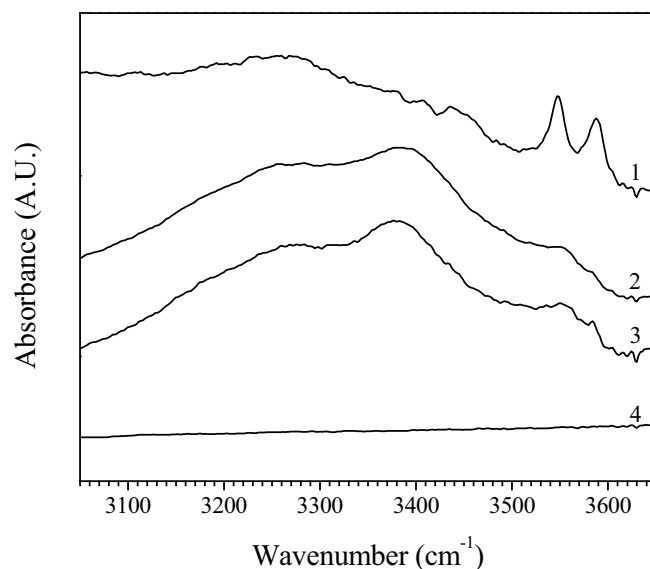


Figure 3.29 ATR-IR spectra of the hierarchical copper-based micro/nanostructures in the wavenumber range of hydroxide vibrational modes, $2800 - 3800$ cm^{-1} . The spectra correspond to structures that were freshly deposited (1), and reduced at -0.70 V vs. SCE (2) or at -1.50 V vs. SCE (3) for 15 min in 0.10 M Na_2SO_4 . The spectrum of PPy-PSS is also shown (4).

These three classes of OH groups are observed in both the spectra of antlerite and brochantite in similar positions [59], hence the deposited structures before and after reduction have the characteristic features of the OH groups of the copper hydroxysulfate compounds. The bands observed in the range $700-1000$ cm^{-1} have received little attention in the literature and no assignment is available.

A direct comparison, between the experimental spectra recorded for the copper-based structures and those of antlerite and brochantite, is shown in Figure 3.30. It is apparent from this schematic representation that after reduction of the copper-based structures, four new bands, labeled as A, B, C and D, are observed. This spectrum is in good agreement with that recorded for brochantite. The changes

observed in the spectrum upon reduction of the copper-based structures are probably related to the formation of copper hydroxide. Since the fresh structures contain a mixture of copper sulfate hydroxide hydrate and posnjakite, the hydroxide ions, which are generated during the reduction of dissolved oxygen (Section 3.2.4), may facilitate the conversion of the micro/nanostructures from this mixture to brochantite, $\text{CuSO}_4[\text{Cu}(\text{OH})_2]_3$, and/or posnjakite, $\text{CuSO}_4[\text{Cu}(\text{OH})_2]_3 \cdot \text{H}_2\text{O}$.

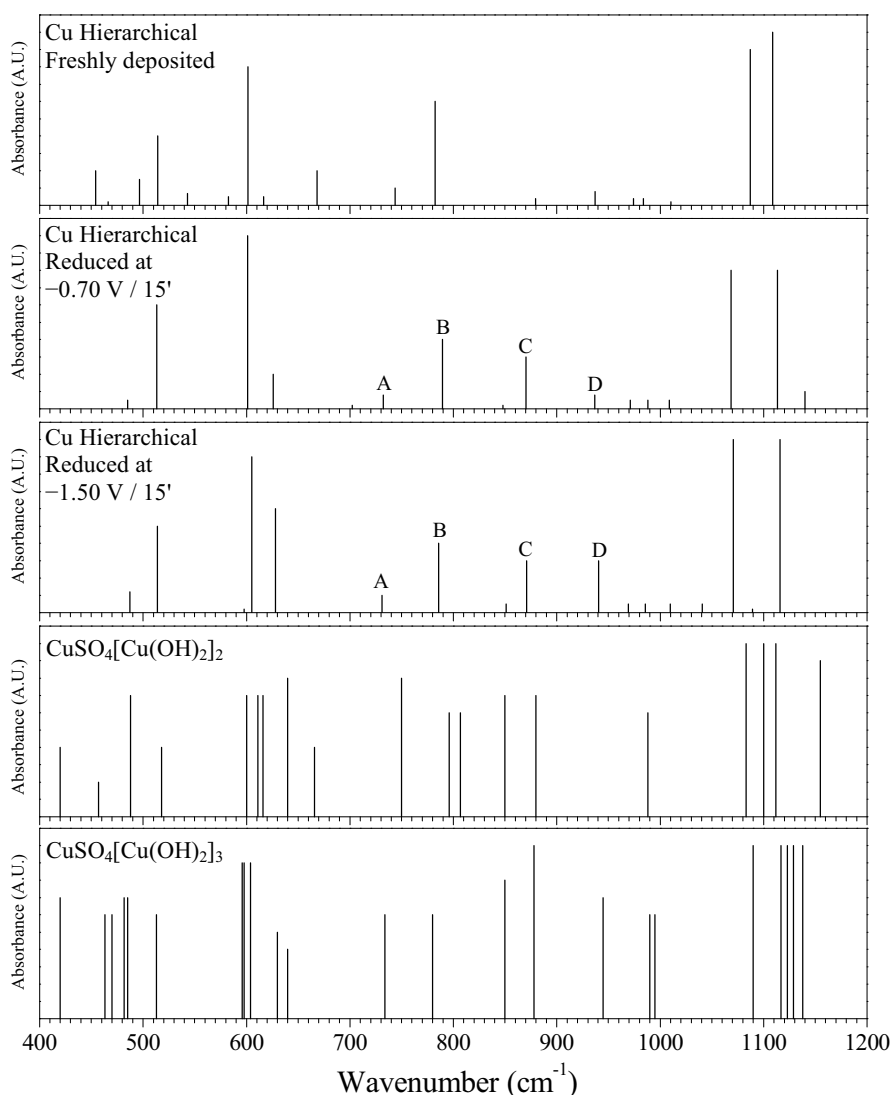


Figure 3.30 Dropline representation of the ATR-IR spectra of the hierarchical copper-based micro/nanostructures and reference copper hydroxysulfate compounds. The position and height of the lines correspond to the position and relative intensity of the peak maxima. The data of antlerite $\text{CuSO}_4[\text{Cu}(\text{OH})_2]_2$ and brochantite $\text{CuSO}_4[\text{Cu}(\text{OH})_2]_3$ were taken from Secco [59].

3.2.2.7 Raman Spectroscopy

The hierarchical copper-based micro/nanostructures were also analyzed using Raman spectroscopy (Section 2.5.4.2) in order to obtain additional information about the component materials. The Raman spectra of the pristine PPy-PSS films and the one with freshly deposited micro/nanostructures are reported in Figure 3.31. The features of both spectra are those of the polypyrrole film, the band positions and corresponding assignments are listed in Table 3.5. It follows that none of these peaks can be related to the presence of copper hydroxysulfates in the micro/nanostructures.

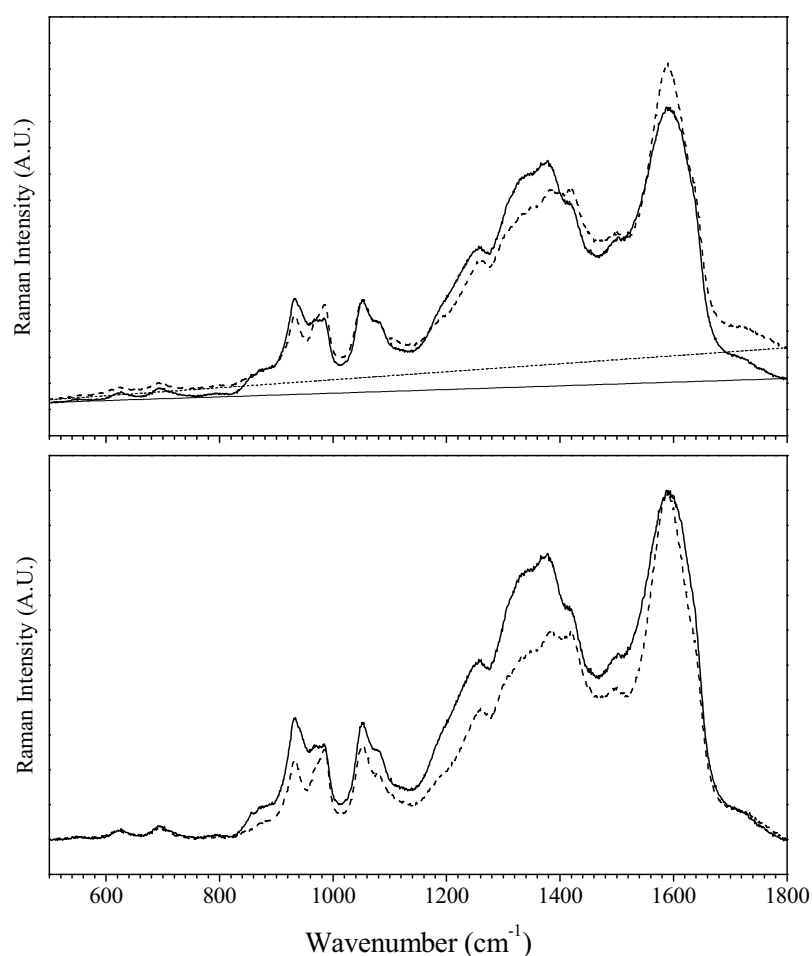


Figure 3.31 Raman spectra of the hierarchical copper-based micro/nanostructures prepared at PPy-PSS films in oxygen saturated 0.10 M CuSO_4 at 0.10 V vs. SCE. The spectrum of a film modified with the copper-based micro/nanostructures (—) is compared to the spectrum of a pristine film (---). The top graph shows the raw spectra, while the bottom graph shows the spectra obtained after subtraction of the baseline and normalization to the band maximum at 1588 cm^{-1} .

The fact that the spectrum of the copper-based micro/nanostructures is dominated by the scattering of PPy can be explained in term of resonance Raman scattering (Section 2.5.4.2). In fact, at the wavelength of the probing laser (514 nm), the Raman band associated with the C=C stretching of polypyrrole is greatly enhanced by a strong resonance Raman effect [63]. It is well-known that a resonance band can be over 10^6 times stronger than a normal band, and for this reason the weaker signals of the copper hydroxysulfates are not observed.

Table 3.5 Raman band positions of the PPy-PSS film modified with hierarchical copper-based micro/nanostructures (spectrum given in Figure 3.31). The figures in parentheses are the band positions of the normalized spectra.

Assignment	Raman Shift (cm ⁻¹)				
	PPy-PSS/Cu Hierarchical		PPy-PSS		Literature*
C=C backbone stretching	1591	(1590)	1588	(1588)	1590 1575
Ring stretching	1379	(1378)	1385	(1385)	1380 1365
N-H in-plane deformation	1259	(1259)	1260	(1260)	1250 1245
C-H in-plane deformation	1051	(1052)	1051	(1052)	1050 1040
Ring deformation	976	(975)	984	(984)	980 975
C-H out-of-plane deformation	932	(932)	932	(932)	930 930

* Raman maxima of PPy reported in the literature. The first figure is for PPy-PSS excited at 633 nm [64], the second figure is for PPy-ClO₄ excited at 514 nm [65].

In order to possibly identify any weak signals that might be buried underneath the strong scattering of PPy-PSS, the normalized spectrum of the pristine polymer was subtracted from the one of the copper-based structures (the normalized spectra were prepared as described in Figure 3.31). The resulting difference spectrum is presented in Figure 3.32. None of the peaks correspond to the presence of copper(I) oxide, in fact the main Raman band of Cu₂O is centered at about 600 cm⁻¹ [66, 67]. Copper(II) oxide cannot be considered as its Raman scattering is placed below the range of analysis with a characteristic peak at about 300 cm⁻¹ [67]. The copper hydroxysulfates have a characteristic peak at about 1078 cm⁻¹ [68, 69] that could correspond to the small peak at 1071 cm⁻¹ in the spectra. However, such a peak is

20 times weaker than the main one that is observed, for example, for antlerite and brochantite at about 985 cm^{-1} and 990 cm^{-1} , respectively [68, 69]. The remaining peaks do not correspond to any of the copper hydroxysulfates. For this reason, the peaks are most probably related to the change in the oxidation state of the PPy film after the deposition process which is known to affect the Raman spectrum [70].

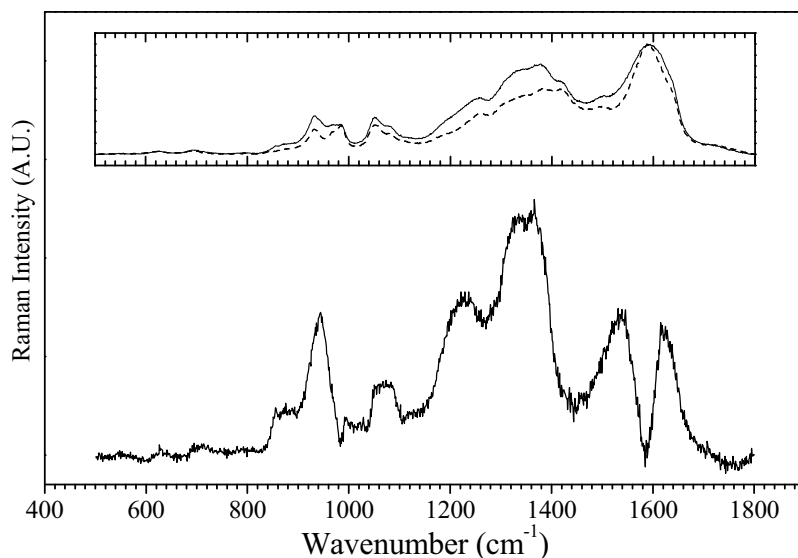


Figure 3.32 Calculated Raman spectrum obtained from the difference of the spectra of the hierarchical copper modified and pristine PPy-PSS films. In the inset, the spectra of the copper modified (—) and pristine (---) PPy-PSS films, taken from Figure 3.31, are shown. The wavenumber scale of the inset is the same as in the main graph.

3.2.3 Mechanism of Deposition of Hierarchical Copper-Based Micro/Nano-structures

3.2.3.1 Mechanism of Formation and Hierarchical Arrangement

The mechanism of formation of the hierarchical copper-based micro/nanostructures was studied by analyzing the copper structures at different phases of growth. The experiments were terminated at different stages during the deposition of the copper-based micro/nanostructures and the modified electrode surfaces were analyzed using SEM. The resulting micrographs are presented in Figure 3.33. The micrographs shown are designated as 1a, 1b, 2a, 2b, 3a and 3b and present the evolution of the structure as a function of time. At the very early stages (1a),

a bone-shaped copper-based stick is observed and it appears to sit on top of the polymer film; the size of the stick is about 3 μm long and 1 μm wide. At this stage, the stick is already made of several layers, a few tens of nanometers thick. Copper-based nanoparticles of about 20-50 nm are seen aligned along the length of the stick, forming numerous nanowires (1b). With the progression of the electrodeposition, other sticks, similar to the first one, are formed to give an almost centered structure (2a). At this stage, the sticks are still made of nanowires/nanoparticles (2b). Once the structure become larger, it resembles the final flowerlike hierarchical shape (3a) and nanowire ends can still be seen at the edge of the sticks (3b). At this stage, the flowers are made up of sticks, with each stick assembling to give what could be described as a petal of a flower. By the end of the electrodeposition, a cluster of compact petals is formed (Figure 3.8).

At the beginning of the flower formation (1a), the nanoparticles are likely to nucleate directly at the film surface, most probably from the copper(II) ions that are captured and aligned along the macromolecule of the film. This assumption is based on the work by Yang *et al.* [36] in which it is shown that thin films of PPy-PSS (30-60 nm) are made of polymer chains lying parallel to each other on the electrode surface. The nanoparticles are formed from the electrocrystallization of copper hydroxysulfates (Section 3.2.2) through the capture of copper ions, the generation of hydroxide ions by the reduction of oxygen (Section 3.2.4) and the presence of sulfate ions in solution. Other nanoparticles are then crystallized at the same site causing the formation of nanowires that extend to give the growth of nanosheets (Figure 3.33). Until this point, the deposition process is governed by the electrochemistry at the polymer surface with the consequent nucleation and growth of the first group of petals. In the meantime, the nanoparticles grow in diameter, and smooth petals are eventually formed with no particles visible at the petal edges in the finished flowers (Figure 3.8). During this part of the growth, the copper hydroxysulfates are likely to be electrodeposited directly on the already formed petals and not at the polymeric film. It follows that both the surface nucleation and the direct deposition of ‘copper-on-copper’ must occur to lead to the formation of the hierarchical micro/nanostructures.

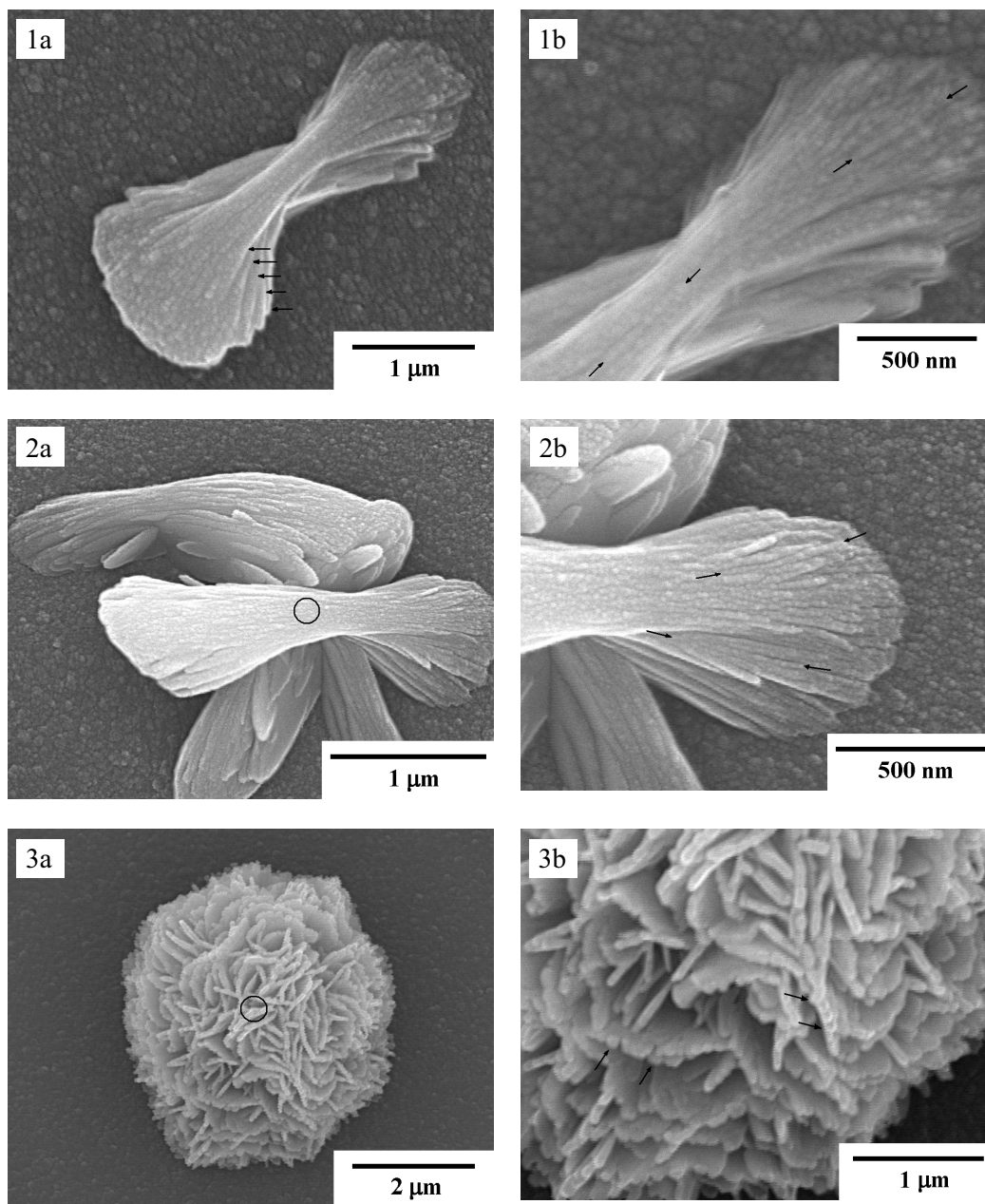


Figure 3.33 SEM micrographs showing the mechanism of growth of the hierarchical copper-based micro/nanostructures on a PPy-PSS film after deposition from aerated 0.10 M CuSO₄ at 0.10 V vs. SCE. 1a) First stage of growth with copper-based stick made of several layers (arrows pointing at the edges). 1b) Each layer is made of copper-based nanoparticles aligned to form nanowires (arrows pointing at the ends). 2a) Early stage of growth with a new copper-based stick formed in the same area as the first one. The sticks form a centered small cluster (circle at the center). 2b) Each stick is made of copper-based nanoparticles aligned to form nanowires (arrows pointing at the ends). 3a) Advanced stage of growth with a fully centered cluster already formed (circle at the center); each stick contributes to a symmetrical petal. 3b) Each petal is formed of nanowires (arrows pointing at the ends).

3.2.3.2 Mechanism of Nucleation and Growth

In this section, the mechanism of nucleation and growth of the hierarchical copper-based micro/nanostructure is examined in detail by further analyzing the current and mass responses of electrochemical deposition. The following analysis is directly related to the analysis in Section 3.2.2.3 which was based on the calculation of the mass-to-charge ratios during the deposition process.

The potentiostatic deposition of three-dimensional structures from multiple nucleation sites in the diffusion-controlled regime is described by the Scharifker-Hills model [71]. According to this model, two diagnostic relationships, Equations 2.2 and 2.3, given in Section 2.5.2.1, can be used to determine whether the nucleation of the copper-based micro/nanostructures is instantaneous or progressive. In order to compare the experimental data to the model equations, the current-time data are plotted in the dimensionless coordinates $(i/i_{\text{MAX}})^2$ and t/t_{MAX} , where i_{MAX} is the current maximum of the chronoamperometric response reached at time t_{MAX} . In the present case $t_{\text{MAX}} = 195$ s and $i_{\text{MAX}} = -0.171$ mA/cm², and the resulting curve is shown in Figure 3.34.

The solid and dashed traces represent the dimensionless profiles of instantaneous and progressive nucleation, respectively. At the start of the nucleation, corresponding to the minimum of the current-time response just above $\frac{1}{2}t_{\text{MAX}}$, the experimental data follow closely the model of progressive nucleation. The same is true around the current maximum at t_{MAX} . This part of the current profile is typical of depositions in which the formation of new nuclei is faster than the growth of existing nuclei [71]; the result is the progressive superposition of the currents of formation and growth of each nucleus. The data start departing from both models at about $2 \cdot t_{\text{MAX}}$ as a result of the changes in the deposition process, such as precipitation from the solution rather than direct nucleation on the film surface or changes of pH and composition of the solution during the deposition [72]. However, the progressive nucleation is also evident from Figure 3.35, where a large number of nucleation sites is found, with each hierarchical structure growing in an independent manner. The structures have different sizes, confirming that the nucleation is progressive, with new sites being established during the electrodeposition period.

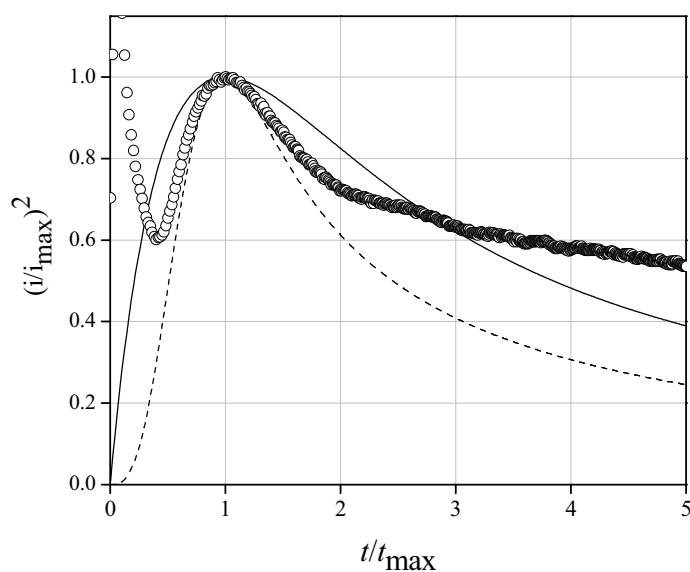


Figure 3.34 Dimensionless plot of the current-time response for the deposition of hierarchical copper-based micro/nanostructures, experimental data taken from Figure 3.19. The solid and dashed traces are the profiles for instantaneous and progressive nucleation, respectively, from the Scharifker-Hills model described in Section 2.5.2.1.

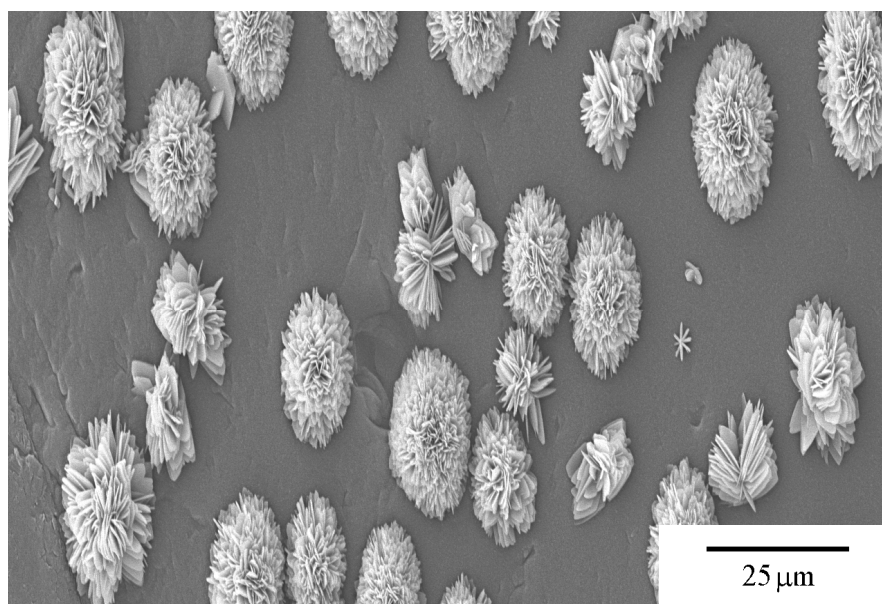


Figure 3.35 SEM micrograph of the hierarchical copper-based micro/nanostructures formed on the PPy-PSS films in aerated 0.10 M CuSO_4 at 0.10 V vs. SCE. The overall charge of deposition was 80 mC/cm^2 , which is double the value typically used. The presence of structures of different sizes is indicative of the progressive formation and growth of new nuclei during the electrodeposition period.

The mechanism of formation of the copper-based micro/nanostructures can also be analyzed by comparing current, mass and mass-to-charge ratios during the electrochemical deposition, as shown in Figure 3.36. The mass-to-charge ratio, R , is the mass deposited per unit of charge and is proportional to the molar mass, M , of the deposited material ($R = M / nF$). The ratio is calculated from the slope of the mass-charge curve. The value of the ratio at each single time of the deposition is labeled as the instantaneous ratio, R_{inst} , in order to distinguish it from the average value, which is calculated over a period of time (Section 2.5.2.4).

The electrodeposition of the hierarchical copper-based micro/nanostructures can be divided into five stages, as shown in Figure 3.36. In the first stage there is an increase of current without any significant amount of deposited mass, consequently the R_{inst} is close to zero. This stage lasts less than 20 s. The charge passed during this stage is used to reduce either oxygen or the polymer film. A current maximum is then reached and this is followed by a decrease in the current, but this time with a corresponding increase in mass. This second stage lasts about 60 s and is mainly related to the capture of Cu^{2+} ions by the polymer film (Section 3.2.1.2). The third stage corresponds to an increase in current and extends from about 75 to 200 s. This is the current of nucleation without overlapping (Section 2.5.2.1, Figure 2.4). Meanwhile, the mass begins to increase and R_{inst} climbs towards its first plateau value, all within about 120 s. On closer inspection of Figure 3.36, it is seen that the mass increase lags behind the current increase, so that the increase in R_{inst} does not mirror exactly the increase in current. This is related to the fact that part of the charge consumed is connected with the reduction of dissolved oxygen and the generation of hydroxide ions (Section 3.2.4). Only when the concentrations of Cu^{2+} and OH^- have reached a critical value, the nucleation of the copper hydroxysulfate micro/nanostructures begins in the presence of SO_4^{2-} . This gives rise to an increase in mass and a corresponding sharp increase in R_{inst} . Evidence indicates that the shape of the deposited structures at this stage is the simple bone-shaped stick, shown in Figure 3.33, Micrograph 1a. Other sticks start forming at the nucleation site (Figure 3.33, Micrograph 2a) while the current surpasses a maximum value corresponding to the current of growth with overlapping nuclei (Section 2.5.2.1, Figure 2.4).

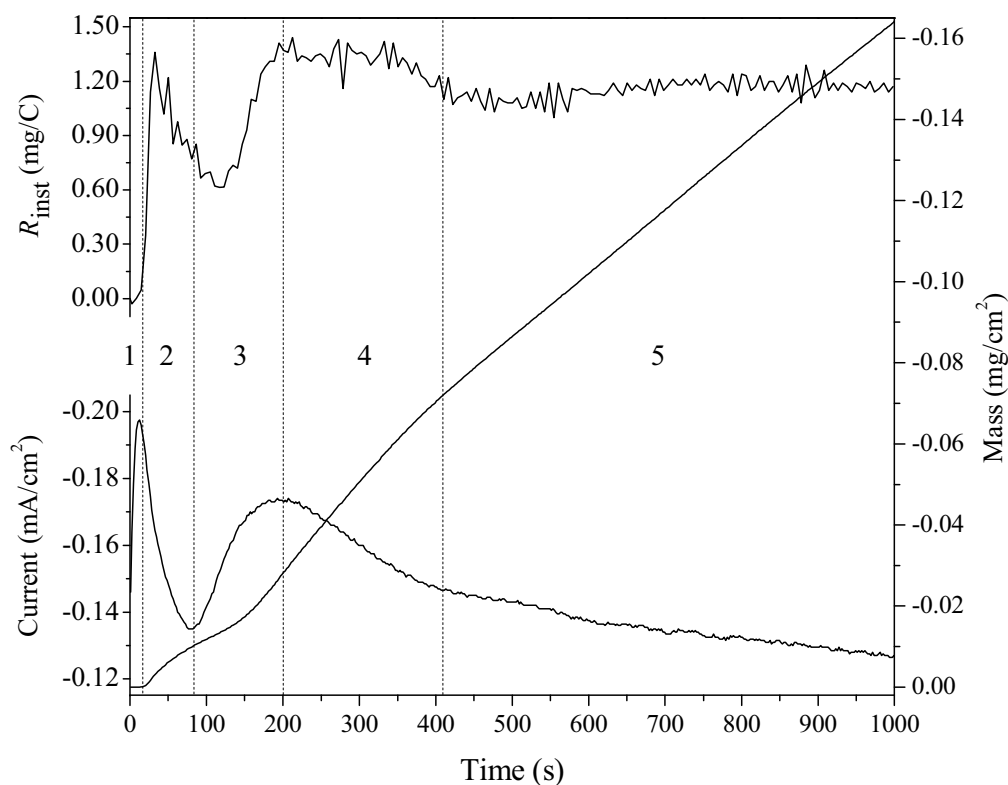


Figure 3.36 Current, mass and instantaneous mass-to-charge ratio for the electrodeposition of hierarchical copper-based micro/nanostructures formed on 120 nm PPy-PSS films in oxygen saturated 0.10 M CuSO_4 at 0.10 V vs. SCE.

In the fourth stage, the current starts decreasing due to the competitive superposition of the diffusion layers of the growing nuclei. Correspondingly, the mass increase starts to slow down giving a R_{inst} almost constant at around 1.323 mg/C (Section 3.2.2.3, Figure 3.20, Plot B). During this stage that lasts about 200 s, the sticks have grown in number and size to form hierarchical clusters which are not yet completely developed (Figure 3.33, Micrograph 3a).

The fifth and last stage is characterized by a monotonic decrease of current and a linear increase in mass with a rate (slope) slightly lower than the previous stage. In the meantime the R_{inst} has shifted to a lower value of 1.161 mg/C (Section 3.2.2.3, Figure 3.20, Plot C). This change could be due to the reciprocal hindrance that each cluster is now experiencing from the surrounding ones. At this final stage the hierarchical copper-based micro/nanostructures take the form shown in Figure 3.35.

3.2.4 Oxygen Reduction at Polypyrrole-Polystyrene Sulfonate Films

The oxygen reduction reaction (ORR) was examined electrochemically to evaluate the influence of dissolved oxygen on the electrodeposition of the hierarchical copper-based micro/nanostructures. Oxygen is a key reactant for the deposition of the copper-based structures, as without it the electrodeposition does not occur (Section 3.2.1.2). Hydroxide ions are present in the structures composed of copper hydroxysulfates (Section 3.2.2). In fact, oxygen is reduced to hydroxide ions which then cause the electroprecipitation of the micro/nanostructures on the film surface. Hydroxide ions cannot be added directly in the electrolyte as insoluble copper hydroxide or hydroxysulfate species would form in solution rather than at the film/solution interface. A series of experiments was performed with PPy-PSS modified electrodes in solutions with or without dissolved oxygen. It was found that the ORR is effectively enhanced by the PPy-PSS films.

The influence of oxygen on the electroactivity of the PPy-PSS modified electrodes was analyzed using cyclic voltammetry (Section 2.5.2.2). The cyclic voltammograms of the bare and modified electrodes were recorded either in nitrogen (A) or oxygen (B) saturated solutions or in aerated (C) solution (Figure 3.37). It is evident that both the electrodes have a wave corresponding to the ORR and that the rate of the reaction increases with the concentration of dissolved oxygen.

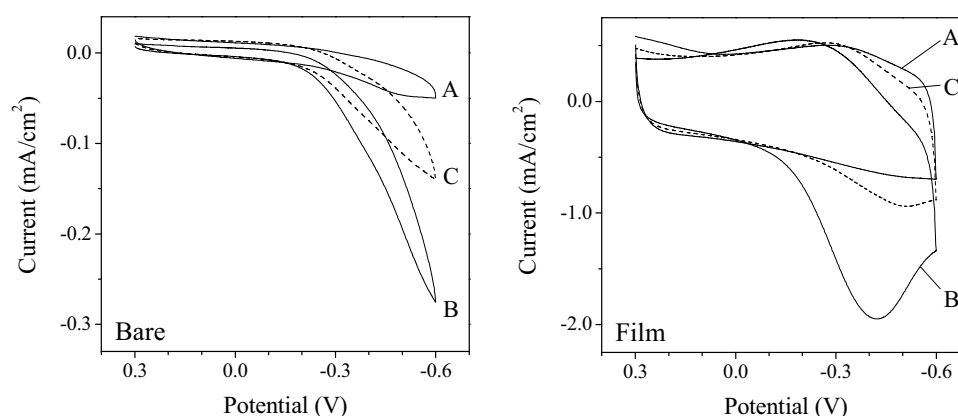


Figure 3.37 Effect of oxygen on the cyclic voltammograms of bare and PPy-PSS modified glassy carbon electrodes. The voltammetric scans were carried out at 100 mV/s in 0.10 M Na_2SO_4 saturated with either nitrogen (A) or oxygen (B), or otherwise aerated (C) solution.

The reduction of oxygen at these potentials is not surprising considering the positive value of its standard redox potential (Section 1.4.2.4), however it is well-known that the ORR is very slow and thus affected by large overpotentials [73].

The ORR at the PPy-PSS modified electrodes was further examined with a rotating disk electrode, RDE (Section 2.5.2.3). The bare and film-modified electrodes were scanned over the same potential range, but this time with the electrode spinning at 2000 rpm. This rotation ensured an efficient transport of oxygen to the surface and consequently larger reduction signals were observed. The net currents of reduction were calculated by subtracting the current measured in nitrogen (A) from the one measured in the oxygen (B) saturated solutions (Figure 3.38). The highest net current was registered at the film-modified electrodes showing the enhanced effect of the film on the ORR.

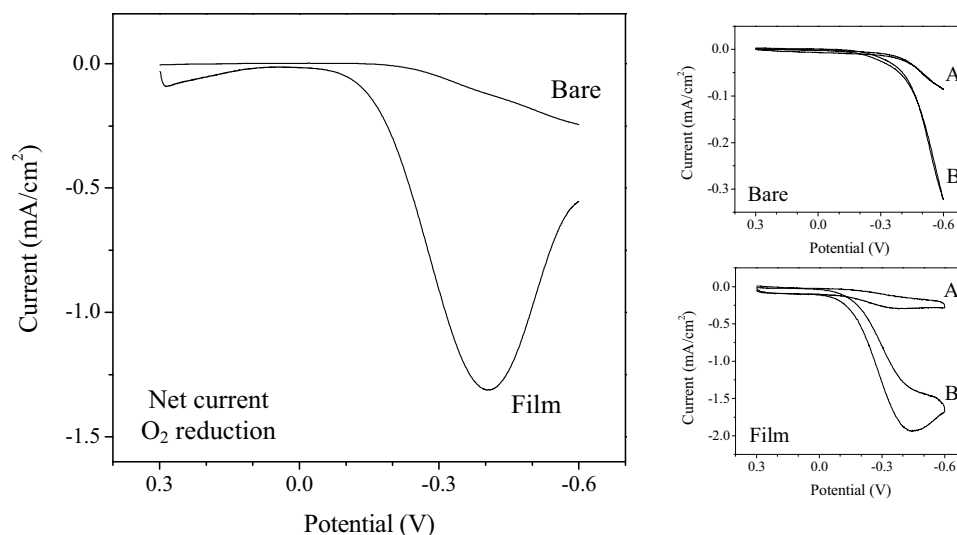


Figure 3.38 Net current of oxygen reduction at bare and PPy-PSS modified rotating disk glassy carbon electrodes (on the left). Cyclic voltammograms of the same electrodes recorded in 0.10 M Na₂SO₄ saturated with either nitrogen (A) or oxygen (B) (on the right). The net current was calculated by subtracting the first reduction sweep in nitrogen (A) from the first one in oxygen (B). The scans were performed at 10 mV/s and 2000 rpm.

The shape of the curves in Figure 3.38 is informative of the nature of the reduction processes. It is evident that none of the curves have the typical sigmoidal shape characteristic of the steady-state mass transport condition (Section 2.5.2.3, Figure 2.5). The reduction process at the bare electrode is probably slow and a plateau

current is not reached. Instead, the peak current at the film-modified electrode might be due to the limited diffusion of oxygen in the polymer film. Since the actual ORR is taking place at the electrode/polymer interface [18, 19], the current starts dropping after the depletion of oxygen present in the film. It is likely that the diffusion of oxygen through the film is too slow to sustain the current flow. However, the ORR at the modified electrodes is clearly enhanced when compared to the bare electrode.

The amount of oxygen reduced at the bare and PPy-PSS modified electrodes was estimated in terms of the net current and charge of reduction at constant potential. Three potentials were considered 0.10, 0.00 and -0.10 V vs. SCE. The net current was calculated from the values recorded in nitrogen (A) and in oxygen (B) saturated solutions (Figure 3.39 and 3.40).

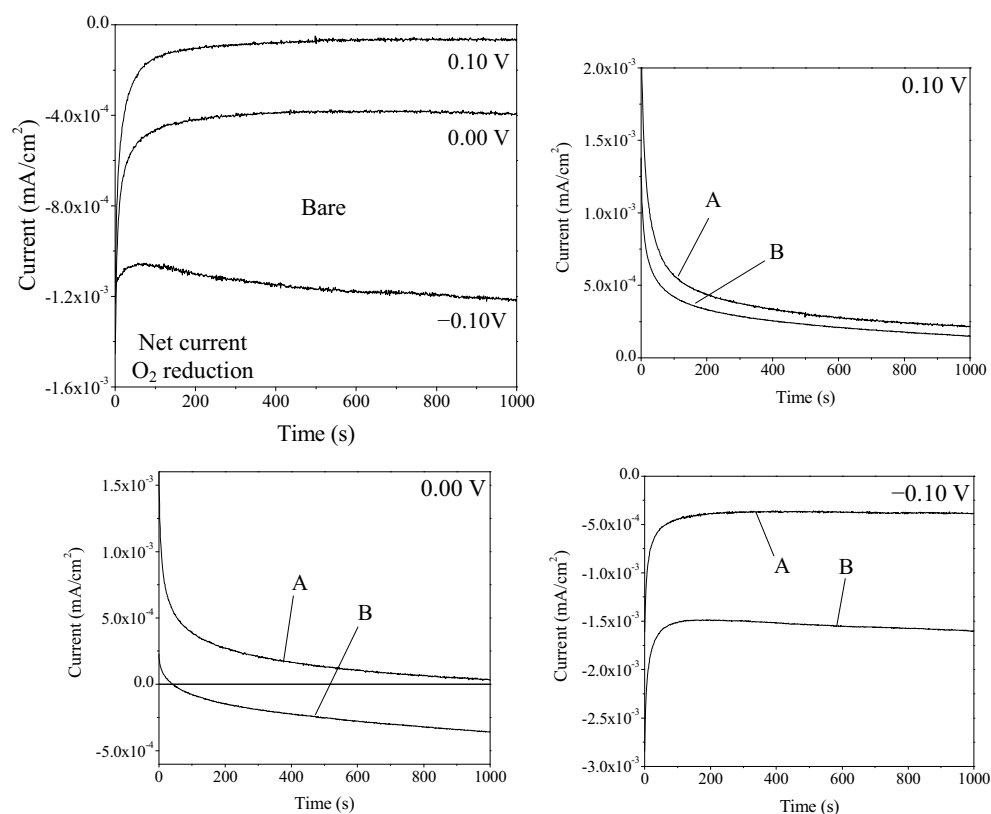


Figure 3.39 Net current of oxygen reduction at a bare rotating disk glassy carbon electrode recorded at 0.10, 0.00 and -0.10 V vs. SCE (large plot). Current profiles registered at the same electrode in 0.10 M Na_2SO_4 saturated either with nitrogen (A) or oxygen (B) at the three different potentials (small plots). The net current was calculated by subtracting the current in nitrogen (A) from the one in oxygen (B). The measurements were performed at 2000 rpm.

The resulting net currents are all reduction currents which become larger at more negative potentials. At the bare electrode, there is a four-fold increase on comparing the currents at 0.10 and 0.00 V vs. SCE, while the current increases twelve times on going from 0.00 to -0.10 V vs. SCE, Figure 3.39. These increases are higher, about five-fold and twenty-fold, respectively, at the modified PPy-PSS electrode, Figure 3.40.

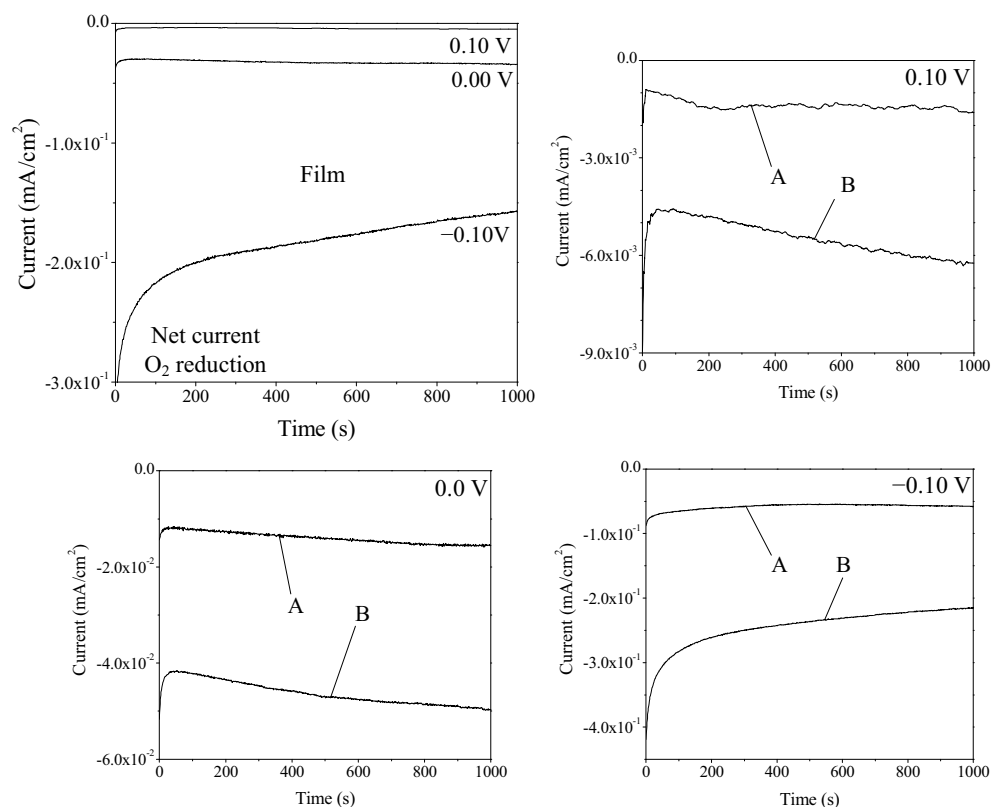


Figure 3.40 Net current of oxygen reduction at a PPy-PSS film-modified rotating disk glassy carbon electrode recorded at 0.10, 0.00 and -0.10 V vs. SCE (large plot). Current profiles registered at the same electrode in 0.10 M Na_2SO_4 saturated either with nitrogen (A) or oxygen (B) at the three different potentials (small plots). The net current was calculated by subtracting the current in nitrogen (A) from the one in oxygen (B). The measurements were performed at 2000 rpm.

The net charge of oxygen reduction can be calculated from the integration of the corresponding currents. The resulting values are plotted in Figure 3.41. The amount of oxygen reduced at the film-modified electrode is considerably larger than that reduced at the bare electrode. This is strong evidence for the significant increase in the rate of the ORR at the PPy-PSS films.

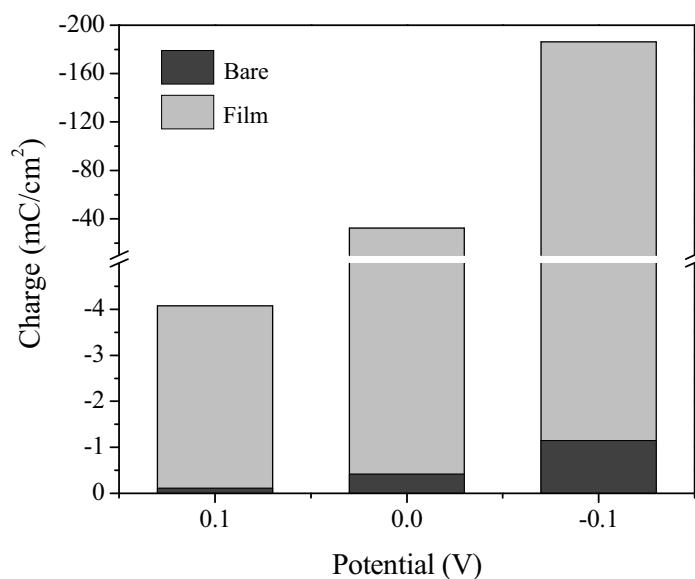


Figure 3.41 Net charge of oxygen reduction at bare and PPy-PSS film-modified rotating disk glassy carbon electrodes obtained from the potentiostatic measurements at 0.10, 0.00 and -0.10 V vs. SCE, corresponding data are shown in Figures 3.39 and 3.40.

In conclusion, the PPy-PSS films enhance the electrochemical reduction of the oxygen dissolved in solution. The fact that the hierarchical micro/nanostructures are made of copper hydroxysulfates (Section 3.2.2) and that the polymer film is deprotonated during the electrodeposition reactions (Section 3.2.2.5), are further evidence of the reduction of oxygen to hydroxide ions at the PPy-PSS films.

3.3 Summary

The present chapter is focused on the electrochemical deposition, characterization and formation of hierarchical copper-based micro/nanostructures made of hydrated mixtures of copper hydroxysulfates. The structures were formed potentiostatically at 0.10 V vs. SCE on polypyrrole-polystyrene sulfonate (PPy-PSS) thin films from 0.10 M CuSO_4 solutions in the presence of dissolved oxygen. The Cu^{2+} and SO_4^{2-} ions present in solution along with the OH^- ions, generated from the reduction of the dissolved oxygen, allowed the progressive formation of the micro/nanostructures. Starting from the nucleation of single nanothin sheets made of nanoparticles, the structures grew hierarchically into the final microclusters.

The main composing elements of the hierarchical micro/nanostructures were Cu, S and O as evidenced from both EDX and XPS analysis (Sections 3.2.2.4 and 3.2.2.5). The presence of SO_4^{2-} and OH^- was confirmed by the ATR-IR spectrum of the structures where the characteristic bands of the two ions were found at about $600\text{-}650\text{ cm}^{-1}$ and $1050\text{-}1150\text{ cm}^{-1}$ for sulfate ions, and about $3300\text{-}3500\text{ cm}^{-1}$ for hydroxide ions. The presence of SO_4^{2-} was further confirmed using XPS with the S 2p and O 1s signals characteristic of sulfate ions.

The hierarchical copper-based micro/nanostructures were composed of a mixture of copper sulfate hydroxide hydrate, $[\text{CuSO}_4]_2[\text{Cu}(\text{OH})_2]_3 \cdot 5\text{H}_2\text{O}$, and posnjakite, $\text{CuSO}_4[\text{Cu}(\text{OH})_2]_3 \cdot \text{H}_2\text{O}$. These two compounds were identified from the XRD pattern of the micro/nanostructures (Section 3.2.2.2). The EQCM data showed a mass-to-charge ratio in agreement with the deposition of such species (Section 3.2.2.3). The ATR-IR spectrum was also characteristic of copper hydroxysulfate compounds with specific features close to brochantite, $\text{CuSO}_4[\text{Cu}(\text{OH})_2]_3$ (Section 3.2.2.6). The XPS spectrum showed the presence of a material rich in CuSO_4 , compared to the hydroxysulfate compounds, at the surface of the micro/nanostructures. The Raman spectra did not allow the identification of any characteristic feature of the copper hydroxysulfate because of the dominant resonance Raman scattering from the PPy-PSS film (Section 3.2.2.7). The stoichiometric ratio of Cu and S in the copper-based structures was estimated from the EDX spectra, but was in poor agreement with the results obtained with the other techniques (Section 3.2.2.4). This discrepancy was due to the fact that the EDX response is strongly biased by the morphology of the sample especially in the case of uneven surfaces (Section 2.5.3.1).

The chemical composition of the micro/nanostructures changed upon reduction at -0.70 and -1.50 V vs. SCE for 15 min. The ATR-IR spectra of the electrode surfaces showed that after reduction the pristine structures were converted from a mixture of copper hydroxysulfates to brochantite and/or posnjakite (Section 3.2.2.6).

The copper-based micro/nanostructures were formed following the occurrence of two simultaneous processes, namely the capture of Cu^{2+} and formation of OH^- both promoted by the PPy-PSS film. The PPy-PSS thin film is known to be a cation exchanger and accordingly can capture the Cu^{2+} cations present in solution upon reduction at 0.10 V vs. SCE (Section 3.2.1.1). Also, the oxygen reduction reaction

(ORR) was strongly promoted by the presence of the polymer film with consequent formation of hydroxide ions (Section 3.2.4). The Cu^{2+} and OH^- ions were concentrated on the polymer surface, which in the presence of the SO_4^{2-} from the electrolyte solution, allowed the electrocrystallization of the hierarchical micro/nanostructures. The SEM micrographs of the different stages of formation of the micro/nanostructures showed that the structures were formed from nanoparticles. The nanoparticles were aligned along nanowires that were then arranged into layered nanosheets. The nanosheets were then arranged concentrically to each other to finally form the hierarchical clusters (Section 3.2.3.1). The nucleation was shown to be progressive and characterized by two distinctive stages of growth. The growth of the nanosheets within the single clusters gave a current profile typical of overlapping nuclei. This was followed by the bulk growth of the microclusters and a corresponding change in the rate of deposition. This change was probably due to the hindrance of the diffusion layers of the micro/nanostructures (Section 3.2.3.2).

Separate studies proved that the ORR was strongly promoted by the presence of the PPy-PSS thin films. The electrochemical measurements showed that the charge of oxygen reduction had a twenty-fold increment in going from the bare to the film-modified electrodes (Section 3.2.4). The formation of hydroxide ions was confirmed using XPS. The N 1s signal had a large peak component due to imine-like nitrogen which was related to the deprotonation of the pyrrolic nitrogen due to the generation of hydroxide ions (Section 3.2.2.5). As shown in the literature (Section 3.2.4), the ORR is enhanced by the film entrapment of the hydrogen peroxide generated at the electrode/polymer interface allowing its improved conversion to hydroxide ions.

At the potential of formation of the copper-based micro/nanostructures, Cu^{2+} can also be partially reduced to Cu^+ when stabilized by the interaction with the pyrrolic nitrogen of PPy (Section 1.5.1.2). The cyclic voltammograms of the films after electrodeposition showed the presence of two redox peaks typical of the Cu(II)/Cu(I) redox couple (Section 3.2.2.1). In the XPS Cu 2p_{3/2} signal a peak related to Cu(I) species was also found after deconvolution, while the presence of Cu species in the film was also confirmed using EDX (Section 3.2.2.5). The amount of Cu(I) after reduction at -1.00 V vs. SCE for 5 min was estimated to be about 36 % of the total deposited copper (Section 3.2.2.1).

3.4 References

- [1] Lakes R; *Nature*, **1993**, 361(6412), 511
- [2] Xu J, Tang YB, Zhang WX, Lee CS, Yang ZH, Lee ST; *Crystal Growth & Design*, **2009**, 9(10), 4524
- [3] Zhang YJ, Or SW, Wang XL, Cui TY, Cui WB, Zhang Y, Zhang ZD; *European Journal of Inorganic Chemistry*, **2009**, (1), 168
- [4] Liu JP, Huang XT, Li YY, Sulieman KM, He X, Sun FL; *Journal of Materials Chemistry*, **2006**, 16(45), 4427
- [5] Lai CX, Wu QB, Chen J, Wen LS, Ren S; *Nanotechnology*, **2010**, 21(21),
- [6] Wang YJ, Tsai AT, Yang CS; *Materials Letters*, **2009**, 63(11), 847
- [7] Xu KJ, Ding WP; *Materials Letters*, **2008**, 62(29), 4437
- [8] Zhang X, Guo YG, Zhang PY, Wu ZS, Zhang ZJ; *Materials Letters*, **2010**, 64(10), 1200
- [9] Dubal DP, Dhawale DS, Salunkhe RR, Jamdade VS, Lokhande CD; *Journal of Alloys and Compounds*, **2010**, 492(1-2), 26
- [10] Zhang Y, He XL, Li JP, Zhang HG, Gao XG; *Sensors and Actuators B-Chemical*, **2007**, 128(1), 293
- [11] Cao AM, Monnell JD, Matranga C, Wu JM, Cao LL, Gao D; *Journal of Physical Chemistry C*, **2007**, 111(50), 18624
- [12] Guo ZG, Liu WM, Su BL; *Applied Physics Letters*, **2008**, 92(6),
- [13] Xiang JY, Tu JP, Zhang L, Zhou Y, Wang XL, Shi SJ; *Electrochimica Acta*, **2010**, 55(5), 1820
- [14] Kwak CH, Cho IS, Lee S, An JS, Hong KS; *Journal of Nanoscience and Nanotechnology*, **2010**, 10(2), 1185
- [15] Xu JS, Xue DF; *Journal of Physical Chemistry B*, **2005**, 109(36), 17157
- [16] Guo ZG, Fang J, Hao JC, Liang YM, Liu WM; *Chemphyschem*, **2006**, 7(8), 1674
- [17] Carbajal Arizaga GG, Satyanarayana KG, Wypych F; *Solid State Ionics*, **2007**, 178(15-18), 1143
- [18] Jakobs RCM, Janssen LJJ, Barendrecht E; *Electrochimica Acta*, **1985**, 30(8), 1085
- [19] Jakobs RCM, Janssen LJJ, Barendrecht E; *Electrochimica Acta*, **1985**, 30(11), 1433
- [20] Jerome C, Martinot L, Strivay D, Weber G, Jerome R; *Synthetic Metals*, **2001**, 118(1-3), 45
- [21] Mangold KM, Weidlich C, Schuster J, Juttner K; *Journal of Applied Electrochemistry*, **2005**, 35(12), 1293
- [22] Weidlich C, Mangold KM, Juttner K; *Electrochimica Acta*, **2005**, 50(7-8), 1547
- [23] Baker CK, Reynolds JR; *Journal of Electroanalytical Chemistry*, **1988**, 251(2), 307
- [24] Asavapiriyant S, Chandler GK, Gunawardena GA, Pletcher D; *Journal of Electroanalytical Chemistry*, **1984**, 177(1-2), 229

-
- [25] Baker CK, Qiu YJ, Reynolds JR; *Journal of Physical Chemistry*, **1991**, 95(11), 4446
- [26] Naoi K, Lien M, Smyrl WH; *Journal of the Electrochemical Society*, **1991**, 138(2), 440
- [27] Armstrong RD, Harrison JA; *Journal of the Electrochemical Society*, **1969**, 116(3), 328
- [28] Cioffi N, Torsi L, Losito I, Di Franco C, De Bari I, Chiavarone L, Scamarcio G, Tsakova V, Sabbatini L, Zambonin PG; *Journal of Materials Chemistry*, **2001**, 11(5), 1434
- [29] Liu YC, Hwang BJ; *Thin Solid Films*, **1999**, 339(1-2), 233
- [30] Kang MC, Gewirth AA; *Journal of Physical Chemistry B*, **2002**, 106(47), 12211
- [31] Kautek W, Gordon JG; *Journal of the Electrochemical Society*, **1990**, 137(9), 2672
- [32] Mayer ST, Muller RH; *Journal of the Electrochemical Society*, **1992**, 139(2), 426
- [33] Pyun CH, Park SM; *Journal of the Electrochemical Society*, **1986**, 133(10), 2024
- [34] Noda T, Inagaki M; *Bulletin of the Chemical Society of Japan*, **1964**, 37(10), 1534
- [35] Suh IK, Ohta H, Waseda Y; *Journal of Materials Science*, **1988**, 23(2), 757
- [36] Yang R, Naoi K, Evans DF, Smyrl WH, Hendrickson WA; *Langmuir*, **1991**, 7(3), 556
- [37] Yang R, Evans DF, Christensen L, Hendrickson WA; *Journal of Physical Chemistry*, **1990**, 94(15), 6117
- [38] Buckley LJ, Roylance DK, Wnek GE; *Journal of Polymer Science Part B-Polymer Physics*, **1987**, 25(10), 2179
- [39] Yoder CH, Gotlieb NR, Rowand AL; *American Mineralogist*, **2010**, 95(1), 47
- [40] Frost RL, Williams PA, Martens W, Leverett P, Kloprogge JT; *American Mineralogist*, **2004**, 89(7), 1130
- [41] Mrose ME; *American Mineralogist*, **1961**, 46(1-2), 146
- [42] Goldstein J, Newbury DE, Joy DC, Lyman CE, Echlin P, Lifshin E, Sawyer L, Michael JR; *Scanning Electron Microscopy and X-ray Microanalysis*; 2003, 3rd ed., Springer
- [43] Kanani N; *Electroplating: Basic Principles, Processes and Practice*; 2005, Elsevier Science
- [44] Hayez V, Franquet A, Hubin A, Terryn H; *Surface and Interface Analysis*, **2004**, 36(8), 876
- [45] Klein JC, Chung PL, Hercules DM, Black JF; *Applied Spectroscopy*, **1984**, 38(5), 729
- [46] Klein JC, Proctor A, Hercules DM, Black JF; *Analytical Chemistry*, **1983**, 55(13), 2055
- [47] Hammond JS, Winograd N; *Journal of the Electrochemical Society*, **1977**, 124(6), 826
- [48] Zotti G, Zecchin S, Schiavon G, Louwet F, Groenendaal L, Crispin X, Osikowicz W, Salaneck W, Fahlman M; *Macromolecules*, **2003**, 36(9), 3337
-

-
- [49] Nefedov VI, Zhumadilov EK, Kopytova TY; *Journal of Structural Chemistry*, **1977**, 18(4), 549
- [50] Nefedov VI, Salyn YV, Solozhenkin PM, Pulatov GY; *Surface and Interface Analysis*, **1980**, 2(5), 170
- [51] Strohmeier BR, Leyden DE, Field RS, Hercules DM; *Journal of Catalysis*, **1985**, 94(2), 514
- [52] Ruangchuay L, Schwank J, Sirivat A; *Applied Surface Science*, **2002**, 199(1-4), 128
- [53] Kang ET, Neoh KG, Tan KL; *Photoelectron Spectroscopy of Conducting Polymers, Pyrrole Polymers*, Handbook Of Organic Conductive Molecules And Polymers: Conductive Polymers: Spectroscopy And Physical Properties, Volume 3, 1997, John Wiley & Sons Ltd.
- [54] Liu YC, Yang KH, Ger MD; *Synthetic Metals*, **2002**, 126(2-3), 337
- [55] Li S, Qiu YB, Guo XP; *Reactive & Functional Polymers*, **2009**, 69(10), 743
- [56] Tan KL, Tan BTG, Kang ET, Neoh KG; *Journal of Chemical Physics*, **1991**, 94(8), 5382
- [57] Aykanat A, Iroh JO; *Composite Interfaces*, **2002**, 9(1), 61
- [58] Liang CY, Krimm S; *Journal of Polymer Science*, **1958**, 27(115), 241
- [59] Secco EA; *Canadian Journal of Chemistry-Revue Canadienne De Chimie*, **1988**, 66(2), 329
- [60] Ramamurthy P, Secco EA; *Canadian Journal of Chemistry*, **1970**, 48(22), 3510
- [61] Omori K, Kerr PF; *Geological Society of America Bulletin*, **1963**, 74(6), 709
- [62] Burke ML, Madix RJ; *Journal of Physical Chemistry*, **1988**, 92(7), 1974
- [63] Choi CS, Tachikawa H; *Journal of the American Chemical Society*, **1990**, 112(5), 1757
- [64] Qu LT, Shi GQ; *Journal of Polymer Science Part a-Polymer Chemistry*, **2004**, 42(13), 3170
- [65] Vigmond SJ, Ghaemmaghami V, Thompson M; *Canadian Journal of Chemistry-Revue Canadienne De Chimie*, **1995**, 73(10), 1711
- [66] Balamurugan B, Mehta BR, Avasthi DK, Singh F, Arora AK, Rajalakshmi M, Raghavan G, Tyagi AK, Shivaprasad SM; *Journal of Applied Physics*, **2002**, 92(6), 3304
- [67] Gong YS, Lee CP, Yang CK; *Journal of Applied Physics*, **1995**, 77(10), 5422
- [68] Frost RL; *Spectrochimica Acta Part a-Molecular and Biomolecular Spectroscopy*, **2003**, 59(6), 1195
- [69] Martens W, Frost RL, Kloprogge JT, Williams PA; *Journal of Raman Spectroscopy*, **2003**, 34(2), 145
- [70] Liu YC, Hwang BJ, Jian WJ, Santhanam R; *Thin Solid Films*, **2000**, 374(1), 85
- [71] Scharifker B, Hills G; *Electrochimica Acta*, **1983**, 28(7), 879
- [72] Eliaz N, Eliyahu M; *Journal of Biomedical Materials Research Part A*, **2007**, 80A(3), 621
- [73] Nørskov JK, Rossmeisl J, Logadottir A, Lindqvist L, Kitchin JR, Bligaard T, Jøsson H; *Journal of Physical Chemistry B*, **2004**, 108(46), 17886
-

Chapter 4

Electrochemical Conversion of Hierarchical Copper Micro/Nanostructures to Metallic Copper Nanoparticles and their Application to Nitrate Sensing

4. Electrochemical Conversion of Hierarchical Copper Micro/Nanostructures to Metallic Copper Nanoparticles and their Application to Nitrate Sensing

4.1 Introduction

The equations governing the thermodynamic (Nernst) and kinetic (Butler-Volmer) evolution of electrochemical processes imply a direct correlation between applied potential, surface concentrations and current [1, 2]. In relation to the present case, the changes of composition and structure of the copper deposits, upon a controlled decrease of electrode potential, are normal effects of this correlation. Consequently, as described in this chapter, the hierarchical micro/nanostructures are replaced by simple microstructures and microcrystals following a few hundred millivolts decrease of potential (Section 4.2.1). The variety of structure and composition changes recorded within such a narrow potential range is a direct consequence of the different types of electrochemical processes involved at the PPy-PSS surface. The various structures are combined together through a simple one-pot fabrication procedure to give hybrid microstructures (Section 4.2.2). A less predictable effect of the potential is the conversion of the hierarchical copper-based micro/nanostructures to metallic copper nanoparticles upon application of a strong reduction potential. In this case the structures crumble into particles under the combined action of hydrogen gas evolution and direct electroreduction (Section 4.2.3). The copper nanoparticles are tested for nitrate sensing applications (Section 4.2.5). The sensing performance is further improved by introducing functionalized multiwall carbon nanotubes in the polymer film (Section 4.2.6.3).

Nanoparticles are well known for their catalytic activity and use in electroanalytical applications [3-5]. However, a major drawback of having nanoparticles supported on conducting polymer films is the insulating barrier introduced by the polymer at reduction potentials. This is especially true in sensing applications, where the electrons necessary to reduce the analyte have to go across the resistive film in order to be supplied to nanoparticles. A possible solution to this problem is to introduce conducting pathways in the film by incorporating carbon nanotubes (CNT) which are

superior in terms of electronic properties [6, 7]. The dispersion of CNT in water requires either functionalization or addition of dispersing agents [8, 9]. Accordingly, the multiwall carbon nanotubes (MWNT) used in the present work were functionalized with highly branched polyethylenimine following the synthetic route developed by Liao *et al.* [10].

Copper nanoparticles have been applied for the electrochemical sensing of many different analytes like, for example, carbohydrates, amino acids, nitric oxide, nitrite and nitrate [11]. Nitrate, in particular, is hazardous for both the environment, causing eutrophication of natural water when in the presence of phosphates, and human health, leading to infant methemoglobinemia from nitrate dietary intake [12, 13]. Nitrate can be detected by several spectroscopic, chromatographic and electrochemical methods [14]. Electrochemical methods are particularly attractive since they are usually simpler to apply. Copper nanoparticles and copper modified electrodes have been already used for the electrochemical sensing of nitrate [11, 15, 16], and detection limits as low as 0.76 μM have been achieved [15]. The limit imposed by the European Drinking Water Directive is 50 ppm in nitrate content corresponding to about 0.8 mM nitrate concentration [17], whereas the US Environmental Protection Agency set a limit of 10 ppm in nitrogen content corresponding to about 0.7 mM nitrate concentration [18].

Copper nanoparticles have been electrodeposited on polypyrrole films using different methods. The electrochemical deposition of copper nanocrystals on ultrathin polypyrrole films allows precise control of the distribution and morphology of the copper deposit through the variation of the polymer thickness, electrode potential and electrolyte concentration [19]. The type of deposition, either galvanostatic or potentiostatic, also influences the characteristics of the copper nano-deposits together with the film thickness [20, 21]. The deposition of metal nanoparticles on conducting polymers is also shown to be affected by the initial oxidation state of the polymer, the presence of metal/polymer interactions, and by the use of metal ion complexes instead of free metal ions [22]. The conversion of the hierarchical micro/nanostructures to nanoparticles, which is described in this chapter, is an additional proof of the variety of nanomaterials that can be electrodeposited on polypyrrole thin films.

4.2 Results and Discussion

4.2.1 Effect of the Potential on the Electrodeposition of Copper Materials

The electrochemical deposition of copper at polypyrrole-polystyrene sulfonate (PPy-PSS) thin films is strongly dependent on the electrode potential. This dependence was studied at three different potentials, 0.10 V, 0.00 V and -0.10 V vs. SCE, and the resulting current-time profiles are shown in Figure 4.1. The deposition at 0.10 V vs. SCE gives the formation of hierarchical copper-based micro/nanostructures as discussed in Chapter 3. The current intensity at 0.00 and -0.10 V vs. SCE increases by one and two orders of magnitude, respectively, when compared to that of the hierarchical structures. This sudden increase of current, in the narrow range of 200 mV, is due to the deposition of other copper species at the film surface (Section 3.2.1.2). The nature of the copper deposits is mainly dependent on the pH at the film surface as predicted by the Pourbaix diagram, and on the presence of the sulfate ions in the electrolyte solutions (Section 1.5.1.2).

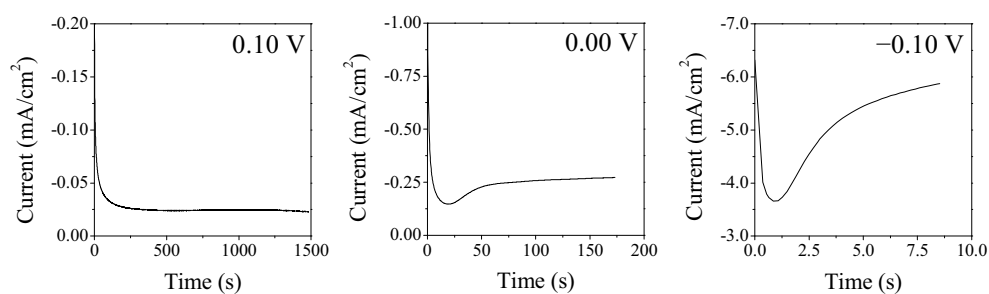


Figure 4.1 Current-time data for the electrodeposition of copper at PPy-PSS films in aerated 0.10 M CuSO₄ at 0.10 V, 0.00 V and -0.10 V vs. SCE. Each current profile corresponds to a total charge of 40 mC/cm². The PPy-PSS films were 120 nm thick.

The pH at the film surface is influenced by the reduction of oxygen, dissolved in solution, to hydroxide ions (Section 3.2.4). Hence, the copper electrodeposits could possibly contain any or a mixture of copper metal, copper oxides and copper hydroxysulfates. In order to shed some light on the actual nature of the deposited materials, the modified films were characterized by SEM-EDX after each electrodeposition. The micrographs and corresponding EDX spectra of the various deposits are shown in Figure 4.2.

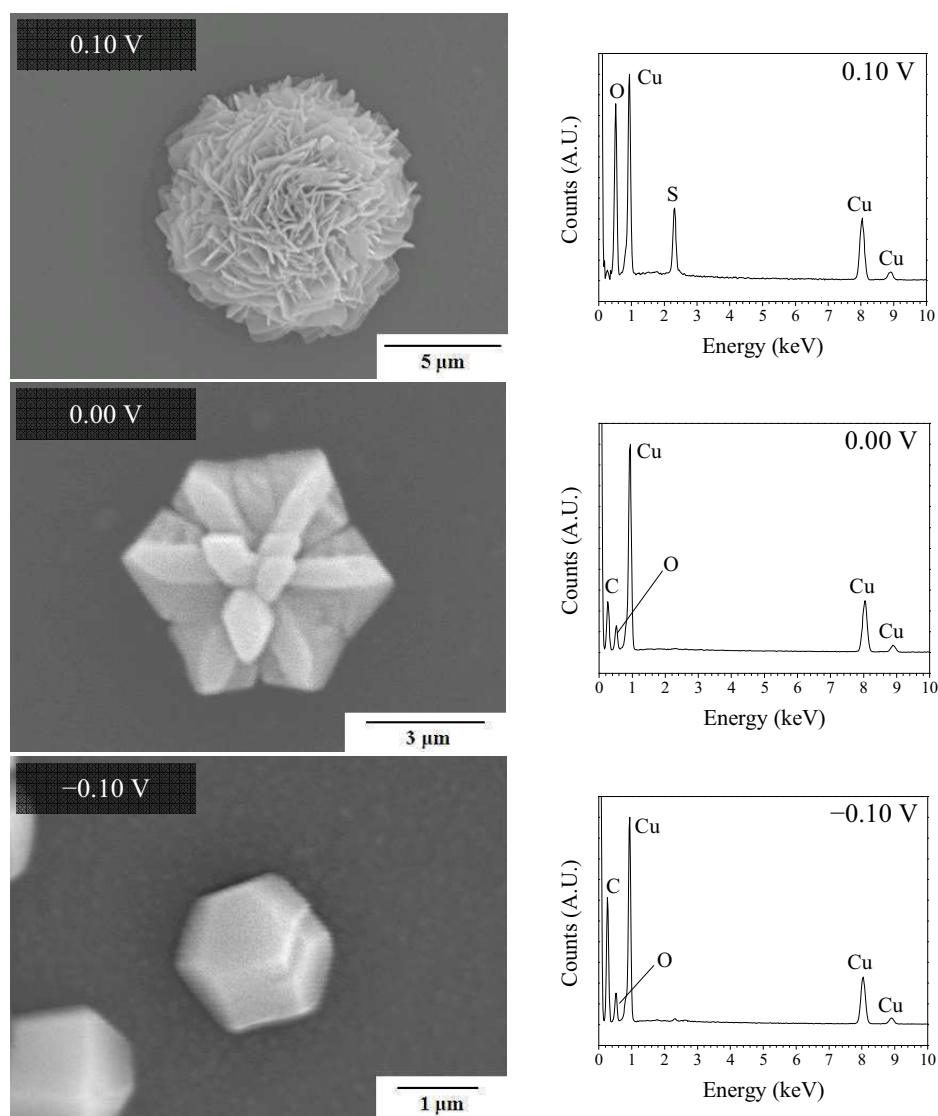


Figure 4.2 SEM micrographs and EDX spectra of copper materials deposited at PPy-PSS films at 0.10 V, 0.00 V and -0.10 V vs. SCE under the same conditions as given in Figure 4.1. The main EDX peaks were assigned to Cu, S and O, as described in Section 3.2.2.4, Figure 3.22. The carbon (C) peak was due to the glassy carbon electrode present underneath the deposits.

The first striking observation is the variation in the shape of the materials with the decrease of the deposition potential. The hierarchical copper-based micro/nanostructures are only formed at 0.10 V vs. SCE. These are replaced with microstructures at 0.00 V vs. SCE and single microcrystals at -0.10 V vs. SCE. The composition is also dependent on the electrode potential. The EDX spectra show the presence of sulfur only in the micro/nanostructures. This was not detected in the samples of the other two materials. Hence, the formation of copper hydroxysulfates at 0.00 V and -0.10 V vs. SCE is excluded.

The Cu and O peaks of the two materials electrodeposited at 0.00 V and -0.10 V vs. SCE are compared to those of the Cu_2O and CuO standards, as shown in Figure 4.3 (more details about the standards are given in Section 3.2.2.4, Figure 3.22). In order to obtain similar signal-to-noise ratios, the count time for the two microdeposits was set 3 and 5 times longer than that of the copper oxide standards, for the 0.00 V and -0.10 V vs. SCE deposits, respectively. For this reason, the peaks of the samples turned out to be narrower than those of the standards excluding a direct comparison of the peak intensities. For both the microdeposits, the relative area of the O peak with respect to the area of the Cu peak was roughly between that of the Cu_2O and CuO standards. As a result, the EDX spectra could not be used to estimate if the deposits were made of Cu_2O or CuO .

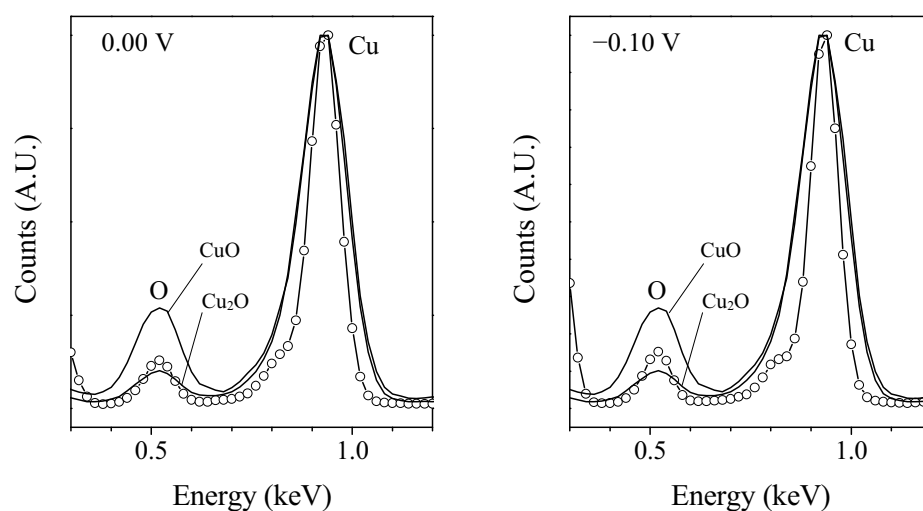


Figure 4.3 Comparison of the EDX spectra of the copper microdeposits ($-\circ-$) prepared at 0.00 V and -0.10 V vs. SCE and the CuO and Cu_2O standards ($—$). The O peak is at about 0.5 keV, while the Cu peak appears at about 0.9 keV. The microdeposits were prepared, as detailed in Figure 4.1.

In the case of the deposit formed at -0.10 V vs. SCE, some general indications can also be obtained from the geometrical shape of the single microcrystals. In Figure 4.4, the shapes of three representative microcrystals are compared to the geometrical shapes of a cubooctahedral crystal. Apparently, the microcrystals have the shape of truncated pyramids, which is characteristic of Cu_2O crystals in the case of similar growth rates along the $\langle 100 \rangle$ and $\langle 111 \rangle$ directions [23, 24]. This finding is interesting,

but this simple analysis only provides a preliminary indication of the structure of the copper deposits. More detailed information using X-ray diffraction is needed before the crystal structure can be identified with certainty.

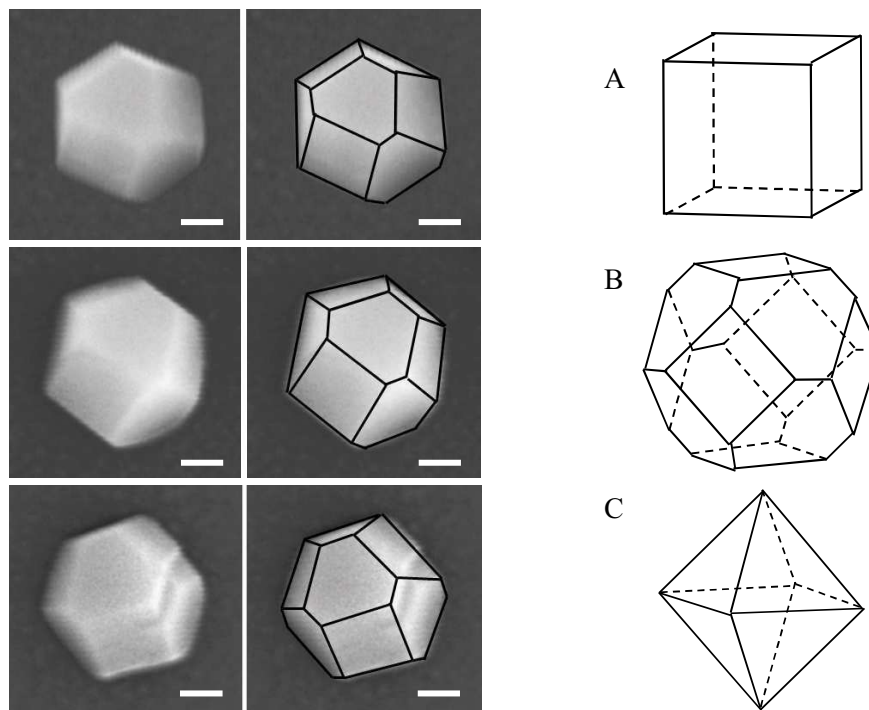


Figure 4.4 SEM micrographs of single microcrystals deposited at PPy-PSS films from 0.10 M CuSO_4 at -0.10 V vs. SCE (all scale bars are 500 nm). The shape of the crystals is evidenced by the black borders and can be compared to the geometrical shapes of the cubooctahedral crystal on the right-hand side. The shape of the cubooctahedron is dependent on the relative magnitude of crystal growth rates along the $\langle 100 \rangle$ and $\langle 111 \rangle$ directions. The shape (A) is obtained when the crystal growth rate along $\langle 111 \rangle$ is prevalent to the one along $\langle 100 \rangle$, vice versa for (C). The shape (B), with truncated pyramids, is obtained at comparable growth rates along the two directions [23, 24].

The variety of structures formed upon a 200 mV change of potential is remarkable evidence of the diverse processes involved at the film/solution interface during the electrochemical depositions. As described in Chapter 3, the capture of Cu^{2+} ions from the solution by the PPy-PSS film is one of these processes. The efficient nucleation of the copper deposits is enhanced by the high localized surface concentration of captured Cu^{2+} ions. However, other simultaneous interfacial reactions determine the shape and composition of the deposits. At 0.10 V vs. SCE, the deposition is governed by the presence of sulfate and hydroxide ions from the electrolyte solution and the oxygen reduction reaction. Again, the film

electrochemistry plays a major role at this stage by enhancing the hydroxide formation. At the lower potentials of 0.00 V and -0.10 V vs. SCE, the reduction of oxygen occurs at a higher rate, leading to the pH increase necessary for formation of sulfur-free copper oxides/hydroxides. For this reason, it can be concluded that a simple electrode modified with a PPy-PSS film is a real inexpensive tool with a broad interfacial chemistry for the deposition of micro/nanomaterials with various properties and compositions.

4.2.2 Fabrication of Hybrid Copper-Based Microstructures

The electrochemical deposition of various kinds of copper materials and structures at the PPy-PSS films is possible because of the different processes involved at the film surface. These processes are in simultaneous competition and the outcome of the electrodeposition is dependent on their relative rates. These rates can be altered by changing the electrode potential, implying that a reaction can be excluded through the application of an appropriate potential. In the present case this reaction is the electrocrystallization of hydroxysulfate species which is dominant at 0.10 V vs. SCE, but excluded below 0.00 V vs. SCE. The same consideration is true if the potentials are applied in the opposite direction. For example, if the first potential applied to the polymer film was -0.10 V vs. SCE, the deposited species would be microcrystals, but then at 0.10 V vs. SCE the deposited species would become hierarchical micro/nanostructures, all on the same electrode modified surface. This would provide the means of coupling the two structures in order to form a hybrid that is actually a new structure different from the original two. This is actually achieved in the present work with relative ease.

The electrochemical deposition of hybrid copper-based microstructures was performed at PPy-PSS films by applying first a short potential pulse at -0.10 V vs. SCE, followed by a prolonged deposition at 0.10 V vs. SCE. The resulting structures are shown in Figure 4.5.

The structures, as expected, are made of two components. The central component is a microcrystal, shown in Figure 4.2, whereas the surrounding material is a contour of welded sheets. Micrograph 1a shows a group of hybrids that are mostly of similar size and shape, with each microcrystal evenly adorned.

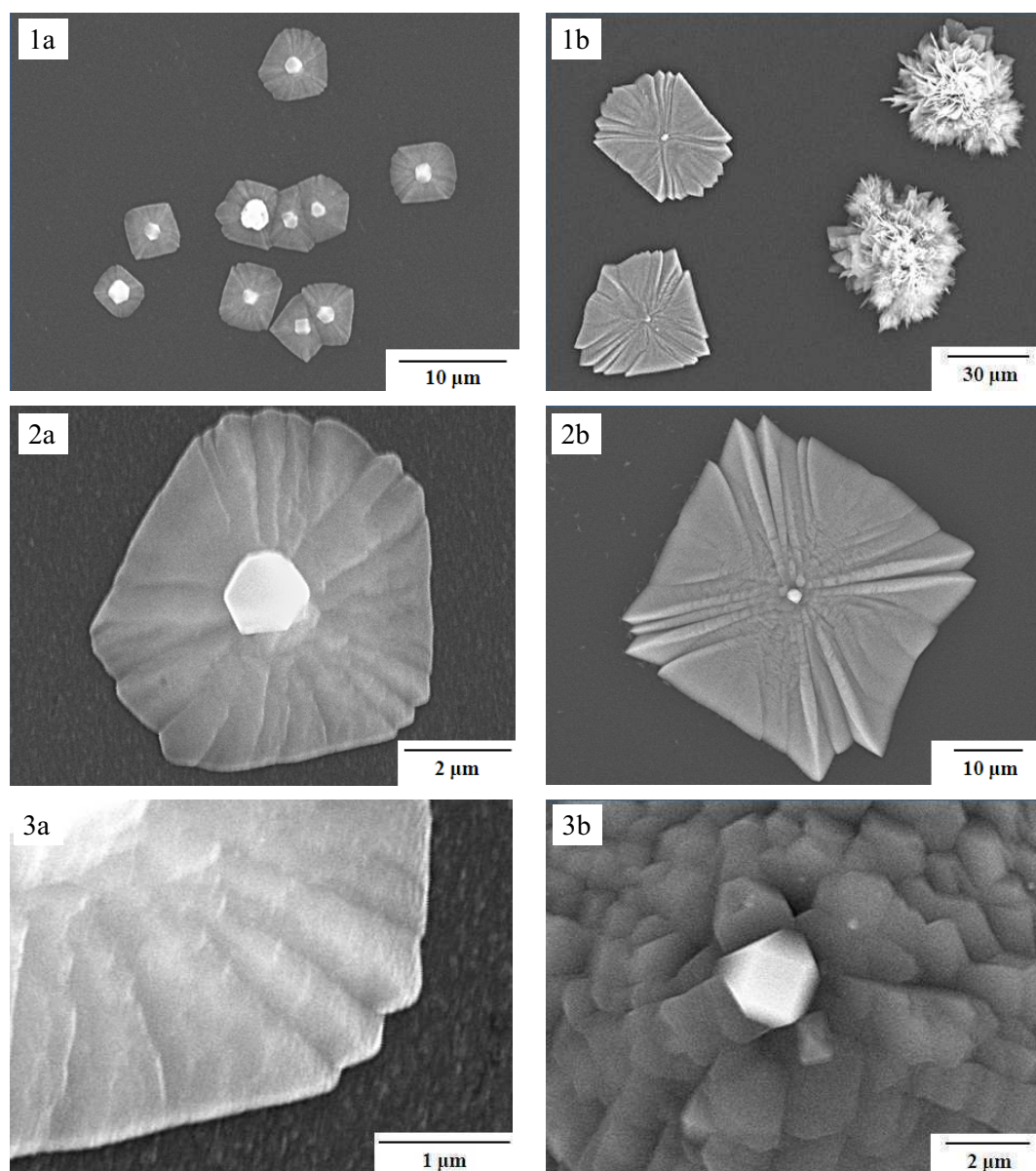


Figure 4.5 Hybrid copper-based microstructures deposited electrochemically on PPy-PSS thin films from a 0.10 M CuSO_4 after a pulse at -0.10 V vs. SCE for 10 s followed by constant potential deposition at 0.10 V vs. SCE for a total charge of (a) 40 mC/cm^2 and (b) 400 mC/cm^2 . The thickness of the films was 120 nm.

Micrographs 2a and 3a show the details of the welded sheets that are concentrically distributed around the microcrystal. The hybrids in 1b, 2b and 3b are larger versions of the ones shown in 1a, 2a and 3a, as they were deposited for a considerably longer period of time at 0.10 V vs. SCE (400 mC/cm^2 compared to 40 mC/cm^2). Interestingly, the central microcrystal does not increase in size with continued deposition at 0.1 V vs. SCE, but, the surrounding welded segment increase considerably to give hybrid dimensions as wide as $50 \mu\text{m}$ (diagonal). Moreover, as

shown from a comparison of micrographs 3a and 3b, the surface morphology of the welded structure becomes rougher with increasing deposition periods. Also, for long deposition periods the formation of independent hierarchical micro/nanostructures is observed on the film, as shown in micrograph 1b.

The flat and welded appearance of the hybrids, instead of being made from clusters of individual nanosheets, is likely to be due to a seeding effect of the central microcrystals [25]. These crystals may act as seeds for the nucleation of the copper hydroxysulfate sheets that expand flat from the center onto the film surface, rather than growing into the hierarchical micro/nanostructure, as seen in Chapter 3. Discrete hybrids are formed, but as evident from micrograph 1a, if the initial microcrystal nucleation sites are not sufficiently far apart, the hybrids can merge to give more complex structures.

4.2.3 Conversion of Hierarchical Copper-Based Micro/Nanostructures to Metallic Copper Nanoparticles

The electrochemical reduction of the hierarchical copper-based micro/nanostructures was performed at various potentials in order to convert the copper present in the structures to copper metal. As shown in Chapter 3, the application of a reduction potential to the copper-based micro/nanostructures has two main effects. These are the formation of Cu(I) species and the conversion of the hierarchical structures from a mixture of copper hydroxysulfates to mostly brochantite and/or posnjakite (Sections 3.2.2.1 and 3.2.2.6). In this section, the effect of the reduction is further examined.

The pristine micro/nanostructures were reduced at -0.70 V, -1.50 V or -2.00 V vs. SCE in aerated 0.10 M Na_2SO_4 . The EDX spectra of the products of reduction are compared to the spectrum of the pristine structures in Figure 4.6. The treatments at -0.70 V and -1.50 V vs. SCE for 15 min leave the morphology of the structure practically unchanged (not shown here), but cause a decrease in oxygen and sulfur content in both cases. This is in agreement with the results presented in Chapter 3, where upon a reduction treatment at -1.00 V vs. SCE for 5 min, some of the Cu(II) hydroxysulfates are converted to Cu(I) species with consequent loss of oxygen and sulfur (*i.e.*, copper-pyrrolic nitrogen complexes or cuprous oxide). The treatment

at -2.00 V vs. SCE for 5 min has a major effect on the composition of the micro/nanostructures. Both the sulfur and oxygen contents are removed almost completely. At this potential, the hierarchical structures are converted to nanoparticles, as shown clearly in Figure 4.7. Considering the high reduction potential and the consequent evolution of a copious amount of hydrogen gas, the nanoparticles are assumed to be made of Cu(0). The small peaks of oxygen and sulfur are likely to be related to the presence of residual sulfate, and to the formation of an oxide layer on the metallic nanoparticles exposed to air when analyzed *ex-situ* [26, 27].

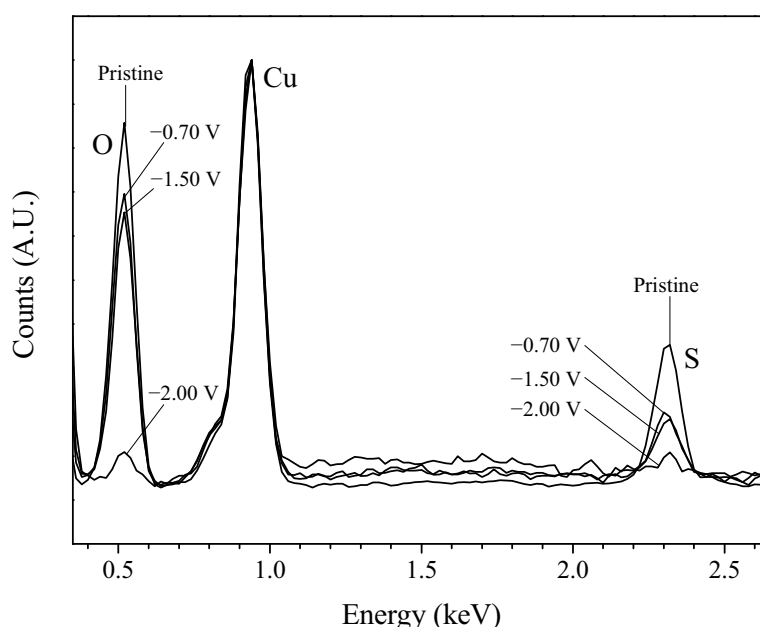


Figure 4.6 EDX spectra of hierarchical copper-based micro/nanostructures pristine and reduced at -0.70 V or -1.50 V vs. SCE for 15 min, or -2.00 V vs. SCE for 5 min in 0.10 M Na_2SO_4 . The three peaks are related to copper (Cu), sulfur (S) and oxygen (O).

The morphological changes of the copper-based micro/nanostructures upon the application of -2.00 V vs. SCE, for two different time intervals, are shown in Figure 4.7. After the application of this potential for 1 min, the hierarchical structures become surrounded by a uniform and sparse distribution of nanoparticles. If the potential is held for 5 min, the hierarchical structures disappear and in their place circular distributions of copper nanoparticles are found. A closer inspection of the micro/nanostructure reveals the actual erosion of the nanosheets due to the reduction, from their smooth appearance

in the pristine state to the jagged borders after reduction. The erosion of the hierarchical structure is probably due to the evolution of hydrogen gas at the film surface.

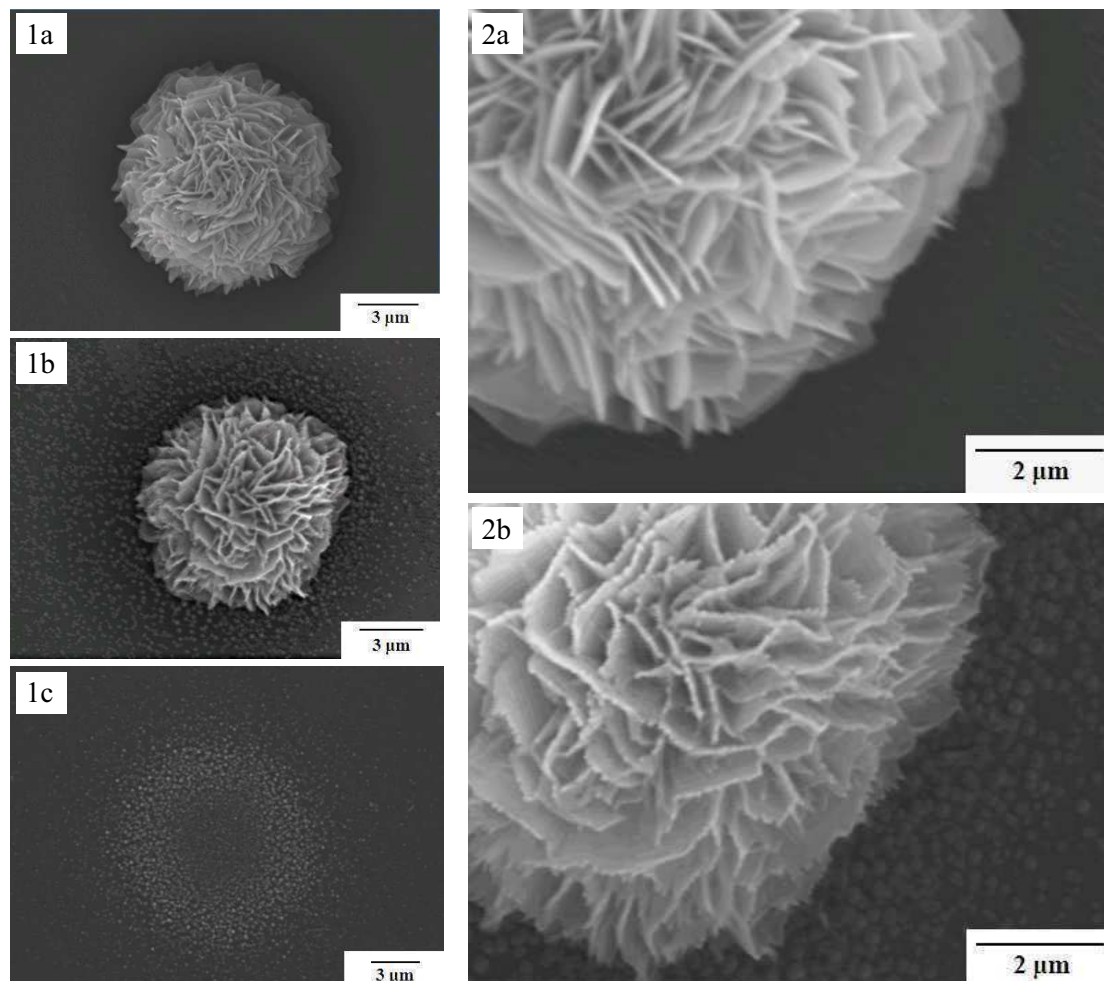


Figure 4.7 SEM micrographs of the hierarchical copper-based micro/nanostructures before and after reduction treatment. The pristine structure in 1a and 2a was reduced at -2.00 V vs. SCE for 1 min to give the eroded structure in 1b and 2b, or at -2.00 V vs. SCE for 5 min to give the distribution of nanoparticles shown in 1c.

The number and distribution of the nanoparticles is dependent on the preceding deposition of the copper-based micro/nanostructures. The deposition of structures from oxygen saturated copper sulfate solutions allows the formation of a larger number of smaller clusters, and consequently the production of higher amounts of copper nanoparticles, as shown in Figure 4.8. The size and arrangement of the nanoparticles on the film surface are given in Figure 4.9.

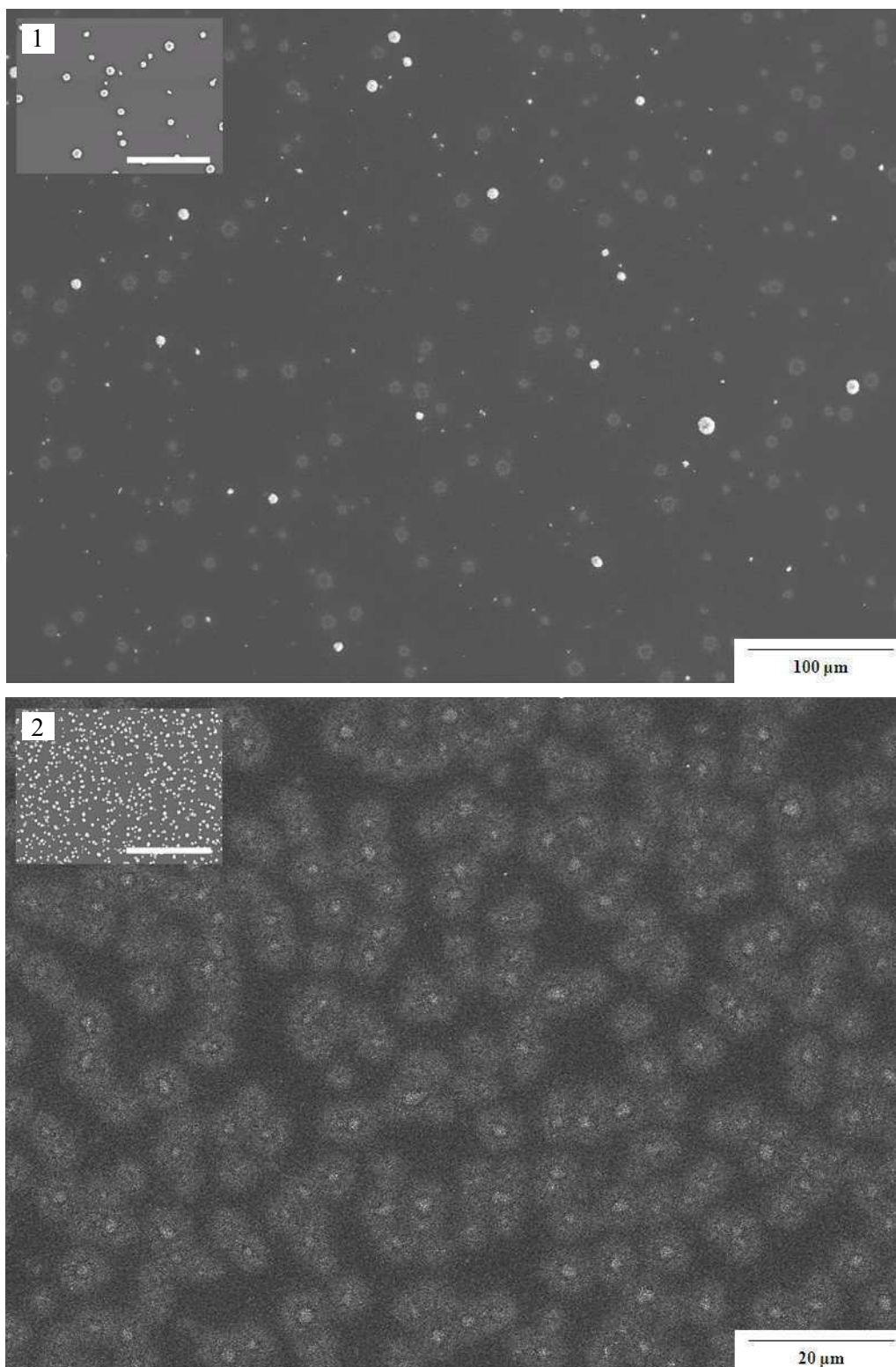


Figure 4.8 Number and distribution of the copper nanoparticles produced from the reduction of hierarchical copper-based micro/nanostructures at -2.00 V vs. SCE in 0.10 M Na_2SO_4 . The nanoparticles were formed from the clusters shown in the insets (the scale bars are both 60 μm). The top micrograph is related to the nanoparticles formed from clusters deposited in aerated 0.10 M CuSO_4 solutions (1), whereas the bottom micrograph is related to clusters deposited in oxygen saturated solutions (2).

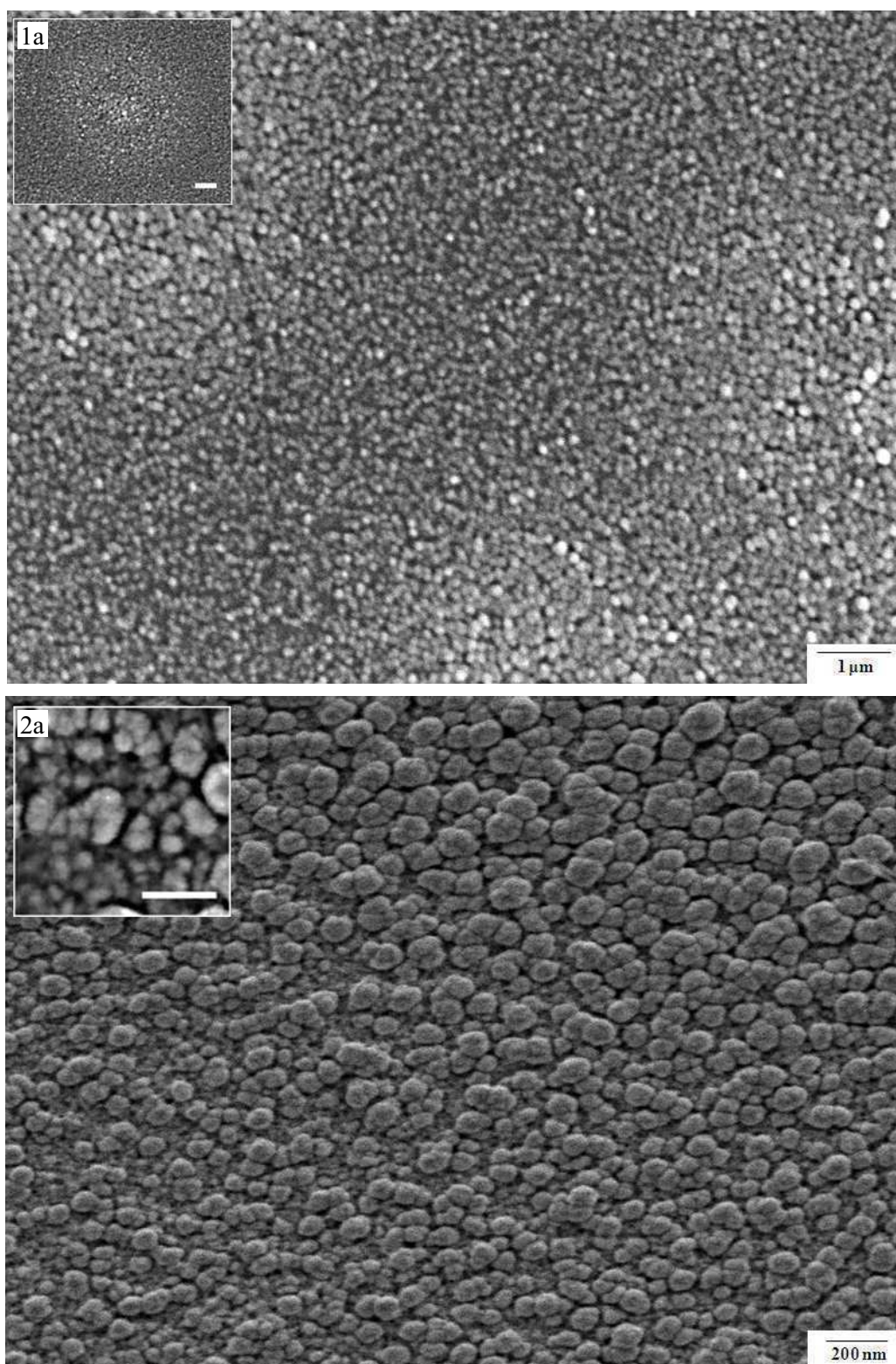


Figure 4.9 Size and arrangement of the copper nanoparticles produced from the reduction of hierarchical copper-based micro/nanostructures at -2.00 V vs. SCE in 0.10 M Na_2SO_4 . The nanoparticles were formed from clusters deposited in oxygen saturated 0.10 M CuSO_4 solutions. The micrographs are related to the same surface. The scale bars in the insets are 1 μm on the top (1a) and 100 nm on the bottom (2a).

The size and distribution of the copper nanoparticles are directly related to the position of the clusters. The larger nanoparticles are formed at the original site of the clusters, while the smaller are distributed in the surrounding areas. It is interesting to note that the large nanoparticles are also distributed around the center forming an O-ring shape (Figure 4.7, Micrograph 1c, and Figure 4.9, Inset 1a). The micrographs at high magnification in Figure 4.9 show the presence of two main size ranges. The larger nanoparticles are approximately 50 to 100 nm, while the smaller nanoparticles are as small as 10 nm, as evident in Figure 4.9, Inset 2a.

4.2.4 Preparation of Metallic Copper Nanoparticles at Polypyrrole-Polystyrene Sulfonate PEI-Multiwall Carbon Nanotube Nanocomposite Films

It is known that the incorporation of carbon nanotubes (CNT) inside conducting polymers can increase the conductivity and capacitance of PPy films [28-30]. CNT, previously functionalized with carboxylic acid groups, can be introduced into PPy films as anionic dopants [30, 31]. In the present case, instead, the CNT were deposited on the electrode surface prior to the electropolymerization. The PPy-PSS films were then deposited on top of the CNT. Water soluble multiwall carbon nanotubes (MWNT), which can be homogeneously and reproducibly drop-cast on the electrode surface, were synthesized following a procedure developed by Liao and co-workers [10]. MWNT modified with branched polyethylenimine (MWNT-PEI) were prepared, as described in Section 2.3.2. These nanotubes are soluble in water and can be easily drop-cast on an anodized glassy carbon surface. The anodization is performed to increase the hydrophilicity of the surface and facilitate an even spreading of the nanotubes. The resulting layer of MWNT-PEI is shown in Figure 4.10. The surface is homogeneously covered by entangled MWNT-PEI. The diameter of the larger nanotubes is around 50 nm compared to the 30 nm of the non-functionalized MWNT (Section 2.3.1). This corresponds to an approximate thickness of about 10 nm for the PEI functionalization. The layer is very porous with some voids that can be seen even at lower magnification. The weight of MWNT-PEI per unit surface is estimated to be about $32 \mu\text{g}/\text{cm}^2$ based on the diameter of the electrode (4 mm), and the volume and concentration of the drop-casting solution (5 μl and 0.08 % w/w, respectively).

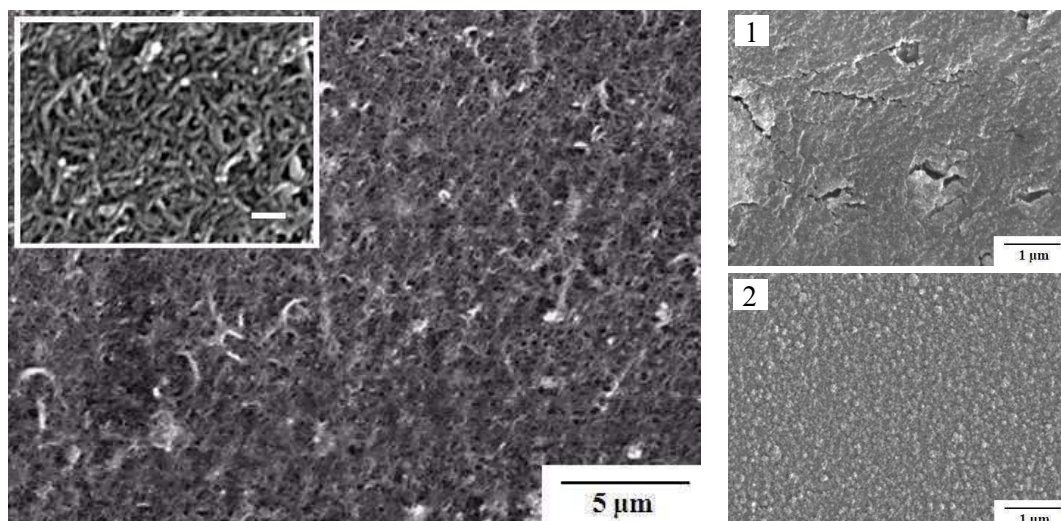


Figure 4.10 SEM micrographs of the electrode surface modified with MWNT-PEI before and after the deposition of the PPy-PSS film. On the left, the carbon nanotubes are homogeneously distributed on the surface, with the diameter of the larger tubes being approximately 50 nm (in the inset, the scale bar is 200 nm). On the right, the PPy-PSS film grown on the MWNT-PEI-modified electrode (1), and a PPy-PSS film formed on the bare glassy carbon electrode (2).

After polymerization of pyrrole in the presence of the polyanionic dopant, PSS, the resulting PPy-PSS-MWNT-PEI nanocomposite film is marked by large cracks, Figure 4.10, Micrograph 1. These are not observed for the PPy-PSS film prepared under similar experimental conditions, Figure 4.10, Micrograph 2. In addition to this microporosity, some mesoporosity is also likely to be present, as observed in comparable PPy films prepared from MWNT-PSS dispersions [32].

The electropolymerization of pyrrole on the MWNT-PEI layer is characterized by a different current profile compared to the one recorded at the bare electrode (Figure 4.11). In the case of the bare electrode, the current increases immediately on application of the potential to reach a plateau value. Instead, on the MWNT-PEI layer, the current remains low for about 2 s and then increases at a fast rate to reach a higher limiting current. This behaviour can be explained by considering the nature of the electrode surface. The surface area is larger for the MWNT-PEI-modified electrode, but the electropolymerization is initially limited by diffusion of the bulky PSS anions to the conducting surface, due to the branched PEI. However, once the electropolymerization is initiated, propagation of the polymer is faster at the higher surface area. The nanotube layer is fully covered with a PPy-PSS film.

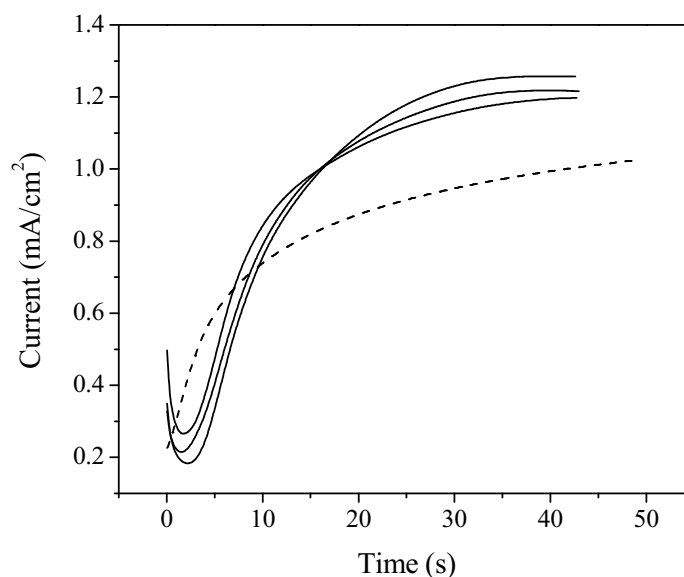


Figure 4.11 Current-time data recorded during the electropolymerization of Py from a 0.15 M Py / 50 mM PSS aqueous solution at 0.60 V vs. SCE on the MWNT-PEI modified (—) and bare (---) electrodes. The overall charge of polymerization was 40 mC/cm².

The redox activity of the PPy-PSS-MWNT-PEI nanocomposite was compared to the simple PPy-PSS film using cyclic voltammetry. The voltammograms of PPy-PSS-MWNT-PEI and PPy-PSS cycled in 0.10 M KCl are compared in Figure 4.12. Clearly, there are some differences between the two voltammograms. There is a slight increase in the capacitance of the PPy-PSS-MWNT-PEI film above -0.30 V vs. SCE, compared to the simple PPy-PSS, however this is much lower than that reported for CNT-PPy supercapacitors [33, 34]. Interestingly, the current arising from the capacitance is substantially higher in the potential range (below -0.70 V vs. SCE) where the PPy-PSS-MWNT-PEI film is reduced. In this potential region, the PPy-PSS film resides in its neutral state and is insulating. The incorporation of the carbon nanotubes substantially improves the electrical properties of the polymer film especially at these more electronegative potentials. This improvement has a beneficial effect on the sensing performance of the electrode modified with copper nanoparticles toward nitrates, as shown later in Section 4.2.5.

The hierarchical copper-based micro/nanostructures were successfully prepared and reduced to copper nanoparticles on the PPy-PSS-MWNT-PEI films, as shown in Figure 4.13. The hierarchical structures were deposited from oxygen saturated solutions under the same conditions used for PPy-PSS films.

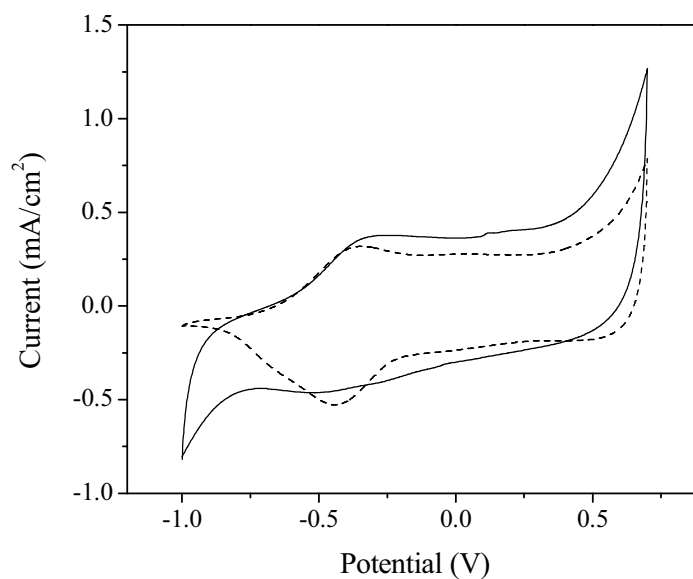


Figure 4.12 Cyclic voltammograms recorded in 0.10 M KCl at 50 mV/s for electrodes modified with MWNT-PEI-PPy-PSS composite film (—) and PPy-PSS film (---). The polymerization charge for both films was 30 mC/cm².

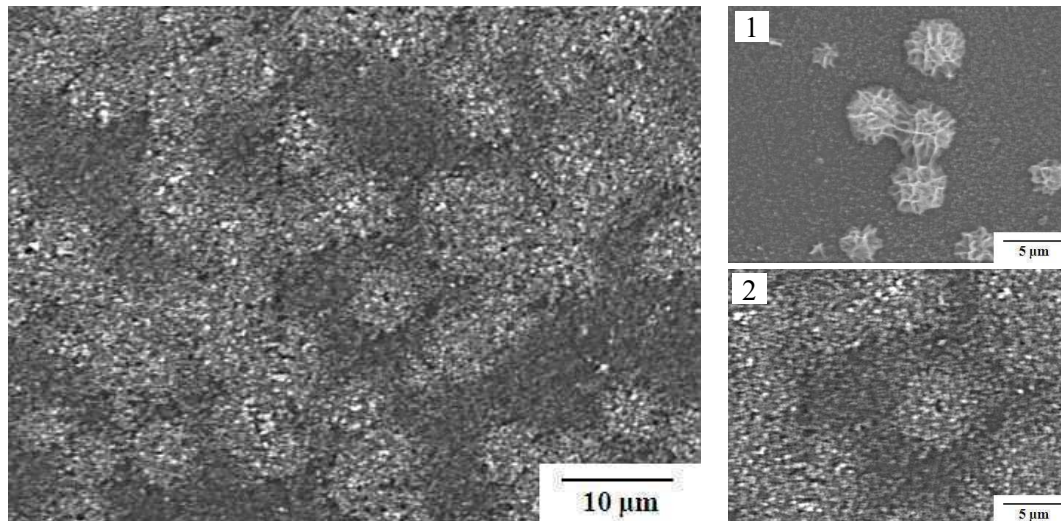


Figure 4.13 SEM micrographs of the copper nanoparticles formed on the PPy-PSS-MWNT-PEI composite films from hierarchical copper-based micro/nanostructures deposited in oxygen saturated 0.10 M CuSO₄ solutions. On the left, a large number of the copper nanoparticles were formed on the PPy-PSS-MWNT-PEI surface. On the right, the micro/nanostructures were reduced at -2.00 V vs. SCE to be partially (1) and fully (2) converted to copper nanoparticles after 5 min and 10 min reductions, respectively.

The copper nanoparticles are distributed on the top of the nanocomposite film in the same way as for the PPy-PSS films (Section 4.2.3, Figure 4.8). The larger nanoparticles are observed on the site of the original micro/nanostructures, while the smaller nanoparticles are distributed in the neighbouring areas. However, in this case, the complete reduction of the micro/nanostructures took 10 min instead of the 5 min usually required with the PPy-PSS films.

4.2.5 Nitrate Sensing with Metallic Copper Nanoparticle Modified Electrodes

Copper nanoparticles (CuNP) are known for their catalytic activity towards the reduction of nitrate ions (Section 4.1). Accordingly, the PPy-PSS films with and without MWNT-PEI and modified with CuNP were tested as nitrate sensors. The mechanism of reduction of nitrate is still object of debate, but the main products formed at transition-metal electrodes are ammonia and hydroxylamine [35]. Nitrite ions can also be formed at copper electrodes [36].

4.2.5.1 PPy-PSS-CuNP Modified Electrode

The nitrate sensing performance of a PPy-PSS-CuNP modified electrode was tested using cyclic voltammetry. Representative data are shown in Figure 4.14. The PPy-PSS-CuNP modified electrode was cycled in the presence of different concentrations of nitrate, ranging from 0.1 mM to 10.0 mM, in a supporting 0.10 M Na₂SO₄ electrolyte. It is evident that the current increases with increasing nitrate concentration. This increase is not observed at PPy-PSS films; hence it is due to the catalytic activity of the CuNP. The broad reduction wave is typical of slow reduction processes, under diffusion controlled conditions (Section 2.5.2.2). The wave can be related to the reduction of nitrates and/or further reduction of the products of nitrate reduction, *e.g.*, nitrite ions. At the highest concentration (10.0 mM) two very small signals emerge from the wave at about -0.90 V and -1.10 V vs. SCE. In order to prepare a calibration curve, the current recorded at -1.20 V vs. SCE is plotted against the nitrate concentration (with previous subtraction of the background current registered without nitrate in solution). This specific potential of -1.20 V vs. SCE is chosen as the MWNT-PEI modified film has a characteristic current plateau at this potential, as shown later in Section 4.2.5.2. Obviously, to obtain results that can be

compared quantitatively, the response of the two electrodes was measured at the same potential. The resulting calibration curve, shown in the inset in Figure 4.14, is linear up to 2 mM, at which point the current starts leveling off.

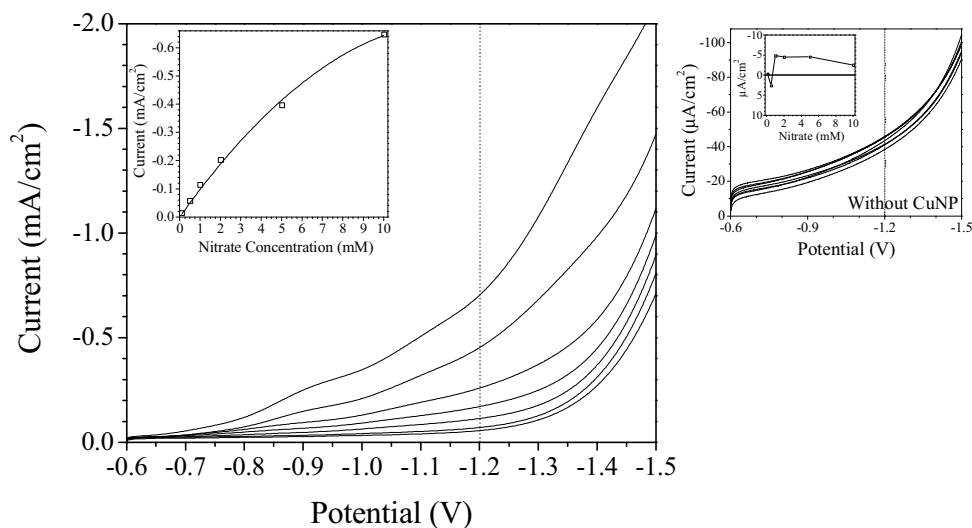


Figure 4.14 Voltammetric response of a PPy-PSS-CuNP modified electrode to nitrate ion. In the main graph, the current response increases with an increase of nitrate concentration, from the bottom to the top curve the concentration of nitrate is 0.0, 0.1, 0.5, 1.0, 2.0, 5.0 and 10.0 mM. In the inset, a plot of the current registered at -1.20 V vs. SCE against the concentration of nitrate (all values of current are corrected by subtracting the background current recorded in the absence of nitrate). In the small graph, the response of a PPy-PSS electrode, without CuNP, to the same concentrations of nitrate, is shown. The amount of copper deposited on the electrodes was 119.4 mC/cm². The curves represent the second reduction segment for cyclic voltammograms recorded at 10 mV/s in 0.10 M Na₂SO₄.

The linear portion of the calibration curve was fitted by linear regression and the results are reported in Figure 4.15. The correlation coefficient (R^2) is 0.996 , indicating that the experimental response is reasonably linear in this range. The sensitivity of the PPy-PSS-CuNP film was computed as 99.0 $\mu\text{A}/(\text{mM}\cdot\text{cm}^2)$. The extrapolated reading of current at zero concentration is -8.5 $\mu\text{A}/\text{cm}^2$, which indicates a residual signal even after background subtraction. This has direct implications on the limit of detection of the sensor, *i.e.*, the smallest amount of nitrate detectable by the electrode [37].

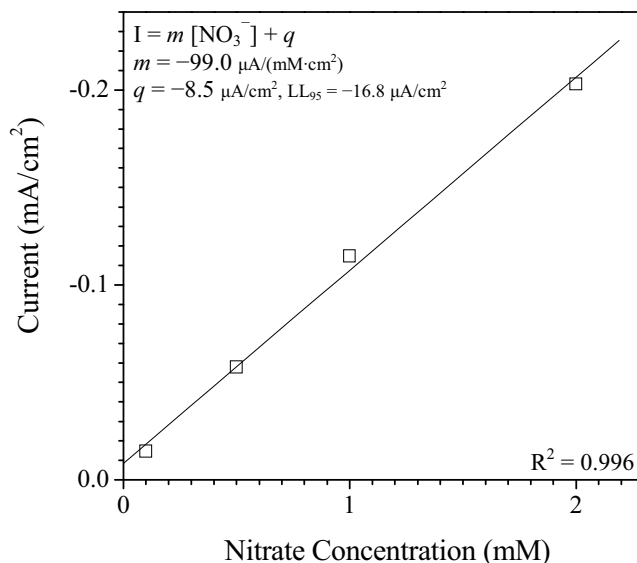


Figure 4.15 Linear regression of the current-concentration data of a PPy-PSS-CuNP modified electrode in the nitrate concentration range of 0.1 – 2.0 mM. The experimental points are taken from the inset of Figure 4.14.

Clearly, the reading at zero concentration, which is the intercept of the regression line, is affected by an error which can be estimated from the experimental points. Because of this error, the intercept has a characteristic distribution around its average value, as shown in Figure 4.16. The limits of this distribution, UL_{95} and LL_{95} , as defined in Figure 4.16, can be used to identify a range of readings that are likely to correspond to the intercept, *i.e.*, to the zero concentration. The limit of interest in this case is the LL_{95} which sits above the intercept in the present plot (since the order of the axis is inverted). The readings that fall below this limit in the plot are likely to correspond to the zero concentration and have only a 5 % probability of being related to the nitrate. Following on from these considerations, the electrode response corresponding to 0.1 mM nitrate, $-14.7 \mu\text{A}/\text{cm}^2$, is slightly below the LL_{95} , $-16.8 \mu\text{A}/\text{cm}^2$, in the plot; hence, it cannot be assigned to the presence of nitrate. On the other hand, all other readings are well above the LL_{95} . The lowest concentration in this group is 0.5 mM and this can be considered the measured detection limit for the PPy-PSS-CuNP modified electrode under the present experimental conditions.

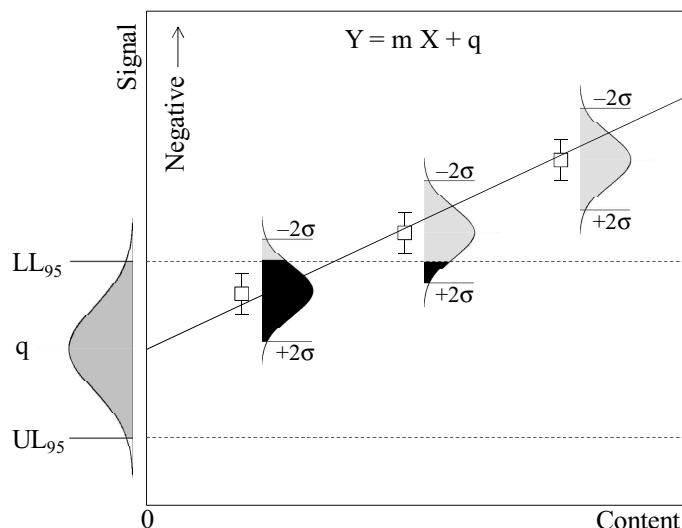


Figure 4.16 Significance of the experimental data points of a linear calibration curve [37]. Three experimental points are fitted with a linear regression ($Y = mX + q$), the points are characterized by normal distributions which are centered about their means and have widths proportional to their standard deviations, σ . The intercept of the regression line has a normal distribution which has lower (LL) and upper (UL) confidence limits defining the range in which a data point is not distinguishable from the intercept (note that the Y axis is inverted). The first data point from the left is below the LL_{95} meaning that there is a probability of 95 % that this point is not significantly different from the intercept. The next point is above the LL_{95} , however a portion of its distribution is below the LL_{95} ; hence, there is a probability that this point can also correspond to the intercept. The last point on the right is above the LL_{95} with all its distribution and it is then significantly different from the intercept. It follows that this last point is the only point corresponding to an experimental response significantly different from that of zero concentration.

4.2.5.2 PPy-PSS-MWNT-PEI-CuNP Modified Electrode

The nitrate sensing performance of a PPy-PSS-MWNT-PEI-CuNP modified electrode was tested using cyclic voltammetry and constant potential amperometry at a rotating disk electrode (RDE). The voltammetric data were recorded using the procedures outlined for the PPy-PSS-CuNP system and are presented in Figure 4.17.

As before, the electrode was cycled in the presence of different concentrations of nitrate (0.1 – 10.0 mM), and the reduction current was monitored, giving an increasing current response with increasing nitrate concentration. The same electrode

without CuNP did not register any increase; indicating that the electrochemical response is due to the catalytic activity of the CuNP. In the response profiles there are two clear peaks at about -0.90 V and -1.10 V vs. SCE, and evidence of a plateau-like current between -1.10 V and -1.30 V vs. SCE.

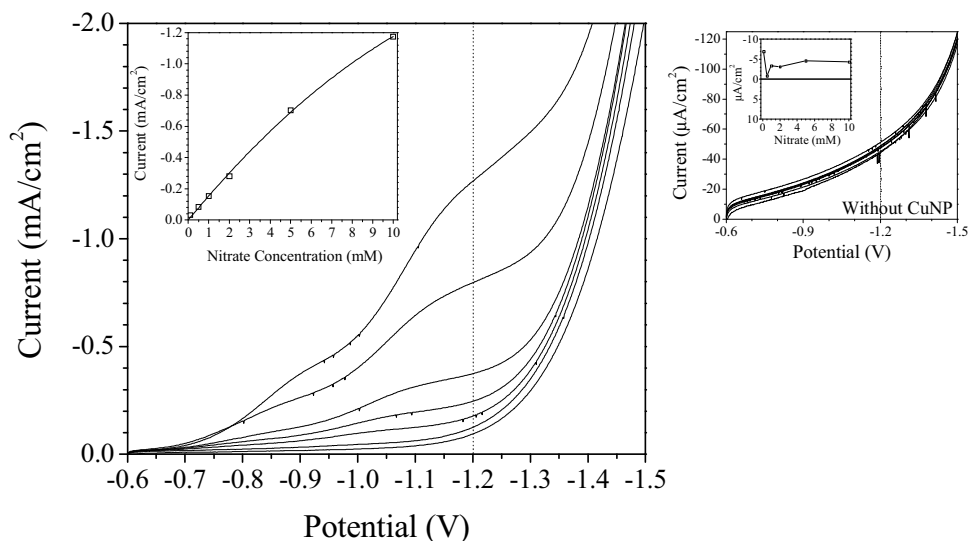


Figure 4.17 Voltammetric response of a PPy-PSS-MWNT-PEI-CuNP modified electrode to nitrate ion. In the main graph, the current response increases with an increase of nitrate concentration, from the bottom to the top the concentration is 0.0, 0.1, 0.5, 1.0, 2.0, 5.0 and 10.0 mM. In the inset, the current registered at -1.20 V vs. SCE is plotted against the concentration of nitrate (all currents are corrected by subtracting the background current recorded in the absence of nitrate). In the small graph, the response of a PPy-PSS-MWNT-PEI film, without CuNP, to the same concentrations of nitrate, is shown. The amount of copper deposited on the electrode was 119.4 mC/cm². The curves represent the second reduction segment for cyclic voltammograms recorded at 10 mV/s in 0.1 M Na₂SO₄.

A calibration curve was prepared by plotting the current values recorded at -1.20 V vs. SCE, against the nitrate concentration (with the previous subtraction of the background current registered without nitrate in solution). The current response for the PPy-PSS-MWNT-PEI-CuNP electrode is higher, compared to that observed for the film without carbon nanotubes, and the linear range is wider. The linear portion of the calibration curve was fitted by linear regression and the resulting plot and parameters are shown in Figure 4.18.

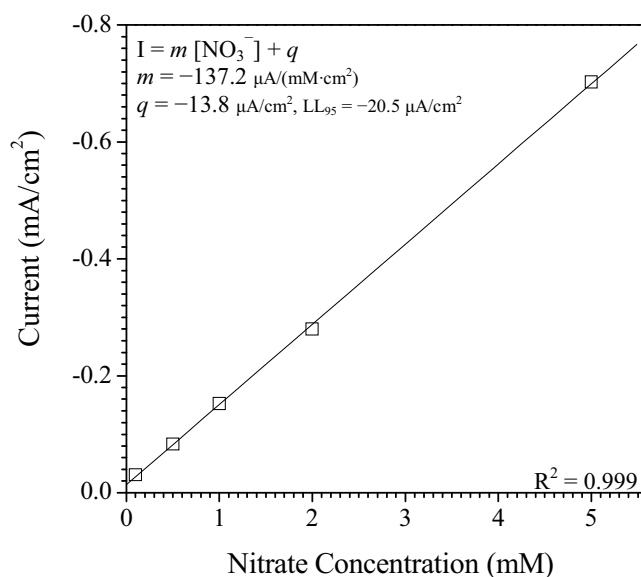


Figure 4.18 Linear regression of the current-concentration data of a PPy-PSS-MWNT-PEI-CuNP modified electrode in the concentration range 0.1 – 5.0 mM nitrate. The experimental points are taken from the inset of Figure 4.17.

The correlation coefficient (R^2) is 0.999, showing the better linearity of the response of the MWNT-PEI modified film compared to the previous film without nanotubes (Section 4.2.5.1, Figure 4.15). The sensitivity of the electrode is also better, $137.2 \mu\text{A}/(\text{mM}\cdot\text{cm}^2)$. Instead, the extrapolated reading of current at zero concentration is slightly higher in the plot, $-13.8 \mu\text{A}/\text{cm}^2$. However, the current response at 0.1 mM nitrate concentration is significantly different from the current at zero concentration. In fact, in this case the reading of current at 0.1 mM concentration, $-30.7 \mu\text{A}/\text{cm}^2$, is above the LL_{95} value, $-20.5 \mu\text{A}/\text{cm}^2$ (LL_{95} is the lower confidence limit discussed in Section 4.2.5.1, Figure 4.16). The measured limit of detection of the carbon nanotube modified electrode is then 0.1 mM using cyclic voltammetry, five times better than the film without nanotubes.

The substantial improvements obtained with the use of the MWNT-PEI were followed up with a further investigation of the electrode performance by constant potential amperometry at RDE. It is known that the RDE can improve the mass transport of the analyte from the solution to the electrode surface and then allow better limits of detection (Section 2.5.2.3). In this case the measurements were made at constant potential, -1.20 V vs. SCE, and the current was recorded while various

aliquots of nitrate ions were added to the solution. The modified electrode was spun at a constant rotational speed, 2000 rpm, during the addition. The amperometric response is characterized by a series of current steps, where the height of the steps is proportional to the added nitrate, as shown in Figure 4.19.

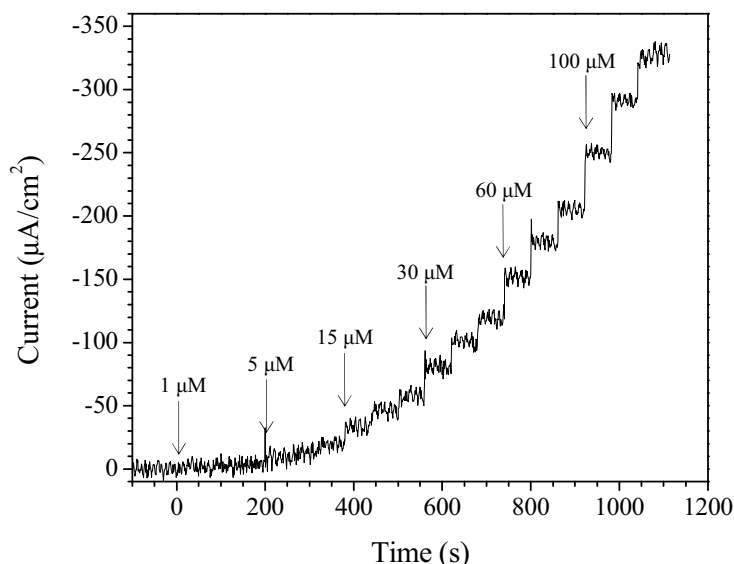


Figure 4.19 Chronoamperometric response of a PPY-PSS-MWNT-PEI-CuNP film modified rotating disk electrode. The potential was held at -1.20 V vs. SCE while the nitrate aliquots were added to a 0.10 M Na_2SO_4 solution in which the electrode was rotated at 2000 rpm. The amount of nitrate for each aliquot is reported in the graph, with each amount added three times in series before the concentration increase. The aliquots were added at a frequency of one per minute. The time zero corresponds to the first addition, however the electrode was kept in solution rotating at constant potential for 2400 s prior to the first additions. The current was set to zero at time $t = 0$ s, for easier reading of the height of the current steps. This current adjustment did not affect the final results as a current step is independent of the absolute value of the current. The current at the start of the addition was about 1.18 mA/cm².

Before proceeding further with the analysis of the results, it is necessary to evaluate the effect of the noise on the measurements. A large portion of instrumental noise was recorded prior to the start of the nitrate addition while the electrode was polarized in solution without the presence of any nitrate. The amplitude of the noise and its frequency counts are given in Figure 4.20. The noise distribution is in good agreement with a normal distribution. Hence, a current reading has to be higher than 3σ in order to be considered different from the noise, *i.e.*, at least more than three times the standard deviation of the noise, 12.69 $\mu\text{A}/\text{cm}^2$, in absolute value.

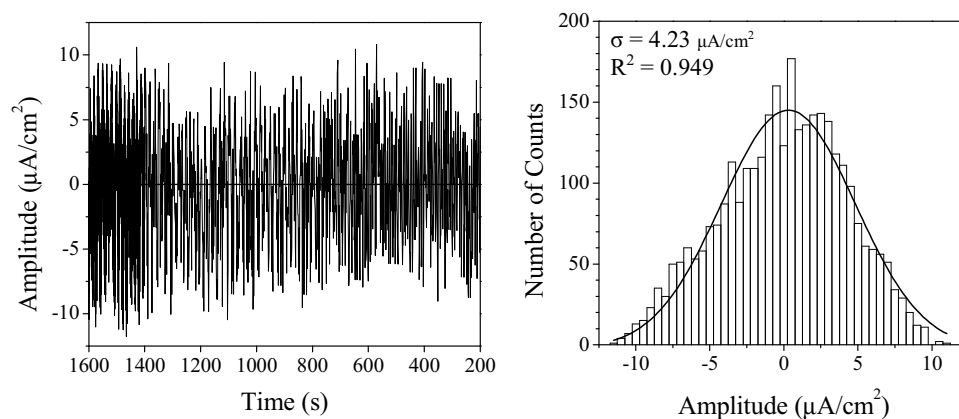


Figure 4.20 Statistical analysis of a noise sample recorded prior to the commencement of the nitrate additions during the stabilization of a PPy-PSS-MWNT-PEI-CuNP modified RDE electrode. The amplitude of the noise is in the left graph. The frequency distribution of the noise amplitudes, fitted by a Gaussian curve, is on the right. The corresponding standard deviation and correlation coefficient, R^2 , are reported in the graph.

In order to decrease the noise, the curve was smoothed by 20-point adjacent averaging and the resulting curve is shown in Figure 4.21.

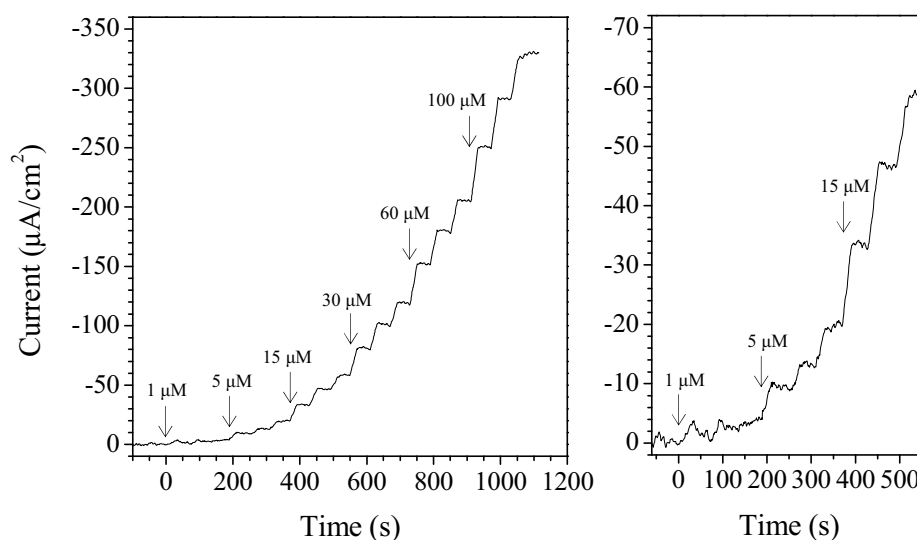


Figure 4.21 Digital smoothing of the current response reported in Figure 4.19, which was performed with a 20-point adjacent averaging. The graph on the right is the enlargement of the portion of the curve corresponding to the smaller additions.

A general feature of the curve is that within each series of the three additions of nitrate, the current steps decrease (this is also evident from the current-concentration curves reported in Figure 4.22). This decrease was likely to be due to poisoning effects due to the progressive addition of nitrate to the solution. The detrimental effect of poisoning on the catalytic activity of copper is a well-known issue [14]. In particular, the current steps registered for the 1 μM nitrate additions decay rapidly towards zero. For this reason, these additions are not considered further in the analysis. The plots of the current responses against the nitrate concentration are reported in Figure 4.22. The responses are collected in three groups corresponding to the order of addition, *i.e.*, 1st, 2nd and 3rd additions.

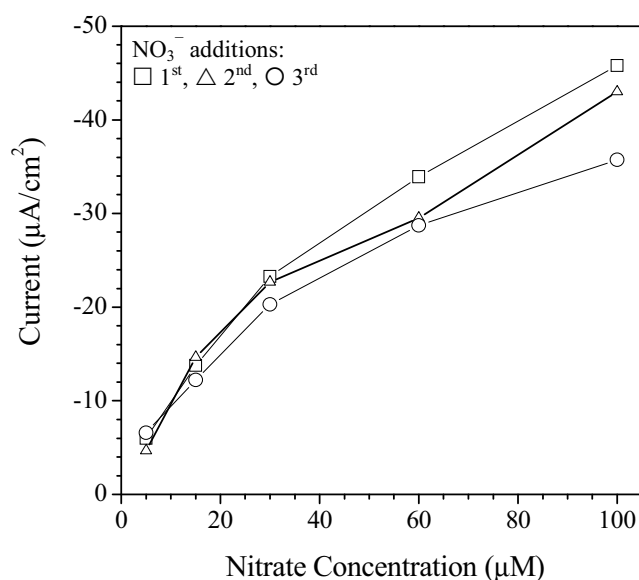


Figure 4.22 Current-concentration plot of PPy-PSS-MWNT-PEI-CuNP to the addition of various aliquots of nitrate ions of different concentrations, the data are taken from Figure 4.19. The curves refer to the order of aliquot addition at each concentration, *e.g.*, the 1st curve (\square) refers to all the 1st additions, the 2nd (\triangle) and 3rd (\circ) curves correspond to all the 2nd and all the 3rd additions, respectively.

On comparing the 1st, 2nd and 3rd additions at the higher concentrations, it is obvious that the overall magnitude of the current response decreases with increasing addition. This was probably related to poisoning of the CuNP. Instead, the responses in the lower concentration range, 5 - 30 μM , are randomly distributed. For this reason, it is reasonable to take their average values and standard deviations to perform the linear regression reported in Figure 4.23.

The correlation coefficient (R^2) is 0.992, indicating some deviation from linearity. The sensitivity of the electrode was computed as $0.64 \mu\text{A}/(\mu\text{M}\cdot\text{cm}^2)$. The extrapolated reading of current at zero concentration is $-3.03 \mu\text{A}/\text{cm}^2$ and its LL_{95} is $-5.11 \mu\text{A}/\text{cm}^2$.

The current reading at the $5 \mu\text{M}$ nitrate concentration, $-5.76 \mu\text{A}/\text{cm}^2$, is slightly higher than the LL_{95} , however in the plot the lower side of its normal distribution overlaps with that of the LL_{95} , *i.e.*, the limiting value $-5.76 + 2\sigma = -3.82 \mu\text{A}/\text{cm}^2$ is lower, in the plot, than LL_{95} . As a result, this current reading is not significantly different from the reading at zero concentration. Hence, it cannot be related to the response of the electrode to the addition of nitrate [37].

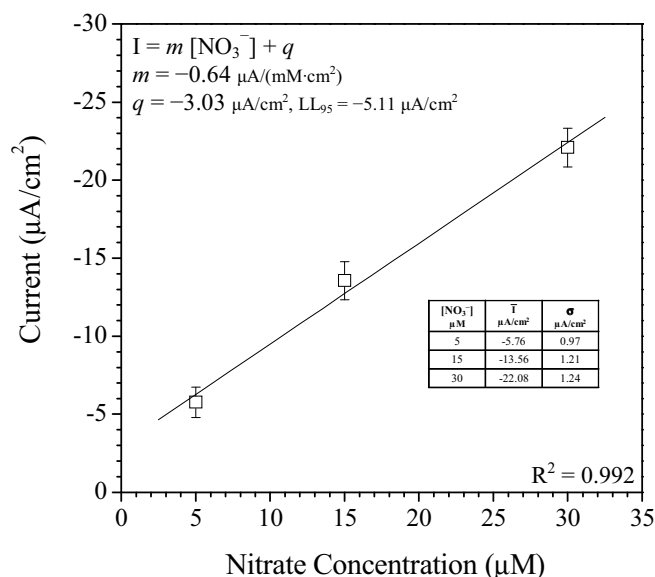


Figure 4.23 Linear regression of the averaged current-concentration data of a PPy-PSS-MWNT-PEI-CuNP modified electrode in the concentration range $5 - 30 \mu\text{M}$ nitrate. The inset table reports the average currents (\bar{I}) and the standard deviations (σ).

The current reading at $15 \mu\text{M}$ nitrate concentration, $-13.56 \mu\text{A}/\text{cm}^2$, is well above the LL_{95} , however it is very near to the detection limit enforced by the noise, $-12.69 \mu\text{A}/\text{cm}^2$. Following the same reasoning as before, the limiting value of this experimental reading, $-13.56 + 2\sigma = -11.14 \mu\text{A}/\text{cm}^2$, is lower in the plot than the detection limit due to the noise, hence there is a finite probability that this signal is due to the noise [37]. It is easy to see that the detection limit of the modified electrode is severely affected by the noise.

Accordingly, the measured detection limit of the PPy-PSS-MWNT-PEI-CuNP electrode is 30 μM nitrate. However, it is important to note that this detection limit is adversely affected by the high level of instrumental noise. If the noise was lower, like for the signal obtained after smoothing (Figure 4.21), the detection limit would be lower. In fact, there are lower concentrations than 15 μM that would be both in the experimental range and fall significantly above the LL_{95} .

In conclusion, the PPy-PSS and PPy-PSS-MWNT-PEI films modified with CuNP proved to be capable of detecting nitrate ions. The performance of the electrodes was enhanced by the presence of the MWNT-PEI, in fact with the nanotubes the sensitivity improved by 37 % and the measured voltammetric detection limit was five times better. The PPy-PSS-MWNT-PEI-CuNP modified electrode achieved a measured amperometric detection limit of 30 μM , but this was severely limited by the instrumental noise. The use of equipment with a lower noise level and the optimization of the electrode are very likely to enhance the performance of the sensor bringing it closer to the best values reported in the literature, 0.1 – 10 μM [14]. However, poisoning issues could affect the reproducibility and long-term performance of the sensor.

4.2.6 Electrochemical Impedance Analysis and Comparison of PPy-PSS and PPy-PSS-MWNT-PEI Thin Films

In the previous sections the nitrate sensing performance of the electrodes modified with CuNP was greatly improved by introducing MWNT-PEI in the PPy-PSS films. In order to evaluate the effect of the MWNT-PEI, the electrical properties of the PPy-PSS films, with and without carbon nanotubes, were investigated using electrochemical impedance spectroscopy, EIS (Section 2.5.2.5). EIS is a powerful technique able to distinguish and describe the dominant processes simultaneously present in an electrochemical system that evolve at different rates. Fast processes are sampled only at high frequency, conversely slow processes only at low frequency. The overall charge transport process is then broken down into its various contributions which are prevalent within different frequency ranges. In general, each contribution is represented by a circuit element, which is part of the equivalent circuit used to describe the electrochemical behaviour of the system.

4.2.6.1 PPy-PSS Modified Electrodes

The PPy-PSS films were prepared at glassy carbon electrodes of diameter 4 mm. The thickness of the films was 120 nm, corresponding to an electropolymerization charge of 40 mC/cm². The impedance measurements were performed in the frequency range from 2 mHz to 65 kHz in aerated 0.10 M Na₂SO₄. Prior to the measurements the films were preconditioned by keeping the electrodes at a fixed potential for 30 min in the same electrolyte solution. This conditioning period was sufficiently long to achieve a steady-state condition. The potentials were set at 0.00 V, -0.50 V and -1.00 V vs. SCE.

PPy-PSS films have been the object of many EIS characterization studies. Ren and Pickup [38, 39] carried out detailed studies of both ion and electron transport in such films. In their works, they used the dual rail transmission line circuit originally proposed by Albery *et al.* [40, 41]. In this circuit two film resistances, one ionic, R_{ion} , and one electronic, R_e , are connected in parallel through a group of capacitors representing the pseudo-capacitance of the film, C_F . They found that above -0.60 V vs. Ag/AgCl the impedance response of the film is described by a single transmission line, R_{ion} , since at this potential R_e is negligible. Below this potential, R_e is comparable to R_{ion} . At more negative potentials, such as below -0.75 V vs. Ag/AgCl, the R_e term dominates over R_{ion} . In this case, the film impedance is reasonably described by a single transmission line governed by R_e . This transition is related to the electrochemistry of the polymer film. In fact, in its oxidized state (low R_e) the film is deprived of mobile counterions (high R_{ion}) since the negative charge of the dopant, PSS, is counterbalanced by the positive charge of oxidized PPy. Conversely, in its reduced state (high R_e) the film is rich in mobile counterions (low R_{ion}) necessary to maintain the charge balance. Komura *et al.* [42] came to the same conclusions that a reduced film has high ionic conductivity due to the incorporation of cations, while the electronic resistance increases with decreasing oxidation level. The present impedance characterization is not intended to be an addition to these studies; rather, it was performed to obtain the experimental data necessary for a direct comparison between PPy-PPS and PPy-PSS-MWNT-PEI films. Furthermore, the experimental conditions used in the present work are different from those of the published studies. In this study, the PPy films are thinner, 0.12 μm compared to

2 μm , and the electrolyte is also different, 0.10 M Na_2SO_4 instead of 0.2 M NaClO_4 or 0.5 M NaCl . These differences can affect the impedance response of the films. In fact, thinner films are characterized by a higher molecular order compared to thicker films [43]. Also, sulfate ions can be exchanged by the PPy-PSS film when cycled in sulfate electrolytes [44]. These ions can act as electrostatic cross-linking points between oxidized moieties of the polymer.

The impedance responses of a PPy-PSS film at 0.00 V, -0.50 V and -1.00 V vs. SCE are reported in Figure 4.24. The general effect of the potential is to decrease the overall impedance of the film, as evident from the shrinking of the impedance responses with decreasing potential.

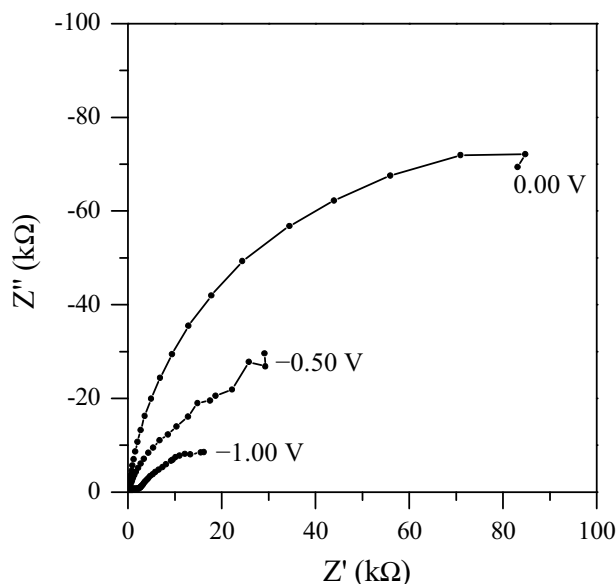


Figure 4.24 Complex plane impedance plot for a PPy-PSS film polarized at 0.00 V, -0.50 V and -1.00 V vs. SCE. The measurements were performed in the frequency range from 2 mHz to 65 kHz in aerated 0.10 M Na_2SO_4 . The AC amplitude was 5 mV peak-to-peak. The film thickness was 120 nm on a glassy carbon electrode.

The best fitting at 0.00 V vs. SCE is obtained with the equivalent circuit reported in Figure 4.25. The average percentage value of the fitting residuals (Section 2.5.2.5) is 1.2 %, indicating very good agreement between experimental and modelled impedance values.

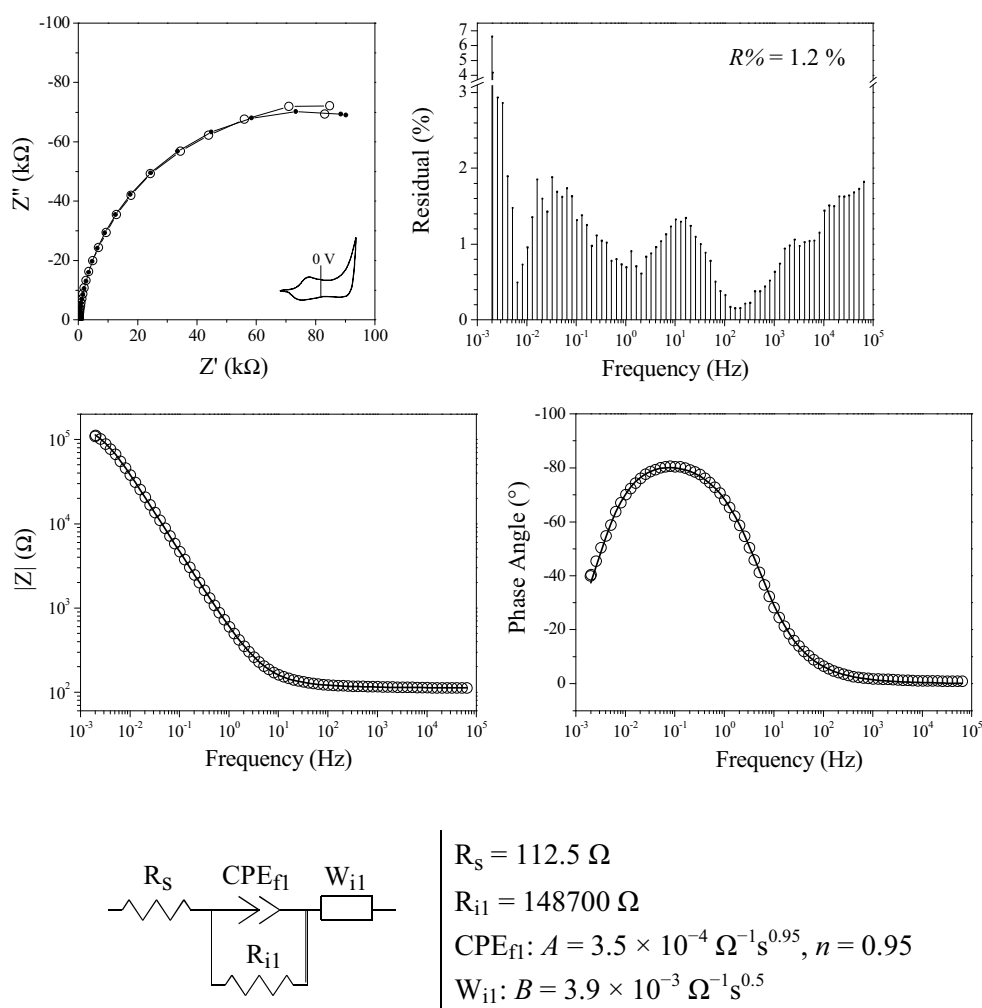


Figure 4.25 Equivalent circuit and fitting analysis of the impedance response of a PPy-PSS film recorded at 0.00 V vs. SCE in 0.10 M Na₂SO₄. The equivalent circuit and the values for the fitting parameters are given in the bottom. The complex plane and bode plots of the impedance response (O) and the corresponding simulated data (—•— and —) are given above the circuit. The inset in the complex plane is the cyclic voltammogram of the film showing the redox state of the polymer at the potential of measurement. The plot of the fitting residuals and the average percentage residual, $R\%$, are given on the top.

The equivalent circuit is composed of four elements. The solution resistance, R_s , is in series with a constant phase element, CPE_{f1} , and a Warburg element, W_{il} , while CPE_{f1} is in parallel to a second resistance, R_{il} . The CPE is often encountered in the modelling of conducting polymers because of their non-ideal capacitive, conductive and diffusive behaviours [45]. As described in detail in Section 2.5.2.5, a CPE is defined by two parameters A and n . Depending on the value of n , which can vary

from -1 to 1 , the CPE can represent a resistor ($n = 0$, $R = 1 / A$), a capacitor ($n = 1$, $C = A$) or an inductor ($n = -1$, $L = 1 / A$). An additional case is $n = 0.5$, in which the CPE becomes a Warburg element, W , describing semi-infinite linear diffusion. Non-ideal behaviour is encountered in cases of distorted resistance ($0 < n \leq 0.2$), capacitance ($0.8 \leq n < 1$), or diffusion ($0.4 \leq n \leq 0.6$). The Warburg constant B is proportional to the square root of the diffusion coefficient, D , of the diffusing species, *i.e.*, $D \propto B^2$.

As discussed before, at 0.00 V vs. SCE the electronic resistance of the film is negligible compared to the ionic resistance [38]. Accordingly, the resistance term, R_{i1} in Figure 4.25, corresponds to the ionic resistance. This resistance is large, reaching 148 k Ω , because there are no free ions available in the oxidized film (Section 3.2.1.1). In fact, at 0.00 V vs. SCE the film is fully oxidized, as shown by the cyclic voltammogram reported in Figure 4.25, and can be represented as a salt made of entangled charged macromolecules, PPy^+PSS^- .

The constant phase element, CPE_{f1} , with $n = 0.95$, is representative of a partially distorted capacitance. This corresponds to the bulk pseudo-capacitance of the film with the oxidation charge of the polypyrrole balanced by the dopant (PPy^+PSS^-). Considering a pure capacitor ($n = 1$), the capacitance of the film is approximately 0.35 mF which per unit mass of film corresponds to about 135 F/g. This value was calculated with the mass of the film, which was taken as 2.6 μg . In fact, the mass-to-charge ratio of PPy-PSS was 5.25×10^{-4} g/C (obtained from the EQCM data of Section 3.2.1.1, Figure 3.3), the volume-to-charge ratio was obtained from the literature 3.00×10^{-4} cm³/C [46], hence the density of the film was 1.75 g/cm³. The volume of the present film was 120×10^{-7} cm \times 0.1256 cm² = 1.51×10^{-6} cm³, and then the mass of the film was 1.51×10^{-6} cm³ \times 1.75 g/cm³ = 2.64×10^{-6} g. For sake of comparison, Ren and Pickup [38] measured, at low frequency, a capacitance of about 35 mF/cm² for a 2 μm thick PPy-PSS film on a 0.0045 cm² Pt disk electrode. The resulting specific capacitance of such a film was 100 F/g which is close to the present value of 135 F/g.

The last element in the circuit is a Warburg element, W_{i1} , which is representative of a diffusion process. At 0.00 V vs. SCE, the polymer is fully oxidized, but given the fact that there are practically no cations in the bulk of the film, as proven by many different experimental results published in the literature [47-50], it is unlikely that

this can be connected to the diffusion of Na^+ inside the film. Instead, it might be due to the presence of diffusion processes at the film/solution interface.

The impedance response at -0.50 V vs. SCE is described by the circuit in Figure 4.26. The average percentage value of the fitting residuals (Section 2.5.2.5) is 1.5 %, indicating again very good agreement between experimental and modeled impedance values.

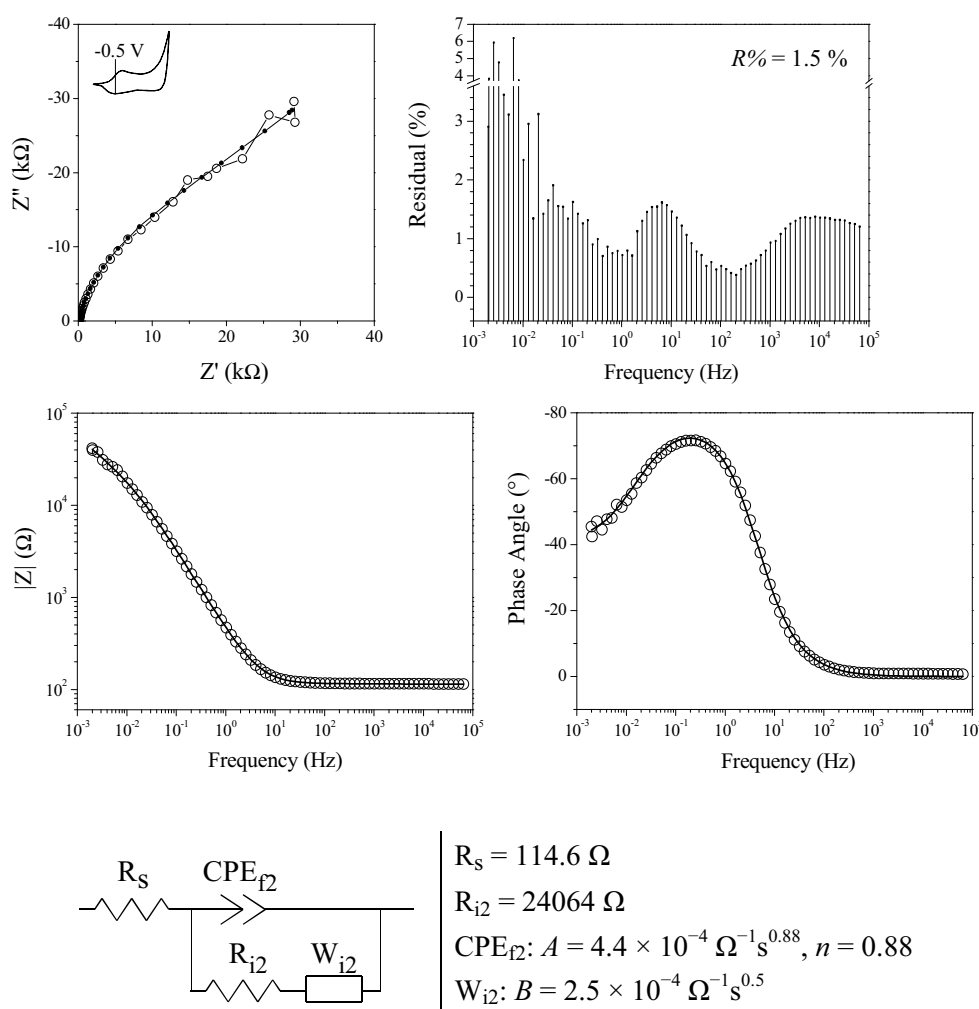


Figure 4.26 Equivalent circuit and fitting analysis of the impedance response of a PPy-PSS film recorded at -0.50 V vs. SCE in 0.10 M Na_2SO_4 . The equivalent circuit and the values for the fitting parameters are given in the bottom. The complex plane and bode plots of the impedance response (O) and the corresponding simulated data (—•— and —) are given above the circuit. The inset in the complex plane is the cyclic voltammogram of the film showing the redox state of the polymer at the potential of measurement. The plot of the fitting residuals and the average percentage residual, $R\%$, are given on the top.

The elements in the equivalent circuit include a solution resistance, R_s , an ionic resistance, R_{i2} , a distorted capacitance, CPE_{i2} , and a Warburg element, W_{i2} . As shown in the accompanying cyclic voltammogram, reported in the complex plane plot, an applied potential of -0.50 V vs. SCE corresponds to the position of the reduction peak. Accordingly, at this potential, the electronic resistance is still negligible because of the partial oxidation of the conducting polymer [38]. Also, upon reduction, Na^+ can enter into the film to balance the negative charge of the dopant. For this reason, the ionic resistance, R_{i2} , is lower compared to R_{i1} in Figure 4.25, with a 6-fold drop from about 148 k Ω at 0.00 V vs. SCE to about 25 k Ω at -0.50 V vs. SCE.

The capacitor, CPE_{i2} , is more distorted ($n = 0.88$) probably because of the ingress of ions with consequent loss of film homogeneity. In this case an estimate of the capacitance is not possible because of the significant distortion of the capacitor. However, as opposed to the system at 0.00 V vs. SCE, the capacitance is a mixture of partially oxidized and reduced PPy, dopant and counterions ($PPy^+PSS^-/PPy^0PSS^-Na^+$). At -0.50 V vs. SCE, the Warburg element, W_{i2} , is in parallel to CPE_{i2} and can be equated to the diffusion of the Na^+ ions within the polymer matrix.

The impedance response at -1.00 V vs. SCE was fitted with two equivalent circuits. The first circuit in Figure 4.27 is the one with the best average residual (1.3 %). However, the capacitance, C_f , estimated with this circuit is in direct contrast to the known properties of PPy-PSS films at this potential. In fact, PPy has an extremely low capacitance at -1.00 V vs. SCE as it is completely reduced to its neutral state. The low frequency capacitance of PPy-PSS was measured by Ren and Pickup [38] at different potentials and it turned out to drop to zero as the potential approaches -1.00 V vs. SCE. Komura *et al.* [42] observed the same trend for films of different thickness. In the present case, the estimated capacitance, $C_f = 1.2$ mF, would correspond to a specific capacitance of about 460 g/F. This value is actually higher than those of supercapacitors based on PPy nanocomposites. It is then evident that the first circuit cannot be used to represent the physicochemical properties of the film. The second equivalent circuit is presented in Figure 4.28. Although, the average residual (3.2%) is poorer, the information deduced from the circuit is in agreement with published studies [39]. The fact that the same experimental data can be fitted by different circuits is a known aspect of EIS which can be the cause of

ambiguities in the formulation of appropriate equivalent circuits. However, one of the main criteria to follow in these situations is to choose the circuit which describes the physical and chemical processes involved [51].

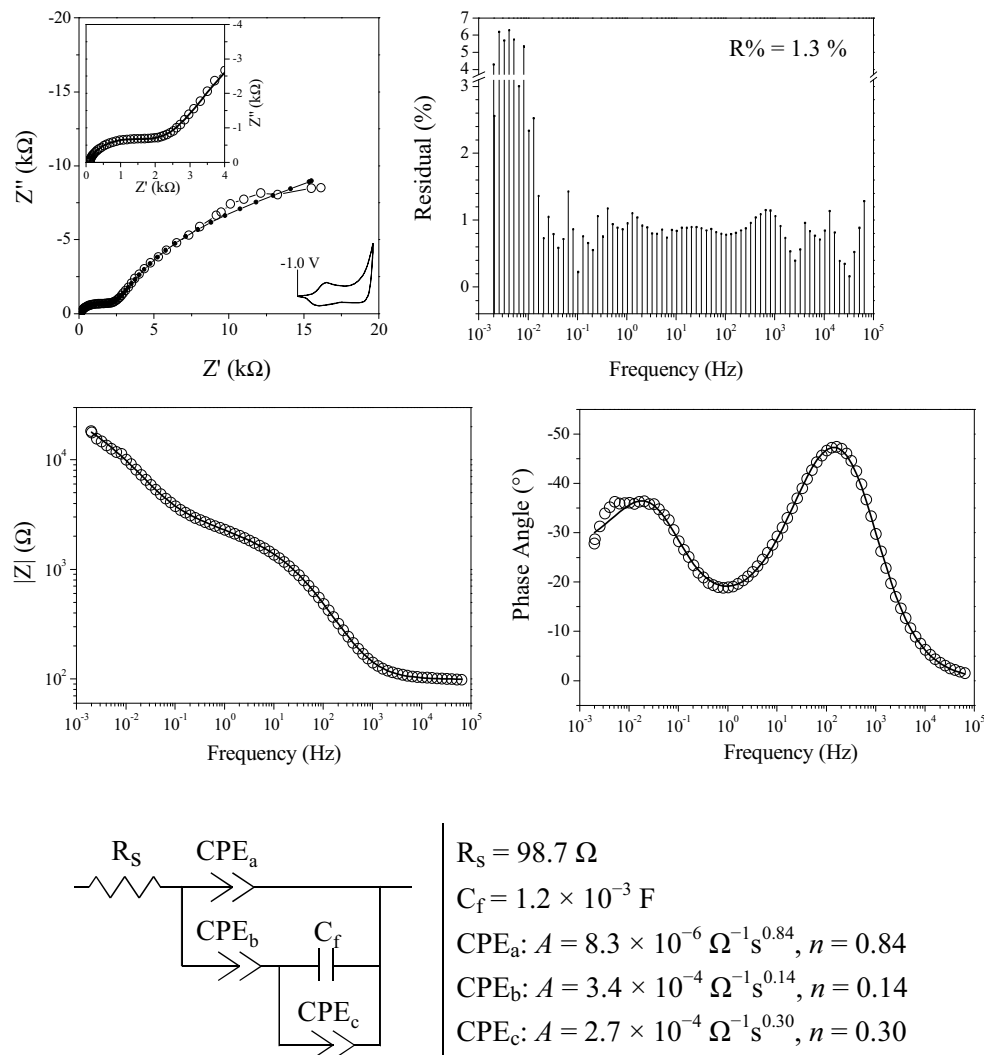


Figure 4.27 First equivalent circuit and fitting analysis of the impedance response of a PPy-PSS film recorded at -1.00 V vs. SCE in $0.10 \text{ M Na}_2\text{SO}_4$. The equivalent circuit and the value for the fitting parameters are given at the bottom. The complex plane and bode plots of the impedance response (O) and the corresponding simulated data (—•— and —) are given above the circuit. The insets in the complex plane are the enlargement of the high frequency portion of the impedance response, and the cyclic voltammogram of the film showing the redox state of the polymer. The plot of the fitting residuals and the average percentage residual, $R\%$, are given on the top.

The second equivalent circuit, given in Figure 4.28, is then the most appropriate to describe the electrochemical behaviour of the PPy-PSS films at -1.00 V vs. SCE.

At this potential, PPy is completely reduced, as shown in the cyclic voltammogram given in Figure 4.28. The charge of the dopant is neutralized by insertion of a further amount of sodium ions to give $\text{PPy}^0\text{PSS}^-\text{Na}^+$. Now, the ionic resistance, R_{ion} , of the film is negligible compared to the electronic resistance, R_e [39]. The electronic resistance, R_e , is about 40 k Ω . Again, this is consistent with the reduction of the film to its insulating state.

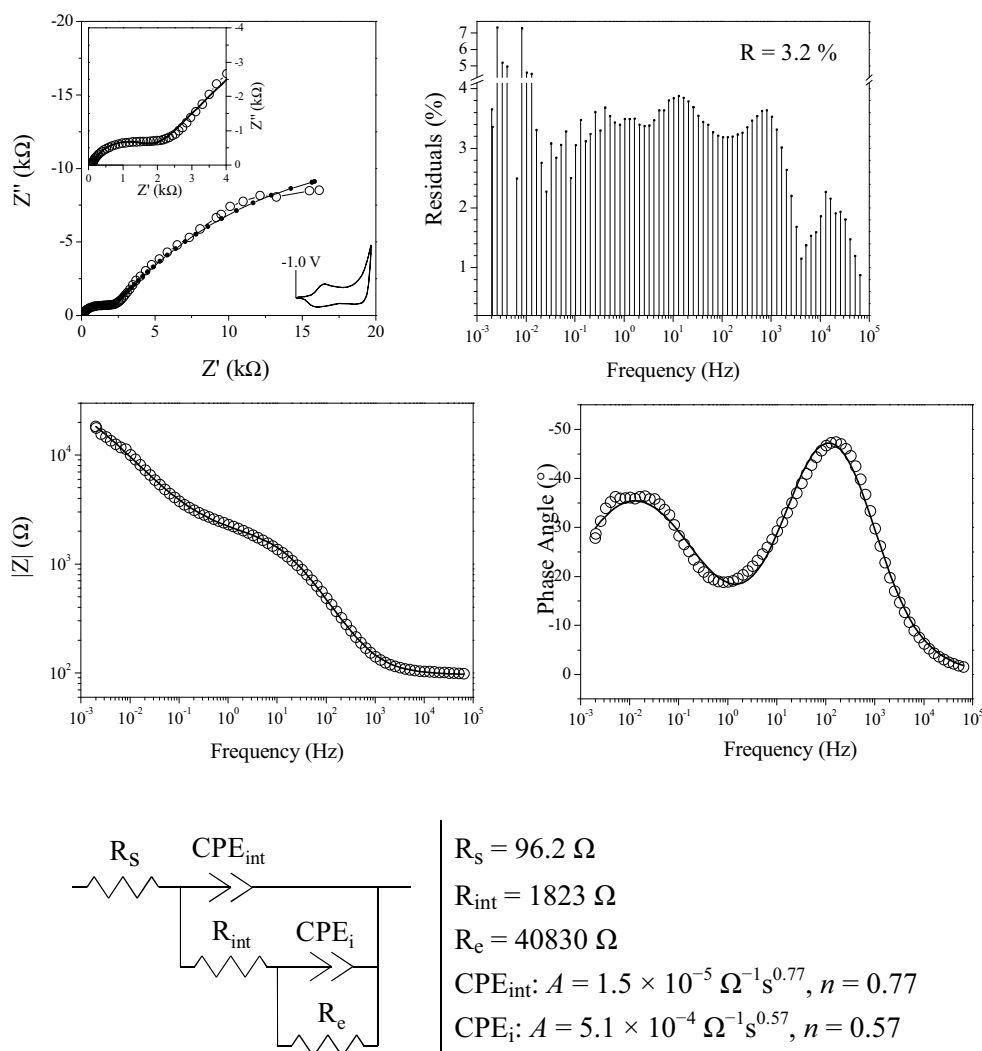


Figure 4.28 Second equivalent circuit and fitting analysis of the impedance response of a PPy-PSS film recorded at -1.00 V vs. SCE in 0.10 M Na_2SO_4 . The equivalent circuit and the value for the fitting parameters are given at the bottom. The complex plane and bode plots of the impedance response (O) and the corresponding simulated data ($-\bullet-$ and $—$) are given above the circuit. The insets in the complex plane are the enlargement of the high frequency portion of the impedance response, and the cyclic voltammogram of the film showing the redox state of the polymer. The plot of the fitting residuals and the average percentage residual, $R\%$, are given on the top.

The constant phase element CPE_i ($n = 0.57$), in parallel to R_e , is due to the diffusion of Na^+ ions inside the reduced film, in fact it represents a slightly distorted Warburg element. At -1.00 V vs. SCE further ingress of cations in the film occurs in order to counterbalance the negative charge of PSS after the reduction of PPy.

The CPE_{int} and R_{int} are related to the capacitance and electron transfer resistance at the electrode/film interface as observed and supported by the impedance analysis of both Ren and Komura [39, 42]. Komura *et al.* [42] found that the R_{int} at the metal/film interface was emerging as a result of the decreasing concentration of hole carriers in the PPy-PSS film.

4.2.6.2 PPy-PSS-MWNT-PEI Modified Electrodes

The PPy-PSS-MWNT-PEI films were prepared at glassy carbon electrodes of diameter 4 mm. The impedance measurements were collected in the frequency range from 10 mHz to 65 kHz in aerated 0.10 M Na_2SO_4 . The composite films were preconditioned prior to the measurements by keeping the modified electrodes at a bias potential for 30 min in the same electrolyte solution. The bias potentials were 0.00 V, -0.50 V and -1.00 V vs. SCE.

There is no previous impedance characterization of PPy-PSS-MWNT-PEI films, since these nanocomposites are presented in this work for the first time. However, different studies on the properties of composites made from PPy and CNT are available. Chen *et al.* [30] used carboxyl-functionalized CNT directly as a dopant for the electrochemical polymerization of Py. In this case, the impedance spectra of the composite films were recorded at 0.20 V, -0.20 V and -0.60 V vs. SCE. The result was a response characterized only by diffusive and capacitive components regardless of the oxidation state of the films. Such behaviour was entirely new as reduced PPy films are insulating. The CNT were responsible for this conductivity in the composite films even when PPy was in its reduced state. Wu and Lin [52] measured conductivities two orders of magnitude higher for PPy modified with MWNT compared to their plain counterparts. In a recent work, Fang *et al.* [53], prepared a composite of PPy-MWNT by pulsed electrodeposition to achieve values of specific capacitance of 427 F/g, while Lin and Xu [54] obtained even higher values up to 890 F/g. These large values of capacitance were related to the combined contribution

of the charge stored in both MWNT and PPy. The overall effect of the addition of MWNT to the PPy is then to improve the conductivity and capacitance of the films. This is also observed in the present study with the PPy-PSS-MWNT-PEI nanocomposites.

The impedance responses of the PPy-PSS-MWNT-PEI films are given in Figure 4.29. Comparing these responses to those of PPy-PSS in Figure 4.24, it is immediately evident that the incorporation of the MWNT-PEI causes a drop of the impedance by two orders of magnitude. Another significant difference is the shape of the curves. For PPy-PSS, these are the typical semi-circles found for resistive-capacitive behaviour, while for PPy-PSS-MWNT-PEI films, almost vertical traces, typical of a diffusive-capacitive response, are observed.

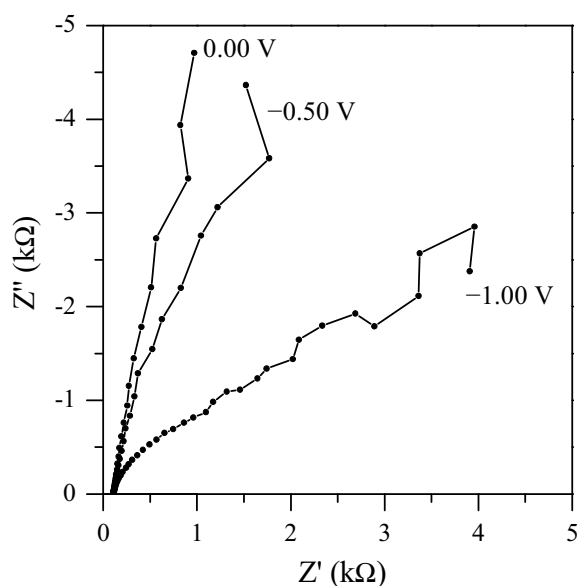


Figure 4.29 Complex plane impedance plot for the PPy-PSS-MWNT-PEI film response at 0.00 V, -0.50 V and -1.00 V vs. SCE. The measurements were run in the frequency range from 10 mHz to 65 kHz in aerated 0.10 M Na₂SO₄. The AC amplitude was 5 mV peak-to-peak. The films were prepared on a glassy carbon electrode.

The impedance response at 0.00 V vs. SCE was fitted with the equivalent circuit reported in Figure 4.30. The average percentage residual is just 0.7 % showing excellent agreement between experimental and simulated data points. The equivalent circuit contains a solution resistance, R_s , a pure capacitor, C_{fl} , and two Warburg components, W_{1a} and W_{1b} .

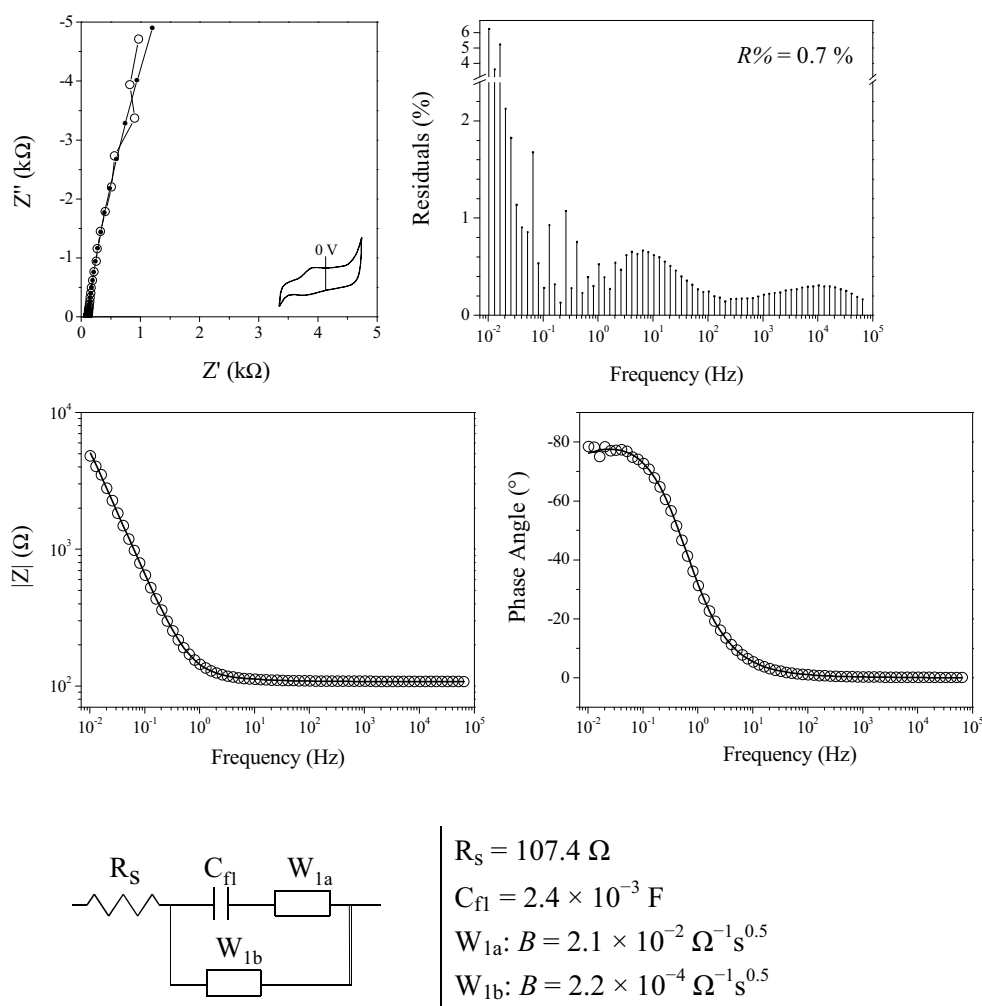


Figure 4.30 Equivalent circuit and fitting analysis of the impedance response of a PPy-PSS-MWNT-PEI film recorded at 0.00 V vs. SCE in 0.10 M Na₂SO₄. The equivalent circuit and the value for the fitting parameters are given in the bottom. The complex plane and bode plots of the impedance response (○) and the corresponding simulated data (—•— and —) are given above the circuit. The inset in the complex plane is the cyclic voltammogram of the film showing the redox state of the polymer at the potential of measurement. The plot of the fitting residuals and the average percentage residual, $R\%$, is given on the top.

A large capacitance, $C_{fl} = 2.4 \text{ mF}$, was computed corresponding to a specific capacitance of about 363 F/g since the weight of the film was 6.6 μg . The amount of PPy-PSS was 2.6 μg , corresponding to a deposition charge of 40 mC/cm^2 , the same as in Section 4.2.6.1; while the amount of MWNT-PEI was 4.0 μg , corresponding to drop-casting of 5 μl of 0.08 % w/w MWNT-PEI solution, as described in Section 2.4.1.2. A capacitance of 363 F/g is of the order of those previously reported for PPy-

CNT films [53]. It is also interesting to note that by adding the nanotubes the capacitive term behaves more like an ideal capacitance, *i.e.*, like a CPE with $n = 1$. The other two components are Warburg elements, one corresponding to a fast diffusion, W_{1a} with $B = 2.1 \times 10^{-2} \Omega^{-1} s^{0.5}$, and one to slow diffusion, W_{1b} with $B = 2.2 \times 10^{-4} \Omega^{-1} s^{0.5}$. The former is likely to be due to the fast diffusion of the Na^+ ions in the microporosity of the film, indeed microscopic cracks were observed by SEM measurement (Section 4.2.4, Figure 4.10). The latter Warburg term is similar to the Warburg element found for the PPy-PSS at -0.50 V vs. SCE (W_{i2} , $B = 2.5 \times 10^{-4} \Omega^{-1} s^{0.5}$), which is associated with the diffusion of Na^+ ions in the partially reduced, *i.e.*, cation-enriched, structure of the PPy-PSS film. This may indicate the formation of a nanoporous texture in the PPy-PPS when deposited on MWNT-PEI-modified surfaces. This texture would allow the diffusion of Na^+ in the polymer even in its reduced state. Nanoporosity has already been observed in PPy-MWNT composites [28].

The best fitting for the impedance response registered at -0.50 V vs. SCE is given in Figure 4.31. The equivalent circuit is the same as the one found at 0.00 V vs. SCE, the average percentage residual is also similar (0.9%). At this potential, the film is partially reduced with a consequent drop of the capacitance to about 270 F/g. The two Warburg elements, W_{2a} and W_{2b} , adopt slightly higher values compared to those, W_{1a} and W_{1b} , recorded at 0.00 V vs. SCE. This is related to a higher ingress of Na^+ ions into the polymer in order to balance the exposed charge of the PSS^- dopant. At this potential the electronic resistance is still negligible as for the plain PPy-PSS films.

The impedance response at -1.00 V vs. SCE is different from the previous two and was fitted with the equivalent circuit given in Figure 4.32. The quality of the fitting is good with an average percentage residual of 1.1 %. The equivalent circuit in this case is composed of a solution resistance, R_s , a distorted film capacitance, CPE_f with $n = 0.91$, and a distorted Warburg element, CPE_i with $n = 0.4$. A new element is also present, the electronic resistance, R_e , of the reduced PPy-PSS-MWNT-PEI film. According to the expected response of the composite, the capacitance of the film drops upon reduction to about 27 F/g.

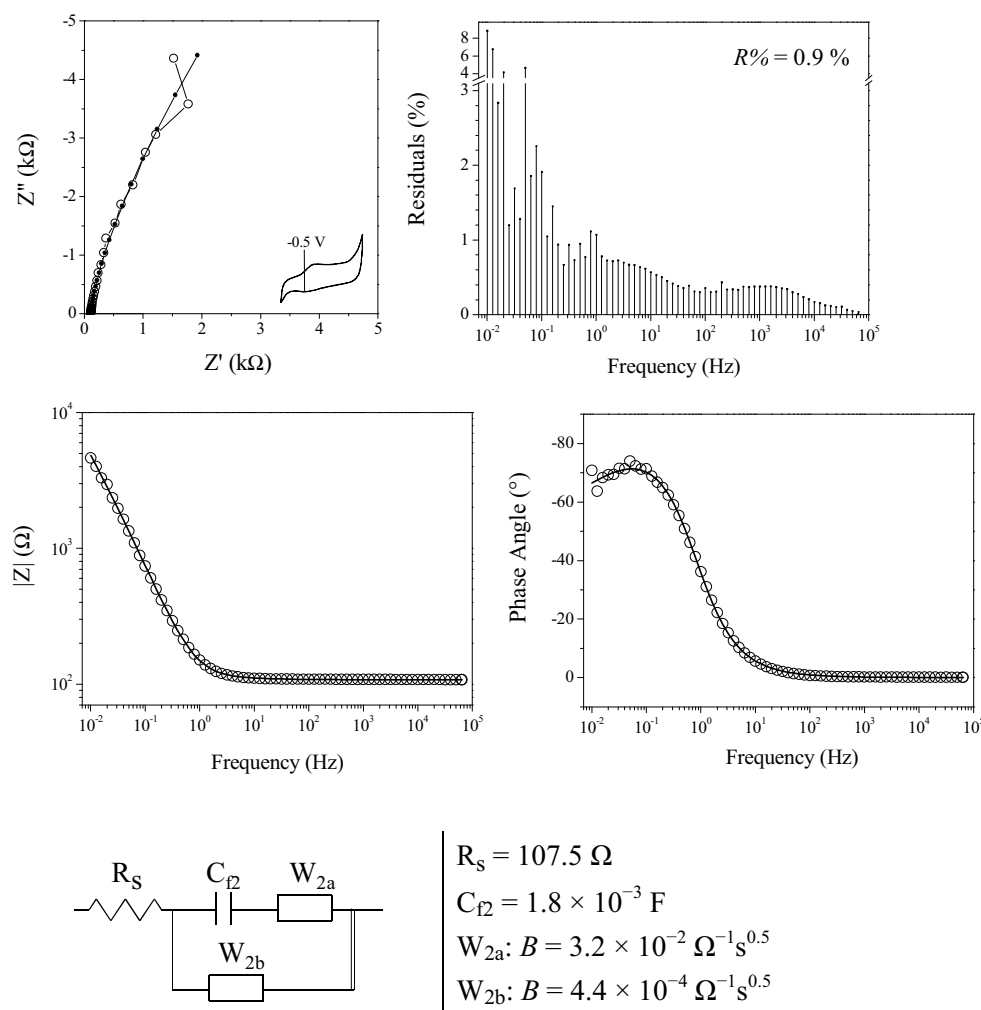


Figure 4.31 Equivalent circuit and fitting analysis of the impedance response of a PPy-PSS-MWNT-PEI film recorded at -0.50 V vs. SCE in $0.10 \text{ M Na}_2\text{SO}_4$. The equivalent circuit and the value for the fitting parameters are given in the bottom. The complex plane and bode plots of the impedance response (O) and the corresponding simulated data (—•— and —) are given above the circuit. The inset in the complex plane is the cyclic voltammogram of the film showing the redox state of the polymer at the potential of measurement. The plot of the fitting residuals and the value of the average percentage residual, $R\%$, is given on the top.

This corresponds to a 10-fold decrease from the capacitance of the nanocomposite at -0.50 V vs. SCE. Such a drop may be related to the reduction of the PPy-PSS-MWNT-PEI film which causes a neutralization of the positive charge originally stored at the conducting polymer backbone. It follows that even at -1.00 V vs. SCE, the film displays some capacitive behaviour. Indeed, this capacitance was also evident in the cyclic voltammetry of the composite (Section 4.2.4, Figure 4.12).

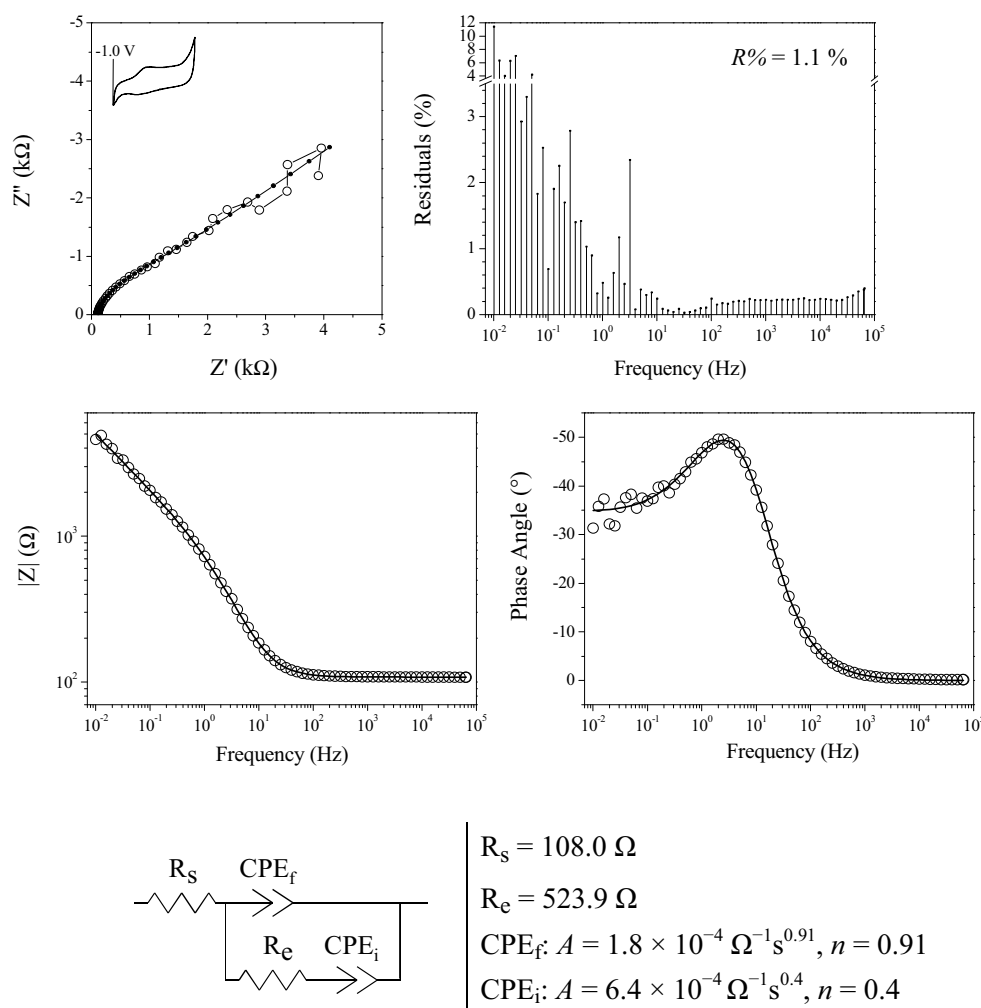


Figure 4.32 Equivalent circuit and fitting analysis of the impedance response of a PPy-PSS-MWNT-PEI film recorded at -1.00 V vs. SCE in 0.10 M Na_2SO_4 . The equivalent circuit and the value for the fitting parameters are given in the bottom. The complex plane and bode plots of the impedance response (O) and the corresponding simulated data ($- \bullet -$ and $—$) are given above the circuit. The inset in the complex plane is the cyclic voltammogram of the film showing the redox state of the polymer at the potential of measurement. The plot of the fitting residuals and the value of the average percentage residual, $R\%$, are given on the top.

The diffusion of Na^+ ions into the film, which enter to counterbalance the negative charge of the dopant, gives rise to an increase in the Warburg constant. On varying the applied potential from -0.50 to -1.00 V vs. SCE, the Warburg term increases from $4.4 \times 10^{-4} \Omega^{-1} s^{0.5}$ to $6.4 \times 10^{-4} \Omega^{-1} s^{0.4}$, although the comparison is only approximate since the Warburg element at -1.00 V vs. SCE is slightly distorted ($n = 0.4$). The key element of this equivalent circuit is the electronic resistance, R_e ,

which appeared once the PPy-PSS-MWNT-PEI film is completely reduced. This is in accordance with the predominant resistive contribution of R_e observed also for the plain PPy-PSS films (Section 4.2.6.1). However, this time the resistance is considerably lower, 524 Ω compared with 40830 Ω . This significantly higher conductivity is consistent with the presence of the MWNT-PEI which allows a more efficient transport of electrons through the reduced film [52].

4.2.6.3 Influence of MWNT-PEI on the Nitrate Sensing Performance

The nitrate sensing performance of the CuNP modified electrodes are greatly improved by the incorporation of MWNT-PEI in the PPy-PSS films. The sensitivity, linear range of the response and the detection limit are all enhanced by the presence of the carbon nanotubes (Section 4.2.5.2). The previous two sections were dedicated to the analysis and comparison of the electrochemical properties of the PPy-PSS and PPy-PSS-MWNT-PEI film-modified electrodes. The electrochemical impedance characterization showed clearly the great improvement of electrical properties upon incorporation of the nanotubes in the films. The reduced PPy-PSS films, that were originally electrical insulators, became conductors thanks to the addition of the modified carbon nanotubes. In particular, the electronic resistance of the films dropped from about 40 k Ω to about 0.5 k Ω at a potential of -1.00 V vs. SCE. The improvement of electrical conductivity is the major factor for the enhanced nitrate sensing performance in the presence of MWNT-PEI.

4.3 Summary

In this chapter the electrochemistry of the PPy-PSS films was exploited to obtain copper hybrid microstructures and metallic copper nanoparticles. Based on the knowledge acquired in Chapter 3, the two main processes of copper capture and oxygen reduction reaction, combined with the direct reduction of copper at film surface, were used to perform the electrodeposition of different copper structures at different potentials (Section 4.2.1). These structures were then combined together through a simple one-pot fabrication procedure to give hybrid microstructures made of a central copper oxide microcrystal and surrounded by copper hydroxysulfate welded sheets (Section 4.2.2). In a separate solution, the hierarchical

micro/nanostructures were reduced to metallic copper nanoparticles. This transition was documented by SEM imaging (Section 4.2.3). The electrode modified with the copper nanoparticles was used to sense nitrate ions both voltammetrically and amperometrically. The sensing performance was further enhanced by introducing polyethyleneimine modified multiwall carbon nanotubes in the polymer film (Sections 4.2.4 and 4.2.5). A detailed electrochemical impedance study showed that the nanotubes had significantly enhanced the conductivity of the films, particularly at potentials where the films were reduced (Section 4.2.6).

In relation to the performance in sensing nitrates, the PPy-PSS-CuNP films gave a sensitivity of $99.0 \mu\text{A}/(\text{mM}\cdot\text{cm}^2)$, a linear range from 0.5 – 2.0 mM, and a measured voltammetric detection limit was 0.5 mM. Instead, in the case of the PPy-PSS-MWNT-PEI-CuNP, the sensitivity was $137.2 \mu\text{A}/(\text{mM}\cdot\text{cm}^2)$, the linear range was between 0.1 – 5.0 mM, and the measured voltammetric detection limit was 0.1 mM. This detection limit was further enhanced to 30 μM by constant potential amperometry at a rotating disk electrode, giving a very good result considering that the signal was affected by significant instrumental noise. The evident improvement of sensing performance upon incorporation of the MWNT-PEI into the conducting polymer film can be attributed to the enhanced conductivity of these films.

4.4 References

- [1] Bard AJ, Faulkner LR; *Electrochemical methods: fundamentals and applications*; 2000, 2nd ed., Wiley
- [2] Paunovic M, Schlesinger M; *Fundamentals of Electrochemical Deposition*; 2006, 2nd ed., Wiley-Interscience
- [3] Campbell FW, Compton RG; *Analytical and Bioanalytical Chemistry*, **2010**, 396(1), 241
- [4] Moshfegh AZ; *Journal of Physics D-Applied Physics*, **2009**, 42(23),
- [5] Welch CW, Compton RG; *Analytical and Bioanalytical Chemistry*, **2006**, 384(3), 601
- [6] Baughman RH, Zakhidov AA, de Heer WA; *Science*, **2002**, 297(5582), 787
- [7] Ajayan PM; *Chemical Reviews*, **1999**, 99(7), 1787
- [8] Sun YP, Fu KF, Lin Y, Huang WJ; *Accounts of Chemical Research*, **2002**, 35(12), 1096
- [9] Shaffer MSP, Fan X, Windle AH; *Carbon*, **1998**, 36(11), 1603

-
- [10] Liao KS, Wan A, Batteas JD, Bergbreiter DE; *Langmuir*, **2008**, 24(8), 4245
- [11] Welch CM, Hyde ME, Banks CE, Compton RG; *Analytical Sciences*, **2005**, 21(12), 1421
- [12] Greer FR, Shannon M; *Pediatrics*, **2005**, 116(3), 784
- [13] Smith VH, Tilman GD, Nekola JC; *Environmental Pollution*, **1999**, 100(1-3), 179
- [14] Moorcroft MJ, Davis J, Compton RG; *Talanta*, **2001**, 54(5), 785
- [15] Ward-Jones S, Banks CE, Simm AO, Jiang L, Compton RG; *Electroanalysis*, **2005**, 17(20), 1806
- [16] Davis J, Moorcroft MJ, Wilkins SJ, Compton RG, Cardosi MF; *Analyst*, **2000**, 125(4), 737
- [17] European Council Directive 98/83/EC; *The Quality of Water Intended for Human Consumption* (1998)
- [18] United States Environmental Protection Agency EPA 816-F-09-004; *National Primary Drinking Water Regulations* (2006)
- [19] Zhou XJ, Harmer AJ, Heinig NF, Leung KT; *Langmuir*, **2004**, 20(12), 5109
- [20] Sarkar DK, Zhou XJ, Tannous A, Louie M, Leung KT; *Solid State Communications*, **2003**, 125(7-8), 365
- [21] Sarkar DK, Zhou XJ, Tannous A, Leung KT; *Journal of Physical Chemistry B*, **2003**, 107(13), 2879
- [22] Tsakova V; *Journal of Solid State Electrochemistry*, **2008**, 12(11), 1421
- [23] Zhou YC, Switzer JA; *Scripta Materialia*, **1998**, 38(11), 1731
- [24] Wang ZL; *Journal of Physical Chemistry B*, **2000**, 104(6), 1153
- [25] Dunitz JD, Bernstein J; *Accounts of Chemical Research*, **1995**, 28(4), 193
- [26] Zhdanov VP, Kasemo B; *Chemical Physics Letters*, **2008**, 452(4-6), 285
- [27] Niklasson GA, Karmhag R; *Surface Science*, **2003**, 532, 324
- [28] Hughes M, Chen GZ, Shaffer MSP, Fray DJ, Windle AH; *Chemistry of Materials*, **2002**, 14(4), 1610
- [29] Hughes M, Shaffer MSP, Renouf AC, Singh C, Chen GZ, Fray J, Windle AH; *Advanced Materials*, **2002**, 14(5), 382
- [30] Chen GZ, Shaffer MSP, Coleby D, Dixon G, Zhou WZ, Fray DJ, Windle AH; *Advanced Materials*, **2000**, 12(7), 522
- [31] Park HM, Kim KH, Lee SH, Park DH, Hong YK, Joo J; *Colloids and Surfaces a-Physicochemical and Engineering Aspects*, **2008**, 313, 72
- [32] Sharma RK, Karakoti A, Seal S, Zhai L; *Journal of Power Sources*, **2010**, 195(4), 1256
- [33] Fang YP, Liu JW, Yu DJ, Wicksted JP, Kalkan K, Topal CO, Flanders BN, Wu JD, Li J; *Journal of Power Sources*, **2010**, 195(2), 674
- [34] An KH, Jeon KK, Heo JK, Lim SC, Bae DJ, Lee YH; *Journal of the Electrochemical Society*, **2002**, 149(8), A1058
-

-
- [35] Dima GE, de Vooy's ACA, Koper MTM; *Journal of Electroanalytical Chemistry*, **2003**, 554, 15
- [36] Aouina N, Cachet H, Debiemme-chouvy C, Thi TMT; *Electrochimica Acta*, **2010**, 55(24), 7341
- [37] Hubaux A, Vos G; *Analytical Chemistry*, **1970**, 42(8), 849
- [38] Ren XM, Pickup PG; *Journal of Physical Chemistry*, **1993**, 97(20), 5356
- [39] Ren XM, Pickup PG; *Journal of Electroanalytical Chemistry*, **1997**, 420(1-2), 251
- [40] Albery WJ, Elliott CM, Mount AR; *Journal of Electroanalytical Chemistry*, **1990**, 288(1-2), 15
- [41] Albery WJ, Chen Z, Horrocks BR, Mount AR, Wilson PJ, Bloor D, Monkman AT, Elliott CM; *Faraday Discussions*, **1989**, 88, 247
- [42] Komura T, Goisihara S, Yamaguti T, Takahasi K; *Journal of Electroanalytical Chemistry*, **1998**, 456(1-2), 121
- [43] Yang R, Naoi K, Evans DF, Smyrl WH, Hendrickson WA; *Langmuir*, **1991**, 7(3), 556
- [44] Li FB, Albery WJ; *Journal of the Chemical Society-Faraday Transactions*, **1991**, 87(18), 2949
- [45] Rubinson JF, Kayinamura YP; *Chemical Society Reviews*, **2009**, 38(12), 3339
- [46] Holzhauser P, Bouzek K; *Journal of Applied Electrochemistry*, **2006**, 36(6), 703
- [47] Weidlich C, Mangold KM, Juttner K; *Electrochimica Acta*, **2005**, 50(7-8), 1547
- [48] Sin SL, Teo LL, Tan KS, Chan CY; *Electrochemistry Communications*, **2000**, 2(10), 685
- [49] Salzer CA, Elliott CM, Hendrickson SM; *Analytical Chemistry*, **1999**, 71(17), 3677
- [50] Baker CK, Qiu YJ, Reynolds JR; *Journal of Physical Chemistry*, **1991**, 95(11), 4446
- [51] Barsoukov E, Macdonald JR; *Impedance Spectroscopy: Theory, Experiment, and Applications*; 2005, Wiley
- [52] Wu TM, Lin SH; *Journal of Polymer Science Part a-Polymer Chemistry*, **2006**, 44(21), 6449
- [53] Fang YP, Liu JW, Yu DJ, Wicksted JP, Kalkan K, Topal CO, Flanders BN, Wu JD, Li J; *Journal of Power Sources*, 195(2), 674
- [54] Lin XQ, Xu YH; *Electrochimica Acta*, **2008**, 53(15), 4990

Chapter 5

Electrochemical Deposition of Nanothin Sheets of Zinc Hydroxysulfates and their Conversion to Dendritic Metallic Zinc at Polypyrrole-Polystyrene Sulfonate Films

5. Electrochemical Deposition of Nanosheets of Zinc Hydroxysulfates and their Conversion to Dendritic Metallic Zinc at Polypyrrole-Polystyrene Sulfonate Films

5.1 Introduction

Zinc hydroxysulfates are well known corrosion products of zinc metal exposed to rural atmospheres, polluted environments (SO_2 and NO_2) or acid rain conditions [1-4]. In general zinc hydroxysulfates are prepared from the precipitation of the double salts of zinc hydroxide and zinc sulfate in water in the presence of a base. For example, large zinc hydroxysulfate nanosheets have been prepared from the hydrothermal treatment of zinc sulfate in the presence of tertiary amines [5]. The possible applications of zinc hydroxysulfates are related to the general properties of layered hydroxide salts [6]. In particular, zinc hydroxysulfates have been applied to the adsorption of chromate ions and pH buffering [7]. A list of zinc hydroxysulfates with many other basic double salts and their respective solubilities is available in the literature [8, 9].

Zinc hydroxysulfates are directly related to ZnO, which is a semiconductor material that has received much attention in the scientific community since it has many possible and important technological applications, such as in light emitting devices, piezoelectric devices, photo-conducting devices, and gas, chemical and biosensors. The preparation, properties and applications of ZnO are thoroughly discussed in various reviews [10-12]. In a recent work, Wang *et al.* [13] described the phase evolution of electrodeposited ZnO to $\text{ZnSO}_4[\text{Zn}(\text{OH}_2)]_6 \cdot 4\text{H}_2\text{O}$ as a function of the sulfate concentration present in the electrolyte. Alternatively, $\text{ZnSO}_4[\text{Zn}(\text{OH}_2)]_3$ can also be converted to ZnO via a pH driven dissolution-precipitation process [14]. This process may account for some of the observations recorded in the present work during the formation of ZnO deposits on the surface of the PPy-PSS films, as shown in Section 5.2.5. Another way to convert zinc hydroxysulfates to zinc oxide is the exposure of the hydroxysulfate to electron bombardment [5].

Zinc hydroxysulfates can also be electrochemically reduced to zero-valent zinc, as shown from the results presented in Section 5.2.5. Metallic zinc bulk and nano materials are known for their dechlorinating catalytic effects towards halogenated organic compounds. Pentachlorophenol and carbon tetrachloride are two examples of poisonous polychlorinated pollutants that can be remediated using zinc metal [15-18].

In this chapter, the electrochemical deposition of zinc hydroxysulfate nanothin sheets is performed on polypyrrole-polystyrene sulfonate (PPy-PSS) thin films with a thorough microscopic and spectroscopic characterization of the resulting materials (Sections 5.2.1 and 5.2.2). The morphology of the nanothin sheets is analyzed along with a characterization of some aspects of their mechanism of nucleation and growth (Section 5.2.3). The experimental conditions, such as the electrode potential, film thickness, type of dopant, nature of the counterion, and the effects of dissolved oxygen and pH, are all considered in terms of their influence on the outcome of the electrodeposition (Section 5.2.4). Finally, the zinc-based nanosheets are converted to metallic zinc micro-dendrites by electrochemical reduction of the modified films (Section 5.2.5). Other minor zinc species are also likely to be formed during the reduction treatment, *e.g.*, zinc oxide, which could be the object of future research work.

5.2 Results and Discussion

5.2.1 Electrodeposition of Zinc-Based Nanothin Sheets

The capture of Zn^{2+} at PPy-PSS thin films was carried out as previously described for Cu^{2+} ions (Section 3.2.1.2). Three PPy-PSS films were immersed in a 0.10 M ZnSO_4 aerated solution and three reduction potential sweeps were performed from 0.60 to 0.00 V vs. SCE at 1.0, 3.0 and 5.0 mV/s, the corresponding mass changes of the films are shown in Figure 5.1. The masses of the films increase during the reduction sweep consistent with the diffusion of Zn^{2+} ions from the solution to the film and their capture within the films. A larger number of ions are captured at lower scan rates as the time available to the ions to diffuse into the film is longer. Also, at the slowest scan rate, 1.0 mV/s, a sharp increase of mass is observed just before 0.00 V vs. SCE, indicative of the presence of an additional deposition process.

This is not observed at higher scan rates. It is likely that this process is connected to the accumulation of a certain concentration of ions, and this critical amount is reached only at the slowest scan rate. This process is related to the electroprecipitation of zinc hydroxysulfates, as shown later in Sections 5.2.2 and 5.2.3. It is convenient to report again in Figure 5.2 the current-potential plot of a PPy-PSS film immersed in aerated 0.10 M ZnSO₄ or aerated 0.10 M CuSO₄ solutions. As previously discussed (Section 3.2.1.2), the plateau current registered below 0.00 V vs. SCE in the ZnSO₄ solution is due to the reduction of oxygen. This plateau region extends to -0.40 V vs. SCE, whereas in the case of the copper system, a wave corresponding to the deposition of copper is recorded at potentials below 0.10 V vs. SCE. This variation is due to the different standard reduction potentials of the two redox systems, $E_{\text{Cu(II)/Cu(0)}}^{\circ} = 0.099$ V vs. SCE and $E_{\text{Zn(II)/Zn(0)}}^{\circ} = -1.003$ V vs. SCE (Sections 1.5.1.2 and 1.5.2.2). In this chapter, it is shown that basic zinc salts can be electrodeposited at constant potential on PPy-PSS films. This is achieved by the simultaneous capture of zinc ions and reduction of dissolved oxygen to hydroxide ions at the PPy-PSS film. Any potential below 0.00 V vs. SCE is suitable for the deposition, since it provides both the zinc and hydroxide ions necessary to form zinc hydroxysulfates, while the sulfate ions are available from the electrolyte.

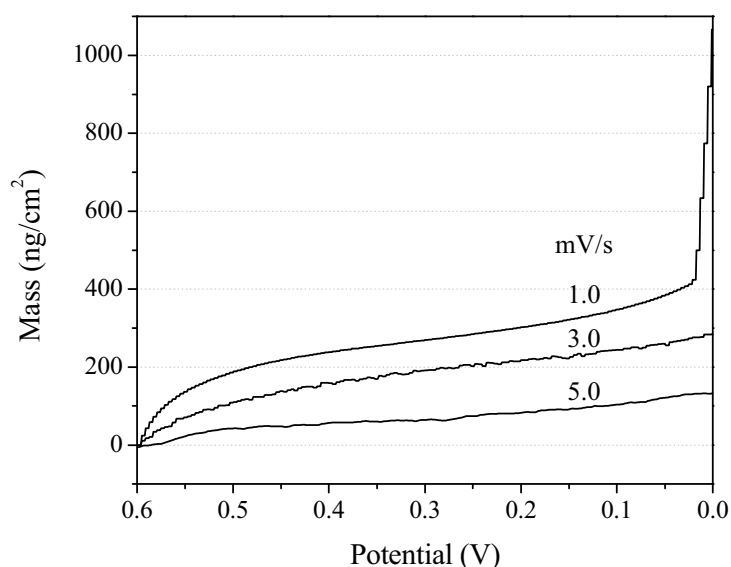


Figure 5.1 Mass changes of PPy-PSS films in aerated 0.10 M ZnSO₄ during reduction potential sweeps. The films were 120 nm thick and deposited on AT-cut quartz crystal gold electrodes. The scan rates were 1.0, 3.0 and 5.0 mV/s as shown in the plot.

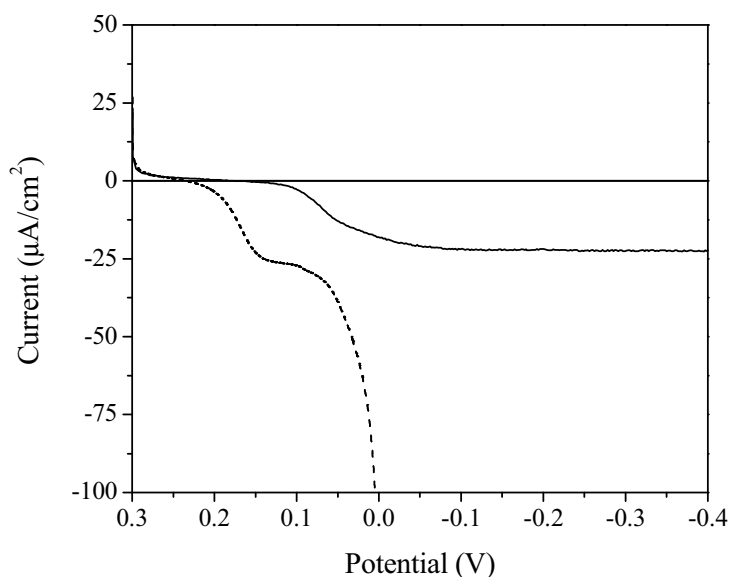


Figure 5.2 Current-potential data recorded at PPy-PSS films in aerated 0.10 M ZnSO₄ (—) and aerated 0.10 M CuSO₄ (---) during a reduction potential sweep. The films were 120 nm thick and deposited on a glassy carbon electrode. The scan rate is 0.1 mV/s.

Three replicates of current and charge, labelled 1, 2 and 3, recorded during the electrodeposition at 0.00 V vs. SCE in aerated 0.10 M ZnSO₄ are given in Figure 5.3. As shown in the figure, the current decays to a minimum. It then increases steadily before reaching an almost constant value that is maintained during the remaining electrodeposition period. Good reproducibility is observed during the early stages of electrodeposition; nearly identical minimum current values are observed at the same times. Instead, at longer deposition times, the plateau, or steady-state current is different. Consequently, the electrodeposition to the same amount of charge, 30 mC/cm², requires different times. This is clearly evident in the inset in Figure 5.3. This difference may be connected with the number of nuclei established during the instantaneous nucleation, as discussed in Section 5.2.3.2. It is also clear that the deposition of the zinc compound is slower than that of the copper compound (Section 3.2.1.2); in fact the steady-state electrodeposition current recorded with the zinc system is $-10 \mu\text{A}/\text{cm}^2$ compared to $-20 \mu\text{A}/\text{cm}^2$ for the copper system.

The zinc-based nanosheets deposited on the surface of the PPy-PSS films are shown in Figure 5.4. These were deposited from 0.10 M ZnSO₄ at 0.00 V vs. SCE as detailed in Figure 5.3. The surface of the film is completely covered by the

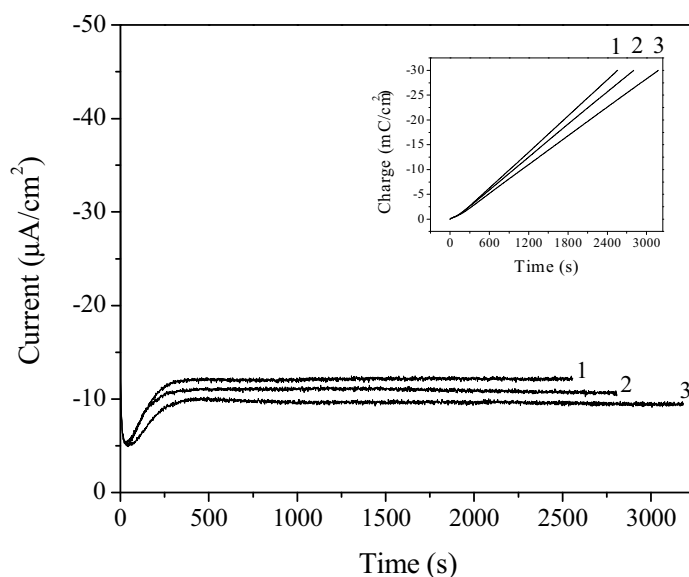


Figure 5.3 Current-time and charge-time plots recorded during the deposition of zinc-based nanothin sheets at PPy-PSS films at 0.00 V vs. SCE in aerated 0.10 M ZnSO₄. Three replicates of the electrodeposition are labelled as 1, 2 and 3. The films were deposited on an AT-cut quartz crystal gold electrode to a thickness of 120 nm.

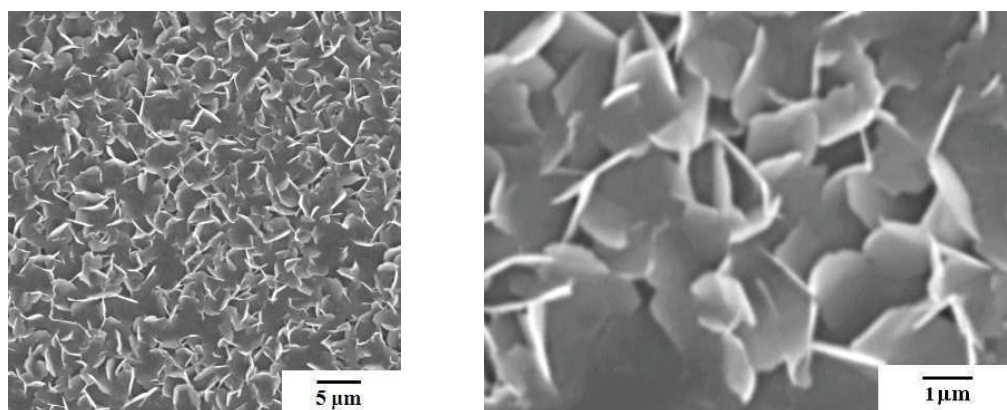


Figure 5.4 Zinc-based nanothin sheets deposited on a PPy-PSS thin film from an aerated 0.10 M ZnSO₄ solution at 0.00 V vs. SCE. A large number of nanosheets covers completely the film (left), a close up of the nanosheets is shown (right). The film thickness was 120 nm on an AT-cut quartz crystal gold electrode.

nanosheets and the underlying polymer surface cannot be observed. The thickness of the sheets is of the order of 100 nm (Figure 5.4). This deposit is very different compared to that observed with copper. In the present case, single sheets form separately at different points on the polymer film, whereas in the case of copper, multiple sheets assemble at the same point forming clusters (Section 3.2.1.2).

The electrodeposition of zinc-based nanosheets can be performed only in the presence of dissolved oxygen in the ZnSO_4 solution. This feature is similar to that already observed for the deposition of hierarchical copper-based micro/nanostructures (Section 3.2.1.2) and it is addressed later with further details in Section 5.2.4.3.

5.2.2 Characterization of Zinc-Based Nanothin Sheets

5.2.2.1 X-Ray Diffraction

The zinc-based nanothin sheets were characterized using X-ray diffraction, XRD (Section 2.5.4.4). In order to identify the crystalline components of the nanosheets, the XRD spectra of the bare and zinc-modified electrodes were analyzed and compared. The overall XRD spectrum of the nanothin sheets is given in Figure 5.5, while the smaller and sharper features are enlarged in Figure 5.6.

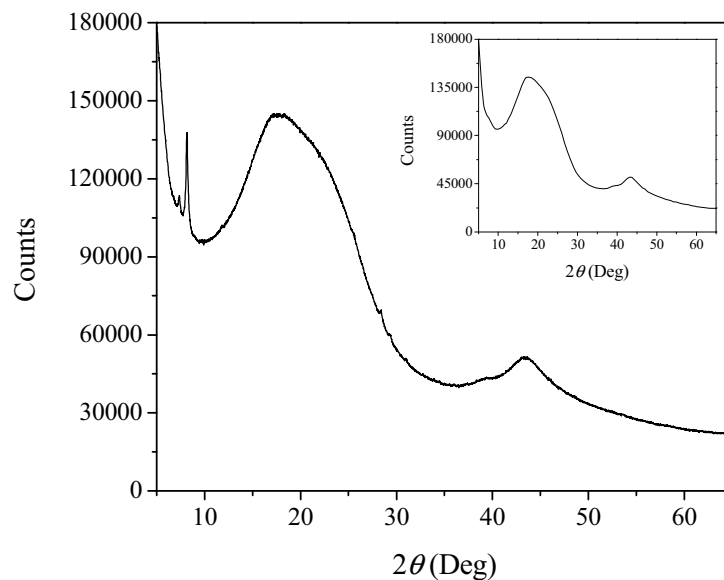


Figure 5.5 XRD spectrum of the zinc-based nanothin sheets electrodeposited on a 120 nm PPy-PSS film from oxygen saturated 0.10 M ZnSO_4 solution at 0.00 V vs. SCE. The electrode material is glassy carbon and the deposited charge 80 mC/cm^2 . In the inset, the background trace that is subtracted from the raw spectrum to obtain the spectrum shown in Figure 5.7.

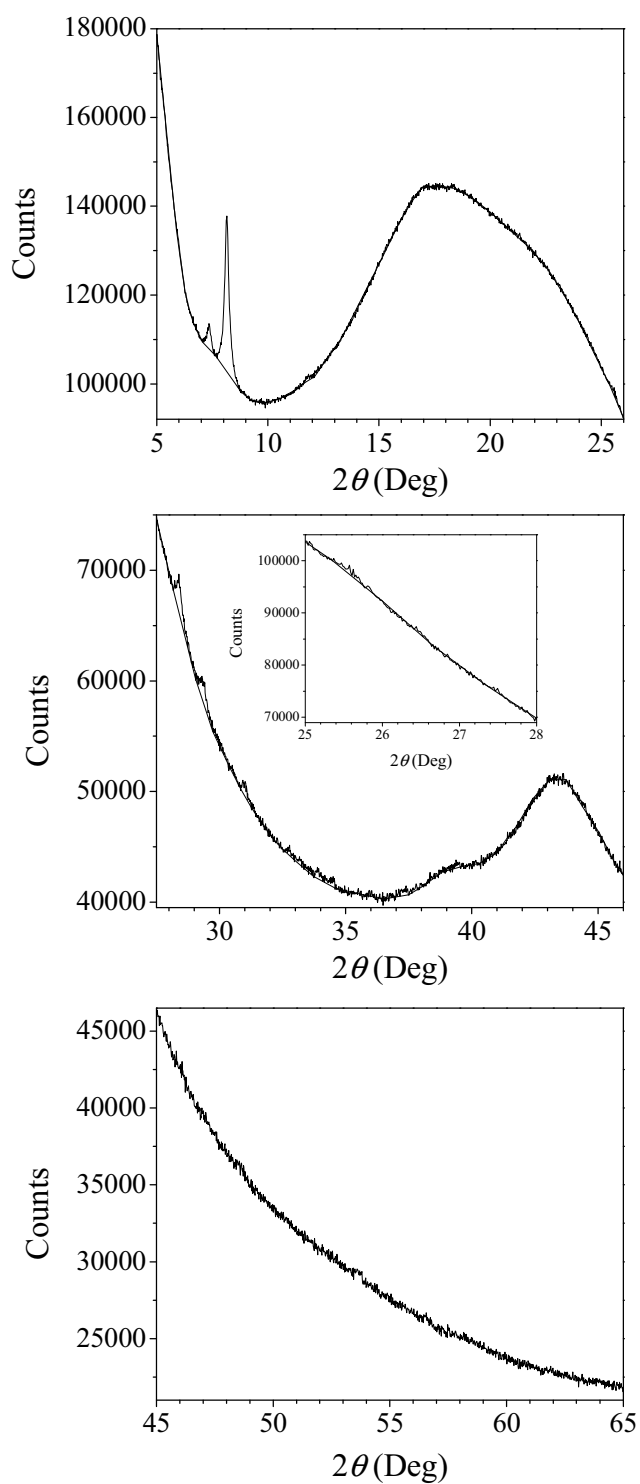


Figure 5.6 Enlargements of the XRD raw and background superimposed spectra of the zinc-based nanosheets given in Figure 5.5. Small diffraction peaks are visible in the portions of the raw spectrum emerging above the background trace. The subtraction of the background spectrum from the raw spectrum allows the clear identification of the diffraction peaks due to the zinc-based nanosheets as shown in Figure 5.7.

The XRD spectrum of a glassy carbon (GC) bare electrode was discussed and shown previously in Section 3.2.2.2, Figure 3.12. In this spectrum, the two broad signals at about 20.0° and 44.0° are characteristic of the background trace of GC, as reported in the literature [19]. These signals are also found in the XRD spectrum of the zinc-based nanosheets as shown in Figure 5.5. The smaller and sharper peaks present above such signals are evidenced by subtracting the background trace to obtain the spectrum in Figure 5.7. This spectrum is compared to the one of the bare electrode in Figure 5.8. The Ag peaks observed in the spectrum of the bare electrode (Section 3.2.2.2) are not present in the case of the zinc-based nanosheets. Also, the peak of the electrode at 8.9° is different in position and shape to the one of the nanosheets at about 8.1° . The only corresponding peaks are those at 28.4° , 29.3° and 31.0° .

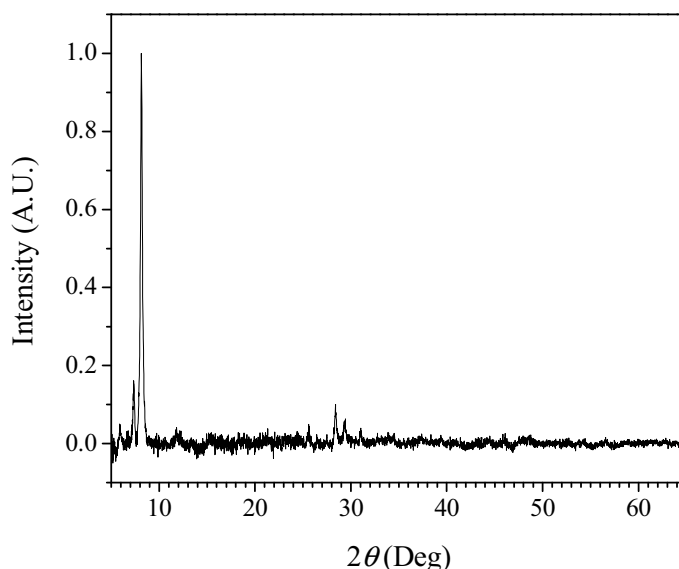


Figure 5.7 XRD spectrum of the zinc-based nanosheets obtained from the subtraction of the raw spectrum and background trace given in Figure 5.5.

The XRD spectrum of the zinc-based nanosheets is characterized by one main peak positioned at exactly 8.142° . This is assigned to the presence of zinc sulfate hydroxide hydrate, $\text{ZnSO}_4[\text{Zn}(\text{OH})_2]_3 \cdot 5\text{H}_2\text{O}$ (ICDD PDF 00-041-0007), the spectrum of which has one main peak at 8.093° as shown in Figure 5.9. The identification of this compound is in agreement with the EQCM, EDX, XPS and ART-IR characterizations as shown in the following Sections 5.2.2.2, 5.2.2.3, 5.2.2.4 and 5.2.2.5, respectively.

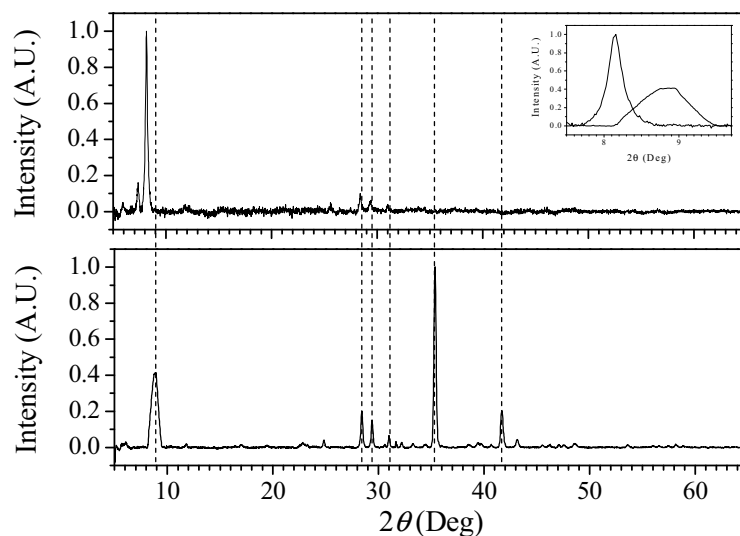


Figure 5.8 Comparison of the XRD spectra of zinc-based nanothin sheets (top) and bare glassy carbon electrode as given in Section 3.2.2.2 (bottom). The inset shows the superimposition of the peaks of the two spectra in the low diffraction angle range, the peak width and position are clearly different. The dashed lines indicate the position of the main peaks of the bare electrode spectrum.

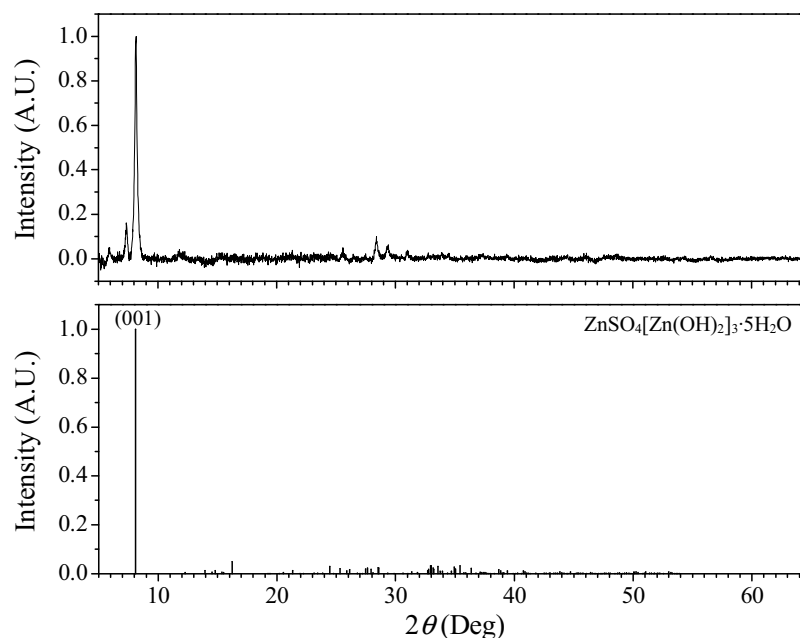


Figure 5.9 XRD peak assignment for the zinc-based nanothin sheets prepared as described in Figure 5.5. The diffraction peak at 8.142° is identified as that of zinc sulfate hydroxide hydrate, $\text{ZnSO}_4[\text{Zn}(\text{OH})_2]_3 \cdot 5\text{H}_2\text{O}$, ICDD PDF 01-078-0246. The correspondent Miller indexes, (hkl), are given for the assigned peak.

5.2.2.2 Electrochemical Quartz Crystal Microbalance

The mass and charge changes at the polymer films during the deposition of the zinc-based nanosheets were followed using an electrochemical quartz crystal microbalance, EQCM (Section 2.5.2.4). The electrodeposition was performed in aerated 0.10 M ZnSO₄ at 0.00 V vs. SCE. The resulting mass-charge responses are shown in Figure 5.10, while the corresponding current-time profiles are given in Figure 5.3. The three depositions are all characterized by an induction period in which a charge flow is observed without any increase of mass. Following this period, the mass starts increasing to reach different values of deposited masses. For larger currents the amount of deposited material is larger, curve 1; while the deposited amount is smaller at lower currents, curve 3. The dependence of the mass on the deposition current can be explained in two ways. Firstly, at lower currents the deposited species are of lower formula weight (per unit charge), or secondly, the efficiency of the deposition process is lower, with some of the charge being consumed by another process. For example, some of the electrogenerated hydroxide ions may be dispersed in solution instead of being incorporated into the hydroxysulfate precipitate. The latter process is feasible particularly at low currents where the hydroxide concentration at the polymer surface does not reach the necessary levels to cause the precipitation of the material.

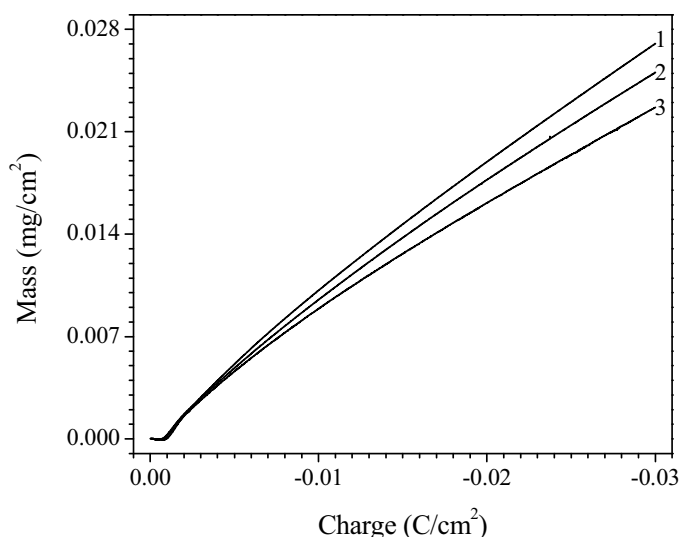


Figure 5.10 Mass-charge responses for the deposition of zinc-based nanosheets at PPy-PSS films in aerated 0.10 M ZnSO₄ at 0.00 V vs. SCE. The three curves, 1, 2 and 3, are related to those reported in Figure 5.3.

Each mass-charge curve is divided into three separate segments, parts 1, 2 and 3, as shown in Figure 5.11. Each part was selected in order to cover a range of charges

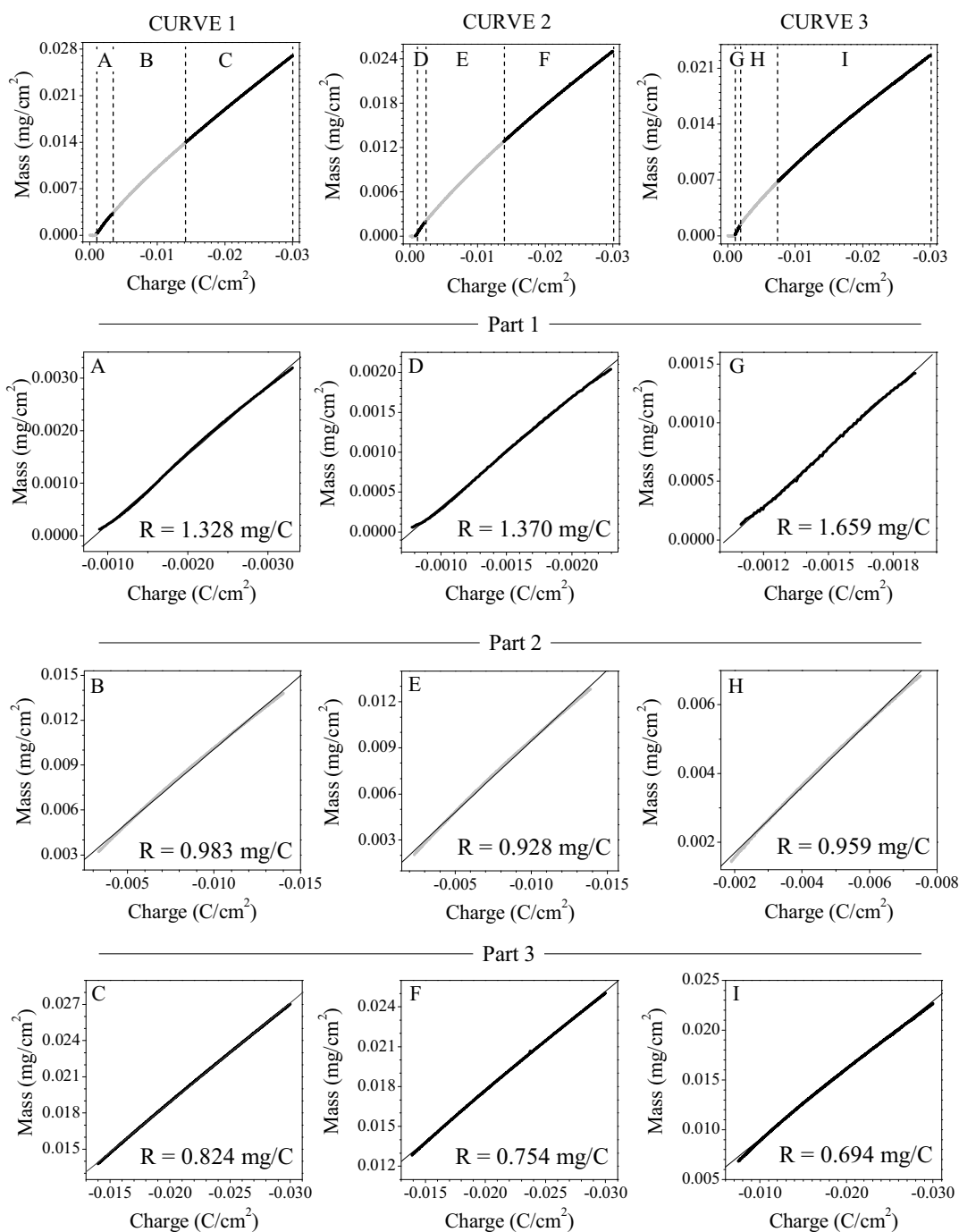


Figure 5.11 Linear regressions of the three mass-charge curves of Figure 5.10 for the deposition of zinc-based nanothin sheets at PPy-PSS films in aerated 0.10 M ZnSO₄ at 0.00 V vs. SCE. The segments labeled in the top plots are individually shown in the plots A, B and C for the first curve, D, E and F for the second curve, and G, H and I for the third curve. The mass-to-charge ratio R (*i.e.*, the absolute value of the slope) is reported in each plot. The correlation coefficient is $R^2 > 0.999$ for all regression lines.

as wide as possible, and to give a linear regression with a correlation coefficient of at least 0.999. The linear regressions were then performed on each segment to obtain the corresponding mass-to-charge ratios, R , for the deposited materials (Section 2.5.2.4, Equation 2.8). The average values and standard deviations of R , with their single values and linear charge ranges, for the three parts of the curves, are listed in Table 5.1. In general, the values of R decrease from an average value of 1.452 mg/C at the beginning of the deposition, to 0.957 mg/C and finally to 0.757 mg/C at the end of the deposition period. The standard deviation of the average mass-to-charge ratios is particularly large for the first part, 0.180 mg/C, corresponding to the nucleation of the zinc-based nanosheets. The linear range of these parts is also variable with the third deposition having the narrowest range and the largest R value of 1.659 mg/C. The second part of the plots is the most reproducible. In this case the average R is 0.957 mg/C with a standard deviation of 0.028 mg/C, corresponding to an error of less than 3 %. In contrast, the third segment is affected by significant variability. These average values of R can be compared to those of the possible species that could be deposited at the PPy-PSS film surface. A list of the possible reactions and products is given in Table 5.2.

Table 5.1 Average values of mass-to-charge ratio (R) and respective standard deviations (σ) for the three parts of the mass-charge curves reported in Figure 5.11. The single values of R and the linear charge ranges are also reported for every part of each curve.

Part	R average (mg/C)	σ (mg/C)	Section	R (mg/C)	Charge Range (mC/cm ²)
1	1.452	0.180	A	1.328	0.9 – 3.3
			D	1.370	0.8 – 2.3
			G	1.659	1.1 – 1.9
2	0.957	0.028	B	0.983	3.3 – 14.0
			E	0.928	2.3 – 12.8
			H	0.959	1.9 – 7.5
3	0.757	0.065	C	0.824	14.0 – 30.0
			F	0.754	12.8 – 30.0
			I	0.694	7.5 – 30.0

Table 5.2 Possible reactions and products for the electrochemical deposition of zinc-based nanothin sheets with relative values of molar mass (M) and mass-to-charge ratio (R).

Electrodeposition reactions & products	M (g/mol)	R (mg/C)
$\text{Zn}^{2+} + 0.5 \text{O}_2 + 2 \text{e}^- \rightarrow \text{ZnO}$	81.4	0.422
$\text{Zn}^{2+} + 0.5 \text{O}_2 + \text{H}_2\text{O} + 2 \text{e}^- \rightarrow \text{Zn(OH)}_2$	99.4	0.515
$3 \text{Zn}^{2+} + \text{O}_2 + 2 \text{H}_2\text{O} + \text{SO}_4^{2-} + 4 \text{e}^- \rightarrow \text{ZnSO}_4[\text{Zn(OH)}_2]_2$	360.3	0.933
$4 \text{Zn}^{2+} + 1.5 \text{O}_2 + 4 \text{H}_2\text{O} + \text{SO}_4^{2-} + 6 \text{e}^- \rightarrow \text{ZnSO}_4[\text{Zn(OH)}_2]_3 \cdot \text{H}_2\text{O}$	477.7	0.825
$4 \text{Zn}^{2+} + 1.5 \text{O}_2 + 6 \text{H}_2\text{O} + \text{SO}_4^{2-} + 6 \text{e}^- \rightarrow \text{ZnSO}_4[\text{Zn(OH)}_2]_3 \cdot 3\text{H}_2\text{O}$	513.7	0.887
$4 \text{Zn}^{2+} + 1.5 \text{O}_2 + 8 \text{H}_2\text{O} + \text{SO}_4^{2-} + 6 \text{e}^- \rightarrow \text{ZnSO}_4[\text{Zn(OH)}_2]_3 \cdot 5\text{H}_2\text{O}$	549.7	0.950
$7 \text{Zn}^{2+} + 3 \text{O}_2 + 10 \text{H}_2\text{O} + \text{SO}_4^{2-} + 12 \text{e}^- \rightarrow \text{ZnSO}_4[\text{Zn(OH)}_2]_6 \cdot 4\text{H}_2\text{O}$	829.9	0.717

In the list of possible compounds metallic zinc, Zn^0 , is not considered since the deposition potential is too high to perform the direct electrodeposition of zinc metal. The zinc sulfate species, $\text{ZnO}[\text{ZnSO}_4]_2$, is not considered as it is generated from the thermal treatment of ZnSO_4 at high temperature [20]. The possible zinc species, which could be formed at 0.00 V vs. SCE, if the pH reached sufficiently basic values (Section 1.5.2.2), would be ZnO and Zn(OH)_2 . Other probable species are zinc hydroxysulfates. The general formula of basic zinc hydroxysulfates is $\text{ZnSO}_4[\text{Zn(OH)}_2]_m \cdot n\text{H}_2\text{O}$ with $1 \leq m \leq 7$ and $0 \leq n \leq 5$ [21]. Most of these zinc hydroxysulfate species are found in nature or prepared synthetically. The zinc analog of antlerite, $\text{ZnSO}_4[\text{Zn(OH)}_2]_2$, has been recently prepared hydrothermally [9]. The various hydrated forms of zinc hydroxysulfate, $\text{ZnSO}_4[\text{Zn(OH)}_2]_3 \cdot n\text{H}_2\text{O}$ with $n = 1-5$, are also known and commonly found as corrosion products of zinc metal in the presence of sulfate ions [1, 22]. In the table, the mono-, tri- and penta-hydrate forms are listed for comparison. Another known zinc hydroxysulfate species generated from the corrosion of zinc and zinc alloys is $\text{ZnSO}_4[\text{Zn(OH)}_2]_6 \cdot 4\text{H}_2\text{O}$ [23]. Recently, $\text{ZnSO}_4[\text{Zn(OH)}_2]_6 \cdot 4\text{H}_2\text{O}$ has been electrochemically deposited onto F-doped tin oxide electrodes at -0.85 V vs. SCE from a dilute solution of ZnSO_4 [13]. Other zinc hydroxysulfate compounds, *e.g.*, $[\text{ZnSO}_4]_2[\text{Zn(OH)}_2]_3$ and $\text{ZnSO}_4[\text{Zn(OH)}_2]_4$, have been considered in the literature [9], however these are not listed in the present table as they are rarely found in nature.

The two experimental values, 1.452 mg/C and 0.957 mg/C, are both significantly greater than those of ZnO and Zn(OH)₂ excluding the formation of considerable amounts of these species during the first and second parts of the deposition. The experimental *R* value for the first part, 1.452 mg/C, is higher than any of the computed *R* values given in Table 5.2. This may be due to the accumulation of charge in the polymer film at the beginning of the deposition and to the generation of hydroxide ions, as it was also found for the deposition of copper in Section 3.2.3.2. The formation of ZnSO₄[Zn(OH)₂]₂ is excluded since it is two orders of magnitude more soluble than ZnSO₄[Zn(OH)₂]₃·5H₂O, and it is formed in dilute solutions of ZnSO₄ or through the slow addition of hydroxide ions [9]. The possible formation of zinc sulfate hydroxide hydrate, ZnSO₄[Zn(OH)₂]₃·5H₂O, is supported by the experimental *R* value of the second part of the curves, 0.957 mg/C, which is in very good agreement with the computed *R* value of 0.950 mg/C. The electrodeposition of zinc sulfate hydroxide hydrate is actually confirmed by the XRD characterization of the nanothin sheets (Section 5.2.2.1). The electrodeposition of sulfated species is also confirmed by the EDX, XPS and ATR-FTIR characterizations (Sections 5.2.2.3, 5.2.2.4 and 5.2.2.5). The third and last part of the deposition is characterized by a lower *R*, 0.757 mg/C, which could be due to either the deposition of lighter species, *e.g.*, ZnO, along with the hydroxysulfates, or to the formation of ZnSO₄[Zn(OH)₂]₆·4H₂O (*R* = 0.717 mg/C), or to a decrease of deposition efficiency. Indeed, a substantial amount of Zn–O–Zn oxide-like species is found on the surface of the zinc-based nanosheets in the XPS measurements (Section 5.2.2.4).

5.2.2.3 Energy Dispersive X-Ray Analysis

The elemental composition of the zinc-based nanothin sheets was analyzed using energy dispersive X-ray analysis, EDX (Section 2.5.3.1). The EDX spectrum and the SEM micrograph of the zinc-based nanosheets are given in Figure 5.12. The spectral peaks are identified as those of zinc, oxygen, sulfur and carbon. The presence of carbon was due to the polymer film and underlying electrode material (glassy carbon) which are also probed since the zinc sheets are too thin to prevent them from being reached by the electron beam. The presence of sulfur and oxygen is also confirmed by the results obtained from the XPS and ATR-IR characterizations (Sections 5.2.2.4 and 5.2.2.5).

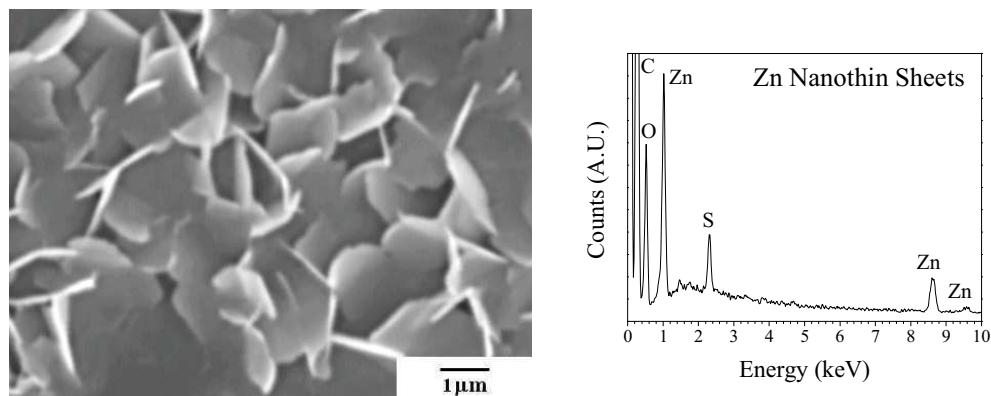


Figure 5.12 SEM micrograph and EDX spectrum of the zinc-based nanothin sheets prepared at PPy-PSS films in aerated 0.10 M ZnSO₄ at 0.00 V vs. SCE. The EDX peaks were assigned as described in Figure 5.13.

The EDX spectrum of the zinc-based nanosheets is compared to the EDX spectra of zinc metal (99.9 %), zinc oxide (99.99 %) and zinc sulfate heptahydrate (≥ 99.0 %), which were recorded using similar experimental conditions (Figure 5.13). The spectrum of zinc metal has three characteristic peaks that are also present in the spectrum of the zinc-based nanosheets. The same three peaks are also present in the spectrum of zinc oxide, which has an additional peak due to the presence of oxygen. The zinc (II) sulfate heptahydrate has an additional peak corresponding to sulfur. In all standards the main zinc peak, Zn(L α), is more intense than the peaks of all the other elements. The surface morphology of the zinc oxide is rough as shown by the SEM micrograph, but some areas of the standard were purposely flattened in order to give reproducible EDX measurements.

The EDX spectra of the zinc-based nanothin sheets and the standards are compared in Figure 5.14. The peak heights are all normalized to the height of the peak Zn(L α) in order to allow easier comparison of peak intensities. It is apparent that the oxygen content of the zinc-based nanosheets is well above that of zinc oxide, whereas it is lower than that of zinc sulfate. The sulfur content is also lower in the zinc-based nanosheets compared to zinc sulfate. These spectral features are all in agreement with the assumption that the nanosheets are made of zinc hydroxysulfates, *e.g.*, ZnSO₄[Zn(OH)₂]₃·5H₂O. In fact, the oxygen and sulfur contents of these materials are lower (per unit of zinc) than that of zinc sulfate heptahydrate.

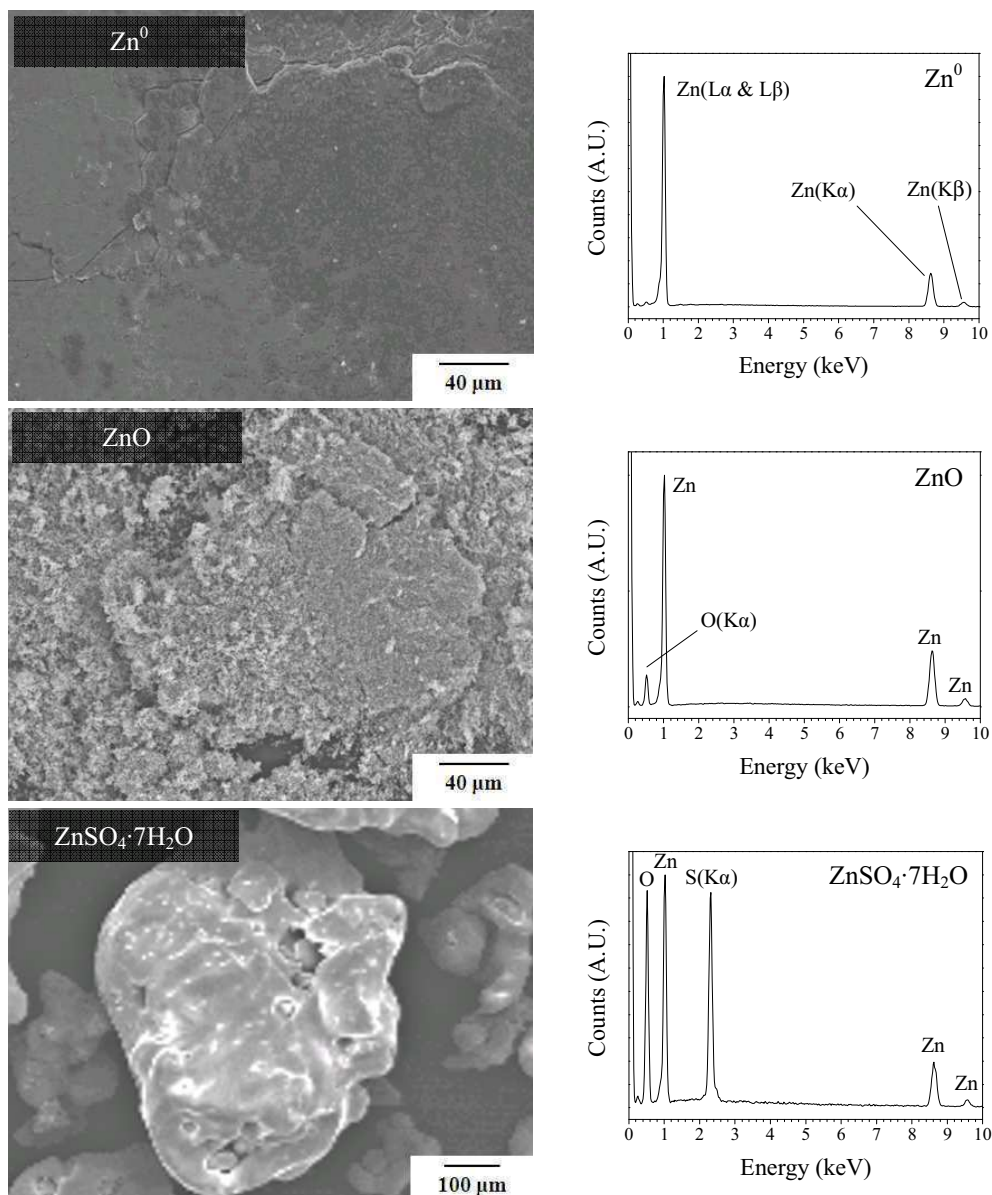


Figure 5.13 SEM micrographs and EDX spectra of zinc(0) metal, zinc(II) oxide, and zinc(II) sulfate heptahydrate. The EDX peaks were assigned to Zn ($L\alpha$ 1.01 keV, $L\beta$ 1.03 keV, $K\alpha$ 8.64 keV, $K\beta$ 9.57 keV), O ($K\alpha$ 0.52 keV) and S ($K\alpha$ 2.31 keV).

The intensity of the EDX peak is proportional to the concentration of the corresponding element in the sample [24, 25]. It follows that the ratio of the peak heights in the EDX spectrum is proportional to the stoichiometric ratio of the elements in the material. However, it should be noted that the stoichiometric ratio obtained in this way is only indicative, since the quantitative analysis is affected by various factors which can influence the EDX response (Section 2.5.3.1). Therefore, the relative amounts of two elements in an unknown substance can only be estimated

from the ratio of their peak heights when compared to that of the same elements of a standard material. The Zn/S ratio was calculated for the zinc-based nanosheets from the comparison to those of zinc sulfate heptahydrate, as given in Table 5.3.

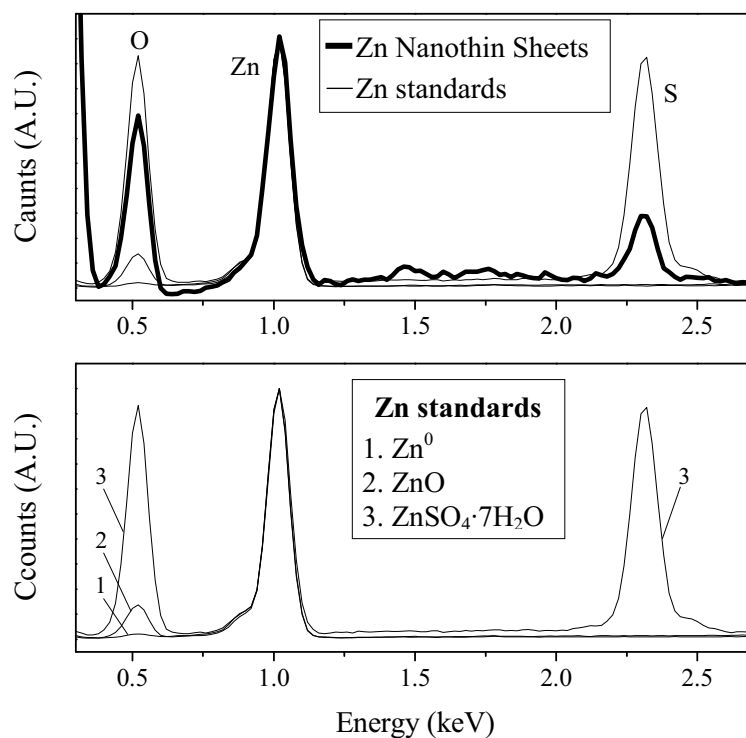


Figure 5.14 Comparison of the EDX spectra of nanosheet zinc sheets (Figure 5.12) and zinc standards (Figure 5.13). The spectra are all normalized to the height of the Zn peak. The selected lines are Zn(L α), O(K α) and S(K α).

The stoichiometric ratios of the various zinc hydroxysulfates and zinc sulfate heptahydrate are obtained from their respective chemical formulas, whereas those of the zinc-based nanosheets were calculated, as reported in the footnotes in Table 5.3. The calculated value of the Zn/S ratio for the zinc-based nanosheets is 3.7, which is close to the stoichiometric value of 4.0 for the $\text{ZnSO}_4[\text{Zn}(\text{OH})_2]_3$ based compounds. Hence, the EDX analysis is consistent with the formation of $\text{ZnSO}_4[\text{Zn}(\text{OH})_2]_3 \cdot n\text{H}_2\text{O}$ nanosheet sheets. This result is in agreement with the XRD and EQCM data which confirm the formation of zinc sulfate hydroxide hydrate, $\text{ZnSO}_4[\text{Zn}(\text{OH})_2]_3 \cdot 5\text{H}_2\text{O}$, species during the deposition (Section 5.2.2.1 and 5.2.2.2).

Table 5.3 Peak height and stoichiometric ratio of zinc to sulfur (Zn/S) of the zinc-based nanothin sheets. The ratio is compared to those of $\text{ZnSO}_4 \cdot 7\text{H}_2\text{O}$, $\text{ZnSO}_4[\text{Zn}(\text{OH})_2]_2$, $\text{ZnSO}_4[\text{Zn}(\text{OH})_2]_3 \cdot 5\text{H}_2\text{O}$ and $\text{ZnSO}_4[\text{Zn}(\text{OH})_2]_6 \cdot 4\text{H}_2\text{O}$.

	Zn/S Ratio	
	Peak height*	Stoichiometric
$\text{ZnSO}_4 \cdot 7\text{H}_2\text{O}$	1.06	1.0
Zn Nanosheets	3.96	3.7**
$\text{ZnSO}_4[\text{Zn}(\text{OH})_2]_2$	—	3.0
$\text{ZnSO}_4[\text{Zn}(\text{OH})_2]_3 \cdot 5\text{H}_2\text{O}$	—	4.0
$\text{ZnSO}_4[\text{Zn}(\text{OH})_2]_6 \cdot 4\text{H}_2\text{O}$	—	7.0

* The peak height ratio was calculated from the ratio of the peak heights of the elements.

** The stoichiometric ratio of the nanosheets was extrapolated from its peak height ratio by multiplying it by the quotient of the stoichiometric and peak height ratios of zinc sulfate heptahydrate.

5.2.2.4 X-Ray Photoelectron Spectroscopy

The chemical composition and oxidation state of the elements present on the surface of the zinc-based nanothin sheets were characterized using X-ray photoelectron spectroscopy, XPS (Section 2.5.4.3). The zinc-based nanosheets were electrodeposited on PPy-PSS thin films from an aerated 0.10 M ZnSO_4 solution at 0.00 V vs. SCE. The XPS survey and high-resolution spectra of the nanosheets are given in Figure 5.15. The main peaks are labeled with their corresponding element and electronic orbital of photoemission. Four chemical elements were identified in the survey spectra, namely zinc, sulfur, oxygen and carbon. The first three were also identified as elements of the zinc-based nanosheets using EDX (Section 5.2.2.3). The carbon signal is related to carbon from the PPy-PSS film and adventitious carbon. Interestingly, the C 1s signal is about seven times less intense compared to the signal recorded for the hierarchical copper-based micro/nanostructures (Section 3.2.2.5). Furthermore, the nitrogen signal for the PPy-PSS film is below the detection limit of the instrument. Accordingly, it can be concluded that the polymer film is predominantly covered by zinc-based nanosheets. The other XPS peaks in the survey spectra are all due to zinc, Zn 3d (10 eV), Zn 3p_{3/2} (89 eV), Zn 3s (140 eV) and Zn LMM Auger peaks (475 and 495 eV).

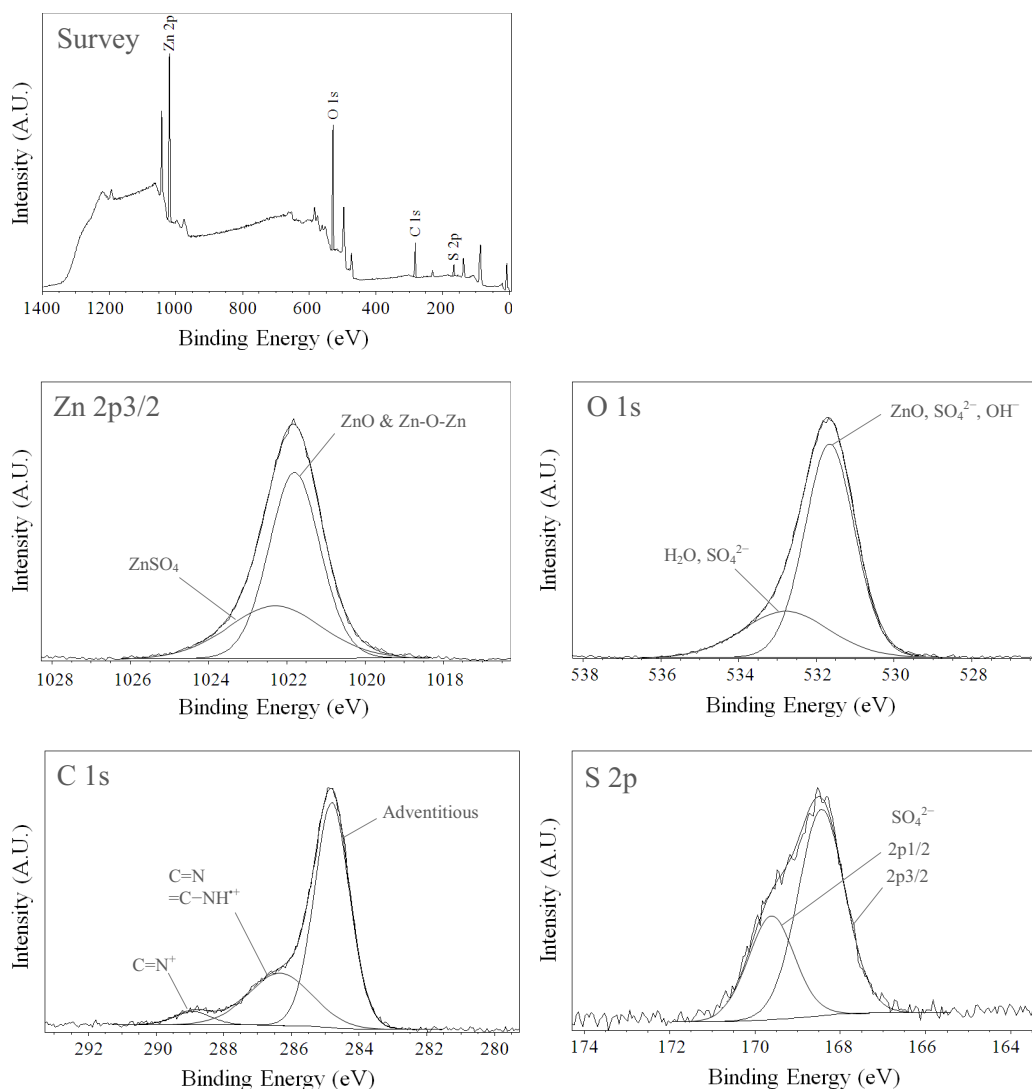


Figure 5.15 XPS spectra of the zinc-based nanothin sheets formed at the PPy-PSS films in aerated 0.10 M ZnSO_4 at 0.00 V vs. SCE.

As shown in Figure 5.15, the high-resolution spectrum of the zinc signal ($\text{Zn } 2p_{3/2}$) has one single peak at 1021.8 eV. This peak is deconvoluted into two peaks at 1021.8 eV and 1022.4 eV. The former peak is associated with the presence of zinc metal and/or zinc oxide [26, 27], while the latter peak is related to the presence of ZnSO_4 species [28]. The formation of zinc metal is ruled out as the electrodeposition potential, 0.00 V vs. SCE, is too electropositive to obtain the direct reduction of Zn^{2+} to Zn^0 , $E_{\text{Zn(II)/Zn(0)}}^0 = -1.003$ V vs. SCE. The presence of zinc oxide is in agreement with the EQCM measurements, which suggests the electrodeposition of low formula weight species along with zinc hydroxysulfates (Section 5.2.2.1). In analogy to the electrochemical deposition of hierarchical copper-based micro/nanostructures, the peak at 1021.8 eV could possibly be due to the presence of Zn–O–Zn oxide-like

bonds, as reported in the literature for copper hydroxysulfates (Section 3.2.2.5). The peak at 1022.4 eV is characteristic of zinc ions in the presence of sulfate anions. This is additional confirmation for the incorporation of sulfate anions into the deposit.

The high-resolution spectrum of the sulfur signal (S 2p) has a single peak at 168.5 eV with a sizeable shoulder at higher binding energy (Figure 5.15). The deconvolution of this signal allows the identification of two peaks at 168.4 eV and 169.7 eV. These peaks are identified as the doublets (2p_{1/2}, 2p_{3/2}) of sulfate ions in hydrated zinc sulfate [29].

The high-resolution spectrum of the oxygen signal (O 1s) has one peak at 531.7 eV (Figure 5.15). This peak is deconvoluted to give two peaks at 531.7 eV and 532.8 eV. The peak at 531.7 eV is normally associated with the presence of ZnO [27], or alternatively, to sulfate and hydroxide ions, as reported by Castaño *et al.* [1]. In the latter paper, the authors deposited zinc hydroxysulfate, ZnSO₄[Zn(OH)₂]₃, corrosion products by treating zinc plates in a humid SO₂ and NO₂ atmosphere. The layer was characterized using XPS and the resulting O 1s signal, found at 531.8 eV, was assigned to SO₃²⁻, SO₄²⁻ and OH⁻. A peak at 532.8 eV was also observed and was assigned to water, although the oxygen from sulfate is also found at a similar binding energy [30]. It is then difficult to unequivocally assign these two peaks. However, the possible species related to these signals are in agreement with the formation of hydrated zinc hydroxysulfates.

The high-resolution spectrum of the carbon signal (C 1s) has three overlapping peaks at 284.8 eV, 286.3 eV and 288.9 eV, which can be separated by deconvolution (Figure 5.15). The peak at 284.8 eV is attributed to adventitious carbon which is always present as a contaminant due to the exposure of the sample to the environment. The dominant peak at 286.3 eV is due to the imine-like (C=N) and polaron (C=N⁺-H) moieties of PPy, while the peak at 288.9 eV is attributed to the bipolarons (C=N⁺). As noted before, the polymer film was homogeneously covered by zinc-based nanosheets and the amount of pyrrolic carbon detected in the sample was much smaller than that found for the hierarchical copper-based micro/nanostructures (Section 3.2.2.5).

In conclusion, it is reasonable to state that the top layer of the zinc-based nanosheets is mainly composed of hydrated forms of zinc hydroxysulfates with a strong oxide-like bond component.

5.2.2.5 Attenuated Total Reflectance Infrared Spectroscopy

The component species of the zinc-based nanothin sheets were characterized using attenuated total reflectance infrared spectroscopy, ATR-IR (Section 2.5.4.1). The ATR-IR spectra were collected from 450 cm^{-1} to 4000 cm^{-1} , the background spectrum of the PPy-PSS film was also taken, as shown in Figure 5.16. In the two spectra there are two bands between 2000 and 2400 cm^{-1} . These are characteristic of the internal reflection element of the ATR sampling equipment. All other bands originate from the zinc-based nanothin sheets.

The main absorption bands of the zinc deposit are located in three characteristic regions at $450\text{--}1250\text{ cm}^{-1}$, $1500\text{--}1650\text{ cm}^{-1}$ and $3050\text{--}3650\text{ cm}^{-1}$. The features of these bands are all in excellent agreement with those of the mineral osakaite, ideally $\text{ZnSO}_4[\text{Zn}(\text{OH})_2]_3 \cdot 5\text{H}_2\text{O}$ [31]. The absorption band in the region $3050\text{--}3650\text{ cm}^{-1}$ can be attributed to the stretching of O–H, while the small absorption band in the region $1500\text{--}1650\text{ cm}^{-1}$ is related to the bending of H–O–H. The same features have been observed in the IR spectrum of zinc hydroxysulfate hydrates [13].

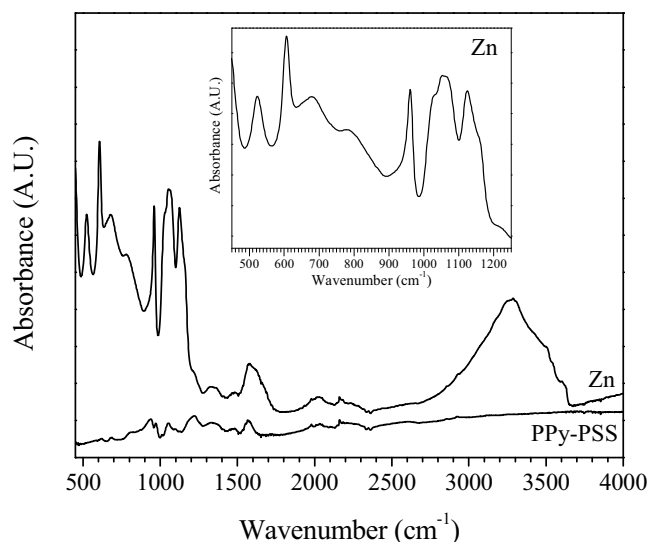


Figure 5.16 ATR-IR spectra of zinc-based nanothin sheets prepared at PPy-PSS films in aerated 0.10 M ZnSO_4 at 0.00 V vs. SCE, and of PPy-PSS films. In the inset, magnification of the zinc-based nanosheets spectrum in the $450\text{--}1250\text{ cm}^{-1}$ region.

The absorption peaks at 1125 cm^{-1} and 1155 cm^{-1} are associated with the ν_3 SO_4 -stretching, while the sharp peak at 960 cm^{-1} is due to the ν_1 SO_4 -stretching. In particular, the last peak is characteristic of the presence of hydrated forms of zinc

sulfate, as it is found at about 980 cm^{-1} in the spectrum of $\text{ZnSO}_4 \cdot 7\text{H}_2\text{O}$ and at 1020 cm^{-1} in the spectrum of anhydrous ZnSO_4 [32]. The peaks at 605 cm^{-1} and 520 cm^{-1} are due to the ν_4 and ν_2 SO_4 -bending modes, respectively. A brief description of the vibrational modes of sulfate is given in Section 3.2.2.6, Figure 3.28. The ATR-IR spectrum of the deposit provides strong evidence that the zinc-based nanosheets are composed of hydrated zinc hydroxysulfate, most likely, $\text{ZnSO}_4[\text{Zn}(\text{OH})_2]_3 \cdot 5\text{H}_2\text{O}$.

5.2.3 Mechanism of Deposition of Zinc-Based Nanothin Sheets

5.2.3.1 Morphology and Growth

The morphology and growth of the zinc-based nanosheets were analyzed at different deposition times. The electrodeposition experiments were terminated and the electrodes were characterized using SEM. The resulting micrographs are given in Figure 5.17. The micrographs labeled as 1a and 1b show some nanosheets lying in contact with the polymer film. The sheets are clearly of hexagonal shape, although none of the nanosheets are ideal hexagons. The typical size of the sheets is about 3 to 5 μm . At this stage, the single sheets seem to be made of nanoparticles (1b), however this morphology could also be due to the polymer underneath covered by a very thin layer of zinc deposit. It is evident from these micrographs that zinc deposits are formed on top of the sheets; hence the nucleation takes place at both the polymer and the nanosheet surface. In the micrographs, 2a and 2b, the nanosheets are shown after the deposition of a larger amount of material. In this case the sheets have irregular shape and appear smoother. They appear to grow both parallel to the polymer surface, which at this stage is almost fully covered, and perpendicular to it at the contact point of two or more nanosheets. Single sheets are also observed on top of vertical nanosheets far from the film (2b). It follows that the concentrations of zinc, hydroxide, and sulfate ions necessary for the electrocrystallization process can be established above a complete layer of nanosheets. In the micrographs, the vertical nanosheets, formed at the points of contact of parallel nanosheets, are ‘bright white’ and clearly distinguishable from those lying on the film. The density of ‘bright’ vertical nanosheets increases with the deposition time, as shown from micrographs 3 to 4. The final deposit is then a random distribution of entangled zinc hydroxysulfate nanothin sheets, as previously shown in Figure 5.4.

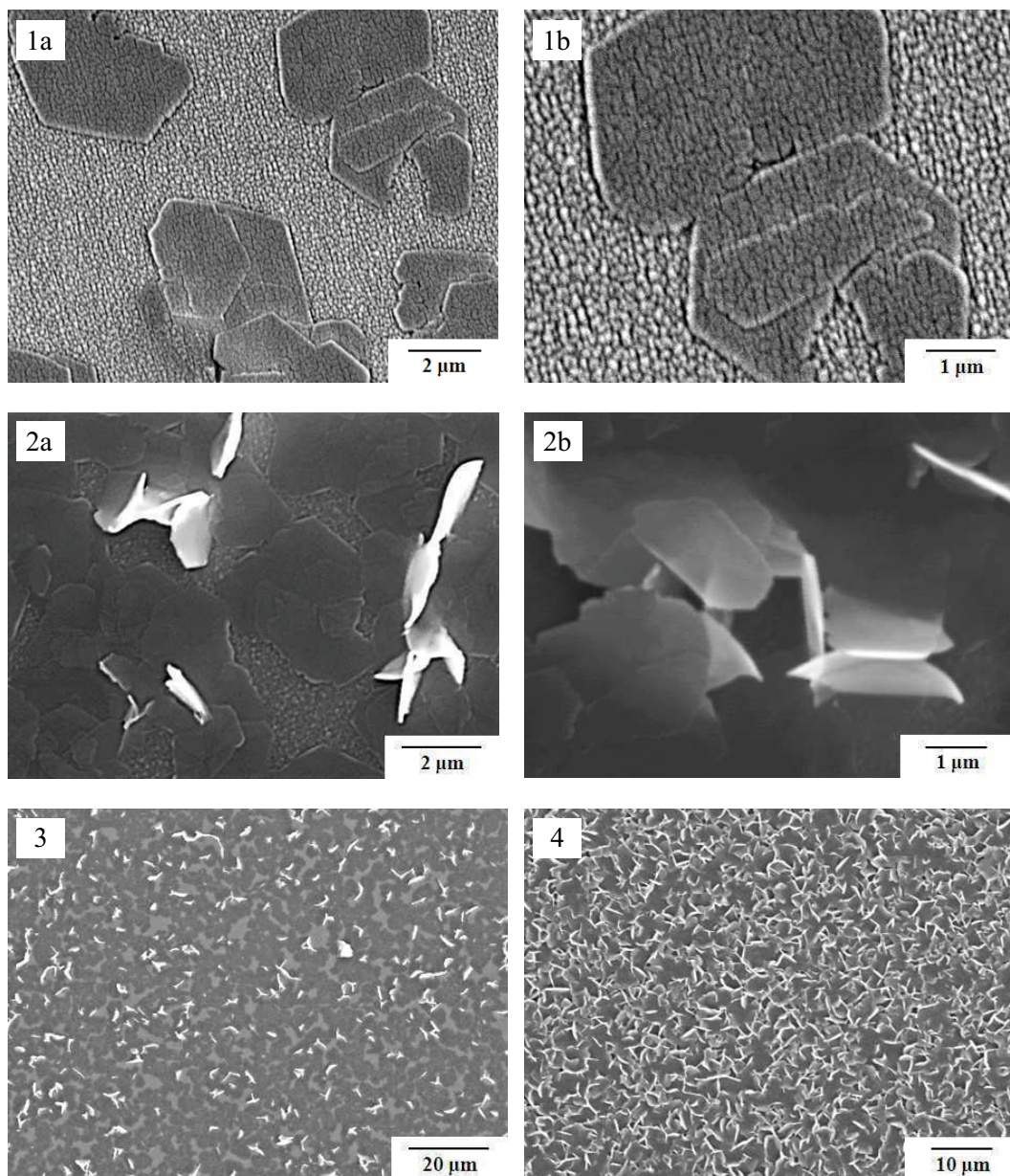


Figure 5.17 SEM micrographs showing the morphology and growth of the zinc-based nanosheets found on a PPy-PSS film after deposition from aerated 0.10 M ZnSO_4 at 0.00 V vs. SCE. 1a) Single nanosheets lying on the surface of the polymer film. 1b) An additional zinc layer grown on one already formed. 2a) Zinc-based nanosheets grow perpendicular to the polymer surface at the point of contact with those lying on the surface. 2b) Zinc-based nanosheets grow directly on the top of vertical nanosheets without being in contact with the polymer film. 3) The polymer film is almost all covered and the vertical nanosheets are seen. These appear ‘bright white’ in contrast to those dark gray that lie on the film. 4) With increasing deposition times, the number of vertical nanosheets increases as shown by the larger number of bright sheets.

An interesting aspect of the deposition is whether the nanosheets grow preferentially onto the polymer film or on top of the nanosheets. The micrographs in Figure 5.18 show that both processes are likely to happen during the electrodeposition. The ‘hexagons’ in the micrographs 5a and 5b are all made of more than one layer which means that a series of multiple nucleations is involved in the formation of each single ‘hexagon’. Also, larger islands made of multiple layers are found along with the ‘hexagons’, micrographs 5c and 5d. Such islands could be formed either of neighboring sheets which come into contact during the deposition or from the expansion of a starting ‘hexagon’. It is evident that the deposition can then proceed on both the film and nanosheet surfaces. Hexagonal nanothin crystals of $\text{ZnSO}_4[\text{Zn}(\text{OH})_2]_3 \cdot 5\text{H}_2\text{O}$ have been reported in the literature [5]. These were prepared from the thermal treatment of equimolar solutions of ZnSO_4 and hexamethylenetetramine in water–ethanol solvent.

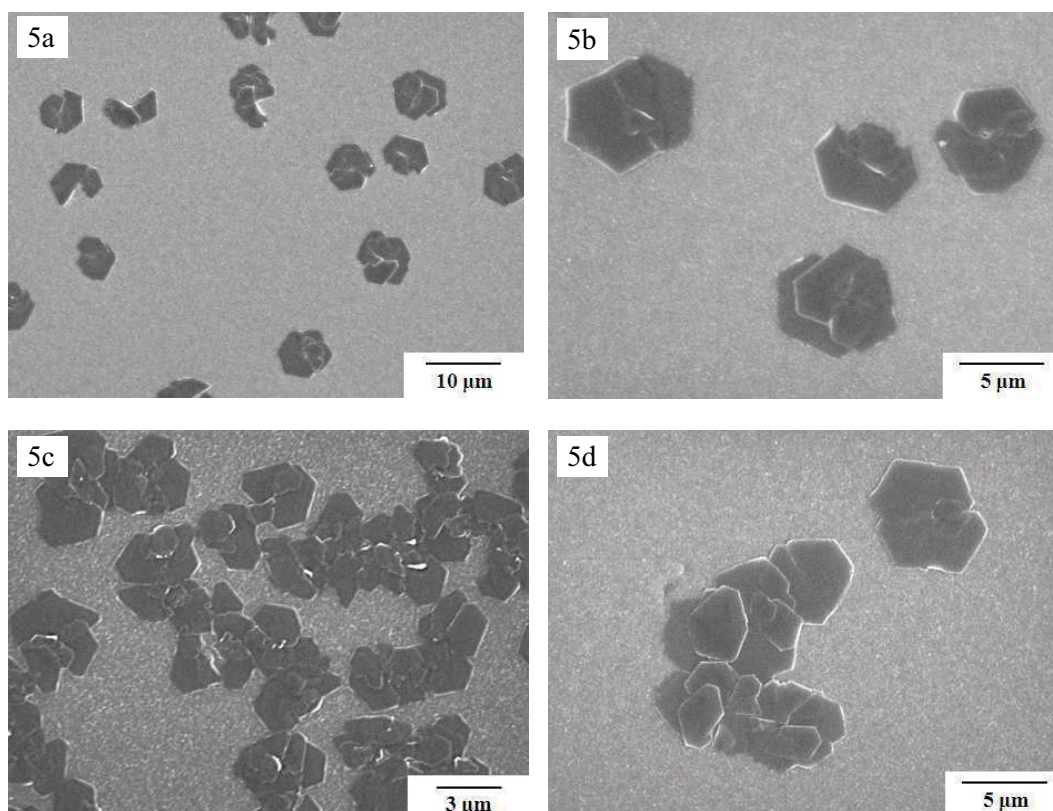


Figure 5.18 SEM micrographs showing the layered structure of the zinc-based nanosheets formed on PPy-PSS film after deposition from aerated 0.10 M ZnSO_4 at 0.00 V vs. SCE. In 5a and 5b the hexagonal deposits are made of several layers of zinc-based nanosheets (charge of electrodeposition 10 mC/cm^2). In 5c and 5d irregular and larger islands are formed from the connection of numerous zinc-based nanosheets.

5.2.3.2 Mechanism of Nucleation and Growth

The mechanism of nucleation and growth of the zinc-based nanothin sheets was studied in more detail by analyzing the current and mass responses of the electrochemical deposition of the zinc deposit. The following analysis is related to the previous investigation in Section 5.2.2.2, in which the electrodeposition was studied in terms of the evolution of the mass-to-charge ratios during the deposition process.

The potentiostatic deposition of three-dimensional structures from multiple nucleation sites in the diffusion-controlled regime is described by the Scharifker-Hills model [33]. According to this model, there are two diagnostic relationships, Equations 2.2 and 2.3 given in Section 2.5.2.1, which can be used to determine whether the nucleation of the zinc-based nanothin sheets is instantaneous or progressive. In order to compare the experimental data to the model equations, the current-time data are plotted in the dimensionless coordinates $(i/i_{\text{MAX}})^2$ and t/t_{MAX} , where i_{MAX} is the current maximum of the chronoamperometric response reached at time t_{MAX} .

In the present case the extraction of the current and time maxima, i_{MAX} and t_{MAX} , is not trivial since the current profiles reach either a plateau value or decrease slightly with time (Section 5.2.1, Figure 5.3). In order to correctly and consistently identify these maxima, a simple extrapolation procedure was applied to each profile. The resulting current maxima are shown in Figure 5.19. In this procedure a 50-point average smoothing was employed to find the average current curves (solid lines) of the experimental data (open circles). The current maxima were identified either as the maxima of the curves (Profiles 1 and 3) or as the first point reaching the plateau current (Profile 2). In each curve the i_{MAX} was calculated as the average current within a time interval of 60 s centered at t_{MAX} . In Figure 5.19, t_{MAX} is shown by a solid vertical line, while the vertical dashed lines correspond to 30 s periods lower and higher than t_{MAX} . The resulting $(i_{\text{MAX}}, t_{\text{MAX}})$ are $(-12.10 \mu\text{A}/\text{cm}^2, 477 \text{ s})$, $(-11.04 \mu\text{A}/\text{cm}^2, 457 \text{ s})$ and $(-9.98 \mu\text{A}/\text{cm}^2, 450 \text{ s})$ for the current profiles 1, 2 and 3, respectively.

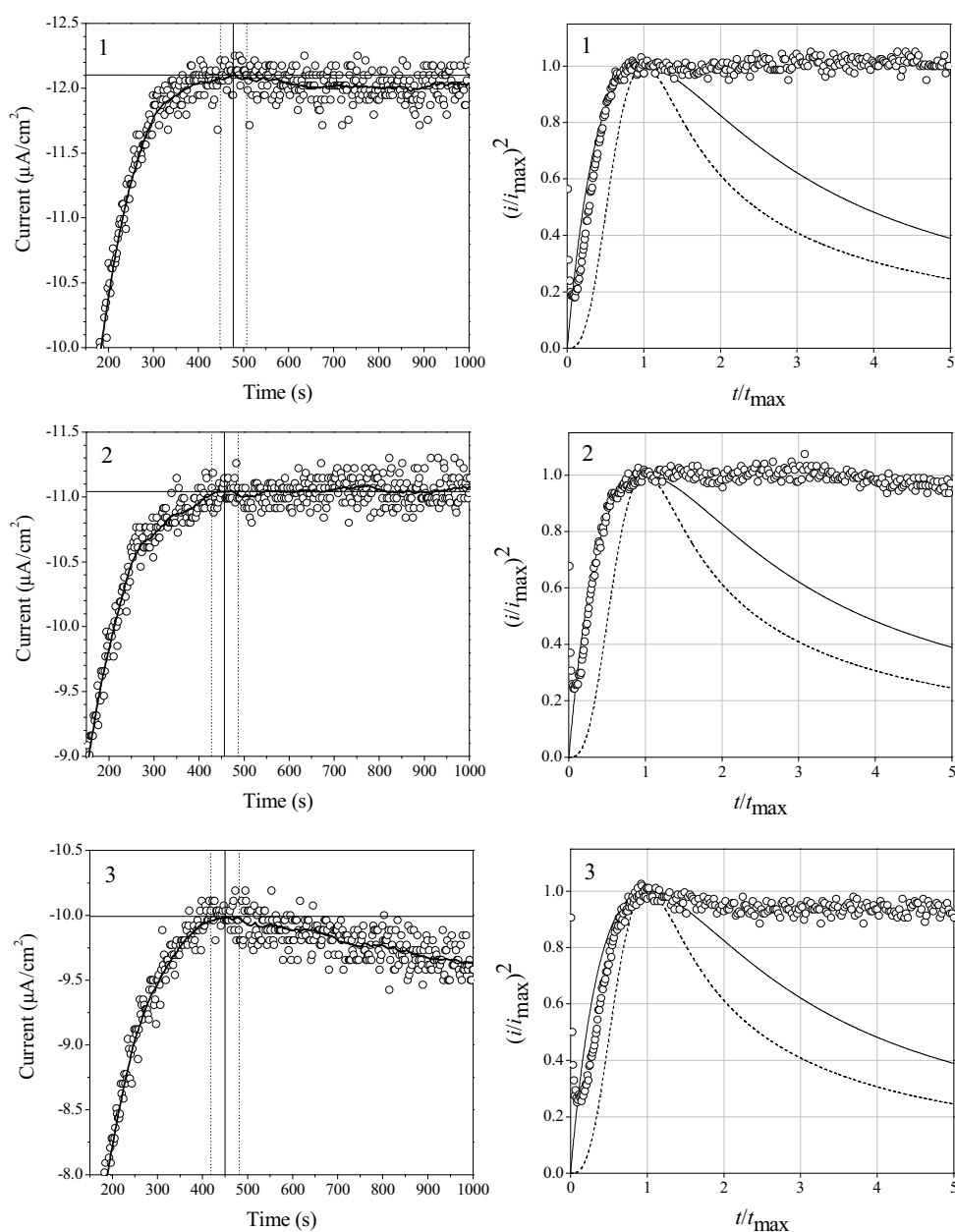


Figure 5.19 Current-time profiles and corresponding dimensionless plots for the deposition of zinc-based nanothin sheets. The open circles are the experimental data taken from Figure 5.3, profiles 1, 2 and 3. On the left, the current and time maxima, i_{MAX} and t_{MAX} , are shown on the current-time profiles. On the right, the solid and dashed traces are the profiles for instantaneous and progressive nucleation, respectively, from the Scharifker-Hills model described in Section 2.5.2.1.

Using the current and time maxima extrapolated as above, the dimensionless experimental curves are plotted along with the theoretical traces for the instantaneous and progressive growth. The resulting plots are shown in Figure 5.19. It is evident

that all the curves follow closely the instantaneous nucleation profile at the start of the electrodeposition process, with very good agreement between the experimental data and the simulated plots between t/t_{\max} values of 0 and 1. However, there is poor correlation between the experimental and theoretical data after the current maxima; neither the instantaneous nor the progressive nucleation models fit the experimental data. The departure of the experimental curves from the theoretical traces may be related to changes in the deposition process during the electrodeposition. In fact, at the start of the electrodeposition process, the nucleation takes place at the polymer film surface, while later the growth, as shown in Section 5.2.3.1, proceeds also on top of the zinc-based nanosheets. This transition from one substrate to another may account for the lack of a clear i_{\max} . The ease of growth of the deposit on the zinc-based nanosheets is clearly evident from the fact that the nanosheet crystals are also found on top of completed layers of deposit far from and not in contact with the polymer film (Section 5.2.3.1, Figure 5.17).

The mass-charge responses of the three electrodepositions, which were previously given in Figure 5.10, are considered further in order to obtain some additional information about the mechanism of formation of the zinc-based nanosheets. The instantaneous mass-to-charge ratios, R_{inst} , calculated for these responses are shown in Figure 5.20 (the definition and method of calculation of R_{inst} are reported in Section 2.5.2.4). The variation of R_{inst} during the nucleation and growth of the zinc-based nanosheets is clearly similar for all the electrodepositions. The ratio increases sharply at the beginning of the deposition to reach a maximum value, at about 1.8 mC/cm^2 . Then the ratio decreases progressively towards an average plateau value of 0.76 mg/C , as reported in Table 5.1 of Section 5.2.2.2.

Given the close agreement between these three responses, the first set of data was considered as representative of the electrodeposition of the zinc-based nanosheets and was analyzed further, as shown in Figure 5.21. Here, the current, mass and R_{inst} are compared and divided into four segments, 1, 2, 3 and 4. The charge consumed at the end of each segment is reported on the top of the plot. The dot-dashed line at 10.0 mC/cm^2 refers to the deposition of zinc hydroxysulfate ‘hexagons’ as they are reported in the micrographs 5a and 5b of Figure 5.18 (Section 5.2.3.1).

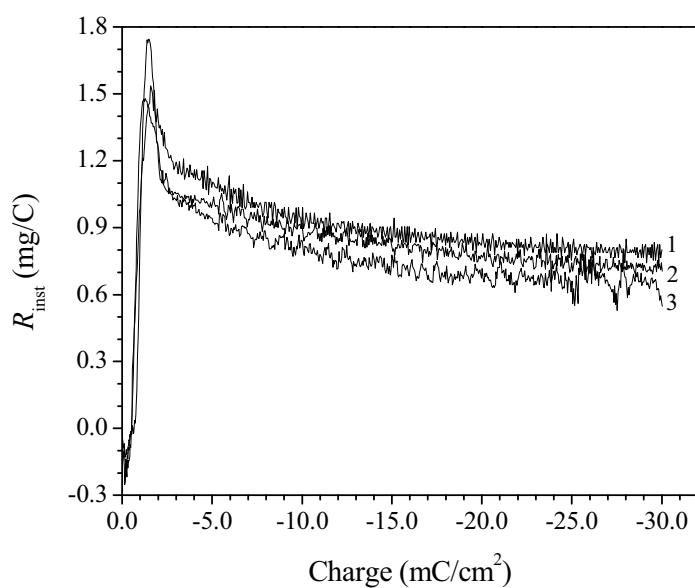


Figure 5.20 Variation of the instantaneous mass-to-charge ratio during the electrodeposition of the zinc-based nanothin sheets. The depositions are numbered after the mass-charge responses of Figure 5.10.

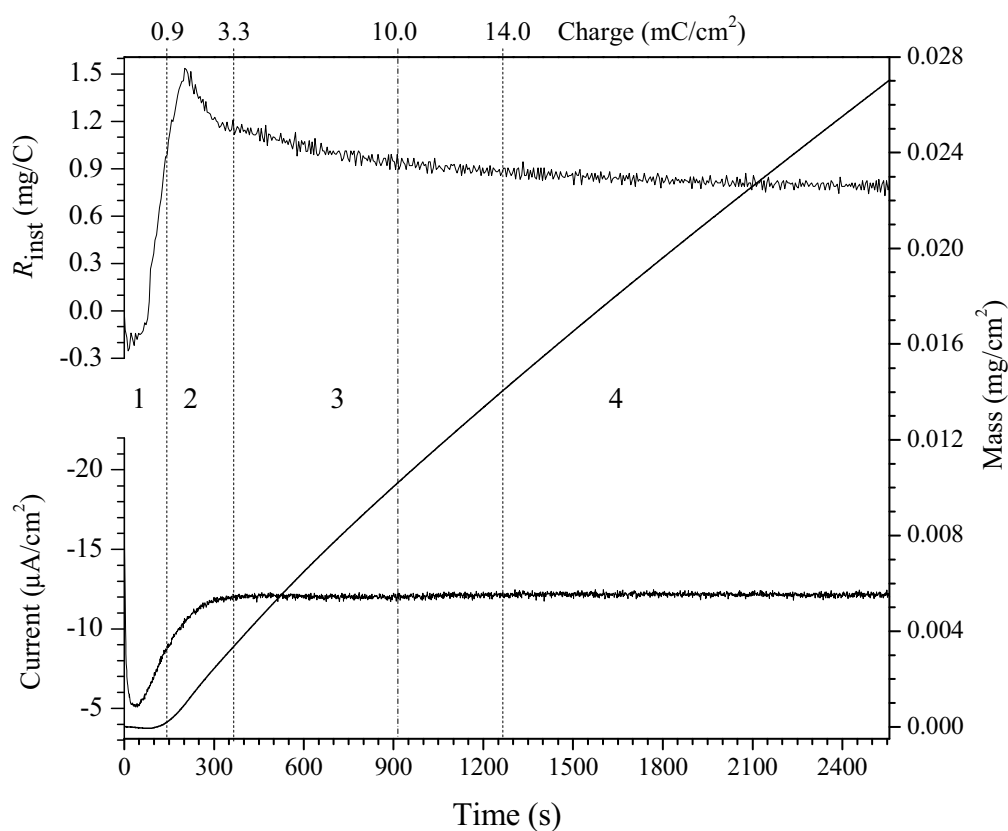


Figure 5.21 Current, mass and R_{inst} for the electrodeposition of zinc-based nanothin sheets on the PPy-PSS films in aerated 0.10 M ZnSO_4 at 0.00 V vs. SCE.

In the first segment, marked as 1, the current decays to a minimum value and then rapidly increases, while the mass of the electrode seems not to change appreciably, except towards the end of the period. On the other hand, the rapid increase of R_{inst} shows that a significant amount of material (per unit of charge) is deposited at the electrode surface just after the minimum current is reached. This increase of R_{inst} corresponds to the instantaneous nucleation of the nanothin sheets (Figure 5.20).

In the second part, the mass increase is more pronounced while the rate at which the current increases slows down to reach the start of a plateau region. The mass increase lags behind the current increase since part of the charge is used for the reduction of dissolved oxygen to the hydroxide ions necessary for the electrocrystallization of the zinc hydroxysulfate nanosheets. The same behavior was observed during the deposition of the hierarchical copper-based micro/nanostructures (Section 3.2.3.2). Accordingly, R_{inst} goes through a maximum value since the calculation of R_{inst} accounts for the mass of the precipitating basic salts, but not for the charge previously consumed during the generation of the hydroxide ions.

In the third part the current is nearly constant, the mass increase is linear, and R_{inst} decreases slowly towards a plateau value. During this part of the electrodeposition process the average mass-to-charge ratio, $R = 0.957 \text{ mg/C}$, is very close to the value computed for $\text{ZnSO}_4[\text{Zn}(\text{OH})_2]_3 \cdot 5\text{H}_2\text{O}$, $R = 0.950 \text{ mg/C}$ (Section 5.2.2.1, Tables 5.1 and 5.2). At this stage, the growth of the zinc-based nanosheets proceeds on both the polymer surface and on the already formed nanosheets. Indeed, the micrographs taken after a charge of 10.0 mC/cm^2 is consumed (dot-dashed line), show the presence of separate multilayered ‘hexagons’ which can grow over the film surface or act as nucleation points for other zinc-based nanothin layers (Section 5.2.3.1, Figure 5.18).

In the fourth and last part of the electrodeposition, both the current and R_{inst} are practically constant, and the mass increase is linear. In this case the average mass-to-charge ratio is $R = 0.757 \text{ mg/C}$. At this stage the formation of lighter species, such as ZnO, is also postulated from the results obtained using EQCM and XPS characterization techniques (Sections 5.2.2.1 and 5.2.2.4).

Clearly, the electrochemical deposition of zinc hydroxysulfate nanosheets and copper hydroxysulfate hierarchical micro/nanostructures are different in two major aspects. The nucleation of the copper-based structures is progressive, while the zinc-based nanosheets is instantaneous. The growth of the copper-based clusters is limited by diffusion and the clusters do not cover the polymer film fully, while the zinc deposits appear to proceed without diffusion limitations covering the film surface fully.

5.2.4 Effect of the Experimental Conditions on the Electrochemical Deposition of Zinc-Based Nanosheets

5.2.4.1 Effect of Film Thickness and Deposition Potential

The electrochemical deposition of zinc-based nanosheets was performed on PPy-PSS films of various thicknesses and at various electrode potentials in aerated 0.10 M ZnSO₄. The results are presented in Figure 5.22 and Figure 5.23, respectively.

As shown in Figure 5.22, the thickness of the polymer film has a profound effect on the deposition of the zinc-based nanosheets. The evaluated thicknesses are 60, 120 and 240 nm. The film thickness was estimated as described in Section 2.4.1.1.

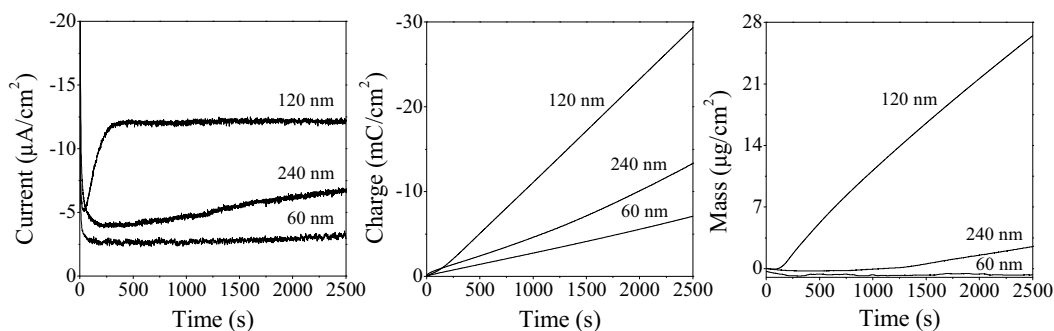


Figure 5.22 Current, charge and mass-time plots for the electrodeposition of zinc-based nanosheets at PPy-PSS films of various thicknesses in aerated 0.10 M ZnSO₄ at 0.00 V vs. SCE. The thickness of the films is indicated beside the curves 60, 120 and 240 nm.

The highest electrodeposition current is recorded with the 120 nm film, whereas the lowest is observed for the 60 nm film. The reduction current measured at the 240 nm

film increases only slowly with time. A minimum value is found at about 250 s corresponding to the start of the nucleation; this value is five times longer than that required with the 120 nm film. The charges consumed during deposition for the 60 and 240 nm films are roughly 1/3 and 1/2 of that of the 120 nm film, respectively. These charges are in striking contrast with the amount of material deposited on the films. In fact, the mass deposited at the 60 nm film is negligible, while the mass deposited at the 240 nm is only 1/10 of that of the 120 nm film. It follows that the current flow at the 60 and 240 nm films does not produce a proportional deposition of material.

These results can be explained by considering the critical ion concentrations and pH required for the electrodeposition event. It is known from the literature [34, 35] that PPy films can improve the reductive conversion of oxygen to hydroxide ions by extending the residence time of hydrogen peroxide (another product of oxygen reduction) at the electrode surface. It follows that at the 60 nm film the residence time is probably too short to allow the sufficient conversion of oxygen to hydroxide ions, while at the 240 nm, the film may be too thick for the efficient diffusion of hydroxide ions to the film surface. In both cases the concentration of hydroxide ions (*i.e.*, pH) at the film surface is not sufficiently high for the electroprecipitation of the zinc-based nanosheets. The optimal thickness, 120 nm, represents a good trade between an adequate conversion of oxygen and diffusion of hydroxide ion to the sites of deposition.

The electrochemical deposition of the zinc-based nanosheets was performed on 120 nm PPy-PSS films in aerated 0.10 M ZnSO₄ solution at four different potentials 0.00, -0.25, -0.50 and -1.00 V vs. SCE. The SEM micrographs and EDX spectra of the resulting materials are presented in Figure 5.23. It is evident from the spectra that the elemental composition of the zinc-based nanosheets remains unchanged at all potentials. Also, the relative heights of the peaks are similar; only at -0.25 V vs. SCE is the peak of oxygen slightly smaller. In terms of morphology, the nanosheets become progressively smaller with the decrease of potential. Probably, at lower potentials, the number of active nucleation sites increases and consequently the formed nanosheets are smaller.

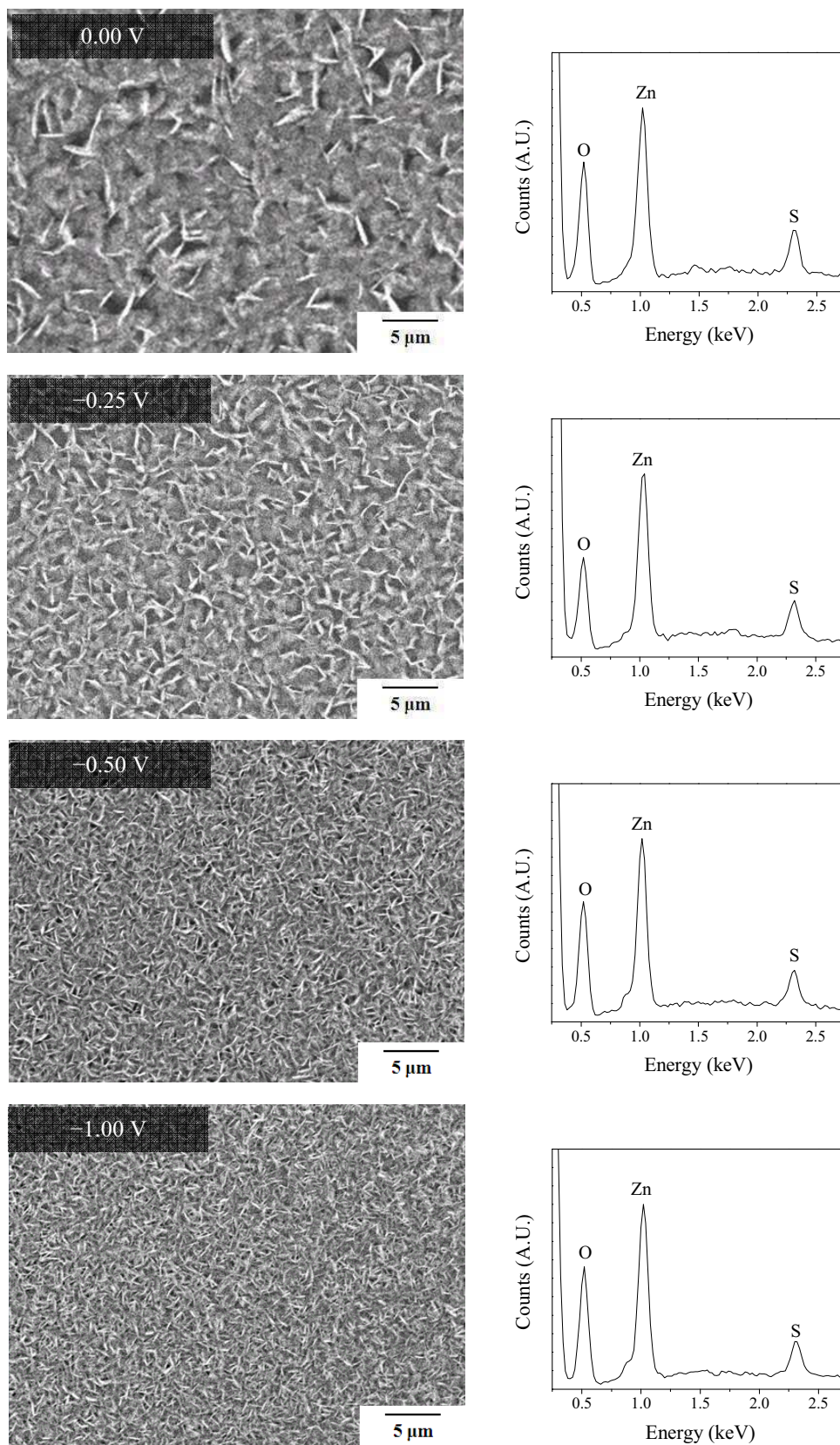
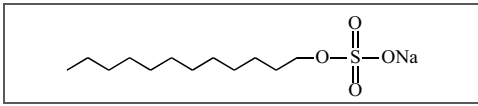
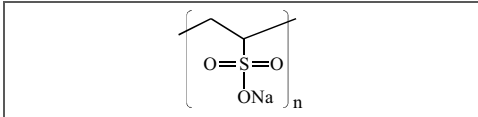
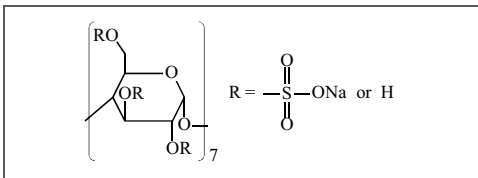
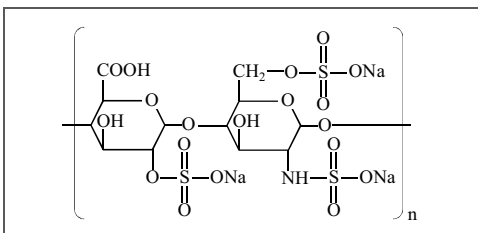


Figure 5.23 SEM micrographs and EDX spectra of zinc-based nanothin sheets deposited at PPy-PSS thin films, 120 nm, at 0.00, -0.25, -0.50 and -1.00 V vs. SCE from aerated 0.10 M ZnSO₄ for a total charge of 30 mC/cm².

5.2.4.2 Effect of Dopant and Counterion

The electrochemical deposition of zinc-based nanothin sheets was performed at PPy films doped with different anions or polyanions in order to evaluate the dependence of the deposition process on the nature of the dopant. The four additional dopants that were considered are listed in Table 5.4. These are all sodium salts of organic compounds in which the anionic function is either a sulfate ($-\text{OSO}_3^-$) or a sulfonate ($-\text{SO}_3^-$) group. The currents, charges and masses recorded on electropolymerization of pyrrole in the presence of these dopants are shown in Figure 5.24.

Table 5.4 List of anionic and polyanionic dopants used to form PPy films. The charged moieties are either sulfate ($-\text{OSO}_3^-$) or sulfonate ($-\text{SO}_3^-$).

Dodecyl Sulfate (DS), Sodium Salt	
Polyvinyl Sulfonate (PVS), Sodium Salt	
β -Cyclodextrin Sulfate (β CD), Sodium Salt (7-11 mol $-\text{SO}_3\text{Na}$ per mol β CD)	
Heparin (Hep), Sodium Salt	

The resulting conducting polymers are polypyrrole-dodecyl sulfate (PPy-DS), polypyrrole-polyvinyl sulfonate (PPy-PVS), polypyrrole- β -cyclodextrin sulfate (PPy- β CD), and polypyrrole-heparin (PPy-Hep) films. All films were deposited to a total charge of 40 mC/cm^2 . The mass-to-charge ratios, R , of the polymers are different depending on the formula weight and amount of dopant included in the film along with solvent molecules. The thickness of the polymeric films is dependent on the density and porosity of the polymers; hence it could be different to the 120 nm PPy-PSS film, even though all polymers were deposited to a constant charge of 40 mC/cm^2 .

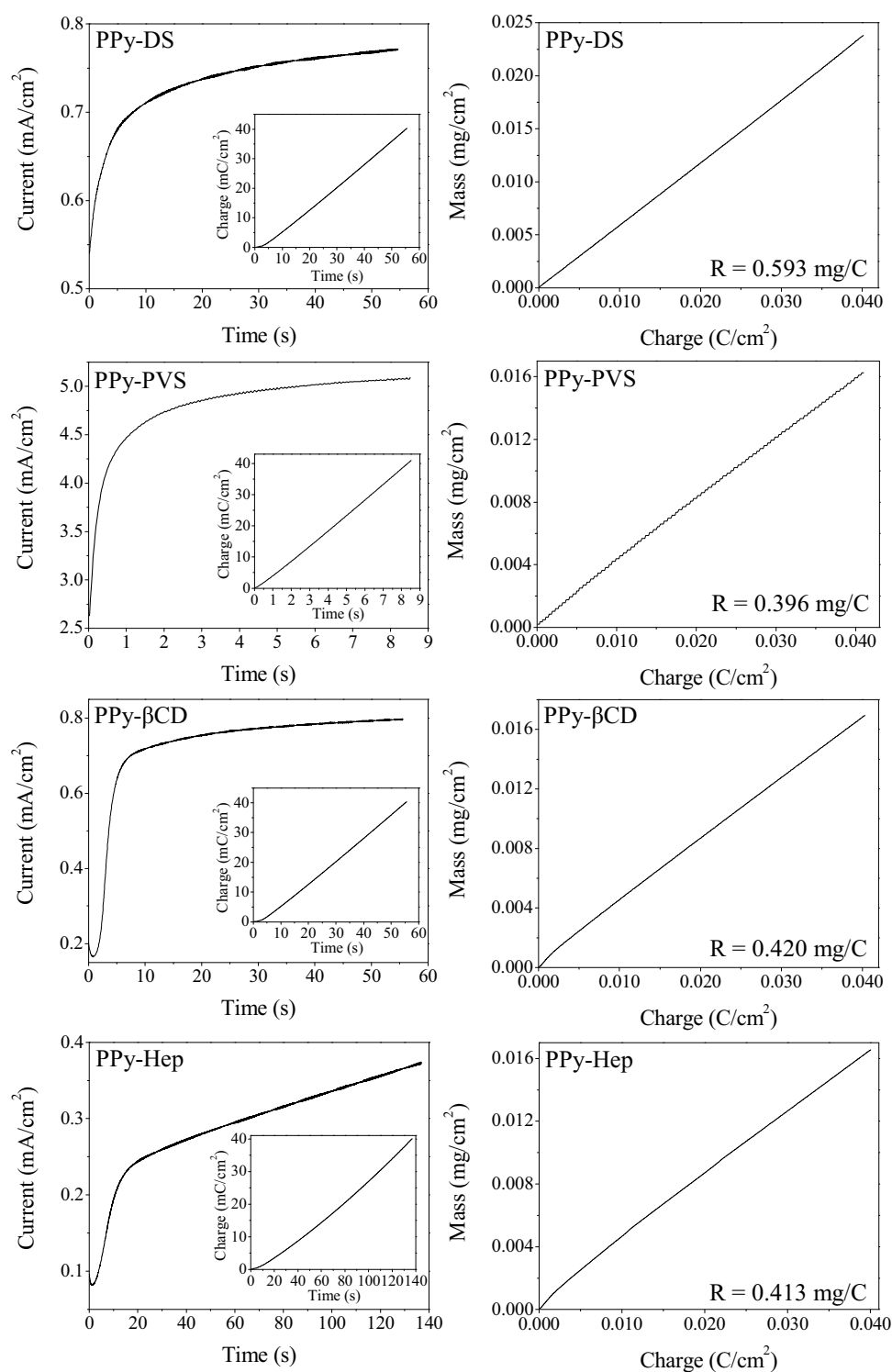


Figure 5.24 Current, charge and mass-time plots recorded for the electropolymerization of pyrrole in the presence of dodecyl sulfate (DS), polyvinyl sulfonate (PVS), β -cyclodextrin sulfate (β CD), and heparin (Hep). The concentrations were 0.15 M Py with 50 mM DS, or 0.10 M PVS in monomeric units, or 11.3 g/l β CD, or 7.2 g/l Hep. The electrode potential was 0.60 V vs. SCE, with the exception of 0.80 V vs. SCE for PPy-PVS.

The mass responses for the electrodeposition of zinc at PPy-PSS, PPy-DS, PPy-PVS, PPy- β CD and PPy-Hep are given in Figure 5.25. The largest amount of material is deposited at the PPy-PSS film, the morphology of the deposit is described in detail in Section 5.2.3.1. The mass of the PPy-DS film decreases instead of increasing. It has been shown in the literature [36] that PPy films doped with DS undergo dopant leakage upon reduction in the potential range from 0.6 to 0.0 V vs. Ag/AgCl. In the present case the mass decrease is quite large, about 10 %; it is then likely that some solvent molecules are also released by the film during the reduction. In the case of PPy- β CD and PPy-Hep the mass increases are relatively small. A microscopy examination of the film surfaces did not reveal any significant deposit on the PPy- β CD, whereas dendrite agglomerates were found on the PPy-Hep film after prolonged deposition (> 3 h), as shown in Figure 5.26. These deposits were not characterized further. In the case of PPy-PVS the mass increase is larger, although still much smaller than the values observed for PPy-PSS. The deposited materials found on the film surface after prolonged deposition (> 2 h) were beautiful flower-like structures. Representative examples are shown in Figure 5.26. In all cases, zinc-based nanothin sheets were obtained only at PPy-PSS thin films where the deposition was much faster and efficient.

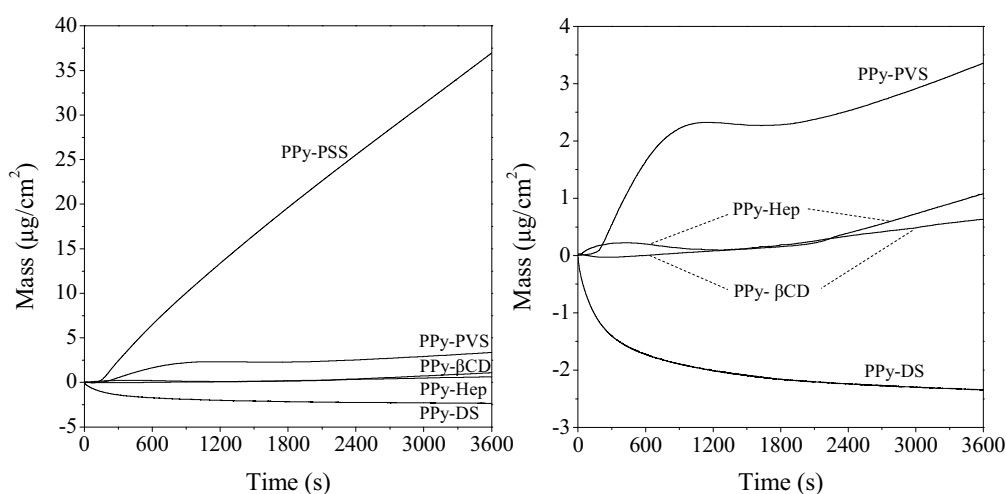


Figure 5.25 Mass-time curves for the electrodeposition of zinc at PPy-PSS, PPy-DS, PPy-PVS, PPy- β CD and PPy-Hep films prepared as described in Figure 5.24. The electrochemical depositions were performed in aerated 0.10 M ZnSO₄ at 0.00 V vs. SCE.

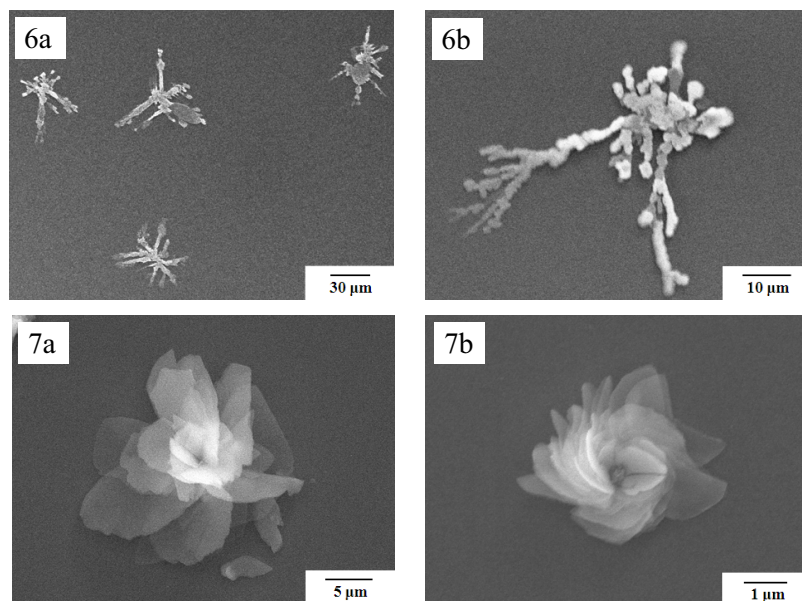


Figure 5.26 SEM micrographs of the zinc materials deposited at PPY-Hep (6a, 6b) and PPY-PVS (7a, 7b) films in aerated 0.10 M ZnSO₄ at 0.00 V vs. SCE. The depositions were performed for total charges of 40 and 50 mC/cm² at the PPY-Hep and PPY-PVS, respectively.

The deposition of basic salts other than hydroxysulfates was also considered by using aerated 0.10 M ZnCl₂ and 0.10 M Zn(NO₃)₂ solutions as supporting electrolytes. The current and mass responses for the depositions in these two electrolytes on PPY-PSS thin films at 0.00 V vs. SCE are given in Figure 5.27. It is evident that in presence of chloride or nitrate anions the increase of mass is negligible compared to the deposition in the sulfate electrolyte. Taking into account three of the representative basic salts, Zn₅(OH)₈Cl₂, Zn₅(OH)₈(NO₃)₂ and Zn₄(OH)₆SO₄, with their respective solubility product values of 1.0×10^{-73} , 4.0×10^{-71} and 2.0×10^{-57} [8, 9], it is clear that the different outcomes of the electrodepositions do not depend on the solubility of the salts. In fact, the zinc hydroxysulfate is the most soluble among the three species. Sulfate ions have a higher charge density compared to chlorides and nitrates. It has been shown in the literature [37] that owing to their larger charge density, sulfate ions can be attracted into the film by the positive charge of polypyrrole. This effect may aid and promote the electroprecipitation of zinc hydroxysulfates. Interestingly, the addition of a small amount of zinc sulfate to the zinc-based nitrate electrolyte was sufficient to increase the amount of deposited mass, as shown in Figure 5.27. In the presence of 10 mM ZnSO₄, electroprecipitation is observed after a large delay or induction period of about 1000 s. This shows clearly the influence and importance of the sulfate anions.

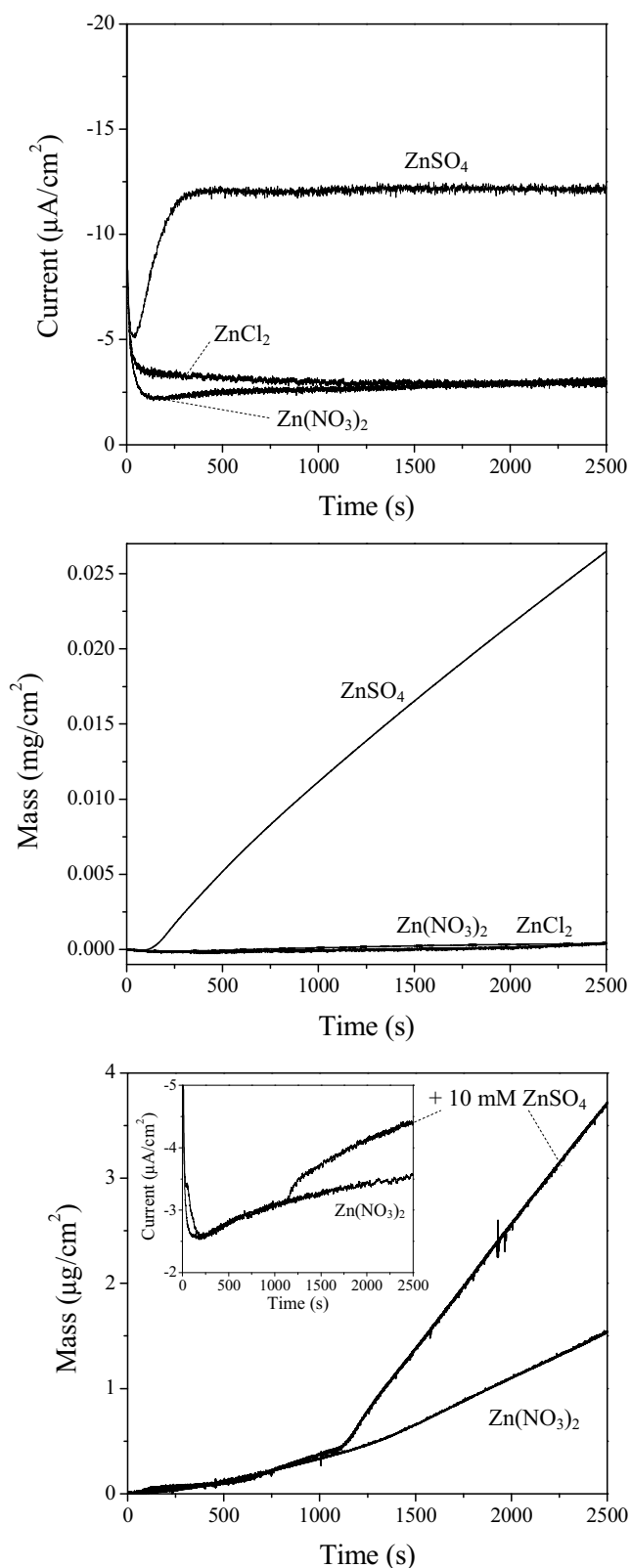


Figure 5.27 Current-time and mass-time responses for the electrodeposition of zinc-based materials at PPy-PSS films in various aerated solutions, 0.10 M ZnCl_2 , 0.10 M $\text{Zn}(\text{NO}_3)_2$ and 0.10 M ZnSO_4 , at 0.00 V vs. SCE. The bottom plot shows the effect of the addition of 10 mM ZnSO_4 to a 0.10 M $\text{Zn}(\text{NO}_3)_2$ solution. The film thickness was 120 nm.

5.2.4.3 Effect of Oxygen and pH

The electrochemical deposition of zinc-based nanothin sheets was performed on PPy-PSS thin films from 0.10 M ZnSO₄ solutions saturated with nitrogen, air or oxygen. The mass of a PPy-PSS modified electrode was monitored while performing the electrodeposition at 0.00 V vs. SCE in nitrogen saturated 0.10 M ZnSO₄ solution. As shown in Figure 5.28, the mass of the electrode does not increase until the nitrogen flux is stopped allowing air to enter into the electrochemical cell. The mass of the electrode starts increasing once the presence of oxygen is restored in solution. It is interesting to note that, as previously seen in Section 5.2.3.2, the mass increase is delayed compared to the current increase. This is due to the fact that oxygen must be converted to hydroxide in order to initiate the electroprecipitation of the zinc-based nanosheets.

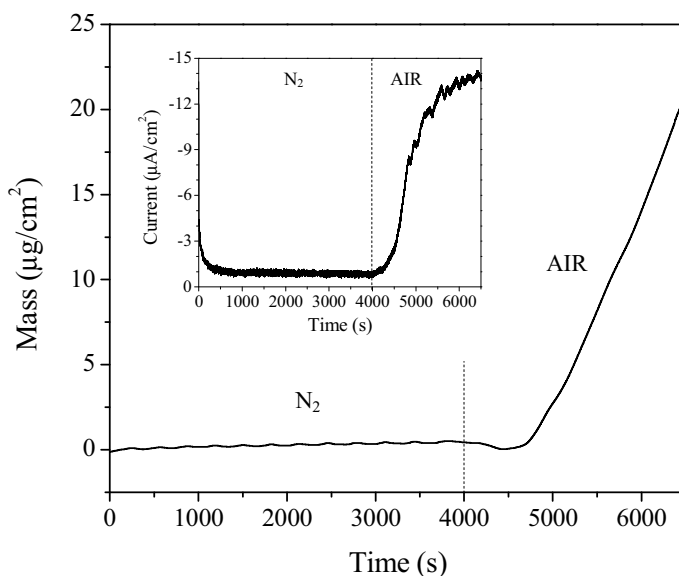


Figure 5.28 Current and mass-time curves recorded during the electrodeposition of zinc-based nanothin sheets on 120 nm PPy-PSS film in 0.10 M ZnSO₄ at 0.00 V vs. SCE in saturated nitrogen (N₂) or air (AIR). The electrodeposition was performed under a nitrogen atmosphere until 4000 s at which point air was introduced into the electrochemical cell.

To gain further information on the role of oxygen, a slow potential scan at 1.0 mV/s was performed from 0.60 to 0.00 V vs. SCE in aerated and oxygen saturated 0.10 M ZnSO₄ solutions. The resulting gravimetric responses are shown in Figure 5.29. In the oxygen saturated solution the electrodeposition occurs faster, as evidenced from

the rapid increase in the mass at the onset of the deposition. Furthermore, the deposition occurs at a potential about 100 mV more electropositive compared to the aerated solution. These observations clearly show the ease of deposition in the oxygen-enriched solutions. Some mass fluctuations are observed between 0.45 and 0.10 V vs. SCE in the oxygen saturated solution. It has been shown in the literature [38] that the volume and mass of PPy-PSS can change with the solution pH. It follows that these fluctuations may be related to the local variation of pH (*i.e.*, volume) at the polymer film interface, which will be greater in the oxygen saturated solutions.

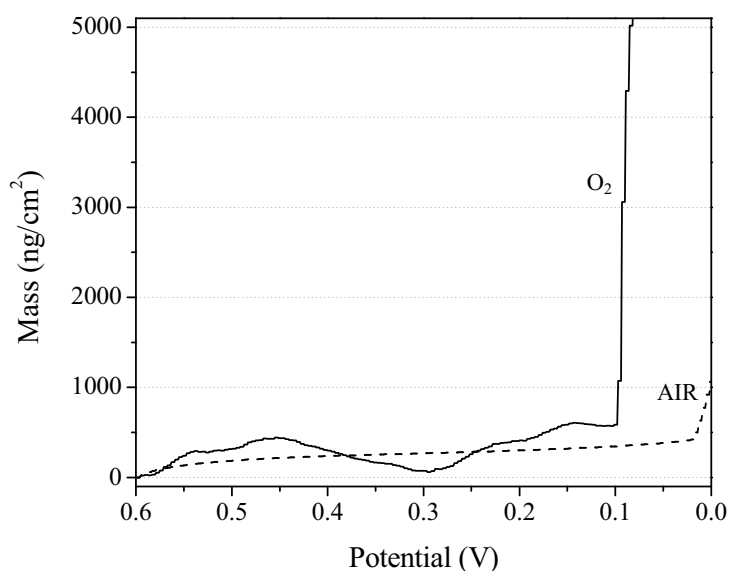


Figure 5.29 Mass-potential curves recorded during reduction potential sweeps of PPy-PSS films in 0.10 M ZnSO₄ oxygen saturated (—) and aerated (---) solutions. The films were deposited to 120 nm and cycled at 1.0 mV/s.

Hydrogen peroxide was also considered as a source of oxygen as it spontaneously disproportionates to water and molecular oxygen. The resulting mass response in the presence of hydrogen peroxide is shown in Figure 5.30. It is seen that the addition of 50 mM H₂O₂ to the electrolyte causes a faster electrodeposition. Also, the mass increase is observed immediately after the application of the potential avoiding the conditioning period necessary in the case of aerated solutions. It is interesting to note that the slope of the curve decreases with time to become somewhat parallel to the one in air. Such a decrease is likely to be related to the consumption of H₂O₂ and once depleted the electrodeposition proceeds with the oxygen supplied from the air.

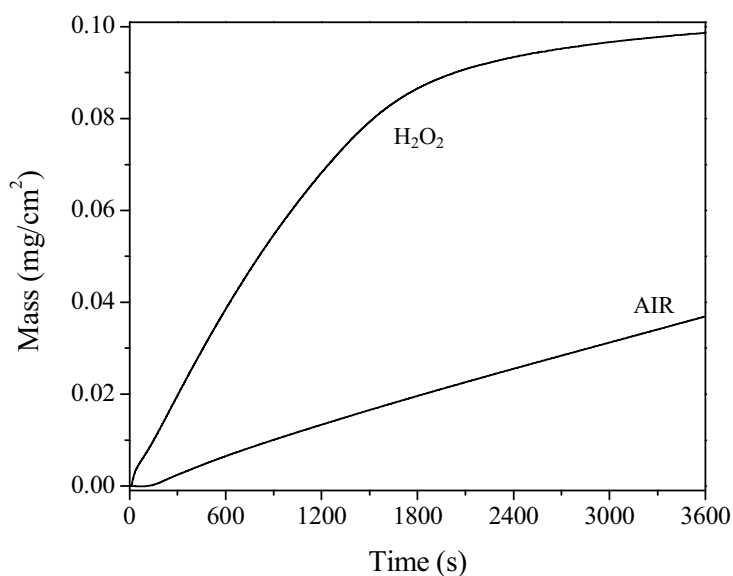


Figure 5.30 Electrochemical deposition of zinc-based nanosheets onto 120 nm PPy-PSS films in 0.10 M ZnSO₄ at 0.00 V vs. SCE in aerated (AIR) and aerated with 50 mM hydrogen peroxide (H₂O₂) solutions.

As shown in Figure 5.31, the electrodeposition of zinc-based nanosheets in aerated electrolyte solution forms less and larger nanosheets compared to the deposition in oxygen saturated solutions. The presence of oxygen allows the nucleation of nanosheets at more sites on the polymer surface with each nucleus growing to give smaller sheets. Actually, at this stage of growth the nanosheets have hexagonal shape, as shown in Section 5.2.3.1.

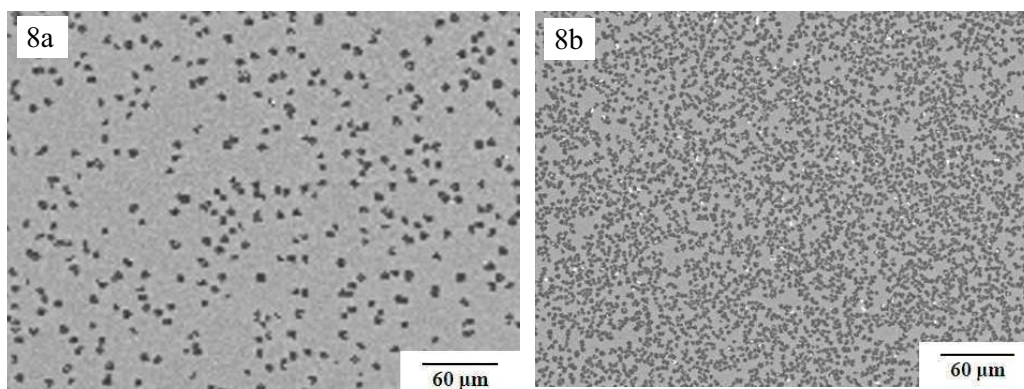


Figure 5.31 SEM micrographs of zinc-based nanosheets deposited at 120 nm PPy-PSS films in 0.10 M ZnSO₄ at 0.00 V vs. SCE in aerated (8a) and oxygen saturated (8b) solutions. The total charge consumed during deposited at the surface was 30 mC/cm².

The zinc-based nanothin sheets were electrodeposited in oxygen saturated 0.10 M ZnSO_4 solution at three different potentials 0.00, -0.50 and -1.00 V vs. SCE. The SEM micrographs and EDX spectra of the resulting materials are presented in Figure 5.32. It is evident from the spectra that the elemental composition of the zinc-based nanosheets remains unchanged at all potentials; also, the nanosheets became progressively smaller with the decrease of potential, as already observed for the aerated solutions (Section 5.2.4.1).

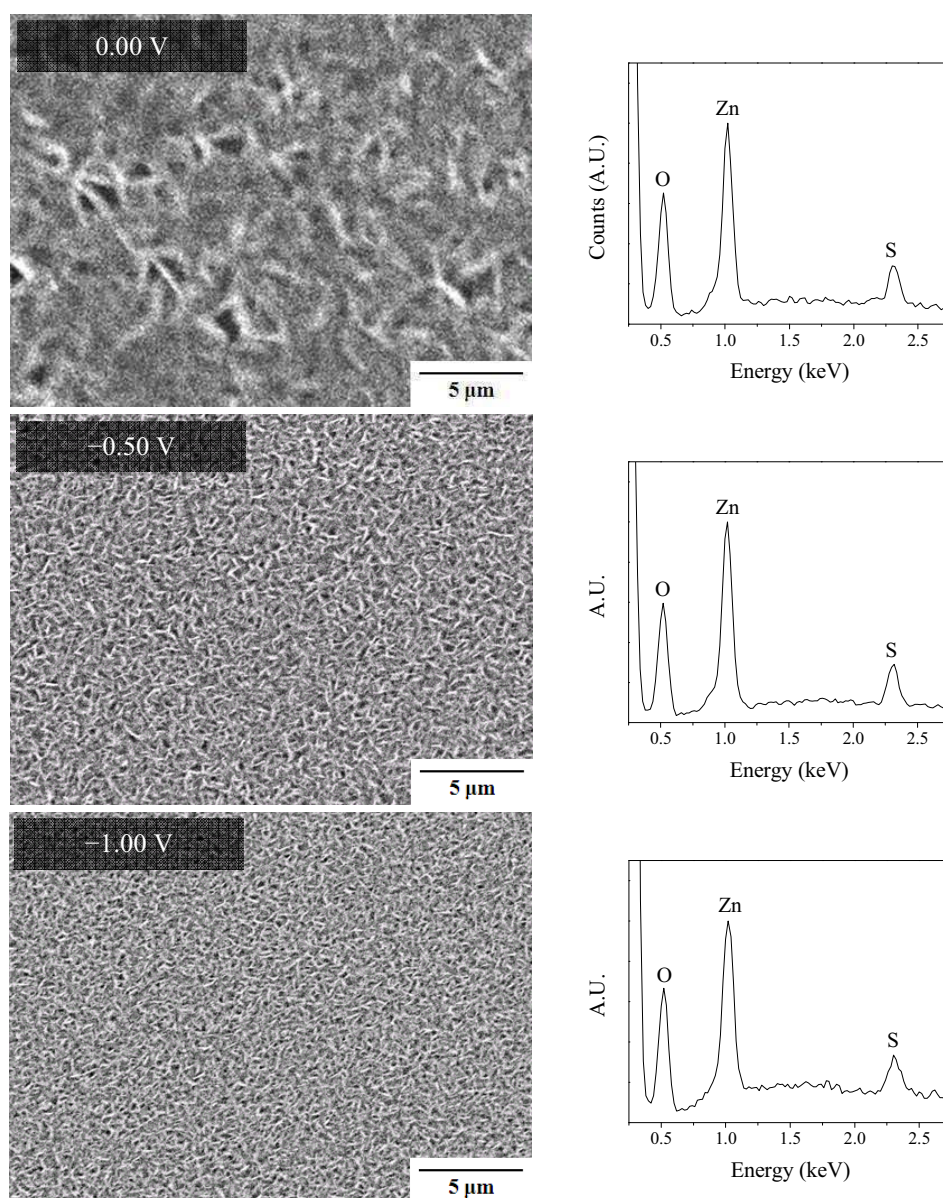


Figure 5.32 SEM micrographs and EDX spectra of zinc-based nanothin sheets deposited at 120 nm PPy-PSS thin films at 0.00, -0.50 and -1.00 V vs. SCE from oxygen saturated 0.10 M ZnSO_4 for a total charge of 30 mC/cm^2 . The elements identified are zinc, oxygen and sulfur.

The electrodeposition of zinc-based nanothin sheets was also performed in 0.10 M ZnSO_4 at three different pH values of 2.9, 5.1 and 6.1. The as prepared electrolyte solution had a pH of 5.1, while the pH was adjusted to 2.9 with the dropwise addition of 0.5 M H_2SO_4 , and 0.2 M NaOH was used to adjust the pH to 6.1. However, at pH 6.1, white deposits of insoluble $\text{Zn}(\text{OH})_2$ were observed in the solution. The electrodeposition experiments were performed at 0.00 V vs. SCE and the resulting mass responses are shown in Figure 5.33. At pH 5.1, the mass increased linearly with time as seen in the previous sections. However, at pH 2.9, no increase in mass was observed even after a period of 10 h, while at pH 6.1, an increase in mass was measured following a 2 h induction period. It follows that under acidic conditions, with a bulk pH of 2.9, a sufficiently high concentration of hydroxide, to trigger the nucleation of zinc hydroxysulfate, is not achieved at the PPy-PSS film. Instead, at a higher pH of 6.1, the $\text{Zn}(\text{OH})_2$ is sparingly soluble ($K_{\text{sp}} = 3.0 \times 10^{-17}$ [39]) and after 2 h the Zn^{2+} and OH^- species reach the critical concentrations necessary to initiate the electrodeposition. At the end of the electrodeposition, approximately 10 h, the electrolyte solution was completely clear indicating that all $\text{Zn}(\text{OH})_2$ was dissolved and/or electrodeposited onto the film.

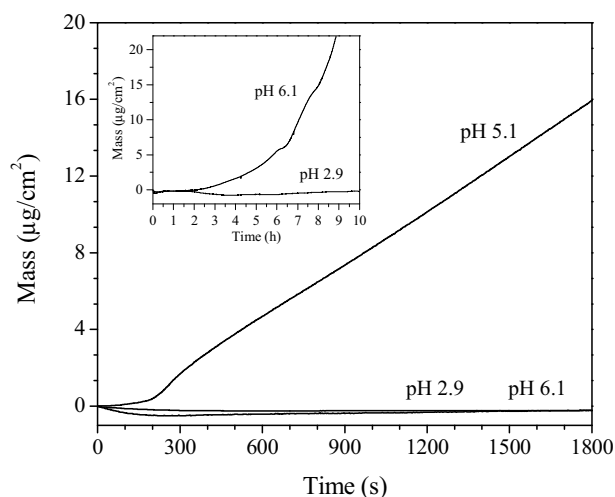


Figure 5.33 Electrochemical deposition of zinc-based nanothin sheets onto 120 nm PPy-PSS films in aerated 0.10 M ZnSO_4 at 0.00 V vs. SCE at pH = 2.9, 5.1 and 6.1.

The effect of the oxygen and pH on the formation of the deposits is additional confirmation of the fundamental role of hydroxide ions in the electrocrystallization of the copper and zinc hydroxysulfates, which can proceed only in basic pH conditions.

5.2.5 Conversion of Zinc-Based Nanosheet Sheets to Metallic Zinc Dendrites

The zinc-based nanosheet sheets formed at the PPy-PSS films were reduced at various applied potentials in an attempt to convert them to other species, for example, zinc oxide or metal.

The reduction at -1.50 V vs. SCE in 0.10 M Na_2SO_4 aerated solution does not produce any change in the morphology and elemental composition of the zinc-based nanosheets. It is necessary to apply potentials as low as -2.00 V vs. SCE to induce partial conversion of the nanosheets to metallic zinc micro-dendritic clusters; the results are presented in Figure 5.34. The micrographs show that only a very limited portion of the zinc sheets are converted to zinc metal clusters after reduction at -2.00 V vs. SCE.

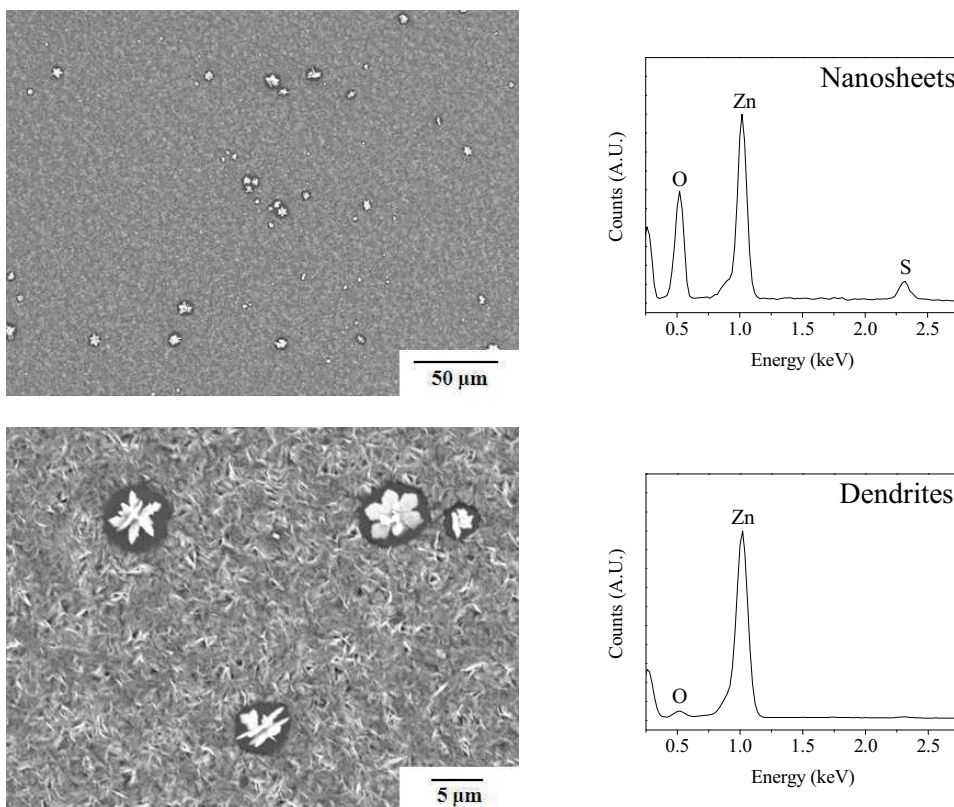


Figure 5.34 SEM micrographs and EDX spectra of the zinc-based nanosheet sheets after reduction at -2.00 V vs. SCE for 10 min in 0.10 M Na_2SO_4 . The amount of deposited zinc was 80 mC/cm^2 from oxygen saturated 0.10 M ZnSO_4 at 0.00 V vs. SCE. The spectra are those of the zinc-based nanosheets which remained unchanged after reduction treatment and of the metallic zinc dendritic clusters formed from the reduction of the nanosheets.

The clusters in Figure 5.34 are produced from the localized conversion of the nanosheets to zinc dendrites. The elemental compositions obtained from the EDX spectra are those of zinc hydroxysulfate for the remaining nanosheets and of zinc metal for the micro-dendrites. The small oxygen peak present in the spectrum of the dendrites is likely to be due to the passivation of the metallic clusters to form a surface layer of zinc oxide. The absence of the sulfur peak is proof that sulfate is removed from the dendrites upon reduction treatment.

A series of SEM micrographs of the metallic zinc dendrites is given in Figure 5.35. It is interesting to note that the immediate area surrounding the dendrites is clear showing a complete conversion of the nanosheets. The dendrites are characterized by a layered structure with crystal components having dimensions below a few hundred nanometers. The size of the micro-dendrites is about 2 to 5 μm and they seem to arise or extend from the film surface.

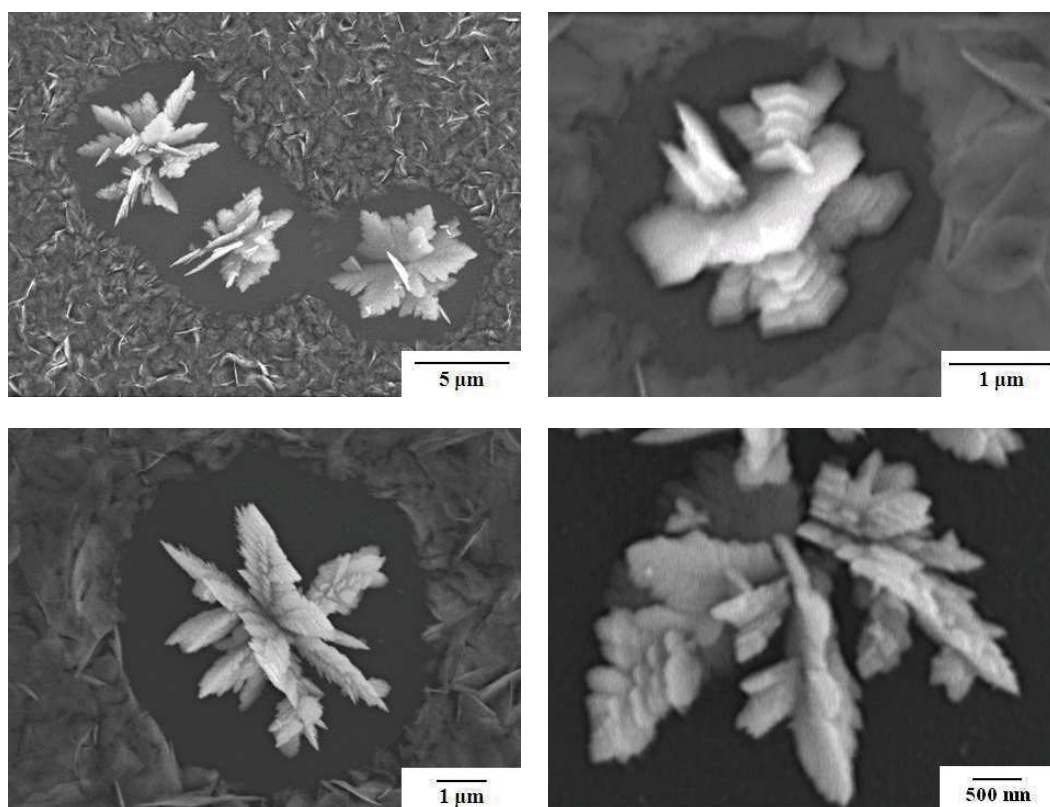


Figure 5.35 SEM micrographs showing the details of the zinc metal dendrites formed from the reduction of zinc-based nanosheet thin sheets at -2.00 V vs. SCE for 10 min, as described in Figure 5.34.

The reduction at -2.50 V vs. SCE in 0.10 M Na_2SO_4 aerated solution caused the complete conversion of the zinc-based nanosheets to dendrites. The micrographs in Figure 5.36 show that larger islands of sparse deposits were also found on the film surface after reduction treatment. The islands were distributed randomly on the polymer surface and had an average size of several tenths of a micrometer. Zinc dendrites were also found in the area covered by the islands showing that both materials could be formed at the same place on the polymer film.

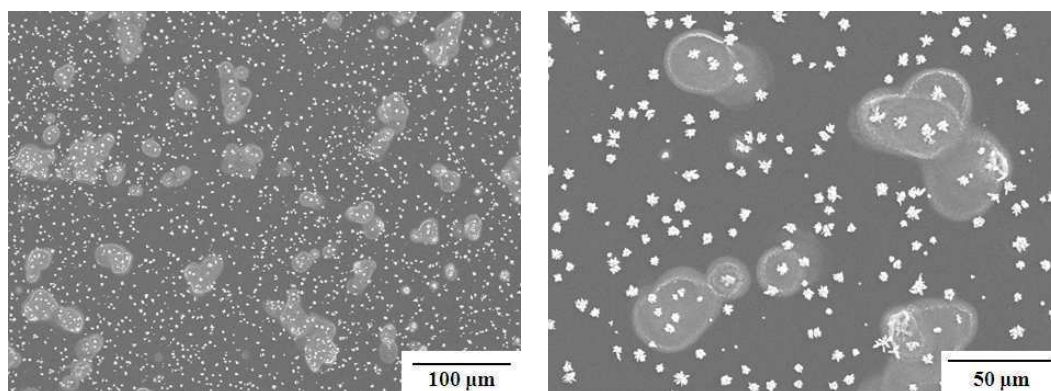


Figure 5.36 SEM micrographs of the products of reduction of the zinc-based nanosheet reduced at -2.50 V vs. SCE for 10 min in 0.10 M Na_2SO_4 . The amount of deposited zinc was 80 mC/cm^2 from oxygen saturated 0.10 M ZnSO_4 at 0.00 V vs. SCE.

A closer inspection of this thin deposit (Figure 5.37) showed that the material was ‘fluffy’ and ‘shapeless’ both being the typical features of hydroxide flocculants. The EDX spectrum of this deposit revealed that the component elements of the flocculant were zinc and oxygen but not sulfur. The amount of oxygen was larger than that for zinc oxide (Section 5.2.2.3) indicative of the possible formation of zinc hydroxide. The presence of zinc hydroxide after the application of such a negative potential, -2.50 V vs. SCE, could be due to the corresponding generation of large amounts of hydroxide ions during reduction treatment. This local increase of the pH may result in the conversion of the zinc hydroxysulfate to zinc hydroxide.

Another different form of zinc deposit was found in some zones of the polymer film. These deposits were composed of agglomerates of small crystals with different morphology compared to the zinc metal dendrites, as shown in Figure 5.38.

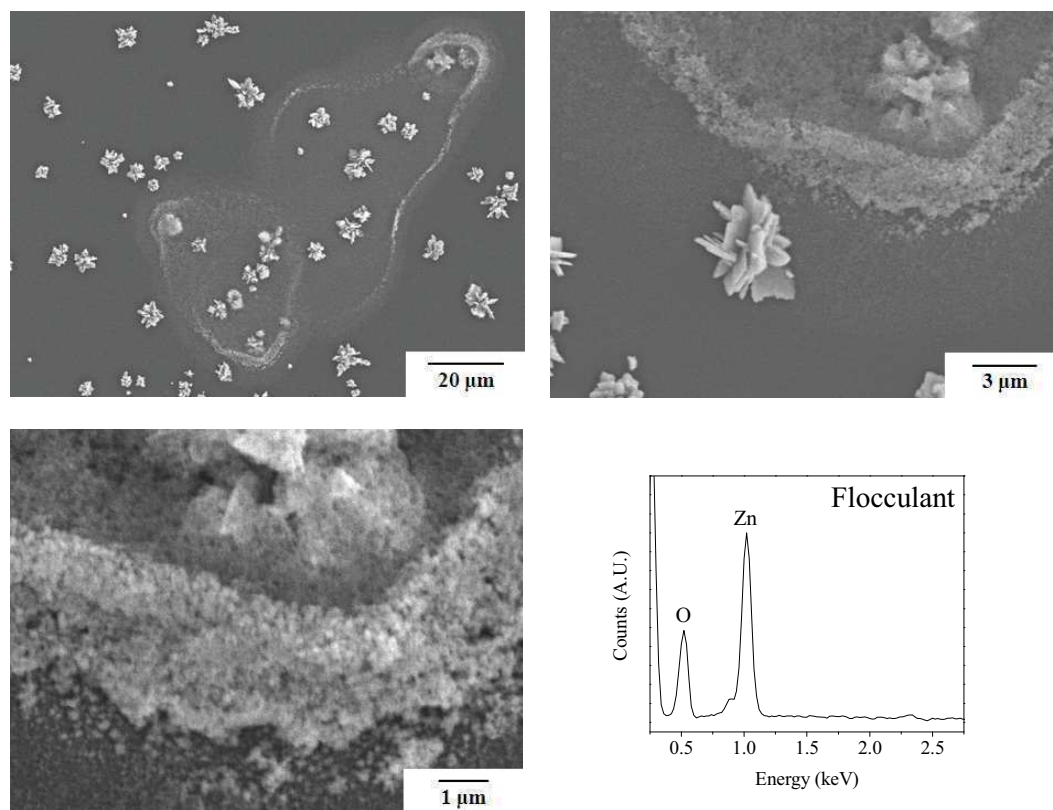


Figure 5.37 SEM micrograph of the deposits formed after reduction of zinc-based nanothin sheets at -2.50 V vs. SCE for 10 min in aerated 0.10 M Na_2SO_4 , as described in Figure 5.36. The EDX spectrum of the flocculant is shown beside the corresponding micrograph.

The agglomerated species appears flatter than the dendrites and are made of a large number of nanocrystals with dimension corresponding to a few hundred nanometers. The EDX spectrum reveals that the agglomerates are made of zinc and oxygen but again no sulfur is present. The oxygen peak is smaller compared to that observed with the flocculants and comparable to that of zinc oxide (Section 5.2.2.3). It follows that the agglomerates could be made of zinc oxide which could be formed from the dissolution of zinc hydroxysulfate and/or zinc hydroxide at higher pH [14].

The reduction treatment at -2.50 V vs. SCE was performed on a smaller amount of deposited zinc-based nanosheets in order to attempt the formation of reduction products of smaller size. The resulting products are shown in Figure 5.39. In this case the film surface is almost all cleared and only a few residual zinc 'hexagons' can be seen.

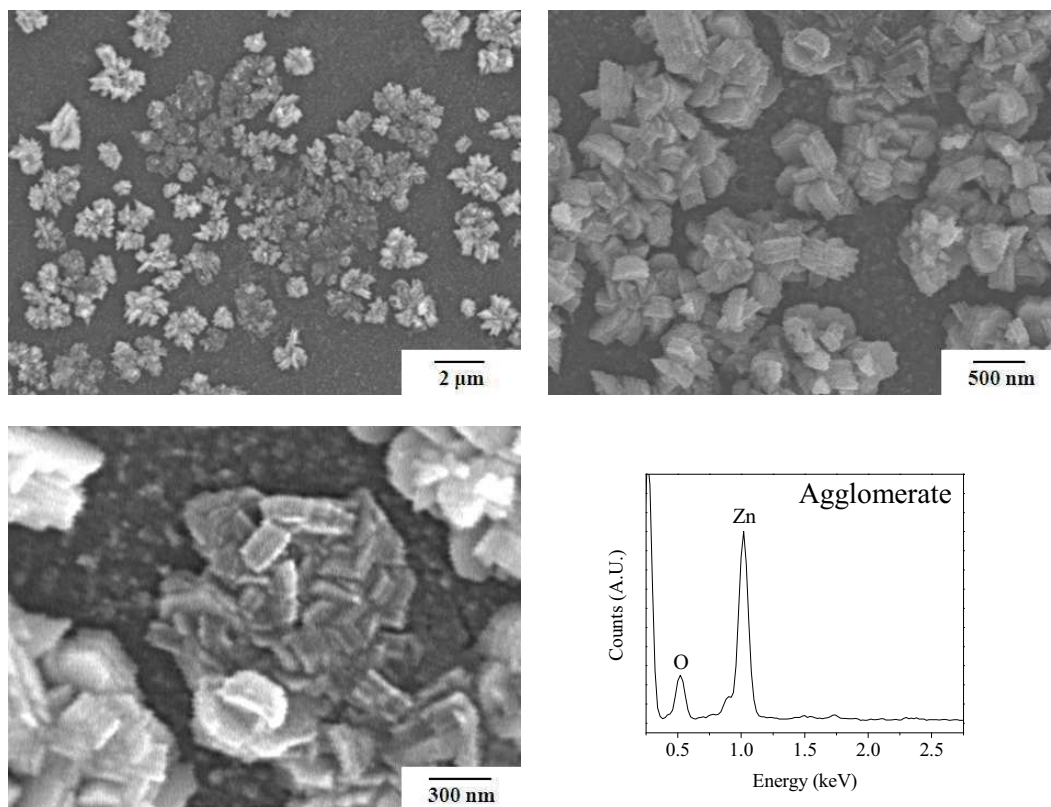


Figure 5.38 SEM micrograph of the deposits formed after reduction of zinc-based nanoribbon sheets at -2.50 V vs. SCE for 10 min in 0.10 M Na_2SO_4 , as described in Figure 5.36. The EDX spectrum of the bulky agglomerates is shown beside the corresponding micrograph.

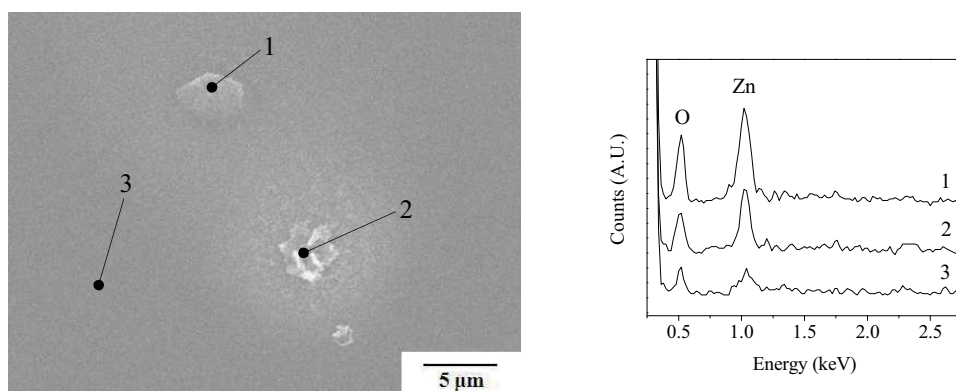


Figure 5.39 SEM micrographs and EDX spectra of the PPy-PSS thin film modified with zinc-based nanoribbon hexagonal sheets reduced at -2.50 V vs. SCE for 10 min in 0.10 M Na_2SO_4 . The amount of deposited zinc was 10 mC/cm² from oxygen saturated 0.10 M ZnSO_4 at 0.00 V vs. SCE. The spectra labeled 1, 2 and 3 were measured on the film as indicated in the micrograph.

These residual ‘hexagons’ are made of zinc and oxygen probably either from zinc oxide and/or hydroxide, or mixtures of both (EDX spectra 1 and 2). Traces of zinc are also found in the polymer film (EDX spectrum 3).

It is evident from these results that several processes are involved in the reductive conversion of the zinc-based nanothin sheets. The electrochemical conversion of zinc hydroxysulfate nanosheets to zinc oxide is of particular technological interest considering the numerous and important application of zinc oxide which are reported in Section 5.1. This task could be the object of further research studies.

5.3 Summary

The subject of the present chapter is the electrodeposition, characterization and conversion of zinc hydroxysulfate nanothin sheets prepared with the aid of polypyrrole-polystyrene sulfonate (PPy-PSS) thin films. The nanosheets were deposited at a constant potential of 0.00 V vs. SCE on top of the polymer films from 0.10 M ZnSO₄ solutions in the presence of dissolved oxygen. The nanosheets were subsequently reduced in 0.10 M Na₂SO₄ aerated solutions to zinc metal micro-dendrites possibly with a minor amount of ZnO clusters.

The electrocrystallization of the zinc-based nanosheets was driven by the capture of Zn²⁺ and formation of OH⁻ at the PPy-PSS film. The PPy-PSS thin film is a cation exchanger and accordingly it can be employed to capture the Zn²⁺ ions from the electrolyte solution. Once reduced at 0.00 V vs. SCE, the film can capture the metal ions from the solution (Section 5.2.1). Also, the oxygen reduction reaction (ORR) was enhanced by the polymer film with the formation of additional hydroxide ions (Section 3.2.4). In this way, the polymer film served as an assembling tool, where the Zn²⁺ ions were concentrated and precipitated with the OH⁻, generated from the reduction of the dissolved oxygen, and the SO₄²⁻ ions of the electrolyte.

The zinc-based nanothin sheets were composed of Zn, S and O, as determined from both EDX and XPS analysis (Sections 5.2.2.3 and 5.2.2.4). The presence of SO₄²⁻ and OH⁻ was identified using the ATR-FTIR spectrum of the nanosheets in which the characteristic bands of the two ions were found at about 950-1250 cm⁻¹ and 3000-3500 cm⁻¹, respectively. The presence of SO₄²⁻ was also confirmed using XPS with the presence of the S 2p and O 1s signals characteristic of sulfate ions.

The zinc-based nanothin sheets were made of zinc hydroxide sulfate hydrate, $\text{ZnSO}_4[\text{Zn}(\text{OH})_2]_3 \cdot 5\text{H}_2\text{O}$. This was confirmed using several experimental techniques. The XRD pattern of the nanosheets corresponds to the one of zinc hydroxide sulfate hydrate (Section 5.2.2.1). The ATR-IR spectrum of the nanosheets was in excellent agreement with the mineral osakaite, ideally $\text{ZnSO}_4[\text{Zn}(\text{OH})_2]_3 \cdot 5\text{H}_2\text{O}$ (Section 5.2.2.5). The stoichiometric ratio of Zn to S obtained from the EDX spectrum of the nanosheets using appropriate standards was also in good agreement with the proposed chemical formula (Section 5.2.2.3). The EQCM measurements were in agreement with the deposition of zinc hydroxysulfate compounds especially during the first steady state growth phase established after the nucleation of the nanosheets (Section 5.2.2.2). The XPS spectra gave evidence for the presence of zinc oxide-like species in the outermost layers of the nanothin sheets (Section 5.2.2.4).

The morphology of the zinc-based nanosheets was analyzed in detail during the electrodeposition process (Section 5.2.3.1). At the start of the deposition the nanosheets had hexagonal shape and lay entirely on the surface of the PPy-PSS film. The sheets then grew to form irregular islands composed of several adjacent sheets that were deposited on the polymer and on top of already formed nanothin sheets. At this stage the nanosheets grew perpendicular to the film at the point of contact of two or more sheets. The final appearance of the deposit was a dense network of entangled and randomly oriented nanosheets. The nucleation of the zinc-based nanosheets onto the polymer film was shown to be instantaneous (Section 5.2.3.2) followed by a growth characterized by the deposition of material on both the film and the nanosheets, which were previously formed.

The effect of several parameters on the deposition of the zinc-based nanosheets was examined in detail (Section 5.2.4). Three main factors were identified as key elements necessary to facilitate the deposition. These were: the presence of dissolved oxygen in the electrolyte (Section 5.2.4.3), the use of the specific dopant PSS (Section 5.2.4.2), and an appropriate thickness of the PPy-PSS film (Section 5.2.4.1).

The zinc-based nanothin sheets were converted to zinc metal dendrites at -2.50 V vs. SCE (Section 5.2.5). The conversion was complete with minor amounts of $\text{Zn}(\text{OH})_2$ or ZnO clusters.

5.4 References

- [1] Castaño JG, Arroyave C, Morcillo M; *Journal of Materials Science*, **2007**, 42(23), 9654
- [2] El-Mahdy GA, Kim KB; *Corrosion*, **2005**, 61(5), 420
- [3] Odnevall I, Leygraf C; *Corrosion Science*, **1994**, 36(6), 1077
- [4] Qu Q, Yan CW, Wan Y, Cao CN; *Corrosion Science*, **2002**, 44(12), 2789
- [5] Gao XD, Li XM, Yu WD, Peng F, Zhang CY; *Materials Research Bulletin*, **2006**, 41(3), 608
- [6] Carbajal Arizaga GG, Satyanarayana KG, Wypych F; *Solid State Ionics*, **2007**, 178(15-18), 1143
- [7] Hongo T, Iemura T, Satokawa S, Yamazaki A; *Applied Clay Science*, 48(3), 455
- [8] Yoder CH, Rowand JP; *American Mineralogist*, **2006**, 91(5-6), 747
- [9] Yoder CH, Gotlieb NR, Rowand AL; *American Mineralogist*, **2010**, 95(1), 47
- [10] Ozgur U, Alivov YI, Liu C, Teke A, Reshchikov MA, Dogan S, Avrutin V, Cho SJ, Morkoc H; *Journal of Applied Physics*, **2005**, 98(4),
- [11] Pearton SJ, Norton DP, Ip K, Heo YW, Steiner T; *Progress in Materials Science*, **2005**, 50(3), 293
- [12] Wang ZL; *Journal of Physics-Condensed Matter*, **2004**, 16(25), R829
- [13] Wang LD, Liu GC, Zou LJ, Xue DF; *Journal of Alloys and Compounds*, **2010**, 493(1-2), 471
- [14] Kawano T, Imai H; *Journal of Crystal Growth*, **2005**, 283(3-4), 490
- [15] Kim YH, Carraway ER; *Environmental Technology*, **2003**, 24(12), 1455
- [16] Lin CH, Tseng SK; *Chemosphere*, **1999**, 39(13), 2375
- [17] Bryndzia LT; *Environmental Science & Technology*, **1996**, 30(12), 3642
- [18] Boronina T, Klabunde KJ, Sergeev G; *Environmental Science & Technology*, **1995**, 29(6), 1511
- [19] Noda T, Inagaki M; *Bulletin of the Chemical Society of Japan*, **1964**, 37(10), 1534
- [20] Brittain RD, Lau KH, Knittel DR, Hildenbrand DL; *Journal of Physical Chemistry*, **1986**, 90(10), 2259
- [21] Bear IJ, Grey IE, Madsen IC, Newnham IE, Rogers LJ; *Acta Crystallographica Section B-Structural Science*, **1986**, 42, 32
- [22] Muster TH, Cole IS; *Corrosion Science*, **2004**, 46(9), 2319
- [23] Ramanaukas R, Quintana P, Bartolo-Perez P, Diaz-Ballote L; *Corrosion*, **2000**, 56(6), 588
- [24] Goldstein J, Newbury DE, Joy DC, Lyman CE, Echlin P, Lifshin E, Sawyer L, Michael JR; *Scanning Electron Microscopy and X-ray Microanalysis*; 2003, 3rd ed., Springer
- [25] Kanani N; *Electroplating: Basic Principles, Processes and Practice*; 2005, Elsevier Science
- [26] Evans S; *Surface and Interface Analysis*, **1985**, 7(6), 299
- [27] Battistoni C, Dormann JL, Fiorani D, Paparazzo E, Viticoli S; *Solid State Communications*, **1981**, 39(4), 581

- [28] Strohmeier BR, Hercules DM; *Journal of Catalysis*, **1984**, 86(2), 266
- [29] Yu XR, Liu F, Wang ZY, Chen Y; *Journal of Electron Spectroscopy and Related Phenomena*, **1990**, 50(1-2), 159
- [30] Nefedov VI; *Journal of Electron Spectroscopy and Related Phenomena*, **1982**, 25(1), 29
- [31] Ohnishi M, Kusachi I, Kobayashi S; *Canadian Mineralogist*, **2007**, 45, 1511
- [32] SDBSWeb National Institute of Advanced Industrial Science and Technology, 22 July 2010. <http://riodb01.ibase.aist.go.jp/sdbs/>
- [33] Scharifker B, Hills G; *Electrochimica Acta*, **1983**, 28(7), 879
- [34] Jakobs RCM, Janssen LJJ, Barendrecht E; *Electrochimica Acta*, **1985**, 30(11), 1433
- [35] Jakobs RCM, Janssen LJJ, Barendrecht E; *Electrochimica Acta*, **1985**, 30(8), 1085
- [36] Weidlich C, Mangold KM, Juttner K; *Electrochimica Acta*, **2005**, 50(7-8), 1547
- [37] Li FB, Albery WJ; *Journal of the Chemical Society-Faraday Transactions*, **1991**, 87(18), 2949
- [38] Hwang JH, Pyo M; *Bulletin of the Korean Chemical Society*, **2006**, 27(12), 2067
- [39] Lide DR; *CRC Handbook of Chemistry and Physics*; 2010, 90th ed., CRC Press

Chapter 6

Conclusions

6. Conclusions

In order to achieve the objectives of this study, the electrochemical properties of polypyrrole thin films were used to perform the electrodeposition of copper and zinc nanomaterials. Hierarchical copper-based micro/nanostructures and zinc-based nanothin sheets were obtained by applying suitable potentials to polypyrrole-polystyrene sulfonate (PPy-PSS) film-modified electrodes placed in copper or zinc sulfate electrolyte solutions. In accordance with the objectives, the mechanism of formation, chemical composition and morphology of these materials were characterized using cyclic voltammetry (CV), electrochemical quartz crystal microbalance (EQCM), scanning electron microscopy with energy dispersive X-ray analysis (SEM-EDX), X-ray photoelectron spectroscopy (XPS), attenuated total reflectance infrared spectroscopy (ATR-IR), X-ray diffraction (XRD) and Raman spectroscopy. In addition, these materials were further converted into metallic copper nanoparticles and metallic zinc micro-dendrites by electrochemical reduction. The electrodes modified with the metallic copper nanoparticles were applied for the sensing of nitrate ions. The use of PPy-PSS films as a tool for electrochemical fabrication was also addressed by preparing combined copper microstructures from the deposition of different forms of copper obtained and assembled at different electrode potentials. The key achievements of the study are described in more detail below.

The fundamental processes responsible for the electrodeposition of the nanomaterials were identified and characterized. The first process was related to the ability of the PPy-PSS film to capture or release cations depending on the electrode potential (Section 3.2.1.1). This property was used to increase the concentration of Cu^{2+} or Zn^{2+} at the film surface (Sections 3.2.1.2 and 5.2.1). The second process was the conversion of dissolved oxygen to hydroxide ions through the oxygen reduction reaction, which was enhanced by the PPy-PSS film (Section 3.2.4). This property was used to increase the local pH at the film surface and induce the electroprecipitation of double salts nanomaterials of copper or zinc (Sections 3.2.1.2 and 5.2.1). The third process was the direct deposition of copper or zinc species, such as hydroxides, oxides or metals, depending on the electrode potential and local pH at

the film surface. This property was used to prepare a variety of copper or zinc hydroxide/oxide species (Sections 4.2.1 and 5.2.5).

Hierarchical copper-based micro/nanostructures were prepared and characterized at the PPy-PSS film surface. The film was placed at 0.10 V vs. SCE in contact with an aerated or oxygen saturated 0.10 M CuSO₄ solution. The combination of the Cu²⁺ ions captured by the film, the OH⁻ ions generated from the reduction of the dissolved oxygen, and the SO₄²⁻ ions of the electrolyte solution caused the deposition of the micro/nanostructures. The structures were made of copper sulfate hydroxide hydrate, [CuSO₄]₂[Cu(OH)₂]₃·5H₂O, and posnjakite, CuSO₄[Cu(OH)₂]₃·H₂O. This elemental composition was deduced using EDX and XPS (Sections 3.2.2.4 and 3.2.2.5), the presence of sulfate and hydroxide ions was confirmed using ATR-IR and XPS (Sections 3.2.2.6 and 3.2.2.5), and the exact chemical structures were identified using XRD (Section 3.2.2.2). The EQCM analysis was also in agreement with the electrodeposition of this mixture (Section 3.2.2.3).

The mechanism of nucleation and growth of the copper-based micro/nanostructures were studied in detail to reveal some aspects of the electrodeposition. The structures were made from the assembly of nanoparticles into nanowires, nanosheets and microclusters (Section 3.2.3.1). The microcluster had a flower-like shape and each nanosheet formed a petal of the flower. The nucleation of the structures was shown to be progressive with the formation of new nuclei during the growth of the structures (Section 3.2.3.2). The growth was characterized by the formation of multilayered structures under two distinct diffusion-limited conditions. The first was related to the growth of the petals inside the forming clusters, while the second was probably related to the further growth of the formed clusters (Section 3.2.3.2).

The copper-based micro/nanostructures were reduced to metallic copper nanoparticles, which were used for the sensing of nitrate ions. The effect of the application of different reduction potentials to the micro/nanostructures was analyzed using CV and ATR-IR (Sections 3.2.2.1 and 3.2.2.6). When the micro/nanostructures were held at a potential of -1.00 V vs. SCE, part of the Cu(II) was converted to Cu(I) (Sections 3.2.2.1). When potentials of -0.70 and -1.50 V vs. SCE were applied the micro/nanostructures evolved from a mixture of copper sulfate hydroxide hydrate and posnjakite to brochantite and/or posnjakite (Section 3.2.2.6). The metallic copper

nanoparticles (CuNP) were formed by reduction of the micro/nanostructures at a potential of -2.00 V vs. SCE in 0.10 M Na_2SO_4 (Section 4.2.3). The PPy-PSS films modified with CuNP were investigated for use as a sensing interface for nitrate ions (Section 4.2.5.1). The performance of the sensor was characterized by a sensitivity of $99.0 \mu\text{A}/(\text{mM}\cdot\text{cm}^2)$, a linear range of $0.5 - 2.0$ mM, and a voltammetric detection limit of 0.5 mM nitrate.

The nitrate sensing performance of the CuNP-modified electrode was improved by introducing modified carbon nanotubes into the PPy-PSS films. Multiwall carbon nanotubes functionalized with branched polyethyleneimine (MWNT-PEI) were incorporated in the films which were further modified with CuNP (Section 4.2.4). The resulting PPy-PSS-MWNT-PEI-CuNP nanocomposite films were tested as a sensing interface for nitrate ions (Section 4.2.5.2). The sensor performance was characterized by a sensitivity of $137.2 \mu\text{A}/(\text{mM}\cdot\text{cm}^2)$, a linear range of $0.1 - 5.0$ mM, and a voltammetric detection limit of 0.1 mM nitrate. The detection limit was improved to $30 \mu\text{M}$ by constant potential amperometry using a rotating disk electrode. The electrical properties of the PPy-PSS and PPy-PSS-MWNT-PEI thin films were analyzed using Electrochemical Impedance Spectroscopy (EIS) in order to establish the causes for the improved performance of the nitrate sensor upon incorporation of the carbon nanotubes (Section 4.2.6). The impedance results showed that the use of MWNT-PEI improved the electrical conductivity of the films by decreasing the film resistance by two orders of magnitude (Sections 4.2.6.1 and 4.2.6.2).

Combined copper-based microstructures were prepared at the PPy-PSS film surface. The effect of the electrodeposition potential on the composition and morphology of the copper materials was evaluated at 0.10 , 0.00 and -0.10 V vs. SCE (Section 4.2.1). Different materials were formed at each potential. In particular, copper oxide (possibly Cu_2O) microcrystals were formed at -0.10 V vs. SCE. The hierarchical micro/nanostructures and the microcrystals were combined together to generate new hybrid structures in which the petals of the copper-based structures were deposited all around each microcrystal (Section 4.2.2). This was possible through a simple fabrication procedure where the central microcrystals were deposited first at a potential of -0.10 V vs. SCE and then surrounded with petals at 0.10 V vs. SCE using the same electrolyte solution.

Zinc-based nanothin sheets were formed and characterized on the PPy-PSS films. A film was placed at 0.00 V vs. SCE in contact with a 0.10 M ZnSO₄ aerated or oxygen saturated solution. As seen for copper, the increased concentration of the Zn²⁺, OH⁻ and SO₄²⁻ ions at the film surface caused the deposition of the nanosheets. These were made of zinc sulfate hydroxide hydrate, ZnSO₄[Zn(OH)₂]₃·5H₂O. The elemental composition was confirmed using EDX and XPS (Sections 5.2.2.3 and 5.2.2.4), the presence of sulfate and hydroxide ions was identified using ATR-IR and XPS (Sections 5.2.2.5 and 5.2.2.4), and the exact chemical structure was characterized by XRD (Section 5.2.2.1). The EQCM analysis was also in agreement with the electrodeposition of this compound (Section 5.2.2.2).

The mechanism of nucleation and growth of the zinc-based nanothin sheets was analyzed to elucidate some features of the electrodeposition. Hexagonal-shaped layers were formed on the top of the film during the nucleation stage (Section 5.2.3.1). The nucleation was shown to be instantaneous with all the first nuclei formed at the start of the electrodeposition (Section 5.3.2.3). After the nucleation, other layers were deposited both on top of the layers previously formed and on the film (Section 5.3.2.3). At this stage, the growth of the nanosheets did not follow either an instantaneous or a progressive mechanism.

The zinc-based nanosheets were reduced to metallic zinc micro-dendrites and possibly to zinc oxide nanocrystals. The films modified with the nanosheets were reduced at a potential of -2.50 V vs. SCE in aerated 0.10 M Na₂SO₄ to form metallic zinc micro-dendrites (Section 5.2.5). Two other phases were also found on the film after the reduction treatment. One was likely to be made of zinc hydroxide and the other one of zinc oxide. The zinc oxide deposit was in the form of microclusters made of several nanocrystals.

The electrodeposition of the zinc-based nanosheets was performed under different experimental conditions. (Section 5.2.4). The effect of the dopant, electrolyte counterion and pH, potential of electrodeposition, and presence of dissolved oxygen, were considered. The nanosheets were formed only on PPy-PSS films, and not on PPy films doped with different sulfated/sulfonate dopants (Section 5.2.4.2). The deposition did not take place in chloride or nitrate electrolytes (Section 5.2.4.2) or under acidic conditions (Section 5.2.4.3). The nanosheets formed at lower potentials,

−0.25, −0.50 and −1.00 V vs. SCE, were of smaller size but always of the same elemental composition (Section 5.2.4.1). In nitrogen saturated solutions the deposition did not take place, which indicated that oxygen was a key reactant in the electrodeposition of both the copper-based and zinc-based nanomaterials (Sections 3.2.1.2 and 5.2.4.3).

The electrochemical deposition of nanostructured double basic salts, such as hierarchical copper micro/nanostructures and zinc nanosheets made of hydroxysulfates, at the PPy-PSS film represents a new synthetic route to fabricate materials that are usually formed using hydrothermal methods.

The achievements of the present study are certainly a tangible example of how the subtle control of the interfacial processes of polypyrrole thin films can be used as a tool for the electrochemical deposition and fabrication of micro/nanomaterials.

